

The Elastic Properties of Wadsleyite and Stishovite at High Pressures

Tracing Deep Earth Material Cycles

DISSERTATION

zur Erlangung des akademischen Grades eines Doktors
der Naturwissenschaften (Dr. rer. nat.)
in der Bayreuther Graduiertenschule für Mathematik
und Naturwissenschaften (BayNAT)
der Universität Bayreuth

vorgelegt von

Johannes Buchen

aus *Kirchen (Sieg)*

Bayreuth, 2018

The Elastic Properties of Wadsleyite and Stishovite at High Pressures

Tracing Deep Earth Material Cycles

DISSERTATION

zur Erlangung des akademischen Grades eines Doktors
der Naturwissenschaften (Dr. rer. nat.)
in der Bayreuther Graduiertenschule für Mathematik
und Naturwissenschaften (BayNAT)
der Universität Bayreuth

vorgelegt von

Johannes Buchen

aus *Kirchen (Sieg)*

Bayreuth, 2018

Die vorliegende Arbeit wurde in der Zeit von Mai, 2014 bis August, 2018 in Bayreuth am Bayerischen Geoinstitut unter Betreuung von Herrn Prof. Dr. Hauke Marquardt angefertigt.

Vollständiger Abdruck der von der Bayreuther Graduiertenschule für Mathematik und Naturwissenschaften (BayNAT) der Universität Bayreuth genehmigten Dissertation zur Erlangung des akademischen Grades eines Doktors der Naturwissenschaften (Dr. rer. nat.).

Dissertation eingereicht am: 06. August 2018

Zulassung durch das Leitungsgremium: 08. August 2018

Wissenschaftliches Kolloquium: 13. September 2018

Amtierender Direktor: Prof. Dr. Dirk Schüler

Prüfungsausschuss:

Prof. Dr. Hauke Marquardt (Gutachter)

Prof. Dr. Daniel J. Frost (Gutachter)

PD Dr. habil. Catherine A. McCammon (Vorsitz)

Prof. Dr. Hans Keppler

(Weiterer Gutachter: Prof. Dr. Hans Keppler)

The Elastic Properties of Wadsleyite and Stishovite at High Pressures

— Tracing Deep Earth Material Cycles

Johannes Buchen

To Simon and Hermann Josef

Abstract

Plate tectonics on Earth is integrated into global material cycles that exchange chemical components between Earth's surface and Earth's mantle. At subduction zones, slabs of oceanic lithosphere sink into the mantle and carry basaltic crust and H₂O stored in hydrous minerals into Earth's interior. A fraction of the stored H₂O might reach the transition zone at 410 km depth where the phase transition of the mineral olivine to the high-pressure polymorph wadsleyite, β -(Mg,Fe)₂SiO₄, gives rise to a discontinuity in seismic wave speeds. Under favorable conditions, nominally anhydrous wadsleyite can incorporate up to 3 wt-% H₂O as hydroxyl groups in its crystal structure. The high solubility of H₂O in wadsleyite may have had consequences for deep cycling of H₂O in Earth's mantle throughout the geological past. Even small amounts of H₂O in Earth's mantle may lower the melting point and viscosity of mantle rocks and affect the geodynamical and geochemical evolution of the mantle. Despite the key role of the transition zone in deep cycling of H₂O, little is known about the amount and distribution of H₂O in the transition zone. Seismic waves that travel through the transition zone or reflect off the 410-km seismic discontinuity carry a signature of the compositional and thermal state of the transition zone. To read this signature, the elastic properties of relevant minerals and rocks are needed, ideally at pressures and temperatures of the transition zone, e. g. 14 GPa and 1500°C at 410 km depth.

I performed high-pressure X-ray diffraction experiments on wadsleyite single crystals up to 20 GPa using a diamond anvil cell and determined the equation of state (EOS) from the variation of unit cell volume as a function of pressure. With Fe/(Mg+Fe) = 0.11 and 0.24 wt-% structurally bound H₂O, the wadsleyite crystals had a chemical composition relevant for the transition zone. I combined the EOS of the here-studied crystals with literature data to construct a multi-end-member model for the EOS of wadsleyite solid solutions. The model shows that the bulk modulus of wadsleyite increases with the ferrous iron content but decreases with increasing contents of H₂O and ferric iron.

To determine the elastic stiffness tensors at high pressures and high temperatures, I performed Brillouin spectroscopy experiments on wadsleyite single crystals that were loaded pairwise into diamond anvil cells. The collected sound wave velocities were inverted to parameters of finite-strain theory using a novel inversion strategy. Aggregate sound wave velocities calculated from the high-pressure elastic properties of the here-studied wadsleyite crystals were compared to literature data on different wadsleyite compositions to assess the effect of structurally bound H₂O on sound wave velocities. At ambient conditions, the incorporation of H₂O reduces the sound wave velocities of Fe-bearing wadsleyite. The comparison with literature data on Fe-bearing wadsleyite with a high H₂O content, however, reveals that both P and S wave velocities of Fe-bearing wadsleyite with high H₂O content converge and potentially cross over with those of the here-studied wadsleyite with low H₂O content at pressures of the transition zone. These findings imply that seismic wave speeds may be less sensitive to H₂O in the transition zone than previously assumed. Instead, modeling of seismic properties based on the experimental results of the present study combined with literature data suggests that a low acoustic impedance contrast and hence a locally reduced reflectivity of the 410-km seismic discontinuity may be a better indicator for H₂O in the shallow transition zone. I further present the first experimentally determined elastic stiffness tensors of wadsleyite at simultaneously high pressures and high temperatures.

Oceanic crust that enters the mantle at subduction zones transforms into an assemblage of dense high-pressure phases that allow basaltic material to sink into the lower mantle. Stishovite, rutile-structured SiO₂, may contribute with up to 20 vol-% to a basaltic rock at

conditions of the lower mantle. The ferroelastic phase transition from stishovite to high-pressure CaCl_2 -type SiO_2 strongly perturbs the elastic properties of these crystalline silica phases. I analyzed X-ray diffraction patterns that were recorded on sintered polycrystalline silica along a compression path across the ferroelastic phase transition and refined the lattice parameters of sintered polycrystalline silica at 30 different pressures between 9 and 73 GPa. Based on the pressure evolution of unit cell volumes and edge lengths, I determined the EOS and described the elastic properties of sintered polycrystalline silica using Landau theory. Unlike silica powder, sintered polycrystalline silica shows a substantial drop of the bulk modulus at the phase transition from stishovite to CaCl_2 -type SiO_2 . Together with the previously predicted shear wave softening, the drop in bulk modulus might affect the propagation of seismic waves raising the possibility to detect silica-rich rocks in Earth's lower mantle and thereby to better constrain mantle convection patterns.

Zusammenfassung

Die Plattentektonik auf der Erde ist in globale Materialkreisläufe eingebunden, die chemische Komponenten zwischen der Erdoberfläche und dem Erdmantel austauschen. An Subduktionszonen sinken Platten ozeanischer Lithosphäre in den Erdmantel und befördern basaltische Erdkruste und in Mineralen gespeichertes Wasser ins Erdinnere. Ein Teil des gespeicherten Wassers könnte die Übergangszone in einer Tiefe von 410 km erreichen, bei welcher der Phasenübergang des Minerals Olivin zum Hochdruck-Polymorph Wadsleyit, β - $(\text{Mg,Fe})_2\text{SiO}_4$, eine Diskontinuität in seismischen Wellengeschwindigkeiten erzeugt. Unter günstigen Bedingungen kann nominell wasserfreier Wadsleyit bis zu 3 Gew-% H_2O als Hydroxylgruppen in seine Kristallstruktur einbauen. Die hohe Löslichkeit von H_2O in Wadsleyit könnte im Laufe der geologischen Vergangenheit Auswirkungen auf den tiefen H_2O -Kreislauf im Erdmantel gehabt haben. Bereits geringe Mengen von H_2O im Erdmantel können den Schmelzpunkt und die Viskosität der Gesteine des Erdmantels herabsetzen und die geodynamische und geochemische Entwicklung des Erdmantels beeinflussen. Trotz der Schlüsselrolle der Übergangszone im tiefen H_2O -Kreislauf ist nur wenig über die Menge und die Verteilung von H_2O in der Übergangszone bekannt. Seismische Wellen, welche die Übergangszone durchlaufen oder an der seismischen Diskontinuität in 410 km Tiefe reflektiert werden, tragen eine Signatur der Zusammensetzung und des thermischen Zustands der Übergangszone. Um diese Signatur zu lesen, bedarf es der elastischen Eigenschaften relevanter Minerale und Gesteine, idealerweise bei Drücken und Temperaturen der Übergangszone, zum Beispiel 14 GPa und 1500°C in 410 km Tiefe.

Ich habe Hochdruck-Röntgenbeugungsexperimente an Wadsleyit-Einkristallen bis zu 20 GPa unter Verwendung einer Diamantstempelzelle durchgeführt und die Zustandsgleichung (EOS) aus der Veränderung des Elementarzellenvolumens als Funktion des Drucks bestimmt. Mit einem Verhältnis von $\text{Fe}/(\text{Mg}+\text{Fe}) = 0.11$ und 0.24 Gew-% in der Kristallstruktur gebundenem H_2O hatten die Wadsleyit-Kristalle eine für die Übergangszone relevante chemische Zusammensetzung. Um ein Modell für die EOS von Wadsleyit-Mischkristallen mehrerer Endglieder zu erstellen, habe ich die EOS der hier untersuchten Kristalle mit Literaturdaten kombiniert. Das Modell zeigt, dass der Kompressionsmodul von Wadsleyit mit dem Gehalt an zweiwertigem Eisen ansteigt aber mit steigenden Gehalten an H_2O und dreiwertigem Eisen abnimmt.

Um die Elastizitätstensoren bei hohen Drücken und hohen Temperaturen zu bestimmen, habe ich Brillouin-Spektroskopie an Wadsleyit-Einkristallen durchgeführt, die paarweise in

Diamantstempelzellen geladen wurden. Die gemessenen Schallwellengeschwindigkeiten wurden mit einer neuartigen Inversionsstrategie zu Parametern der Theorie finiter Dehnungen invertiert. Die Schallwellengeschwindigkeiten polykristalliner Aggregate wurden aus den elastischen Eigenschaften der hier untersuchten Wadsleyit-Kristalle bei hohen Drücken berechnet und mit Literaturdaten für verschiedene Wadsleyit-Zusammensetzungen verglichen, um den Einfluss von in der Kristallstruktur gebundenem H_2O auf die Schallwellengeschwindigkeiten auszuwerten. Bei Raumbedingungen verringert die Aufnahme von H_2O die Schallwellengeschwindigkeiten von Fe-haltigem Wadsleyit. Der Vergleich mit Literaturdaten für Fe-haltigen Wadsleyit mit hohem H_2O -Gehalt zeigt jedoch, dass die Geschwindigkeiten sowohl der P- als auch der S-Wellen von Fe-haltigem Wadsleyit mit hohem H_2O -Gehalt mit denjenigen vom hier untersuchten Wadsleyit mit geringem H_2O -Gehalt bei Drücken der Übergangszone zusammen laufen und sich möglicherweise überkreuzen. Dies bedeutet, dass die Geschwindigkeiten seismischer Wellen weniger empfindlich für H_2O in der Übergangszone sein könnten als bisher angenommen. Stattdessen legt die Modellierung seismischer Eigenschaften basierend auf den experimentellen Ergebnissen der vorliegenden Studie zusammen mit Literaturdaten nahe, dass ein geringer Kontrast in der akustischen Impedanz und damit ein lokal reduziertes Reflexionsvermögen der seismischen Diskontinuität in 410 km Tiefe ein besseres Anzeichen für H_2O in der oberen Übergangszone sein könnte. Des Weiteren lege ich die ersten experimentell bei gleichzeitig hohen Drücken und hohen Temperaturen bestimmten Elastizitätstensoren von Wadsleyit vor.

Ozeanische Erdkruste, die an Subduktionszonen in den Erdmantel gelangt, wandelt sich in ein Gemisch dichter Hochdruck-Phasen um, die es dem basaltischen Material erlauben in den unteren Erdmantel zu sinken. Stishovit, SiO_2 in Rutil-Struktur, könnte mit bis zu 20 Vol-% zu einem basaltischen Gestein unter den Bedingungen des unteren Erdmantels beitragen. Der ferroelastische Phasenübergang von Stishovit zu SiO_2 in einer Hochdruck- CaCl_2 -Struktur verändert stark die elastischen Eigenschaften dieser kristallinen Siliciumdioxid-Phasen. Ich habe Röntgenbeugungsmuster, die an gesintertem polykristallinem Siliciumdioxid entlang eines Kompressionspfades über den Phasenübergang aufgenommen wurden, ausgewertet und die Gitterparameter von gesintertem polykristallinem Siliciumdioxid bei 30 verschiedenen Drücken zwischen 9 und 73 GPa verfeinert. Basierend auf der Veränderung der Volumina und der Kantenlängen der Elementarzelle mit steigendem Druck habe ich die EOS bestimmt und die elastischen Eigenschaften von gesintertem polykristallinem Siliciumdioxid mittels Landau-Theorie beschrieben. Im Gegensatz zu Siliciumdioxid-Pulver zeigt gesintertes polykristallines Siliciumdioxid einen deutlichen Abfall des Kompressionsmoduls am Phasenübergang von Stishovit zu SiO_2 in CaCl_2 -Struktur. Zusammen mit der bereits früher vorhergesagten elastischen Erweichung gegenüber Scherwellen könnte der Abfall des Kompressionsmoduls die Ausbreitung von seismischen Wellen beeinflussen, was die Möglichkeit eröffnen würde, Gesteine reich an Siliciumdioxid im unteren Erdmantel zu erkennen und damit die Muster der Konvektion im Erdmantel besser nachzuvollziehen.

Acknowledgments

I would like to thank my supervisor, Prof. Dr. Hauke Marquardt (University of Oxford & Bayerisches Geoinstitut, BGI), for providing me with the opportunity and freedom to follow my scientific curiosity while, at the same time, guiding me to become an independent researcher, for his continuous support throughout my PhD project, and for his original scientific perspectives that contributed to the findings of the present study in a fundamental way. I thank Dr. Tiziana Boffa Ballaran (BGI) for introducing me into the art of single-crystal X-ray diffraction and for sharing her valuable experience with equations of state and Dr. Alexander Kurnosov (BGI) for his selfless support in preparing and performing experiments and for his critical input to the analysis of sound wave velocities. I further thank Dr. Sergio Speziale (Deutsches GeoForschungsZentrum) for providing access to the Brillouin spectroscopy facility at the Deutsches Elektronen-Synchrotron DESY in Hamburg and for his helpful advice on experimental and theoretical aspects of Brillouin spectroscopy. I appreciate the help of Prof. Dr. Takaaki Kawazoe (University of Hiroshima, formerly BGI), Dr. Svyatoslav Shcheka (BGI), and Dr. Robert Myhill (University of Bristol, formerly BGI) with the synthesis of sample materials and would like to thank Prof. Dr. Norimasa Nishiyama (Tokyo Institute of Technology) for sharing his sample of sintered polycrystalline stishovite. I thank Prof. Dr. Hans Keppler (BGI) for access and instructions to use the FTIR spectrometer and Dr. Catherine McCammon (BGI) for recording and analyzing Mössbauer spectra of wadsleyite and ferropericlase. I thank Hubert Schulze (BGI) and Raphael Njul (BGI) for sample preparation and Detlef Krauß (BGI) and Anke Potzel (BGI) for performing electron microprobe analyses. For getting me involved in their projects, I thank Kirsten Schulze (BGI), Julia Immoor (BGI), Niccolò Satta (BGI), Joana Polednia (BGI), Dr. Morvarid Saki (University of Münster), and Alba San José Méndez (BGI). I also would like to thank the whole BGI staff for providing an excellent professional environment in terms of both scientific infrastructure and human relations and my friends at BGI for life outside of the laboratory.

For lifelong and unconditional support and love, I thank my parents, Hubert and Gertrud, my brothers, Philipp and Stefan, and my family for their patience and understanding.

Contents

1	Introduction	1
1.1	The Link between Water and Tectonics on Earth	1
1.1.1	The Transition Zone in Earth's Mantle	3
1.1.2	The Fate of Oceanic Crust in Earth's Lower Mantle	5
1.2	Geophysical Observables	5
1.2.1	The Velocities of Seismic Waves	6
1.2.2	Seismic Anisotropy	6
1.2.3	Reflection and Scattering of Seismic Waves	7
1.3	Mantle Minerals at Focus	9
1.3.1	Wadsleyite	9
1.3.2	Stishovite and CaCl ₂ -Type Silica	11
2	Experimental	15
2.1	Synthesis of High-Pressure Minerals	15
2.1.1	Synthesis of High-Quality Wadsleyite Single Crystals	15
2.1.2	Synthesis of Ferropicricle Single Crystals	19
2.2	Characterization of Samples for High-Pressure Experiments	23
2.2.1	Electron Microprobe Analysis	23
2.2.2	Assessment of Crystal Quality	26
2.2.3	Fourier-Transform Infrared Absorption Spectroscopy	27
2.3	High-Pressure Experiments with Diamond Anvil Cells	31
2.3.1	Sample Preparation by Focused Ion Beam Cutting	31
2.3.2	Assembly of the Diamond Anvil Cell	32
2.3.3	Pressure and Temperature Determination	33
2.4	Determination of Elastic Properties at High Pressures	35
2.4.1	X-Ray Diffraction at High Pressures	37
2.4.2	Brillouin Spectroscopy at High Pressures	42
3	Results and Discussion	51
3.1	The Equation of State of Wadsleyite	51
3.2	From Sound Wave Velocities to Single-Crystal Elasticity	53
3.3	High-Pressure Single-Crystal Elasticity of Wadsleyite	54
3.4	HP-HT Single-Crystal Elasticity of Wadsleyite	57
3.5	High-Pressure Elasticity of Stishovite	61
	References	65
	List of Manuscripts and Statements of Author Contributions	87

4	The Equation of State of Wadsleyite Solid Solutions: Constraining the Effects of Anisotropy and Crystal Chemistry	89
4.1	Introduction	90
4.2	Experimental	91
4.2.1	Single-Crystal Synthesis and Chemical Composition	91
4.2.2	Mössbauer Spectroscopy	91
4.2.3	Single-Crystal X-Ray Diffraction at Ambient Conditions	92
4.2.4	Fourier-Transform Infrared Absorption Spectroscopy	92
4.2.5	Sample Preparation and High-Pressure Experiments	94
4.2.6	High-Pressure Single-Crystal X-Ray Diffraction	94
4.3	Results and Discussion	94
4.3.1	Equation of State	94
4.3.2	Anisotropic Compression Behavior	96
4.3.3	Equation of State of Wadsleyite Solid Solutions	97
4.3.4	Relationship of Compression Behavior to Crystal Chemistry	102
4.3.5	Bulk Modulus Systematics	103
4.4	Implications	105
	Author Contributions	106
	References	106
5	High-Pressure Elastic Properties of Single Crystals from Sound Wave Velocities: Comparing Self-Consistent Inversion Schemes	113
5.1	Introduction	114
5.2	Outline of the Inversion Procedure	114
5.2.1	Coordinate Systems	115
5.2.2	Sound Wave Velocities in Anisotropic Media	116
5.2.3	Finite-Strain Formulation of High-Pressure Elastic Properties	117
5.3	Testing Inversion Strategies	120
5.3.1	Synthetic Data Set	121
5.3.2	Inversion Strategies	122
5.3.3	Inversion Results: Elastic Stiffness Tensors	123
5.3.4	Inversion Results: Aggregate Elastic Moduli	125
5.4	Discussion of Correlations and Systematic Errors	128
5.5	Conclusions	130
	Author Contributions	131
	References	131
6	High-Pressure Single-Crystal Elasticity of Wadsleyite and the Seismic Signature of Water in the Shallow Transition Zone	133
6.1	Introduction	134
6.2	Experimental	135
6.2.1	Sample Synthesis and Characterization	135
6.2.2	High-Pressure Experiments	136
6.2.3	Brillouin Spectroscopy and X-Ray Diffraction	137
6.3	Results and Discussion	137
6.3.1	High-Pressure Elasticity	137
6.3.2	Aggregate Sound Wave Velocities	139
6.3.3	Modeling of Sound Wave Velocities	142

6.3.4	Sound Wave Velocities of Wadsleyite	142
6.3.5	Seismic Contrasts across the 410-km Discontinuity	144
6.4	Conclusion	148
	Author Contributions	148
	References	149
7	Equation of State of Polycrystalline Stishovite across the Tetragonal-Orthorhombic Phase Transition	155
7.1	Introduction	156
7.2	Experimental	157
7.3	EOS of Sintered Polycrystalline Stishovite	160
7.4	Landau Theory Analysis	163
7.5	Elasticity of Stishovite across the Ferroelastic Phase Transition	166
7.6	Sound Wave Velocities of Stishovite and Geophysical Implications	168
	Author Contributions	171
	References	171
A	Appendix	175
A.1	The Equation of State of Wadsleyite Solid Solutions	175
A.1.1	Supplementary Methods	175
A.1.2	Supplementary Figures	179
A.1.3	Supplementary Tables	185
A.2	High-Pressure Single-Crystal Elasticity of Wadsleyite	192
A.2.1	Supplementary Figures and Tables	192
	Supplementary References	195

Figures

1.1	Deep Cycling of H ₂ O and Dispersal of Basaltic Crust in Earth's Mantle	2
1.2	Seismic Structure and Mineralogy of Earth's Mantle	4
1.3	Crystal Structure of Wadsleyite	10
1.4	Crystal Structures of Stishovite and CaCl ₂ -Type SiO ₂	12
2.1	Phase Diagram of the System (Mg,Fe) ₂ SiO ₄	16
2.2	Oxygen Fugacities for Buffer Reactions	16
2.3	Experimental Setup for Wadsleyite Synthesis in a Multi-Anvil Press	18
2.4	Photomicrographs of Synthesized Wadsleyite Grains	19
2.5	Modeled Fe-Mg Interdiffusion Profiles in (Mg,Fe)O	20
2.6	Setup for Fe-Mg Interdiffusion Experiments in a Piston-Cylinder Press	21
2.7	Photomicrographs of Synthesized Ferropericlase Samples	22
2.8	Photomicrograph of a Ferropericlase Single Crystal	23
2.9	Electron Microprobe Analysis of Wadsleyite	25
2.10	Electron Microprobe Analysis of Fe-Mg Interdiffusion Profiles in (Mg,Fe)O	25
2.11	X-Ray Reflection Profiles of Wadsleyite Crystals	26
2.12	Fourier-Transform Infrared Spectrometer	27
2.13	FTIR Absorption Spectroscopy on Wadsleyite Crystals	28
2.14	Photomicrograph and FTIR Absorption Spectra of a Wadsleyite Twin	30
2.15	Focused Ion Beam Cutting of a Wadsleyite Crystal	32
2.16	Diamond Anvil Cell	33
2.17	Fluorescence Spectra of Ruby and Sm:YAG	34
2.18	Four-Circle Eulerian Cradle	38
2.19	Experimental Setup for Powder X-Ray Diffraction at High Pressures	41
2.20	Inelastic Photon-Phonon Scattering	43
2.21	Dispersion of Acoustic Waves	44
2.22	Experimental Setup for Brillouin Spectroscopy at High Pressures	45
2.23	Analysis of Brillouin Spectra	48
3.1	Isothermal Bulk Modulus of Wadsleyite Solid Solutions	52
3.2	Bulk and Shear Moduli of Hydrous Wadsleyites	55
3.3	HP-HT Sound Wave Velocities of Wadsleyite Single Crystals	58
3.4	HP-HT Sound Wave Velocities of Fe-Bearing Wadsleyite	59
3.5	Acoustic Anisotropy of a Wadsleyite Single Crystal	60
3.6	Compressional Anisotropy of Stishovite	61
3.7	Sound Wave Velocities of Mantle Rocks	63
4.1	Compression Curves of Wadsleyite Crystal Sections	95
4.2	Wadsleyite Compositions of the EOS Data Set	99

4.3	Isothermal Bulk Moduli of Fe-Bearing and Hydrous Wadsleyites	102
4.4	Bulk Modulus Systematics for Wadsleyite Solid Solutions	104
5.1	Sampling of Single-Crystal Sound Wave Velocities	121
5.2	Deviations for Components of the Elastic Stiffness Tensor	124
5.3	Components of the Elastic Stiffness Tensor at High Pressures	125
5.4	Deviations for Elastic Moduli	128
5.5	Correlations between Finite-Strain Parameters	129
6.1	High-Pressure Elasticity Measurements	136
6.2	High-Pressure Single-Crystal Elastic Constants of Different Wadsleyites	138
6.3	Effect of Hydration on the Sound Wave Velocities of Fe-Bearing Wadsleyite	140
6.4	High-Pressure Elastic Properties of Different Wadsleyites	141
6.5	Variation of Sound Wave Velocities with Wadsleyite Composition	143
6.6	Ratios of Sound Wave Velocity Variations for Wadsleyite	144
6.7	Seismic Contrasts across the Olivine-Wadsleyite Phase Transition	146
7.1	X-Ray Diffraction Patterns of Polycrystalline SiO ₂ at High Pressures	158
7.2	Compression Curves of Stishovite and CaCl ₂ -Type SiO ₂	161
7.3	Spontaneous Strains in CaCl ₂ -Type SiO ₂	166
7.4	Elasticity of Stishovite and CaCl ₂ -Type SiO ₂ at High Pressures	168
7.5	Sound Wave Velocities of Stishovite and CaCl ₂ -Type SiO ₂ at High Pressures	169
A.1	Mössbauer Spectrum of Fe-Bearing Wadsleyite	179
A.2	FTIR Absorption Spectra of Wadsleyite Crystal Sections	180
A.3	Analysis of FTIR Absorption Spectra of Wadsleyite	180
A.4	Orientation Relationships for Wadsleyite Crystal Sections	181
A.5	Comparison of the Compression Behavior of Wadsleyite Crystal Sections	181
A.6	<i>F-f</i> Plots for Wadsleyite Crystal Sections	182
A.7	Compression Curves of Fe-Bearing and Hydrous Wadsleyites	183
A.8	Isothermal Linear Moduli of Fe-Bearing and Hydrous Wadsleyites	184
A.9	Sound Wave Velocities and Densities of Different Wadsleyites	192
A.10	Impedance Contrasts across the Olivine-Wadsleyite Phase Transition	192

Tables

2.1	Wadsleyite Synthesis Experiments	17
2.2	Parameters for Electron Microprobe Analysis of Wadsleyite	24
2.3	Hydrogen Concentrations in Wadsleyite Crystals	29
2.4	Brillouin Spectroscopy Setups	47
3.1	Single-Crystal Elastic Properties for Different Wadsleyite Compositions	56
3.2	HP-HT Elastic Properties of Fe-Bearing Wadsleyite Single Crystals	56
3.3	Compression Moduli of Stishovite	62
4.1	Crystallographic Properties of Wadsleyite Crystal Sections	93
4.2	EOS Parameters for Wadsleyite Crystal Sections	96
4.3	EOS Parameters for Wadsleyite End Members (Reuss Model)	100
5.1	Single-Crystal Finite-Strain Parameters	126
5.2	Aggregate Finite-Strain Parameters	126
6.1	Finite-Strain Parameters for Fe-Bearing Wadsleyite	139
6.2	Olivine and Wadsleyite Species for Modeling Seismic Properties	145
7.1	Unit Cell Parameters of Polycrystalline SiO ₂ at High Pressures	159
7.2	EOS Parameters for Stishovite and CaCl ₂ -Type SiO ₂	162
7.3	Landau Theory Parameters for Stishovite and CaCl ₂ -Type SiO ₂	167
A.1	Electron Microprobe Analysis of Fe-Bearing Wadsleyite	185
A.2	Hyperfine Parameters of Fe-Bearing Wadsleyite	185
A.3	EOS Parameters for Wadsleyite End Members (Voigt Model)	185
A.4	Hydrogen Concentrations from FTIR Absorption Spectra of Wadsleyite	186
A.5	Unit Cell Parameters of Fe-Bearing Wadsleyite at High Pressures	187
A.6	Unit Cell Parameters for Different Wadsleyite Compositions	188
A.6	(continued)	189
A.7	Wadsleyite EOS Data Set	190
A.7	(continued)	191
A.8	Elastic Properties of Fe-Bearing Wadsleyite at High Pressures	193
A.9	Covariance and Correlation Matrices	194

Chapter 1

Introduction

This study focuses on the elastic properties of wadsleyite and stishovite at high pressures with the perspective to detect water and silica-rich rocks in Earth's mantle. Seismology offers a variety of observables that promise to improve our conception of deep Earth processes. The translation of seismic observations into the thermal and compositional structure of the mantle, however, relies on information on the thermodynamic and seismic properties of mantle rocks. Here, I emphasize how the interpretation of seismic observables in terms of the hydration state of the transition zone and the entrainment of subducted oceanic crust in Earth's lower mantle critically depends on the elastic properties of wadsleyite and stishovite, respectively. The elastic and thermodynamic properties of these minerals, in turn, reflect processes operating on the atomic scale.

1.1 The Link between Water and Tectonics on Earth

Earth differs from other terrestrial planets in the Solar System by two striking features: oceans and active plate tectonics. Although recent evidence points to surface water on Mars (Ojha et al., 2015; Orosei et al., 2018), and the surface of Mars probably hosted liquid water in the past (Baker et al., 1991; Grotzinger, 2009), oceans are unique to Earth. The present-day distribution of water, or more general H_2O , on Earth between the surface reservoirs of atmosphere and hydrosphere and reservoirs in Earth's crust and mantle reflects the time-integrated results of planetary accretion and differentiation. Today, Earth's mantle differentiates into basaltic crust and depleted peridotite at mid-ocean ridges. Plate tectonics transport oceanic crust away from spreading centers towards subduction zones where cold and dense oceanic lithosphere sinks into the mantle. On the way, basaltic oceanic crust and the underlying peridotite react with ocean water through hydrothermal activity and take up H_2O in the form of hydrous minerals such as amphibole, chlorite, and serpentine (e. g. Humphris and Thompson, 1978; Mével, 2003; Staudigel, 2003; Bach et al., 2004). Most of these hydrous minerals, however, break down during subduction and release H_2O in dehydration reactions. The released aqueous fluids migrate upward into the mantle wedge above the subducting plate where they can trigger melting and give rise to arc volcanism (Pawley and Holloway, 1993; Schmidt and Poli, 1998; Poli and Schmidt, 2002; Eiler, 2003). Aqueous fluids released by dehydration reactions may also react with the overlying peridotite and form serpentine minerals (e. g. Evans, 1977; Hyndman and Peacock, 2003; Hirth and Guillot, 2013). In cold subduction zones, hydrous minerals hosted by different lithologies of subducted slabs may carry H_2O down to depths in excess of 200 km (Poli and Schmidt,

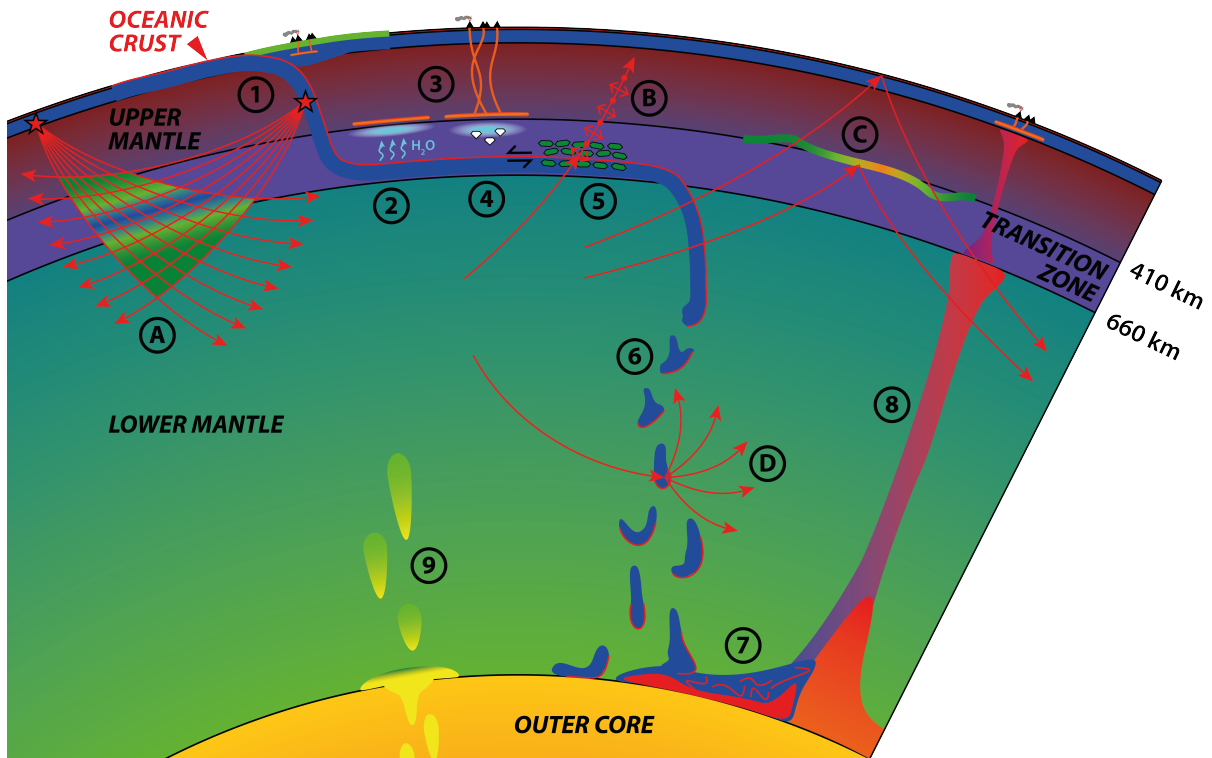


Figure 1.1: Conceptual drawing of deep H_2O cycling and dispersal of basaltic crust in Earth's mantle illustrating potential processes (1–9) and seismic observables (A–D); see text for references. 1) Hydrated oceanic lithosphere (basaltic crust in red, lithospheric mantle in dark blue) sinks into the upper mantle at subduction zones. 2) Release of H_2O from the slab hydrates the transition zone. 3) Melting atop the 410-km seismic discontinuity gives rise to deep seated magmatism. 4) Diamonds form in the transition zone and enclose transition zone minerals and fluids. 5) Deformation aligns anisotropic minerals. 6) Mantle convection disperses subducted oceanic crust in the lower mantle. 7) Subducted oceanic crust accumulates to form geochemical heterogeneities. 8) Plumes probe geochemical heterogeneities. 9) Silica-rich material exsolves from the outer core and gets dispersed in the lower mantle. A) Seismic tomography images three-dimensional variations in seismic velocities. B) Deformed mantle rocks generate seismic anisotropy. C) Seismic discontinuities reflect seismic waves. D) Heterogeneities scatter seismic waves in the lower mantle.

1995; Ono, 1998; Schmidt and Poli, 1998). A chain linking the stability fields of hydrous minerals may allow to transport H_2O into deeper parts of the mantle, at least along cold subduction paths (Poli and Schmidt, 2002; Ohtani et al., 2004; Komabayashi, 2006; Nishi et al., 2014).

The transport of H_2O from Earth's surface into Earth's deep interior via subduction processes highlights the connection between the evolution of terrestrial H_2O reservoirs and plate tectonics. The operation of plate tectonics in a similar way as today, i. e. including cold geotherms, can be traced back to the Neoproterozoic (Stern, 2008) implying the potential to transport H_2O into the mantle for about 1 Ga. The tectonic regime during the Archean remains debated (Condie and Pease, 2008; van Hunen and Moyen, 2012). Petrological evidence can be found in support of both subduction (Foley et al., 2002; Foley, 2008) and delamination-dominated processes (Foley et al., 2003; Johnson et al., 2014; Johnson et al., 2017) that led to the formation of early continental crust. The production of typical

Archean tonalite-trondhjemite-granodiorite (TTG) rocks, however, requires partial melting of hydrated basaltic rocks (Rapp and Watson, 1995; Foley et al., 2002). Similar to modern times, hydrated basaltic rocks might have been the starting point for early cycling of H₂O into Earth's mantle since the Archean. Indeed, the low present-day volume of basaltic crust on Earth indicates substantial recycling of earlier mafic crust into the mantle in the geological past (Anderson and Bass, 1986; Herzberg and Rudnick, 2012), a hypothesis that could also explain geochemical observations (Hofmann and White, 1982; Christensen and Hofmann, 1994; Hofmann, 1997) and reconcile the Mg/Si ratio of the silicate fraction of Earth with those of potential meteoritic building blocks (Anderson and Bass, 1986; Hart and Zindler, 1986; McDonough and Sun, 1995). Two questions emerge from this brief outline linking tectonics and deep H₂O cycling through Earth's history: What happened to H₂O that might have been transported into the deep mantle in the geological past, and what happened to the crustal parts of slabs that potentially carried water into the mantle?

The structure and composition of the mantle today should hold answers to these questions as they reflect the dynamic interactions and feedbacks that arise from the injection of hydrated oceanic lithosphere into the mantle. H₂O, for example, affects many critical geodynamic parameters of mantle rocks such as the viscosity of olivine (Karato et al., 1986; Hirth and Kohlstedt, 1996; Mei and Kohlstedt, 2000) as well as temperatures and degrees of partial melting (Hirth and Kohlstedt, 1996; Asimow and Langmuir, 2003; Asimow et al., 2004; Hirschmann et al., 2006). Subducted oceanic crust is predicted to be denser than ambient pyrolitic mantle throughout most of the mantle (Irifune and Ringwood, 1987; Kesson et al., 1994; Hirose et al., 1999; Ricolleau et al., 2010) and may therefore sink down to the core-mantle boundary and drive convective motions. Figure 1.1 depicts schematically the overall structure of Earth's mantle together with processes related to deep cycling and storage of H₂O and the fate of oceanic crust in the mantle.

1.1.1 The Transition Zone in Earth's Mantle

The transition zone, confined between major seismic discontinuities at 410 km and 660 km depths (Figs. 1.1 and 1.2a), appears to play a pivotal role in deep recycling of H₂O in Earth's mantle (Bercovici and Karato, 2003; Ohtani et al., 2004). The seismic discontinuity at 410 km depth has been attributed to the phase transformation of olivine, α -(Mg,Fe)₂SiO₄, to wadsleyite, β -(Mg,Fe)₂SiO₄, (Bina and Wood, 1987; Agee, 1998; Frost, 2008), which transforms to ringwoodite, γ -(Mg,Fe)₂SiO₄, at higher pressures (Akaogi et al., 1989; Katsura and Ito, 1989; Frost, 2008). The dissociation of ringwoodite into ferropericlasite and bridgmanite, in turn, gives rise to the seismic discontinuity at 660 km (Ito and Takahashi, 1989; Shim et al., 2001; Frost, 2008; Ishii et al., 2018). Alternative explanations for the seismic properties of the transition zone, including the mentioned seismic discontinuities, involve the enrichment of basaltic or eclogitic material within the transition zone (Anderson, 1979; Bass and Anderson, 1984; Anderson and Bass, 1986). Observations by seismic tomography suggest that subducting slabs interact with the transition zone in many ways including the stagnation of slabs within or just below the transition zone (Zhao, 2004; Fukao et al., 2009; Fukao and Obayashi, 2013).

A transition zone rock of pyrolitic composition (Ringwood, 1991; Ita and Stixrude, 1992) would be composed of high-pressure polymorphs of olivine by up to 60 vol-% (Fig. 1.2b; Ringwood, 1991; Ita and Stixrude, 1992; Stixrude and Lithgow-Bertelloni, 2011). Both wadsleyite and ringwoodite are nominally anhydrous minerals. High-pressure experiments have shown, however, that both phases can incorporate several percent H₂O by weight into

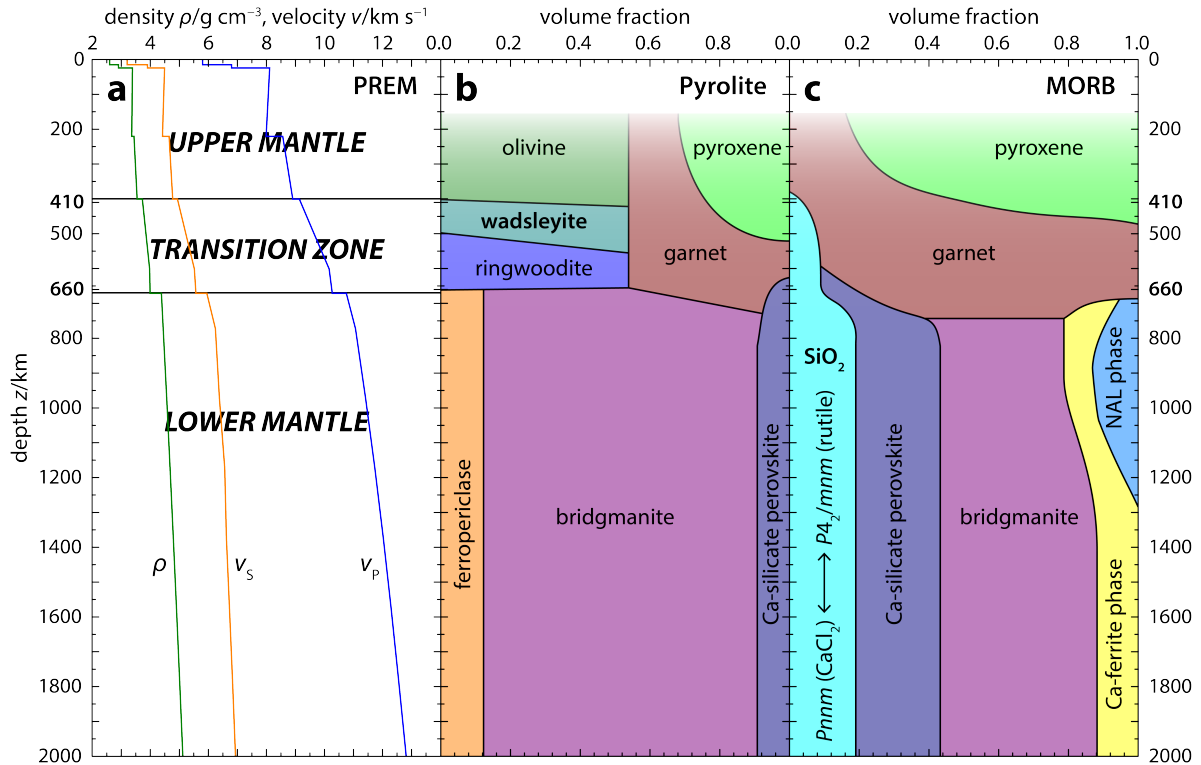


Figure 1.2: a) Variation of density ρ , S wave velocity v_s , and P wave velocity v_p with depth according to PREM (Dziewonski and Anderson, 1981). Phase assemblages in rocks of pyrolitic (b) and basaltic (MORB) (c) compositions as a function of depth; modified after Irifune and Isshiki (1998), Frost (2008), and Irifune et al. (2010) (b) and Perrillat et al. (2006) and Ricolleau et al. (2010) (c). Note the high volume fraction of wadsleyite in the shallow transition zone (b) and the phase transition from rutile-structured stishovite to CaCl_2 -type SiO_2 in the lower mantle (c).

their crystal structures (Inoue et al., 1995; Kohlstedt et al., 1996; Kudoh et al., 2000). The combination of a pyrolitic, or peridotitic, mineral assemblage with the high solubility of H_2O in wadsleyite and ringwoodite turns the transition zone into a potential reservoir for H_2O in Earth's mantle (Smyth and Jacobsen, 2006). A ringwoodite inclusion in diamond with an estimated H_2O content of ~ 1.5 wt-% H_2O dissolved in the ringwoodite grain provides direct evidence for the viability of this hypothesis (Pearson et al., 2014). Similarly, the presence of aqueous fluids in the transition zone has been inferred from ice-VII inclusions in diamond (Tschauer et al., 2018).

Diamond inclusions provide localized samples that cannot constrain the extent of hydration in the transition zone on a global scale. A hydrous transition zone, however, would have far-reaching consequences for the evolution of the mantle. When rising out of the wadsleyite stability field, a hydrated transition zone rock might expel some of the stored H_2O due to the drop in H_2O solubility from wadsleyite to olivine (Bolfan-Casanova, 2005; Inoue et al., 2010; Litasov et al., 2011). The resulting dehydration melting would affect the distribution of geochemical key elements in Earth's mantle (Bercovici and Karato, 2003; Karato et al., 2006; Karato, 2011) and may give rise to an extended melt layer above the 410-km seismic discontinuity (Revenaugh and Sipkin, 1994; Tauzin et al., 2013; Freitas et al., 2017). Detecting and quantifying the extent of hydration in the shallow transition zone and in the vicinity of the 410-km seismic discontinuity therefore stands out as a key challenge to understand the evolution of global H_2O cycles and reservoirs.

1.1.2 The Fate of Oceanic Crust in Earth's Lower Mantle

Following eclogitization, subducted oceanic crust with a typical composition of mid-ocean ridge basalt (MORB) is predicted to undergo a sequence of metamorphic reactions as illustrated in Figure 1.2c (Irifune et al., 1986; Irifune and Ringwood, 1993; Hirose et al., 2005; Ricolleau et al., 2010). Throughout the upper mantle and the transition zone, basaltic crust is denser than pyrolite (Irifune and Ringwood, 1993). The densities of rocks with MORB and pyrolite compositions, however, crossover at around 660 km depth as ringwoodite in a pyrolitic rock decomposes into the denser assemblage of ferropericlase and bridgmanite implying the possibility to accumulate subducted basaltic crust beneath the 660-km seismic discontinuity (Irifune and Ringwood, 1993; Hirose et al., 2005). Once majoritic garnet in a MORB-like rock transforms to an assemblage of bridgmanite, Ca-silicate perovskite, stishovite, and other Ca, Na, and Al-bearing phases at around 720 km depth (Kesson et al., 1994; Hirose et al., 1999; Ono et al., 2001; Perrillat et al., 2006), the density of former basalt exceeds densities given in PREM¹ (Kesson et al., 1994; Hirose et al., 1999; Ono et al., 2001; Perrillat et al., 2006), potentially down to the core-mantle boundary (Hirose et al., 2005; Ricolleau et al., 2010). In addition to density considerations, geodynamic simulations (Christensen and Hofmann, 1994; Xie and Tackley, 2004; Nakagawa and Buffett, 2005; Brandenburg and Keken, 2007) and geochemical constraints (Hofmann and White, 1982; Chase and Patchett, 1988; Blichert-Toft and Albarède, 1997) support the entrainment of former basaltic crust into the lower mantle. Seismic observations provide further evidence for lithospheric slabs entering the lower mantle (Kaneshima and Helffrich, 1999; Grand, 2002; Hutko et al., 2006).

Recycling of crustal material into the lower mantle would have substantially affected the chemical and thermal evolution of the mantle. In terms of H₂O cycling through the mantle, for example, the high silica and alumina contents of basaltic lithologies stabilize minerals that could act as sinks for H₂O at conditions of the lower mantle (Pawley et al., 1993; Nishi et al., 2014; Pamato et al., 2015) where hydrous magnesium silicates in peridotitic rocks break down (Ohtani et al., 2004; Nishi et al., 2014). Potential H-bearing phases in basaltic rocks at conditions of the lower mantle include H-Al-bearing stishovite (Pawley et al., 1993; Panero et al., 2003), aluminous phase D (Pamato et al., 2015), and solid solutions between δ -AlOOH and phase H (Nishi et al., 2014; Ohira et al., 2014). To trace deep material cycles and to better relate geochemical signatures recorded in mantle magmas (Hofmann and White, 1982; Hofmann, 1997; van Keken et al., 2002) to the tectonic regime and the style of mantle convection throughout Earth's history (Christensen, 1989; Tackley, 2000; Ballmer et al., 2017), however, requires more quantitative information about the amount and dispersal of crustal materials in Earth's lower mantle.

1.2 Geophysical Observables

Geophysical methods facilitate remote sensing of Earth's inaccessible interior by probing physical properties of materials at depth such as density, electrical conductivity, and the velocities of seismic waves. Seismology, in particular, offers a variety of observables related to the propagation of seismic waves. A general introduction to seismology and its application to the study of Earth's interior can be found, for example, in Stein and Wysession (2003). Here, I briefly introduce those seismic observables that may be used to detect hy-

¹PREM: Preliminary Reference Earth Model (Dziewonski and Anderson, 1981)

drated regions in the transition zone and subducted oceanic crust in Earth's lower mantle as illustrated in Figure 1.1 and how they relate to physical properties of minerals and rocks. Note that the hydration state of the transition zone can also be inferred from comparing other geophysical observations such as variations in the electrical conductivity (Ichiki et al., 2001; Utada et al., 2003; Kelbert et al., 2009) and viscosity profiles (Peltier, 1998; Mitrovica and Forte, 2004; Soldati et al., 2009) of the mantle with related physical properties of transition zone minerals determined in experiments (Huang et al., 2005; Yoshino et al., 2008; Manthilake et al., 2009; Fei et al., 2017).

1.2.1 The Velocities of Seismic Waves

For propagation in an elastically isotropic medium, the velocities of seismic waves depend on the bulk modulus K , the shear modulus G , and the density ρ of the medium (Poirier, 2000; Stein and Wysession, 2003):

$$v_p = \sqrt{\frac{K + 4G/3}{\rho}} \quad \text{and} \quad v_s = \sqrt{\frac{G}{\rho}} \quad (1.1)$$

with the P wave velocity v_p and the S wave velocity v_s . To a first approximation and throughout most of this study, bulk and shear moduli are assumed to describe the pure elastic response of the medium without taking into account effects of wave attenuation and frequency dispersion that may arise from anelastic relaxation processes (Jackson, 2007; Karato, 2008). In this approximation, seismic waves correspond to acoustic or sound waves that typically have higher frequencies than seismic waves. A central task of modern mineral physics consists in the determination of densities and elastic properties of potential mantle materials as a function of pressure, temperature, and chemical composition.

The elastic properties of minerals and rocks can be combined to calculate the variation of density and sound wave velocities of a given phase assemblage with depth assuming adiabatic self-compression (Anderson and Bass, 1984; Ita and Stixrude, 1992; Stixrude and Lithgow-Bertelloni, 2011). The comparison of such mineral physics predictions with globally averaged one-dimensional seismic profiles such as PREM (Fig. 1.2a; Dziewonski and Anderson, 1981), *iasp91* (Kennett and Engdahl, 1991), and *ak135* (Kennett et al., 1995) has substantially improved our understanding of the structure and composition of the mantle (Anderson and Bass, 1986; Ita and Stixrude, 1992; Xu et al., 2008; Kurnosov et al., 2017). In contrast to averaged one-dimensional seismic profiles, modern seismic tomography images the three-dimensional deviations of seismic velocities in the mantle from an underlying reference model (Grand, 2002; Romanowicz, 2003; Panning and Romanowicz, 2006; Ritsema et al., 2011). For example, seismic tomography has been used to trace subducted slabs on their way through the mantle (Grand, 2002; Fukao et al., 2009; Fukao and Obayashi, 2013). Based on the assumption that the incorporation of water reduces the sound wave velocities of wadsleyite and ringwoodite (Smyth and Jacobsen, 2006; Mao et al., 2008a; Mao et al., 2011; Mao et al., 2012; Thio et al., 2016), lateral variations of seismic velocities within the transition zone have been used to infer the hydration state of the transition zone (Suetsugu et al., 2006; Meier et al., 2009; Houser, 2016).

1.2.2 Seismic Anisotropy

Most minerals are elastically anisotropic. Deformation can align minerals and result in a crystallographic preferred orientation (CPO) of one or several mineral phases in a rock

(Karato, 2008). When anisotropic mineral grains or crystals are aligned in a preferred orientation, their elastic anisotropy is partly transferred to the rock they compose, depending on the intensity of the CPO (Karato, 2008; Mainprice, 2015). The velocities of seismic waves propagating through an anisotropic material vary with propagation direction and polarization of the waves. For example, shear waves with different polarizations may travel at different velocities in the same direction. In section 5.2.2, I provide a more detailed introduction into the propagation of sound waves in elastically anisotropic media. Materials in Earth's interior indeed display seismic anisotropy that can be detected geophysically (Montagner and Kennett, 1996; Mainprice et al., 2000; Panning and Romanowicz, 2006; Mainprice, 2015). In addition to seismic anisotropy related to CPO of minerals, seismic anisotropy can result from the alignment of elongated or tabular objects such as melt lenses or layers of different lithologies that themselves only need to be elastically distinct but not necessarily anisotropic (Karato, 2008; Mainprice, 2015).

Seismic anisotropy may reflect deformation patterns in the transition zone that themselves evolve according to large-scale material flow in the mantle. In a rock of pyrolytic composition, the elastic anisotropy and potential CPO of wadsleyite could be the dominant source for seismic anisotropy in the transition zone given the high volume fraction of wadsleyite (Fig. 1.2b) and the high intrinsic anisotropy as compared to ringwoodite and garnet (Mainprice, 2015). Wadsleyite was shown to develop a CPO under shear deformation (Tommasi et al., 2004; Kawazoe et al., 2013; Ohuchi et al., 2014). Trampert and van Heijst (2002) observed azimuthal seismic anisotropy in the transition zone on a global scale. Visser et al. (2008) found indications for significant radial anisotropy in the transition zone. To relate these global and more local observations (Fouch and Fischer, 1996; Foley and Long, 2011) of seismic anisotropy in the transition zone to mantle convection, however, requires more information on the rheology of transition zone rocks and the elastic properties of transition zone minerals, in particular at relevant pressures and temperatures.

1.2.3 Reflection and Scattering of Seismic Waves

When the seismic properties of the mantle change discontinuously, seismic waves can be reflected, scattered, and converted from P to S waves and vice versa. A seismically reflective interface arises from changes in the properties on a length scale that is comparable to or shorter than the wavelengths of seismic waves, i. e. several kilometers to tens of kilometers (see also Fig. 2.21 on page 44). Consequently, it depends on the magnitude and the gradient of the change in properties how efficiently an interface can reflect or scatter seismic waves. The magnitude of the change in properties across the interface can be quantified by the contrast $d \ln X$ in the property X between the materials on either side of the interface or the gradient. For a seismic wave traveling in a medium A and approaching the interface between medium A and medium B, the contrast in X is calculated as:

$$d \ln X = 2 \times \frac{X_A - X_B}{X_A + X_B} \quad (1.2)$$

The property X can be the density ρ , the propagation velocity v of P or S waves, or the acoustic impedance $Z = \rho v$, i. e. the product of density and velocity. The contrast in acoustic impedance $d \ln Z$, for example, determines the reflection coefficient R_{AB} for normal incidence on the interface between the media A and B (Stein and Wysession, 2003):

$$R_{AB} = \frac{1}{2} d \ln Z \quad (1.3)$$

In Earth's mantle, global seismic discontinuities provide interfaces that efficiently reflect seismic waves (Dziewonski and Anderson, 1981; Shearer and Flanagan, 1999). The seismic discontinuity at a depth of 410 km, for example, is believed to arise from the contrast in seismic properties between olivine above and wadsleyite below the discontinuity (Bina and Wood, 1987; Agee, 1998; Frost, 2008). When taking into account the effect of coexisting garnet on the iron partitioning between the minerals of a pyrolitic rock, it has been shown that the pressure interval of the phase transition from olivine to wadsleyite matches to the depth interval or the *sharpness* of the 410-km seismic discontinuity inferred from seismic observations (Benz and Vidale, 1993; Rost and Weber, 2002; Irifune and Isshiki, 1998; Frost, 2003b; Frost, 2003a). The pressures and hence depths of mineral phase transitions are sensitive to changes in temperature and chemical composition. Higher temperatures displace the olivine-wadsleyite phase transition to greater depths (Frost, 2008) while the presence of H₂O or higher Fe³⁺/ΣFe ratios reduce the transition pressure and expand the transition interval (Wood, 1995; Frost and Dolejš, 2007; Frost and McCammon, 2009). Consequently, lateral variations in the thermal state and composition of the transition zone in Earth's mantle have been inferred from the seismically observed variations in properties, such as topography and reflectivity, of the 410-km and 660-km seismic discontinuities (Chambers et al., 2005b; Chambers et al., 2005a; Schmerr and Garnero, 2007; Meier et al., 2009; Schmerr, 2015; Saki et al., 2015; Houser, 2016).

In addition to global seismic discontinuities, localized seismic inhomogeneities can reflect and scatter seismic waves. Such objects can be located throughout the lower mantle (Hedlin et al., 1997; Kaneshima and Helffrich, 1998; Vinnik et al., 2001; Kaneshima and Helffrich, 2009; Waszek et al., 2018). In many cases, it was even possible to constrain the geometry (Kaneshima and Helffrich, 1999; Kaneshima and Helffrich, 2003; Niu et al., 2003), distribution, or sizes of inhomogeneities (Hedlin et al., 1997; Kaneshima and Helffrich, 2009; Kaneshima and Helffrich, 2010; Waszek et al., 2018). Since many detected inhomogeneities scatter high-frequency seismic waves with wavelengths of about 10 km (Hedlin et al., 1997; Kaneshima and Helffrich, 2009; Kaneshima, 2009; Kaneshima and Helffrich, 2010), their sizes should be on a similar scale or smaller. Fragments of oceanic crust, entrained, stretched, and dispersed by mantle convection (Gurnis and Davies, 1986; Kellogg and Turcotte, 1990), could explain these observations (Kaneshima and Helffrich, 2009; Kaneshima, 2009; Kaneshima and Helffrich, 2010; Waszek et al., 2018). While subducted MORB-like oceanic crust remains denser than PREM and pyrolite throughout the lower mantle (Hirose et al., 2005; Ricolleau et al., 2010; Tsuchiya, 2011), sound wave velocities are predicted to be fairly similar, at least down to about 2000 km depth (Tsuchiya, 2011). Shear wave velocities of basaltic rocks in the lower mantle, however, may be significantly reduced by a phase transition in the free silica phase from stishovite to a CaCl₂-type polymorph of SiO₂ (Karki et al., 1997a; Carpenter et al., 2000; Lakshtanov et al., 2007; Tsuchiya, 2011). As a consequence, seismic scatterers and reflectors in the lower mantle are commonly related to the presence of subducted oceanic crust (Vinnik et al., 2001; Kaneshima and Helffrich, 2009; Kaneshima and Helffrich, 2010; Waszek et al., 2018) or silica-rich material exsolved from Earth's outer core (Hirose et al., 2017; Helffrich et al., 2018). For basaltic oceanic crust, the predicted magnitude of the reduction in shear wave velocities (Tsuchiya, 2011) is compatible with estimated velocity contrasts between seismically detected inhomogeneities and the surrounding mantle (Hedlin et al., 1997; Kaneshima and Helffrich, 1999; Kaneshima and Helffrich, 2010).

1.3 Mantle Minerals at Focus

The comparison of seismic observables to key questions and challenges raised in section 1.1 shows that the elastic properties of wadsleyite and stishovite at conditions of the transition zone and the lower mantle, respectively, are needed to interpret seismic observations in terms of the hydration state of the shallow transition zone and the dispersal of subducted oceanic crust in Earth's lower mantle. The determination of the elastic properties of wadsleyite and stishovite at high pressures therefore constitutes the central aim of this study. Both minerals will be introduced in the following with a focus on their potential stability fields in Earth's mantle and those crystal-chemical and physical properties that significantly affect their elastic properties.

1.3.1 Wadsleyite

In a mantle rock of pyrolitic composition and along a typical adiabatic geotherm, olivine transforms to wadsleyite at a pressure around 14 GPa and a temperature of about 1500°C (Katsura and Ito, 1989; Frost, 2003b; Frost, 2008; Katsura et al., 2010; Stixrude and Lithgow-Bertelloni, 2011). The Fe/(Mg+Fe) ratio of wadsleyite would be close to 0.11 (Frost, 2003b; Frost, 2003a) and the wadsleyite-to-ringwoodite transition encountered around 18 GPa at a temperature roughly 100 K hotter than the olivine-wadsleyite phase transition (Katsura et al., 2010; Stixrude and Lithgow-Bertelloni, 2011; see also Fig. 2.1 on page 16). Between 14 and 18 GPa, wadsleyite would contribute to a pyrolitic mantle rock with 55 to 60 vol-% (Ringwood, 1991; Frost, 2008; Stixrude and Lithgow-Bertelloni, 2011) and therefore be the mineral phase with the highest volume fraction in the shallow transition zone.

The crystal structure of wadsleyite is shown in Figure 1.3. Anhydrous wadsleyite, β -(Mg,Fe)₂SiO₄, adopts an orthorhombic crystal structure with space group *Imma* (Morimoto et al., 1970; Moore and Smith, 1970; Horiuchi and Sawamoto, 1981). Mg and Fe atoms occupy three distinct octahedral sites with iron preferring the *M1* and *M3* sites over the *M2* site (Sawamoto and Horiuchi, 1990; Finger et al., 1993; Hazen et al., 2000). *M3* octahedra form edge-sharing double chains that extend along the **a** axis. The double chains are connected by chains of alternating *M1* and *M2* octahedra along the **b** axis. Silicon tetrahedra are paired to sorosilicate groups that fit into gaps between crossing chains of octahedra. The oxygen atoms are organized in a distorted cubic close-packing (Horiuchi and Sawamoto, 1981). In comparison to spinel-structured ringwoodite (Ringwood and Major, 1966), the distortion from perfect cubic close-packing of oxygens results from the different cationic occupation scheme of available octahedral and tetrahedral sites.

The rearrangement of cations with respect to the spinel structure and the concomitant dimerization of [SiO₄]⁴⁻ tetrahedra to [Si₂O₇]⁶⁻ sorosilicate groups has important consequences for the crystal chemistry of wadsleyite. For example, wadsleyite solid solutions in the system (Mg,Fe)₂SiO₄ are restricted to Fe/(Mg+Fe) ≤ 0.3 (Akaogi et al., 1989; Frost, 2003b; Stixrude and Lithgow-Bertelloni, 2011) while both olivine and ringwoodite form complete solid solutions between magnesian and ferroan end members (Ringwood and Major, 1970; Matsuzaka et al., 2000; Frost et al., 2001). At pressures below 9 GPa, however, the system (Mg,Fe²⁺,Fe³⁺)₂(Si,Fe³⁺)O₄ spans the spinelloid III solid solution that is isostructural with wadsleyite (Woodland and Angel, 1998; Koch et al., 2004; Woodland et al., 2012). An even more intriguing effect arises from the distribution of electrostatic potentials in the wadsleyite crystal structure. Smyth (1987) identified the strongly underbonded O1 position as

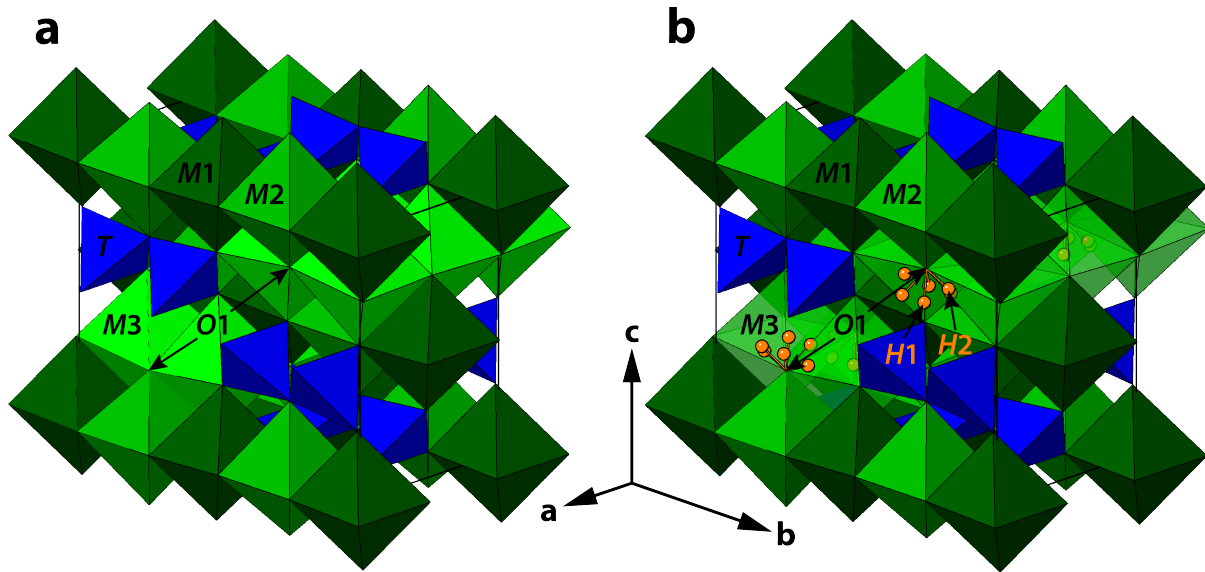


Figure 1.3: Crystal structure of anhydrous (a) and hydrous (b) wadsleyite after Finger et al. (1993) (a) and Sano-Furukawa et al. (2011) (b). $M1$, $M2$, and $M3$: Mg, Fe^{2+} , and Fe^{3+} , T : Si and Fe^{3+} , $H1$ and $H2$: H. Oxygen atoms sit on the corners of each polyhedron. Note that only a fraction of available hydrogen positions ($H1$ and $H2$ in b) is occupied in hydrous wadsleyite and mainly charge balanced by vacancies on the $M3$ site.

a potential site for protonation. The suggestion of Smyth (1987) was supported by a further analysis of electrostatic potentials in wadsleyite by Downs (1989) who found that the $O2$ position might be a favorable site for protonation in addition to the $O1$ site. Infrared absorption and Raman spectra recorded on individual grains of synthetic Mg_2SiO_4 (McMillan et al., 1991) and $(\text{Mg,Fe})_2\text{SiO}_4$ wadsleyite (Young et al., 1993) indeed showed bands around 3330 cm^{-1} and 3600 cm^{-1} , i. e. in the frequency range of O–H stretching vibrations, that were attributed to structurally bonded hydroxyl groups. Subsequent experimental studies confirmed the prediction by Smyth (1994) that nominally anhydrous wadsleyite may incorporate up to $\sim 3\text{ wt}\%$ H_2O as hydroxyl groups in its crystal structure (Inoue et al., 1995; Kohlstedt et al., 1996). Wadsleyite can dissolve substantial amounts of H_2O even at temperatures relevant for the transition zone (Bolfan-Casanova, 2005; Bolfan-Casanova et al., 2006).

Consequently, the crystal structure of hydrous wadsleyite was the subject of numerous studies aiming to understand the exact hydration mechanisms (e. g. Kudoh et al., 1996; Smyth et al., 1997; Kudoh and Inoue, 1999). Smyth et al. (1997) found that hydration results in a slight distortion of the orthorhombic unit cell to monoclinic symmetry (space group $I2/m$). The main hydration mechanism maintains charge balance by creating octahedral vacancies that concentrate on the $M3$ sites (Inoue et al., 1995; Kudoh et al., 1996; Smyth et al., 1997; Kudoh and Inoue, 1999; Litasov et al., 2011). The locations of hydrogen atoms were studied using polarized infrared spectroscopy (Jacobsen et al., 2005; Deon et al., 2010) and nuclear magnetic resonance spectroscopy (Kohn et al., 2002; Stebbins et al., 2009; Griffin et al., 2013). Figure 1.3b shows the crystal structure of hydrous wadsleyite determined by neutron powder diffraction on deuterated Mg_2SiO_4 wadsleyite as reported by Sano-Furukawa et al. (2011). The hydrogen positions found by Sano-Furukawa et al. (2011) indicate that hydroxyl groups are located at the $O1$ site and point along the edges of a vacant $M3$ octahedron to form hydrogen bonds $\text{O}-\text{H}\cdots\text{O}$ with oxygen atoms at the

O4 and O3 sites. These orientations of O–H groups are consistent with the polarization of infrared absorption bands (Jacobsen et al., 2005; Deon et al., 2010) and energetic considerations based on first-principle calculations (Tsuchiya and Tsuchiya, 2009). For Fe-bearing wadsleyite, an additional hydration mechanism has been proposed that involves the replacement of tetrahedrally coordinated Si^{4+} by Fe^{3+} and H^+ (Bolfan-Casanova et al., 2012; Smyth et al., 2014; Kawazoe et al., 2016).

Understanding the incorporation mechanism of hydrogen or H_2O on the atomic level provides the basis to understand the effect of hydration on the elastic and thermodynamic properties of wadsleyite. An overview of available equations of state for wadsleyites with different compositions is given in section 3.1 and chapter 4 (see also Table A.7 on page 190). Merging isolated observations in a simple model spanned by the properties of wadsleyite end members may not only reveal previously undetected relationships between properties and chemical composition but also facilitate thermodynamic calculations on compositions that have not been addressed by experiments or calculations. Therefore, we present a new equation of state for Fe-bearing wadsleyite and construct a multi-end-member model for the equation of state of wadsleyite solid solutions in chapter 4. As I explain in section 3.3 and in chapter 6, currently available elasticity data on different, partly not fully characterized wadsleyite compositions cannot reliably constrain the variation of sound wave velocities of Fe-bearing wadsleyite as a function of hydrogen or H_2O content, in particular not at high pressures. Moreover, the elastic stiffness tensor of wadsleyite has not been determined at simultaneously high pressures and high temperatures. In section 3.4, I present elastic stiffness tensors at combined high pressures and high temperatures for a realistic wadsleyite composition assuming a pyrolitic mantle. Chapter 6 aims at a redefinition of the seismic signature of H_2O in the shallow transition zone based on new experimental results on the high-pressure elasticity of Fe-bearing wadsleyite single crystals. These results can be integrated with a variety of seismic observables that, by their careful and accurate interpretation, promise improvements in detecting reservoirs and tracing pathways of deep H_2O cycling in Earth's mantle.

1.3.2 Stishovite and CaCl_2 -Type Silica

When compressing pure SiO_2 along a typical adiabatic geotherm, coesite would transform to stishovite at about 10 GPa and approximately 1800 K (Hemley et al., 1994; Akaogi et al., 1995; Zhang et al., 1996). Seifertite, a high-pressure SiO_2 polymorph with the $\alpha\text{-PbO}_2$ crystal structure (El Goresy et al., 2008), becomes stable at pressures and temperatures in excess of 120 GPa and 2500 K (Murakami et al., 2003; Tsuchiya et al., 2004; Grocholski et al., 2013). In a rock of basaltic (MORB) composition, the volume fraction of stishovite increases from 0 to about 10 vol-% between 10 and 15 GPa at the expense of clinopyroxene (Irifune et al., 1986; Irifune and Ringwood, 1987). The breakdown of garnet gives rise to a second pulse of stishovite formation between 20 and 30 GPa that raises the volume fraction of stishovite to 20 vol-% (Irifune and Ringwood, 1993; Ono et al., 2001; Perrillat et al., 2006; see also Fig. 1.2c). At higher pressures, stishovite might react with the NAL phase to form bridgmanite. This reaction would decrease the volume fraction of stishovite to about 15 vol-% at 50 GPa where the NAL phase disappears leaving the volume fraction of stishovite unchanged up to about 100 GPa (Perrillat et al., 2006; Ricolleau et al., 2010). Hirose et al. (2005) found the incorporation of alumina into seifertite to stabilize seifertite at around 110 GPa and 2500 K, i. e. at lower pressures than in the pure silica system.

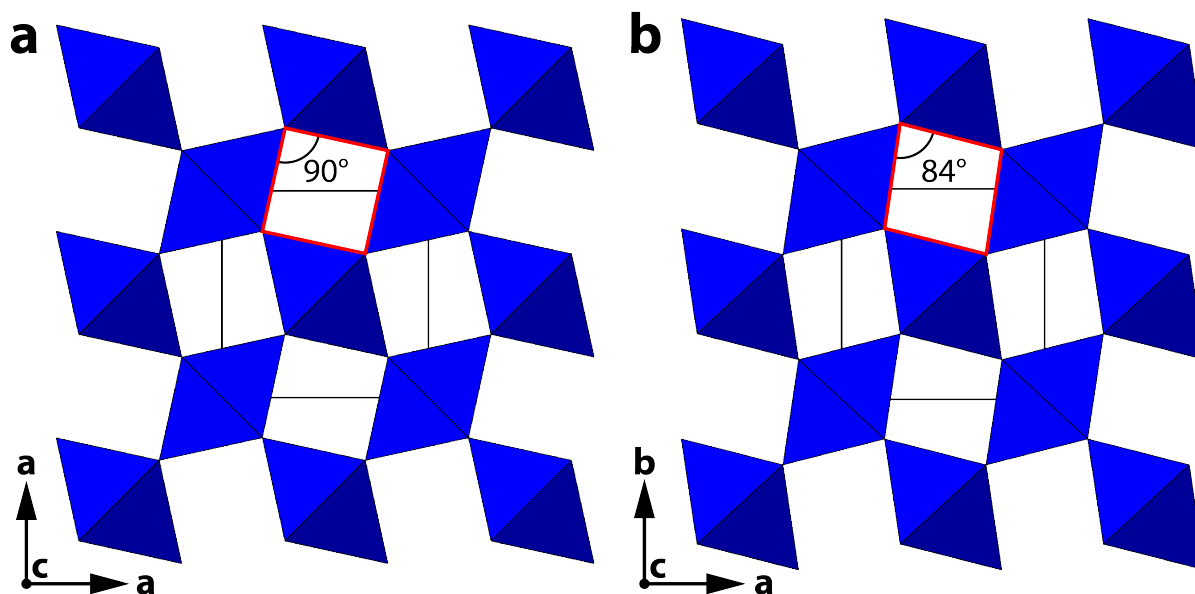


Figure 1.4: Crystal structure of stishovite ($P4_2/mnm$, **a**) and CaCl_2 -type SiO_2 ($Pnmm$, **b**) viewed along the **c** axis; drawn from own unpublished structural data. Si occupies the center of each octahedron formed by oxygen atoms on the corners. Note how the phase transition from stishovite to CaCl_2 -type SiO_2 shears the red square in **a**) into a rhomb in **b**).

Stishovite crystallizes in the rutile structure type with tetragonal symmetry and space group $P4_2/mnm$ (Stishov and Belov, 1962; Sinclair and Ringwood, 1978). In contrast to its adjacent low-pressure polymorph coesite, stishovite hosts silicon in octahedral coordination. $[\text{SiO}_6]^{8-}$ octahedra share two opposing edges with neighboring octahedra to form chains along the **c** axis. Neighboring chains are rotated by 90° and displaced along the **c** axis with respect to each other to link via corner sharing. The alignment of edge-sharing chains along the **c** axis results in a strong elastic and compressional anisotropy (Ross et al., 1990; Andraut et al., 2003; Jiang et al., 2009; see also Fig. 3.6 on page 61). Complete elastic stiffness tensors of stishovite have been determined by Weidner et al. (1982) at ambient conditions, by Brazhkin et al. (2005) up to a temperature of about 800 K at ambient pressure, and by Jiang et al. (2009) up to 12 GPa at ambient temperature. The results of numerous studies on the equation of state of stishovite have recently been compiled by Fischer et al. (2018).

When crystallized in basaltic rocks at high pressures, stishovite was found to contain up to several weight percent Al_2O_3 (Irifune and Ringwood, 1993; Kesson et al., 1994; Hirose et al., 1999). In addition to aluminum, Pawley et al. (1993) demonstrated the presence of structurally bonded hydroxyl groups in stishovite and proposed coupled substitutions with Si^{4+} being replaced by Al^{3+} charge balanced either by H^+ or by oxygen vacancies. These incorporation mechanisms of aluminum and hydrogen were confirmed by later studies (Smyth et al., 1995; Bromiley et al., 2006; Frigo et al., 2018). The alumina content in stishovite was found to be sensitive to pressure and temperature (Ono, 1999; Liu et al., 2006) and potentially increases upon partial melting of a basaltic rock at pressures of the lower mantle (Panero et al., 2003) raising the potential of stishovite to retain H_2O (Chung and Kagi, 2002; Panero et al., 2003). The coupled substitution of Si^{4+} by Al^{3+} and H^+ was also studied by first-principle calculations (Gibbs et al., 2004; Panero and Stixrude, 2004) suggesting a solubility of 0.3 wt-% H_2O in stishovite at 25 GPa and 1500 K (Panero and Stixrude, 2004). A similar H_2O solubility was found experimentally by Litasov et al. (2007). Substantially

higher water contents in excess of 1 wt-% H₂O were found in Al-free stishovite crystallized from silica glass or coesite at pressures of 10 GPa and temperatures below 820 K in the presence of free H₂O (Spektor et al., 2011; Spektor et al., 2016). These very hydrous stishovites incorporate H₂O by a mechanism similar to the hydrogarnet substitution, i. e. 4 H⁺ replace Si⁴⁺ (Ackermann et al., 1983; Spektor et al., 2011; Spektor et al., 2016).

In addition to the potential to transport or retain H₂O in Earth's lower mantle, the stishovite crystal structure provides another geophysically interesting feature. With increasing pressure, the B_{1g} optical vibrational mode softens (Kingma et al., 1995) and couples with acoustic modes that involve shear motions in the **a-b** plane (Hemley et al., 2000; Carpenter et al., 2000; and references therein). The resulting shear instability gives rise to a second-order phase transition around 50 GPa at ambient temperature that involves a reduction in symmetry to $Pn\bar{m}$ and a structural distortion to a CaCl₂-type structure (Kingma et al., 1995; Karki et al., 1997b; Andrault et al., 1998). Figure 1.4 compares the crystal structures of stishovite and CaCl₂-type SiO₂. On the atomic level, the chains of octahedra rotate around the **c** axis by a few degrees with a concomitant change of interatomic distances (Andrault et al., 1998). As the phase transition from stishovite to CaCl₂-type SiO₂ involves a spontaneous shear strain in the **a-b** plane, stishovite becomes infinitely soft with respect to shear stress in this plane, i. e. $(c_{11} - c_{12}) \rightarrow 0$, as the phase transition is approached (Karki et al., 1997a; Carpenter et al., 2000). The elastic softening due to the ferroelastic phase transition is predicted to substantially reduce the sound wave velocities of polycrystalline silica aggregates as well as to increase the elastic anisotropy of silica single crystals (Karki et al., 1997a; Carpenter et al., 2000; Yang and Wu, 2014).

Direct measurements of sound wave velocities across the stishovite–CaCl₂-type SiO₂ phase transition, however, have either been performed on polycrystalline silica compressed under nonhydrostatic stress conditions (Asahara et al., 2013) or were limited to a single direction in a hydrous Al-bearing stishovite single crystal (Lakshtanov et al., 2007). Lakshtanov et al. (2007) found that hydrous Al-bearing stishovite transforms to the CaCl₂-type phase at substantially lower pressures than pure SiO₂. A similar reduction of the transition pressure has been observed for Al-bearing stishovite (Bolfan-Casanova et al., 2009) and hydrous Al-free stishovite (Nisr et al., 2017). Nonhydrostatic stresses were shown to reduce the transition pressure as well (Singh et al., 2012; Asahara et al., 2013). As an alternative to direct sound wave velocity measurements, the changes in elastic properties of stishovite and CaCl₂-type SiO₂ can be evaluated based on the evolution of unit cell parameters across the phase transition using Landau theory (Carpenter and Salje, 1998; Carpenter et al., 2000). In chapter 7, we apply this approach to compression data of sintered polycrystalline silica across the stishovite–CaCl₂-type SiO₂ phase transition and show, by comparison to earlier studies on silica powder (Andrault et al., 2003), that sintered polycrystalline silica behaves differently. Our results emphasize how the strong elastic anisotropy of stishovite may affect the elastic response of a sintered polycrystalline aggregate that to some extent resembles a real rock. Combining the effects of chemical composition and temperature (Nomura et al., 2010; Yamazaki et al., 2014; Fischer et al., 2018) on the ferroelastic phase transition with an accurate model for the elastic properties of silica may turn silica-bearing rocks, such as subducted oceanic crust, into sensors for the thermal and compositional structure of Earth's lower mantle.

Chapter 2

Experimental

This study focuses on the characterization of elastic properties of minerals at high pressures, and only those aspects of synthesis and characterization with a relevant contribution of the author will be included here. Moreover, to separate the results of synthesis experiments and chemical characterization from those of experiments aiming to determine the elastic properties at high pressures, I will include results of synthesis and characterization in this chapter, in particular where they aid to illustrate synthesis and characterization approaches. A brief introduction to elastic properties of minerals at high pressures is included to provide the theoretical background for the analysis of experimental results.

2.1 Synthesis of High-Pressure Minerals

This section describes the synthesis of high-quality single crystals free of inclusions and cracks and of suitable size for Brillouin spectroscopy experiments at high pressures. Sintered polycrystalline stishovite samples that were used for high-pressure experiments in the course of this study (Chapter 7) were provided by Norimasa Nishiyama¹, and their synthesis and characterization have been published elsewhere (Nishiyama et al., 2012; Nishiyama et al., 2014).

2.1.1 Synthesis of High-Quality Wadsleyite Single Crystals

For a composition relevant to Earth's transition zone with $\text{Fe}/(\text{Mg}+\text{Fe}) = 0.11$ (Irifune and Isshiki, 1998; Frost, 2003a), wadsleyite becomes stable at pressures in excess of 14 GPa as can be read from the phase diagram of the $(\text{Mg,Fe})_2\text{SiO}_4$ system (Fig. 2.1). The necessary conditions of pressure and temperature can be reached with multi-anvil presses while retaining a sample volume large enough to facilitate growth and subsequent recovery of single crystals with dimensions of several hundred micrometers. A general introduction into multi-anvil presses and their operation can be found in Keppler and Frost (2005).

Different strategies have been developed to synthesize wadsleyite crystals with dimensions in excess of 100 μm . Sawamoto (1986) and Sawamoto and Horiuchi (1990) obtained large wadsleyite crystals when annealing mixtures of synthetic forsterite and fayalite powders at conditions close to the boundary between the stability fields of wadsleyite and ringwoodite or the respective two-phase field, i. e. at pressures and temperatures around 20 GPa

¹Laboratory for Materials and Structures, Tokyo Institute of Technology, Yokohama 226-8503, Japan, ✉ nishiyama.n.ae@m.titech.ac.jp

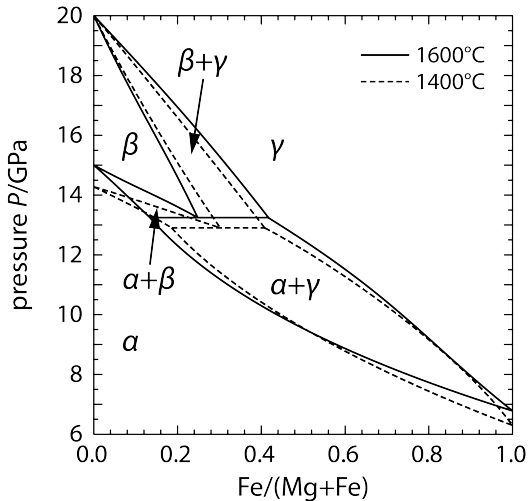


Figure 2.1: Phase diagram of the system $(\text{Mg,Fe})_2\text{SiO}_4$ as a function of pressure and $\text{Fe}/(\text{Mg}+\text{Fe})$ ratio. Phase boundaries at 1400°C and 1600°C are from Frost (2003b) and Finger et al. (1993), respectively. α : olivine, β : wadsleyite, γ : ringwoodite.

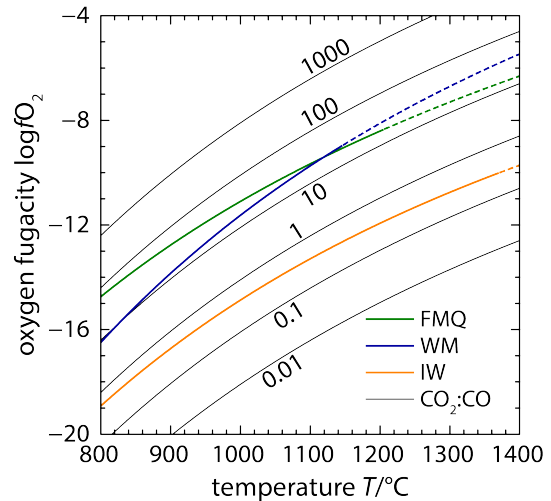


Figure 2.2: Oxygen fugacity as a function of temperature for different buffer reactions and $\text{CO}_2:\text{CO}$ gas mixtures. FMQ: fayalite-magnetite-quartz, WM: wüstite-magnetite, IW: iron-wüstite. Numbers on lines indicate molar $\text{CO}_2:\text{CO}$ ratios. Curves computed based on data given in O'Neill (1987), O'Neill and Pownceby (1993), and Holland and Powell (1998).

and 2000°C . Similarly, Sinogeikin et al. (1998) used San Carlos olivine with $\text{Fe}/(\text{Mg}+\text{Fe}) = 0.086$ as starting material to synthesize single crystals with sizes up to $500\ \mu\text{m}$ at 18 GPa and 1600°C . Shatskiy et al. (2009) grew millimeter-sized wadsleyite crystals from a carbonate flux by imposing a thermal gradient across the sample capsule. A quantitative description on how water and high oxygen fugacities control and enhance grain growth of wadsleyite has been presented by Nishihara et al. (2006).

Here, all three strategies were explored experimentally by using natural and synthetic olivine powders as starting materials and by adding liquid water or a carbonate flux (Table 2.1). Olivine powder with $\text{Fe}/(\text{Mg}+\text{Fe}) = 0.1$ was synthesized from fired oxide powders (48.82(1) wt-% MgO , 10.75(1) wt-% Fe_2O_3 , 40.43(1) wt-% SiO_2) that were reacted at 1150°C and at an oxygen fugacity² of $\log f\text{O}_2 = -11$ or $\Delta\text{FMQ} = -2$ (Fig. 2.2). The oxygen fugacity was buffered by continuously purging the furnace with CO_2 and CO gases in a ratio of $\text{CO}_2:\text{CO} = 69:31$. Prior to each of three consecutive redox annealing steps of 24 h duration, reactant powders were ground and homogenized under ethanol in an agate mortar. The obtained olivine powder was verified to be pure (> 99 vol-%) by powder X-ray diffraction and kept in a drying oven or desiccator to prevent the adsorption of moisture from the air.

For the carbonate-based flux (Shatskiy et al., 2009), K_2CO_3 , MgCO_3 , and FeCl_2 powders were fired at 500°C , 200°C , and 500°C , respectively, to remove any adsorbed wa-

²Oxygen fugacity $f\text{O}_2$ is conventionally reported as the logarithm of the ratio $f\text{O}_2/P_0$ to the base of 10, where P_0 is the reference pressure that is usually set to 1 bar. In mineralogy, oxygen fugacities are commonly reported with respect to redox reactions such as the fayalite-magnetite-quartz (FMQ) equilibrium: $2\text{Fe}_2\text{SiO}_4 + \text{O}_2 \rightleftharpoons 2\text{Fe}_2\text{O}_3 + 2\text{SiO}_2$. In this case, the difference Δ to the respective reaction is given in logarithmic units.

Table 2.1: Wadsleyite synthesis experiments

Synthesis run	#1^a	#2^a	#3	#4
BGI run number	H4015	H4183	H4020	H4077
Starting materials				
Olivine powder	San Carlos	San Carlos	synthetic	synthetic
Fe/(Mg+Fe)	0.1	0.1	0.1	0.1
Water/flux	—	liquid water	—	K ₂ CO ₃ -MgCO ₃ -FeCl ₂
Pre-treatment	—	—	firing	firing
Synthesis conditions				
Capsule material	Re	Pt	Re	Pt
Pressure (GPa)	16	15	16	16
Temperature (°C)	1600	1400	1600	1600
Duration (h)	3	3	3	5
Wadsleyite crystals				
Grain size (µm)	< 500	< 1000	< 100	< 500
Optical clarity	high	high	low	low
Water content (wt-%) ^b	0.24	0.72	n.d.	n.d.

^aSynthesis runs prepared and conducted by Takaaki Kawazoe.

^bSee section 2.2.3; n.d. not determined.

ter. The dried powders were then mixed in the molar ratios K₂CO₃:MgCO₃:FeCl₂ = 9:9:1 (58.41(1) wt-% K₂CO₃, 35.64(1) wt-% MgCO₃, 5.95(1) wt-% FeCl₂) to obtain Fe/(Mg+Fe) = 0.1 and ground under air in an agate mortar. Subsequent storage in a drying oven aimed at preventing hydration of the flux by adsorption of moisture from the air. San Carlos olivine powder was provided by Takaaki Kawazoe³ and was kept at room conditions without provisions to prevent the adsorption of moisture from the air.

San Carlos olivine powder (run #1), San Carlos olivine powder with added liquid water (run #2), synthetic olivine powder (run #3), or a mixture of synthetic olivine powder and carbonate flux (run #4) were packed into metal capsules, 2.7 mm long and 1.6 mm in diameter, that were sealed either by folding the capsule walls or by welding when fabricated from rhenium or platinum, respectively. The capsules containing the starting materials were inserted into assemblies consisting of a resistive heater surrounded by thermal insulation sleeves and the octahedrally shaped pressure-transmitting medium as shown in Figure 2.3b. Annealing of ceramic parts at 1000°C prior to their assembling removed adsorbed moisture. Synthesis runs #1 and #2 were prepared and conducted by Takaaki Kawazoe.

All experiments were carried out with a 1000-ton hydraulic press⁴ using a 6/8 or Kawai-type (Kawai and Endo, 1970) anvil arrangement compressing a 14/8 assembly⁵ (Keppler and Frost, 2005). For synthesis runs #1, #3, and #4 (#2), the compressing force of the press was linearly increased to 8 MN (7 MN) in 4 h (13 h) corresponding to a pressure of 16 GPa (15 GPa) inside the capsule (Keppler and Frost, 2005). Subsequently, the electrical power of the resistive heater was increased to 660 W (560 W) within 20 to 50 min to reach a temper-

³Now at: Department of Earth and Planetary Systems Science, Hiroshima University, Hiroshima 739-8526, Japan, ✉ kawazoe@hiroshima-u.ac.jp

⁴Hymag GmbH, Betzdorf, Germany

⁵The ratio 14/8 describes the ratio of the edge length of the octahedron containing the capsule to the edge length of the triangular truncation of the inner anvils that press on each face of the octahedron (Keppler and Frost, 2005; see also Fig. 2.3a).

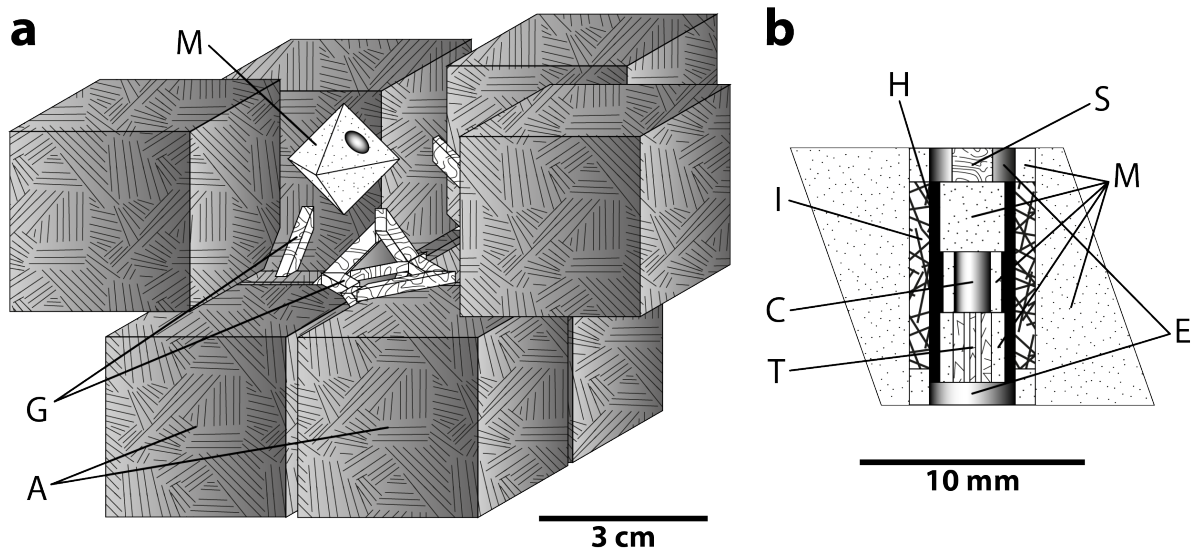


Figure 2.3: Drawing of anvil arrangement (a) around heater and capsule assembly (b) for a multi-anvil experiment. A: anvils (tungsten carbide), G: gaskets (pyrophyllite), M: pressure-transmitting medium (Cr:MgO), C: capsule (rhenium or platinum), H: heater (LaCrO₃), I: thermal insulation (ZrO₂), E: electrodes (molybdenum), T: tubing (Al₂O₃), S: spacer (pyrophyllite).

ature of 1600°C (1400°C) according to a previously established temperature-power relation for 14/8 assemblies. The uncertainty on the temperature was estimated to be $\pm 50^\circ\text{C}$. Pressure and temperature were kept constant for 3 h and 5 h for runs #1, #2, and #3 and run #4, respectively, before quenching by switching off the heater power. The assembly was then slowly decompressed to ambient conditions for 12 to 15 h. The conditions of each synthesis experiment are compiled in Table 2.1.

After recovery, synthesis products were examined with a polarizing microscope⁶ to identify wadsleyite crystals by their optical birefringence. In addition to dark glassy material, all capsules contained aggregates of translucent bluish-green grains of varying sizes that were identified as wadsleyite based in their optical properties and Raman spectra. Synthesis run #3 yielded few wadsleyite grains with maximum sizes of 100 μm . When combined with the carbonate flux as in run #4, the synthetic olivine powder recrystallized to larger wadsleyite grains with diameters between 100 to 500 μm that were, however, flawed by pervasive defects visible with the microscope (Fig. 2.4a). In runs #1 and #2, clear wadsleyite grains with sizes in excess of 500 μm were obtained (Fig. 2.4b). As indicated by their homogeneous extinction between crossed polarizers, most grains appeared to be single crystals and to meet the requirements for subsequent high-pressure experiments. The successful synthesis of high-quality wadsleyite single crystals was published by Kawazoe et al. (2015).

While synthesis runs #1, #3, and #4 aimed to synthesize wadsleyite crystals with low concentrations of hydrogen, a minimum amount of hydrogen appeared to be essential to grow large and clear wadsleyite crystals. During the preparation of synthetic olivine powder and the carbonate flux for runs #3 and #4, I removed water adsorbed to powders by firing starting materials and isolating them from moisture in the air. As a consequence, the water activity inside the capsules of these experiments can be expected to have remained very low. The use of San Carlos olivine powder without any firing or drying, however, resulted in adsorbed water being introduced into the capsule in run #1. In agreement with previous

⁶Laborlux 12 Pol S, Leitz, Wetzlar, Germany

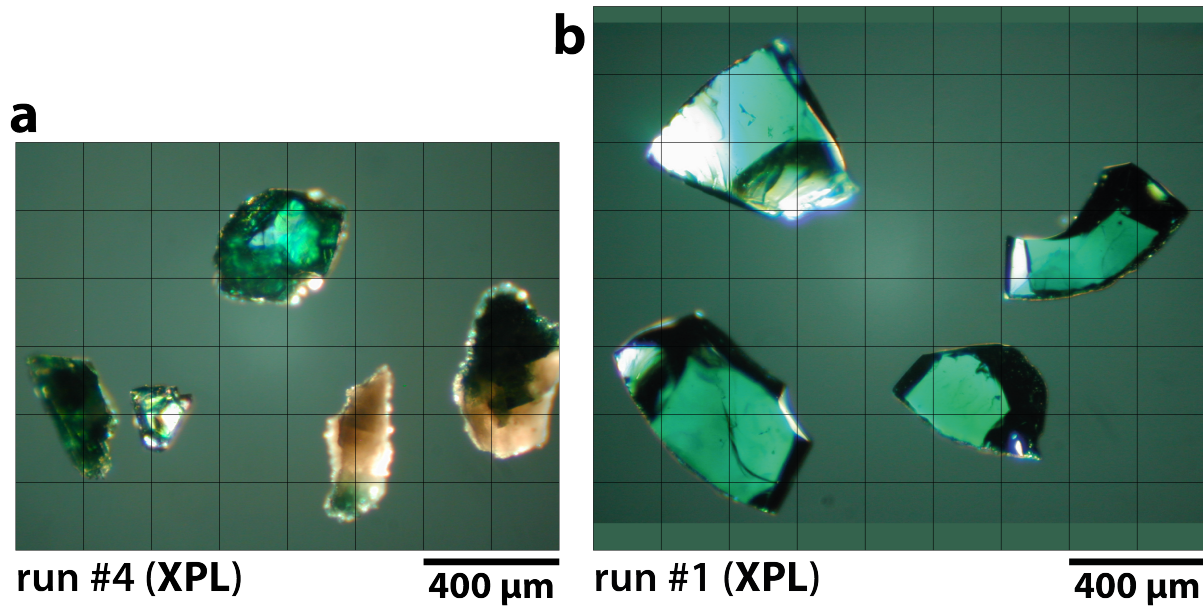


Figure 2.4: Photomicrographs of wadsleyite grains synthesized in run #4 (a) and run #1 (b) viewed between crossed polarizers (XPL).

findings (Nishihara et al., 2006), the higher water activity probably facilitated the growth of large and clear wadsleyite crystals by accelerating diffusive transport. The recrystallization of olivine to wadsleyite is further promoted by high temperatures (Kubo et al., 2004; Kawazoe et al., 2015).

Most wadsleyite crystals used for the high-pressure experiments in this study came from synthesis run #1. In addition to these slightly hydrous wadsleyite crystals, more hydrous wadsleyite crystals from synthesis run #2 were also characterized in the course of this study and served to independently verify the previously reported effects of hydration on the elastic properties of wadsleyite (Mao et al., 2008b; Mao et al., 2011). Some of the wadsleyite grains synthesized in run #2 turned out to be twinned crystals as inferred from the relation of extinction positions between crossed polarizers (Fig. 2.14 on page 30).

2.1.2 Synthesis of Ferropericlasite Single Crystals by Fe-Mg Interdiffusion at High Pressure

As the second most abundant mineral in Earth's lower mantle (Fiquet et al., 2008; Irifune et al., 2010), ferropericlasite is expected to affect seismic properties of lower mantle rocks with potential seismic fingerprints arising from elastic softening related to the spin transition of ferrous iron (Crowhurst et al., 2008; Marquardt et al., 2009b; Wu et al., 2013) and from the strong elastic anisotropy of ferropericlasite (Long et al., 2006; Marquardt et al., 2009a; Immoor et al., 2018). The high-pressure high-temperature single-crystal elastic properties of ferropericlasite formed thus part of the research goals of this study as initially defined. Accordingly, ferropericlasite crystals have been successfully synthesized with $\text{Fe}/(\text{Mg}+\text{Fe})$ between 0.05 and 0.13 and $\text{Fe}^{3+}/\Sigma\text{Fe} < 0.02$. These compositions are close to those expected for ferropericlasite in equilibrium with bridgmanite in Earth's lower mantle (Irifune et al., 2010).

To synthesize ferropericlasite single crystals, we followed a similar protocol as reported by Antonangeli et al. (2011). Oriented MgO single-crystal platelets were embedded in

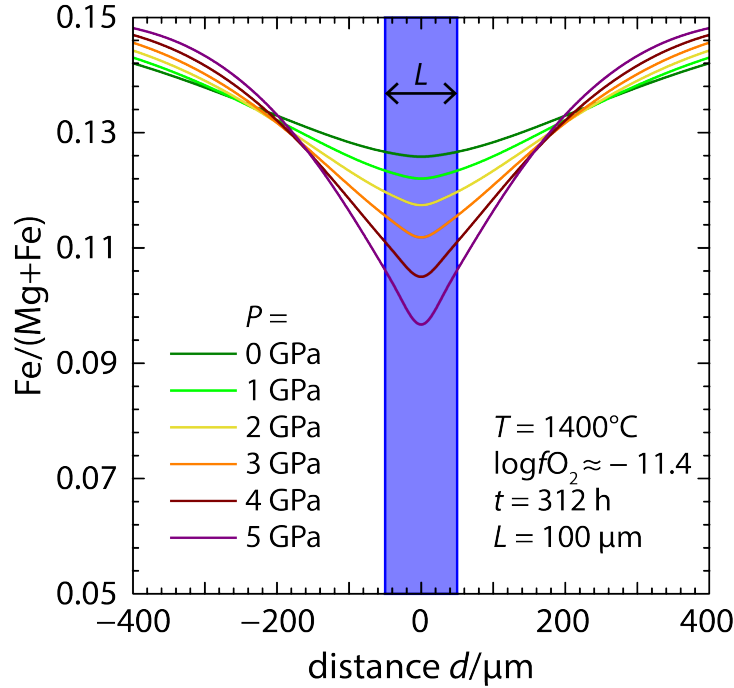


Figure 2.5: Modeled Fe-Mg interdiffusion profiles between an $(\text{Mg}_{0.85}\text{Fe}_{0.15})\text{O}$ source and MgO at different pressures. Blue shading indicates the width of the initial MgO layer.

$(\text{Mg,Fe})\text{O}$ powder with $\text{Fe}/(\text{Mg}+\text{Fe}) = 0.15$ to diffuse iron into the MgO single crystals. Ferropericlase crystals synthesized by Fe-Mg interdiffusion at ambient pressure may contain impurities of magnesioferrite $\text{MgFe}_2^{3+}\text{O}_4$ even for $\text{Fe}/(\text{Mg}+\text{Fe})$ around 0.15 and when synthesized at an oxygen fugacity below the wüstite-magnetite (WM) equilibrium (Fig. 2.2; Jacobsen et al., 2002; Longo et al., 2011). At the reducing conditions of the lower mantle (Frost and McCammon, 2008), however, ferric iron in ferropericlase is predicted to be incorporated mainly as isolated Fe^{3+} point defects on tetrahedral sites rather than forming clusters of Fe^{3+} occupying both tetrahedral and octahedral sites (Otsuka et al., 2010) that resemble the cation arrangement in magnesioferrite. Since high pressures and low oxygen fugacity suppress the formation of ferric iron Fe^{3+} in ferropericlase (McCammon et al., 1998; Otsuka et al., 2010; Otsuka et al., 2013), the diffusion experiment was carried out at 1 GPa and in an iron capsule (Antonangeli et al., 2011).

To optimize the experimental setup and conditions, the Fe-Mg interdiffusion between a pure MgO layer of thickness L and an $(\text{Mg}_{0.85}\text{Fe}_{0.15})\text{O}$ source was modeled prior to the experiment using the following solution for one-dimensional diffusion across opposing faces of the layer (e. g. Philpotts and Ague, 2009):

$$\frac{[\text{Fe}] - [\text{Fe}]_s}{[\text{Fe}]_L - [\text{Fe}]_s} = \frac{1}{2} \left[\text{erf} \left(\frac{L/2 - x}{2\sqrt{Dt}} \right) + \text{erf} \left(\frac{L/2 + x}{2\sqrt{Dt}} \right) \right] \quad (2.1)$$

with the initial iron concentrations $[\text{Fe}]_s$ and $[\text{Fe}]_L$ in the source and in the layer, respectively, and the iron concentration $[\text{Fe}]$ after the time t and at the position x measured from the center of the layer along the symmetric diffusion profile. The diffusion coefficient D was calculated as a function of pressure, temperature, oxygen fugacity, and composition by combining the pressure dependence as given by Holzapfel et al. (2003) with the remaining dependencies given by Mackwell et al. (2005). For each time t and at each position x , the

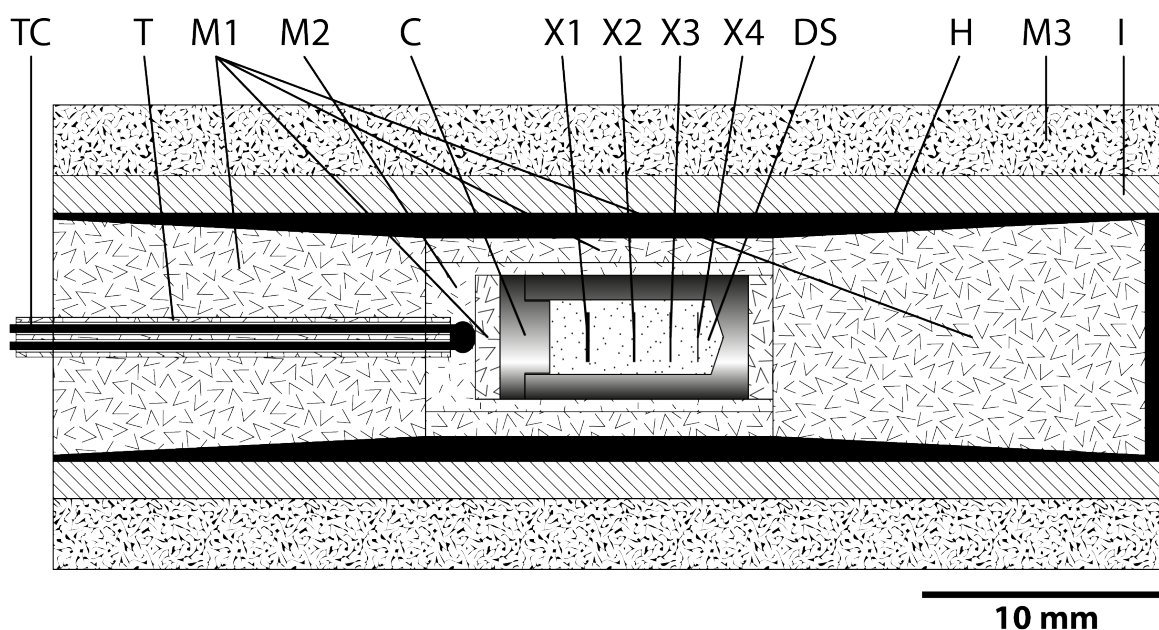


Figure 2.6: Drawing of the setup for Fe-Mg interdiffusion experiments between $(\text{Mg}_{0.85}\text{Fe}_{0.15})\text{O}$ powder and MgO crystals in a piston-cylinder press. M1, M2, M3: pressure-transmitting media (crushable Al_2O_3 , Al_2O_3 powder, talk), C: capsule (iron), X1, X2, X3, X4: MgO single-crystal platelets (150 μm , 98 μm , 73 μm , 47 μm), DS: diffusion source ($(\text{Mg}_{0.85}\text{Fe}_{0.15})\text{O}$ powder), H: heater (graphite), I: thermal insulation (pyrex), TC: thermocouple (type B), T: tubing (Al_2O_3).

diffusion coefficient was approximated by taking the mean of the values calculated for the composition of the source and the composition at the same position x from the previous time step. The modeled effect of pressure on the diffusion profiles through an MgO layer of 100 μm thickness is shown in Figure 2.5.

$(\text{Mg,Fe})\text{O}$ powder with $\text{Fe}/(\text{Mg}+\text{Fe}) = 0.15$ was synthesized from fired oxide powders (74.10(1) wt-% MgO, 25.90(1) wt-% Fe_2O_3) by reacting them in two subsequent cycles of grinding under ethanol and annealing at 1400°C and $\log f_{\text{O}_2} = -7$ ($\Delta\text{WM} = -1.5$; Fig. 2.2) for 24 h. The completeness of the reaction and the purity of the obtained $(\text{Mg,Fe})\text{O}$ powder were verified by powder X-ray diffraction. MgO single crystals⁷ were mechanically cut and double-sided polished parallel to the (100) crystallographic plane to circular plane-parallel platelets with diameters of 2 mm and thicknesses of 47 μm , 73 μm , 98 μm , and 150 μm . The MgO platelets were embedded in the $(\text{Mg,Fe})\text{O}$ powder inside an iron capsule as shown in Figure 2.6. The loaded iron capsule was inserted into a standard $3/4$ inch assembly for a piston-cylinder press⁸ (Fig. 2.6; Keppler and Frost, 2005). Based on the modeled Fe-Mg interdiffusion profiles, the diffusion experiment was run at a pressure of 1 GPa and a temperature of 1400°C for 312 h (13 days). Because the thermocouple that was used to measure the temperature next to the capsule (Fig. 2.6) failed after the first day, the uncertainty on the temperature was estimated to be $\pm 100^\circ\text{C}$.

After the experiment, the capsule was recovered and ground down from the side to expose a cross section along the main diffusion direction. In Figure 2.10a (page 25), the platelets are apparent as dark bars surrounded by fine-grained material. Placed at the bot-

⁷Sigma-Aldrich Chemie GmbH, Steinheim, Germany, www.sigmaaldrich.com

⁸Max Voggenreiter GmbH, Mainleus, Germany, www.voggenreiter-gmbh.de

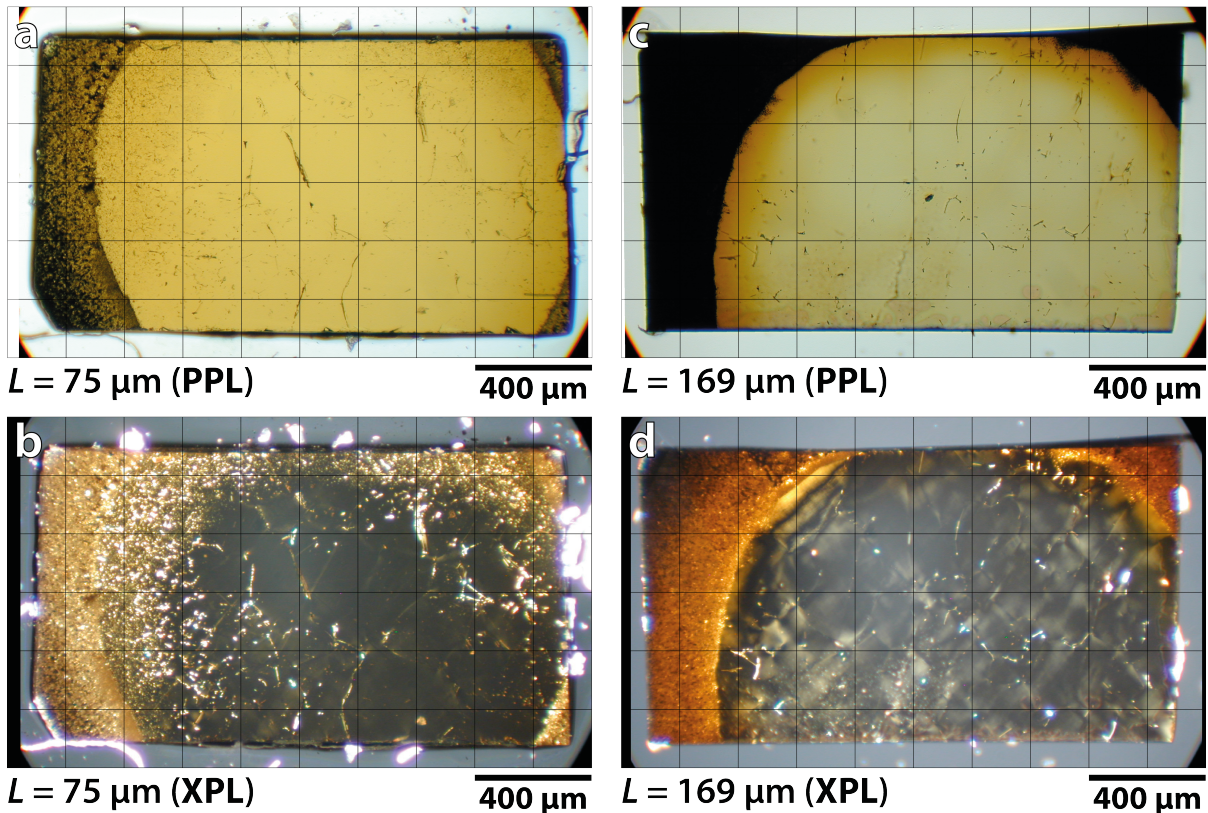


Figure 2.7: Photomicrographs of ferropericlase samples synthesized by Fe-Mg interdiffusion at 1 GPa and 1400°C in an iron capsule. PPL: plane-polarized light, XPL: cross-polarized light.

tom of the capsule, the thinnest platelet could not be recovered and is therefore not visible in Figure 2.10a. A decompression crack cut through the platelet with an initial thickness of 98 μm . Fine-grained metallic material was dispersed throughout the capsule and interpreted as iron that originated from the capsule and reacted with the (Mg,Fe)O powder. All three platelets were separated from the fine-grained material and polished to expose their faces. Figures 2.7a and 2.7c show transmitted light photomicrographs of platelets with initial thicknesses of 73 μm and 150 μm , respectively. Both platelets are transparent with a vivid yellow color. When viewed between crossed polarizers (Figs. 2.7b and 2.7d), both platelets appear to be composed of grains with diameters between 100 μm and 500 μm . This size estimation was also verified by a preliminary inspection of the 73 μm thin platelet using electron back-scattered diffraction.

After fragmentation of the 73 μm thin platelet, a single grain was isolated and oriented using single-crystal X-ray diffraction. A double-sided polished, plane-parallel thin section parallel to the (100) crystallographic plane prepared from this grain is shown in Figure 2.8. The ferropericlase single crystal is free of inclusions and cracks. The homogeneous yellow color indicates chemical homogeneity and low ferric iron contents as later verified by Mössbauer spectroscopy. The synthesized ferropericlase single crystals are of suitable size and quality for future high-pressure experiments. In contrast to the greenish color observed on previously synthesized ferropericlase crystals with similar compositions (Keppler et al., 2007; Antonangeli et al., 2011), the crystals synthesized in this study are yellow and highly transparent up to thicknesses of at least 150 μm (Figs. 2.7a and 2.7c). The change in color is most probably related to slightly higher concentrations of ferric iron as compared with green

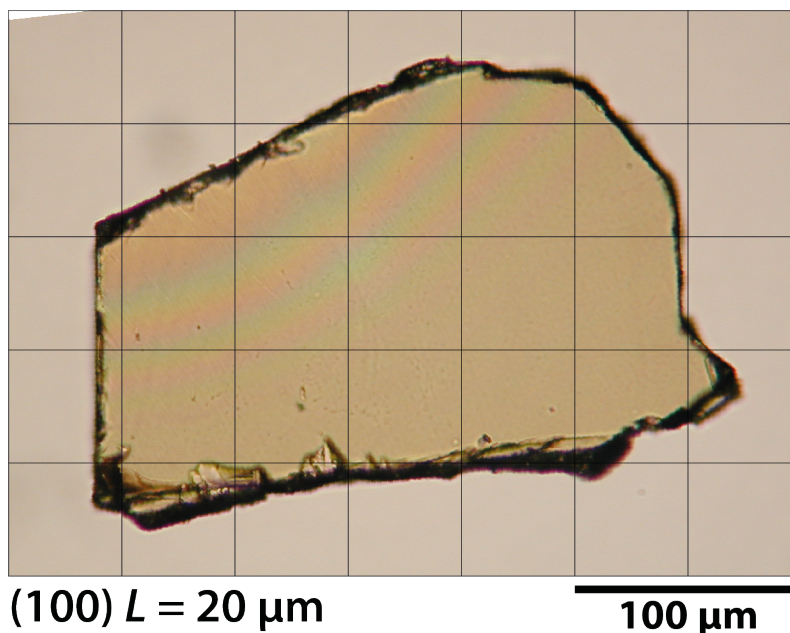


Figure 2.8: Photomicrograph of a ferropericlasite single crystal oriented parallel to the (100) crystallographic plane.

ferropericlasite samples. The effect of ferric iron on the optical properties of ferropericlasite at high pressures and possible implications for radiative heat transport in Earth's lower mantle (Goncharov et al., 2006; Keppler et al., 2007) might be another topic of interest for future investigations on the here-synthesized ferropericlasite single crystals.

2.2 Characterization of Samples for High-Pressure Experiments

Many minerals form solid solutions between two or more end members. As the physical properties of minerals change with chemical composition, chemical characterization forms the basis to resolve the effect of a given chemical element. For the derivation of the elastic properties from sound wave velocities, the density and hence the molar mass of the mineral is needed. While the concentrations of most elements of interest in mantle mineralogy can be accurately determined by electron microprobe analysis, hydrogen concentrations can be quantified by infrared absorption spectroscopy. Given the strong effect of hydrogen incorporation on density and elastic properties, a reliable determination of hydrogen concentrations is of particular importance for wadsleyite single crystals.

2.2.1 Chemical Characterization by Electron Microprobe Analysis

The chemical compositions of synthesized samples were determined by electron microprobe analysis (EMPA). Here, I will focus on the sample specific analysis strategy. A general introduction into the wide field of EMPA can be found, for example, in Goldstein et al. (2018). Measurements were performed on a JEOL⁹ JXA-8200 electron microprobe. X-ray fluores-

⁹JEOL Ltd., Tokyo, Japan, www.jeol.co.jp

Table 2.2: Parameters for electron microprobe analysis

Element	Analyzed X-ray line	energy (keV) ^a	Counting time (s) line	background	Detection limit (μg/g) ^b	Standard material
Wadsleyite						
Si	<i>Kα</i>	1.740	20	2 × 10	62	(Mg,Fe) ₂ SiO ₄ olivine
Al	<i>Kα</i>	1.487	20	2 × 10	43	MgAl ₂ O ₄ spinel
Fe	<i>Kα</i>	6.404	20	2 × 10	105	(Mg,Fe) ₂ SiO ₄ olivine
Mn	<i>Kα</i>	5.899	20	2 × 10	101	MnTiO ₃ pyrophanite
Mg	<i>Kα</i>	1.254	20	2 × 10	60	(Mg,Fe) ₂ SiO ₄ olivine
Ca	<i>Kα</i>	3.692	20	2 × 10	22	CaSiO ₃ wollastonite
Ni	<i>Kα</i>	7.478	20	2 × 10	129	Ni elemental nickel
Ferropericlase						
Si	<i>Kα</i>	1.740	20	2 × 10	57	Mg ₂ SiO ₄ forsterite
Al	<i>Kα</i>	1.487	20	2 × 10	47	MgAl ₂ O ₄ spinel
Fe	<i>Kα</i>	6.404	20	2 × 10	100	Fe elemental iron
Mg	<i>Kα</i>	1.254	20	2 × 10	70	Mg ₂ SiO ₄ forsterite

^aEnergies from Bearden (1967).

^bBased on oxide mass.

cence was excited in the sample by a beam of electrons accelerated with a voltage of 15 kV and focused to a spot size of 1 to 2 μm on the sample surface. The beam current was set to 15 nA. Element specific parameters are listed in Table 2.2 for wadsleyite and ferropericlase. Detection limits and statistical errors on element concentrations were estimated for individual measurements based on Poisson counting statistics. In this case, the estimated standard deviation σ on the absolute photon count N is given by $\sigma = \sqrt{N}$ and was propagated through subsequent calculations. Stated errors reflect standard deviations for average compositions.

For wadsleyite, chemical characterization aimed at assessing the homogeneity of the synthesis products. Figure 2.9 shows the major element compositions of four wadsleyite crystals. As revealed by the line scans, magnesium, silicon, and iron are homogeneously distributed both within each crystal and across the four examined crystals. Full chemical compositions of analyzed wadsleyite crystals including all analyzed elements and chemical formulae have been published in Kawazoe et al. (2015) and in Buchen et al. (2017) (Chapter 4, Table A.1 on page 185).

As the ferropericlase crystals were synthesized by Fe-Mg interdiffusion (see section 2.1.2), we expect concentration gradients across the samples. Figure 2.10 shows the results of line scans across different regions of the synthesis product in terms of the Fe/(Mg+Fe) ratio. Although the Fe/(Mg+Fe) ratio increased from 0 to at least 0.05 even in the center of the thickest platelet, steep concentration gradients persist across the platelets with thicknesses of 98 μm and 150 μm. These gradients are steeper than those predicted by a simple diffusion model (see section 2.1.2 for details). Some parts of the platelets, however, show gradients that might be negligible in view of the typical thickness of samples for diamond anvil cell experiments, i. e. around 20 μm. Moreover, the spread in compositions allows to select crystals with different compositions for comparative studies, for example by loading multiple crystals together inside the same diamond anvil cell (Schulze et al., 2017).

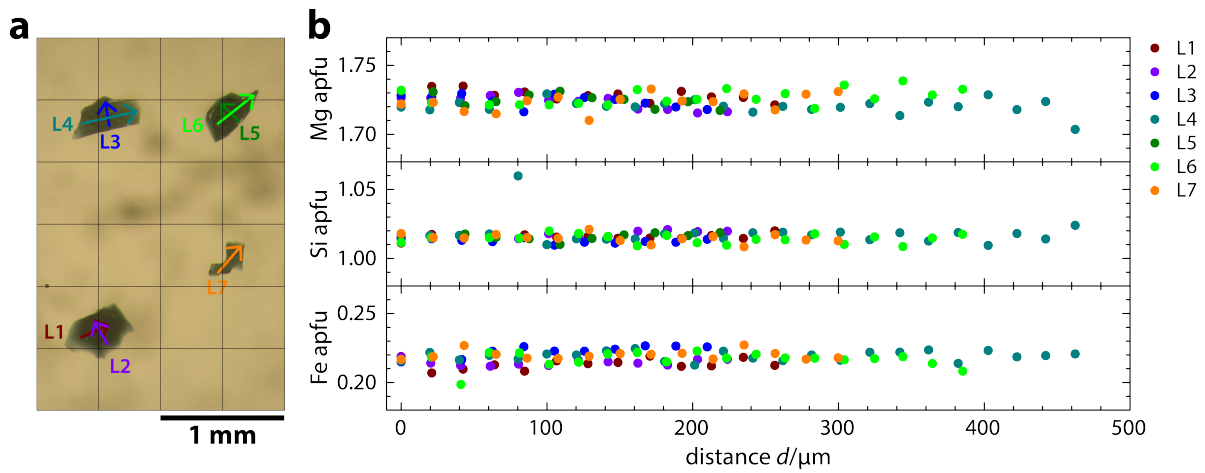


Figure 2.9: Electron microprobe analysis of wadsleyite grains synthesized in run #1 (Table 2.1). Compositions in **b)** were measured along the lines shown in **a)**.

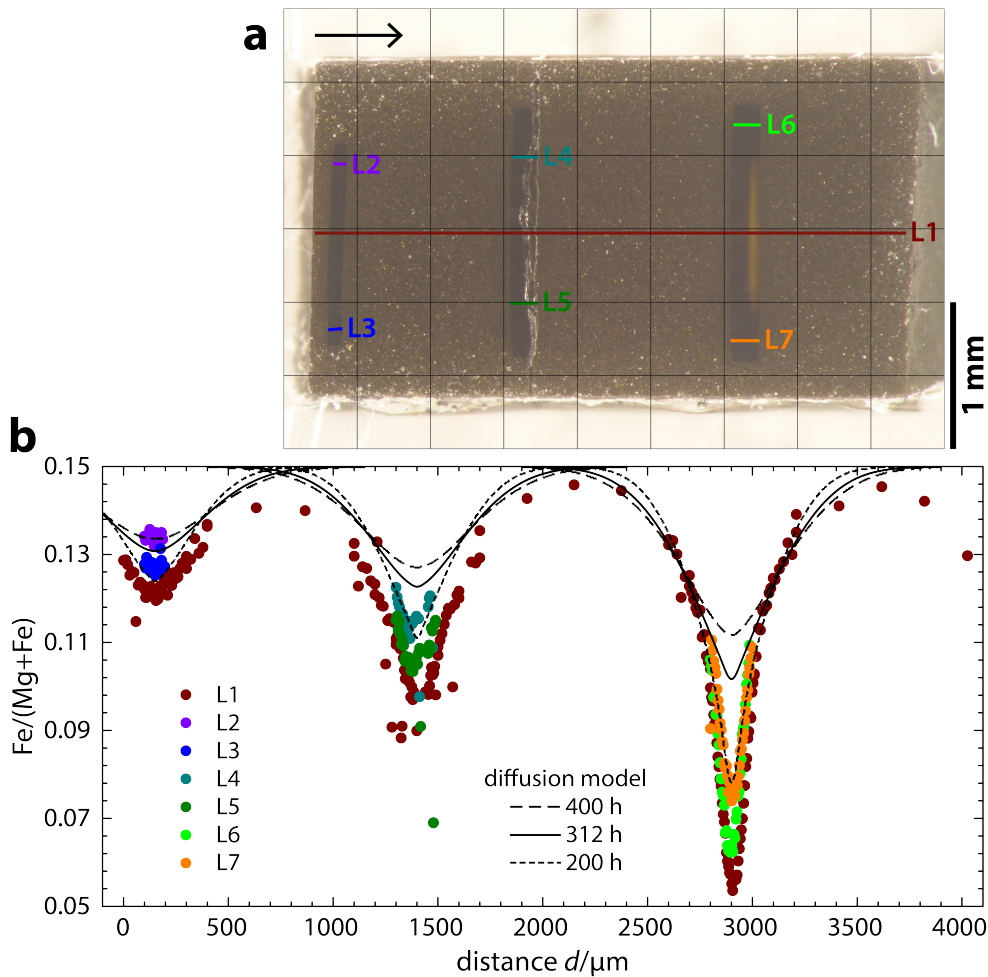


Figure 2.10: Electron microprobe analysis of Fe-Mg interdiffusion profiles. $\text{Fe}/(\text{Mg}+\text{Fe})$ ratios in **b)** were measured along the lines shown in **a)**. Black lines in **b)** show modeled Fe-Mg interdiffusion profiles for the indicated diffusion times.

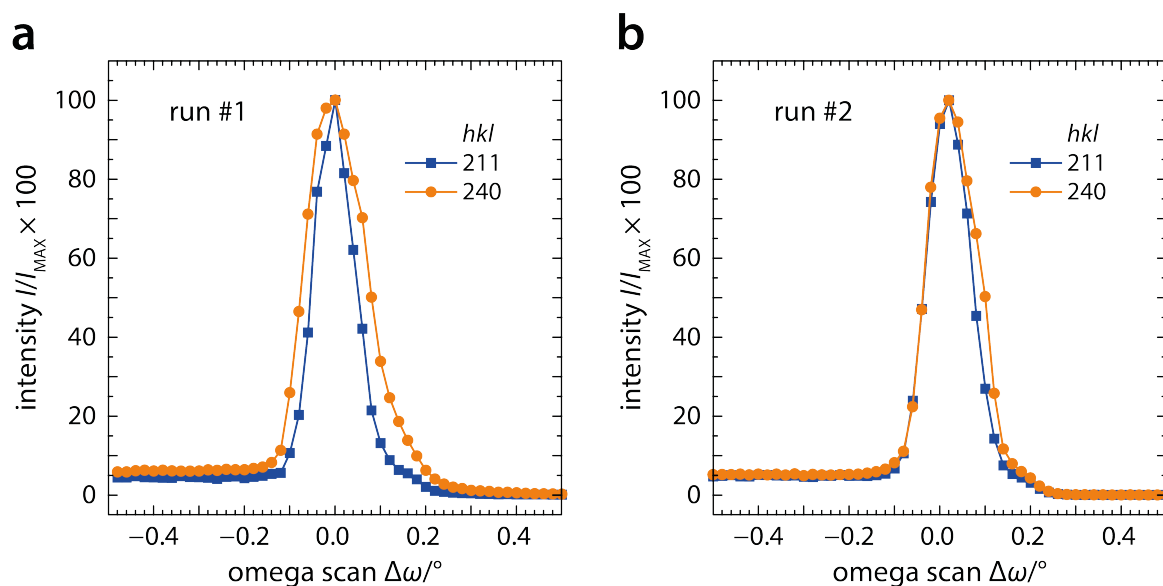


Figure 2.11: Omega profiles of the 211 and 240 reflections recorded on crystals synthesized in run #1 (a) and run #2 (b).

2.2.2 Assessment of Crystal Quality by Single-Crystal X-ray Diffraction

Wadsleyite crystals with homogeneous extinction between crossed polarizers were separated and glued to the tip of a glass fiber. The glass fiber was mounted onto a goniometer head that was inserted into one of the diffractometer systems described in section 2.4.1.1. After determination of the orientation matrix using the XcaliburTM 2²¹ diffractometer, the HUBER²² diffractometer was used to scan ω profiles of individual reflections. Reflection profiles of single crystals contain information about the mosaic structure and hence the quality of the single crystal (Massa, 2011). The broader the ω profile of a given reflection, the higher is the spread in misorientations of domains in the crystal. The widths of ω profiles of individual reflections therefore reflect the degree of internal distortion of a crystal. Only crystals with full widths at half heights of ω scans below 0.15° were retained for further analysis and experiments. Lattice parameters were determined in air using the 8-position centering procedure as described in section 2.4.1.1. Figure 2.11 shows representative reflection profiles of two wadsleyite crystals. Further results of single-crystal X-ray diffraction experiments on wadsleyite crystals at ambient conditions have been published in Kawazoe et al. (2015) and Buchen et al. (2017) (Chapter 4).

After the refinement of lattice parameters, the computed orientation matrix was used to rotate the crystal on the goniometer so as to bring a selected lattice plane in a horizontal position. Without changing the orientation, the crystal was immersed in a droplet of Verifix^{®10} adhesive resting on a horizontally oriented glass slide. The adhesive was cured with UV radiation fixing the crystal with the selected lattice plane parallel to the flat surfaces of the glass slide. Prepared in this way, single crystals were double-sided polished to plane-parallel thin sections by staff¹¹ of the sample preparation laboratory at the Bayerisches Geoinstitut. The orientation of polished crystal sections was preserved within 3° as verified

¹⁰Bohle AG, Haan, Germany, www.bohle-group.com

¹¹Hubert Schulze, ✉ hubert.schulze@uni-bayreuth.de, Raphael Njul, ✉ raphael.njul@uni-bayreuth.de

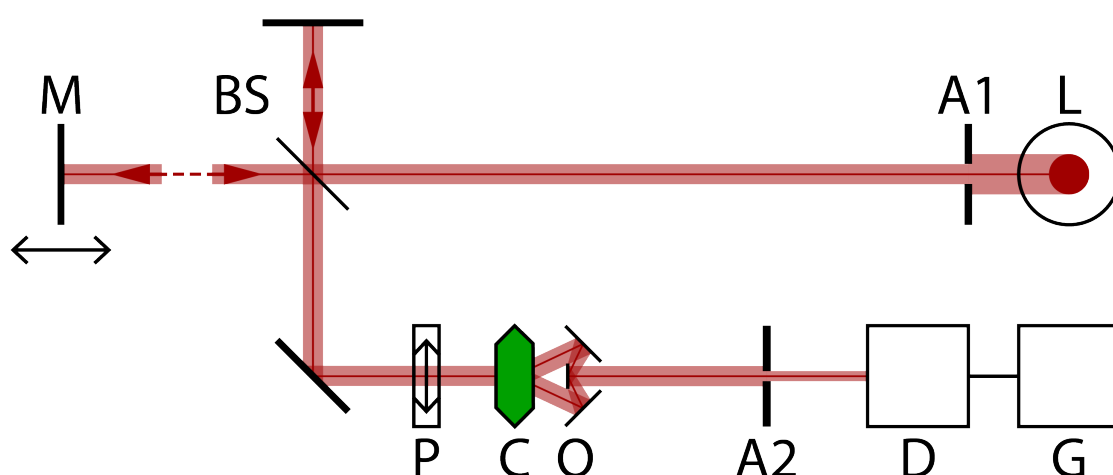


Figure 2.12: Schematic drawing of a Fourier-transform infrared spectrometer. L: light source (tungsten lamp), A1: aperture, BS: beam splitter (Si-coated CaF_2), M: scanning mirror, P: polarizer, C: crystal, O: reflecting optics, A2: variable aperture, D: detector, G: pre-amplifier.

by X-ray diffraction on crystals loaded into diamond anvil cells (see section 2.4.1.1). Most crystal sections deviated by only about 1° from the selected lattice plane.

2.2.3 Determination of Hydrogen Concentrations by Fourier-Transform Infrared Absorption Spectroscopy

The detection and quantification of hydrous species in minerals by means of infrared spectroscopy has evolved to a standard technique in mineralogy (e. g. Rossman, 1988; Rossman, 2006). As explained in section 1.3.1, hydrogen is incorporated into the crystal structure of wadsleyite in the form of hydroxyl groups (Smyth, 1987; McMillan et al., 1991; Young et al., 1993; Jacobsen et al., 2005). While the strength of infrared absorption is related to the concentration of the absorbing species through the Beer-Lambert law (Rossman, 1988; Libowitzky and Rossman, 1997), frequency and polarization of the absorption bands reflect the atomic environment of the absorbing species such as bond length (Nakamoto et al., 1955; Libowitzky, 1999) and orientation (Libowitzky and Rossman, 1996; Jacobsen et al., 2005; Libowitzky, 2006) of hydroxyl groups. Polarized infrared absorption spectra therefore allow discriminating between different types of structurally bonded hydroxyl groups and to recognize hydroxyl groups that are present in phases other than the mineral of interest, for example on grain boundaries or in inclusions. The ability to identify and quantify hydrogen concentrations independently for different types of hydroxyl groups brings about important advantages over other analytical techniques that are blind to the original state of counted hydrogen atoms in the sample such as Secondary Ion Mass Spectrometry (SIMS) and Elastic Recoil Detection Analysis (ERDA) (Rossman, 2006). Both SIMS (Inoue et al., 1995; Demouchy et al., 2005; Deon et al., 2010; Bolfan-Casanova et al., 2012) and ERDA (Bolfan-Casanova et al., 2018) have been used to quantify hydrogen contents of wadsleyite beside numerous infrared spectroscopy studies (e. g. McMillan et al., 1991; Young et al., 1993; Kohlstedt et al., 1996; Jacobsen et al., 2005; Deon et al., 2010).

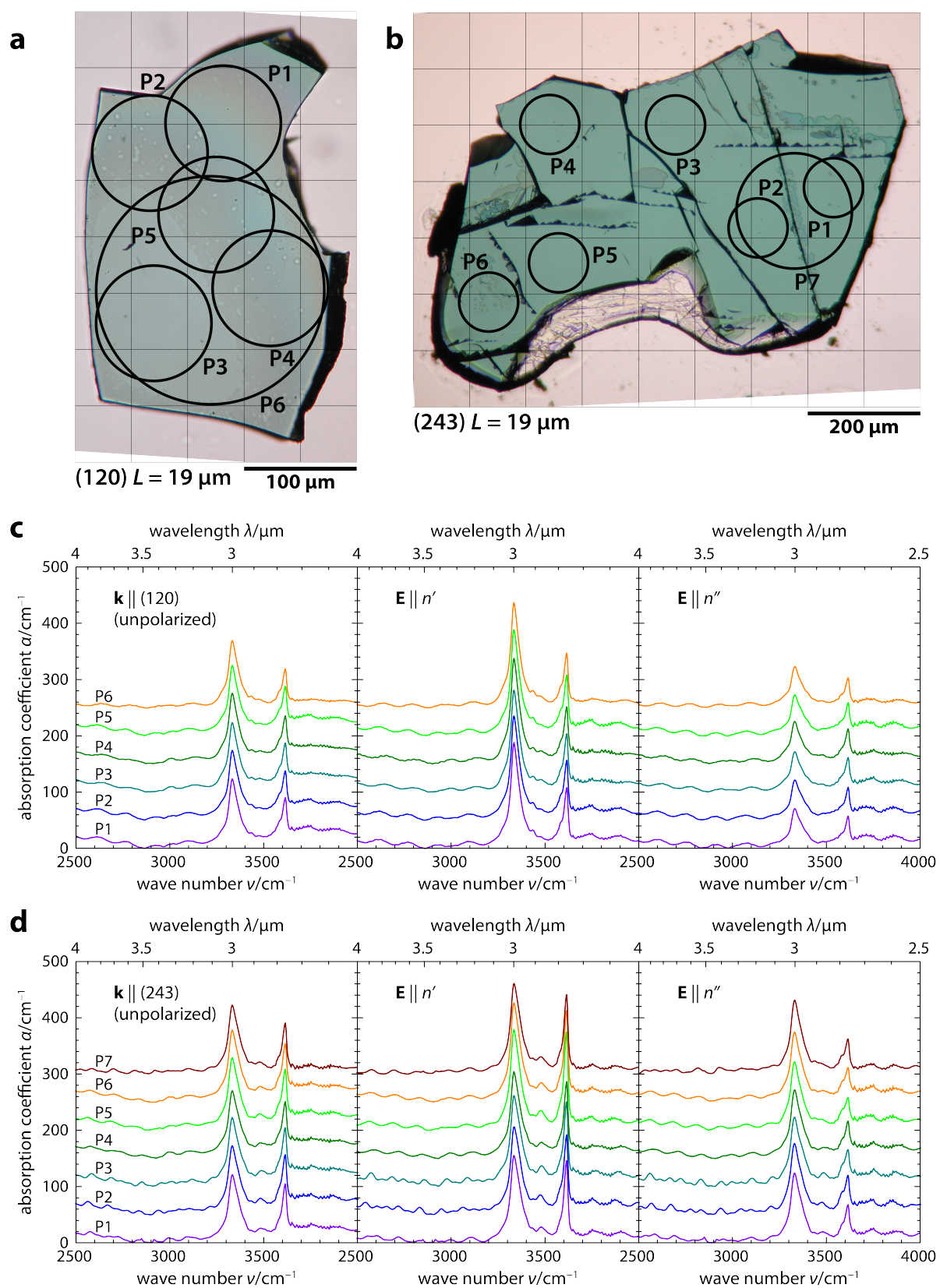


Figure 2.13: Photomicrographs of oriented wadsleyite single crystals (**a,b**) and FTIR absorption spectra (**c,d**) recorded at the spots indicated in **a**) and **b**). Spectra in **c**) were recorded on the crystal section shown in **a**); spectra in **d**) were recorded on the crystal section shown in **b**).

Table 2.3: Hydrogen concentrations in wadsleyite crystals from FTIR spectroscopy

Crystal orientation (<i>hkl</i>)	Number of spectra <i>N</i>	Polarized [H ₂ O] _P (mol l ⁻¹) ^a	Unpolarized [H ₂ O] _U (mol l ⁻¹) ^a	Ratio [H ₂ O] _P / [H ₂ O] _U
Synthesis run #1				
(120)	1	0.51(5)	0.56(7)	0.91(14)
(120)	6	0.41(4)	0.44(6)	0.93(16)
(243)	1	0.43(4)	0.41(6)	1.05(18)
(243)	2	0.59(5)	0.50(7)	1.18(19)
Mean	(mol l ⁻¹)	0.49(5)	0.48(7)	
	(wt-%)	0.24(2)	0.24(3)	
	(mpfu) ^b	0.0198(18)	0.0196(27)	
Synthesis run #2				Mean
(120)	1	<i>1.47(33)</i>	1.60(24)	0.92(15)
(243)	2	<i>1.39(31)</i>	1.25(18)	1.11(19)
Mean	(mol l ⁻¹)	1.43(32)	1.43(21)	
	(wt-%)	0.72(16)	0.72(11)	
	(mpfu) ^b	0.0581(128)	0.0581(85)	

Numbers in *italics* were calculated based on the mean ratio [H₂O]_P/[H₂O]_U for the respective crystal orientation.

^aBased on the calibration by Libowitzky and Rossman (1997).

^bH₂O molecules per formula unit.

Descriptions on the theory and instrumentation of Fourier-Transform Infrared Spectroscopy (FTIR) can be found for instance in McMillan and Hofmeister (1988) and Kuzmany (2009). Here, I concentrate on those aspects essential for this study. Figure 2.12 shows a schematic drawing of the FTIR setup that consisted of an infrared microscope with reflecting optics coupled to a Bruker¹² IFS 120 HR FTIR spectrometer. A detailed description of the experimental procedure has been published in Buchen et al. (2017) (Chapter 4, sections 4.2.4 and A.1.1). FTIR absorption spectra were recorded on plane-parallel wadsleyite single-crystal thin sections that were oriented parallel to the (120) or (243) crystallographic planes and double-sided polished. Polarized and unpolarized spectra were recorded in transmission covering a spectral range from 2500 to 4000 cm⁻¹ with a resolution of 4 cm⁻¹. Immersing the single-crystal thin sections in polychlorotrifluoroethylene oil substantially reduced interference fringes but did not suppress them completely. Intents to reduce inference fringes by placing the thin sections above a small circular aperture in a metal foil instead of using a CaF₂ support plate were to no avail indicating that interference originated within the sample by internal reflections on the plane-parallel polished sample surfaces.

The quantitative analysis of recorded FTIR spectra is explained in detail in section A.1.1 including background correction, deconvolution, and integration of absorption bands arising from structurally bonded hydroxyl groups in wadsleyite. Integrated band absorbances of polarized FTIR absorption spectra were combined and converted to hydrogen concentrations according to the principles laid out by Libowitzky and Rossman (1996) and Libowitzky

¹²Bruker Corporation, Billerica, Massachusetts, USA, www.bruker.com

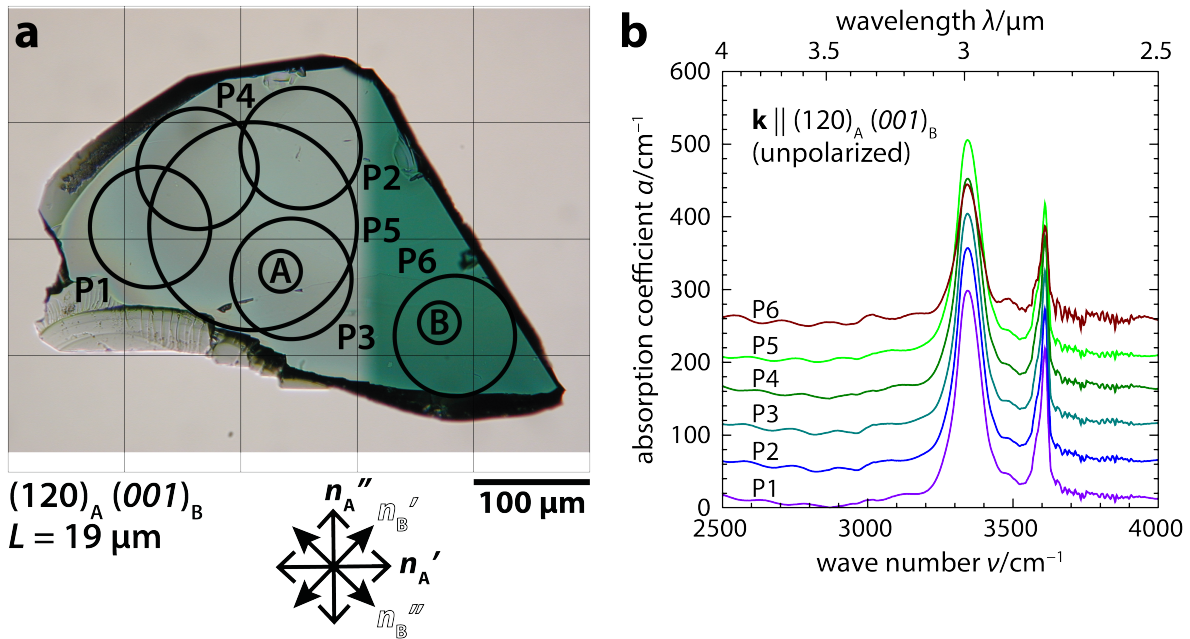


Figure 2.14: Photomicrograph of a twinned wadsleyite crystal (a) and unpolarized FTIR absorption spectra (b) recorded at the spots shown in a). In a), part A (pale green color) was oriented parallel to the (120) crystallographic plane using X-ray diffraction while the tentative orientation of part B (dark green color) was inferred from extinction positions and pleochroism.

and Rossman (1997). In Buchen et al. (2017) (Chapter 4, section 4.2.4), we applied different calibrations to quantify hydrogen in minerals (Paterson, 1982; Libowitzky and Rossman, 1997) and wadsleyite in particular (Deon et al., 2010) by FTIR absorption spectroscopy. Comparing the results for individual absorption bands (Table A.4 on page 186), we concluded that a wave number-dependent absorption coefficient is needed to take into account the band-specific absorption strength, in particular for iron-bearing wadsleyite.

In addition to the determination of hydrogen concentrations, I used FTIR spectroscopy to examine the homogeneity of the synthesized wadsleyite crystals in terms of amount and speciation of structurally bonded hydroxyl groups (see also Kawazoe et al., 2015). Figure 2.13 shows two wadsleyite single-crystal sections and the FTIR absorption spectra that were recorded on different locations on these crystals. Although the two crystals differ substantially in size, both are internally homogeneous in terms of hydrogen concentrations and speciations as can be directly inferred from the similarity of polarized FTIR absorption spectra collected on different spots on each crystal.

Figure 2.14 shows unpolarized FTIR absorption spectra recorded on a more hydrous wadsleyite crystal (run #2 in Table 2.1). Polarized FTIR absorption spectra recorded on this and on another crystal from the same synthesis run showed indications for total absorption of infrared radiation at wave numbers of maximum absorption. The combination of hydrogen concentration and thickness of these crystal sections together with the additional reduction of transmitted light intensity caused by the polarizer might have pushed the transmitted light intensity below a minimum level. When the transmitted light intensity drops below this minimum level, the resulting absorption spectra might be distorted or even cut off at a maximum threshold absorbance. Water contents of these hydrous crystals were therefore estimated from unpolarized spectra and an empirical ratio based on water

contents derived from unpolarized and polarized FTIR absorption spectra of less hydrous wadsleyite crystals. As the unpolarized spectra may be affected by low transmitted light intensities as well, water contents derived in this way are less reliable and best interpreted as lower bounds. Table 2.3 summarizes the water contents determined on wadsleyite crystals used in subsequent experiments.

2.3 High-Pressure Experiments with Diamond Anvil Cells

The transparency of diamond to visible light and X-rays allows to determine a variety of physical properties on samples held at high pressures inside a diamond anvil cell (DAC) (Jayaraman, 1983; Mao and Hemley, 1996). Figure 2.16 shows the essential components of a diamond anvil cell. A comprehensive description of different types of diamond anvil cells, their assembly, and operation can be found in Miletich et al. (2000). Depending on the type of experiment or measurement to be performed on the sample, the components shown in Figure 2.16a need to fulfill specific requirements such as X-ray transparency, temperature stability, or geometric restrictions. The small sample sizes also pose challenges on sample preparation techniques. Brillouin spectroscopy experiments, for example, require plane-parallel and optically clear and transparent samples that are small enough to fit into the DAC but at the same time large enough to ensure the right scattering geometry.

2.3.1 Sample Preparation for High-Pressure Experiments by Focused Ion Beam Cutting

Wadsleyite single crystals were oriented parallel to the (120) or (243) crystallographic planes using X-ray diffraction. Oriented grains were double-sided polished to plane-parallel sections with final thicknesses between 10 and 20 μm . After characterization by FTIR spectroscopy (see section 2.2.3), wadsleyite thin sections were glued onto metallic holders using CrystalbondTM ¹³, nail polish, or UHU[®] ¹⁴ super glue without any conductive coating. Samples were introduced into a FEI¹⁵ SciosTM dual beam device equipped with a liquid metal ion source. A focused Ga⁺ ion beam was used to cut circles with diameters of 110 to 120 μm and, in a second step, semicircles out of the single-crystal thin sections. Ga⁺ ions were accelerated by a voltage of 30 kV and the beam current adjusted between 7 and 30 nA depending on sample thickness and available machine time. To cut wadsleyite samples with thicknesses between 10 and 20 μm , a trench width of about 5 μm was found to be sufficient to ensure clean cutting profiles. Figure 2.15 shows a wadsleyite crystal section after ion beam cutting.

The central advantage in using ion beam cutting techniques consists in the precision with which samples of tailored size and shape can be prepared (Marquardt and Marquardt, 2012). Optimized sample shapes allow to load multiple samples into the same high-pressure chamber of a diamond anvil cell (see Fig. 2.17a). We showed in Schulze et al. (2017) how loading multiple crystals into the same diamond anvil cell improves the precision and accuracy in the determination of elastic properties of materials with low crystal symmetry as well as in the quantification of effects of chemical composition on physical properties at high pressures. A thin section with final thickness of 13 μm was prepared from a sample

¹³Ted Pella Inc., Redding, California, USA, www.tedpella.com

¹⁴UHU GmbH & Co. KG, Bühl, Germany, www.uhu.de

¹⁵FEI Technologies Inc., Hillsboro, Oregon, USA, www.fei.com

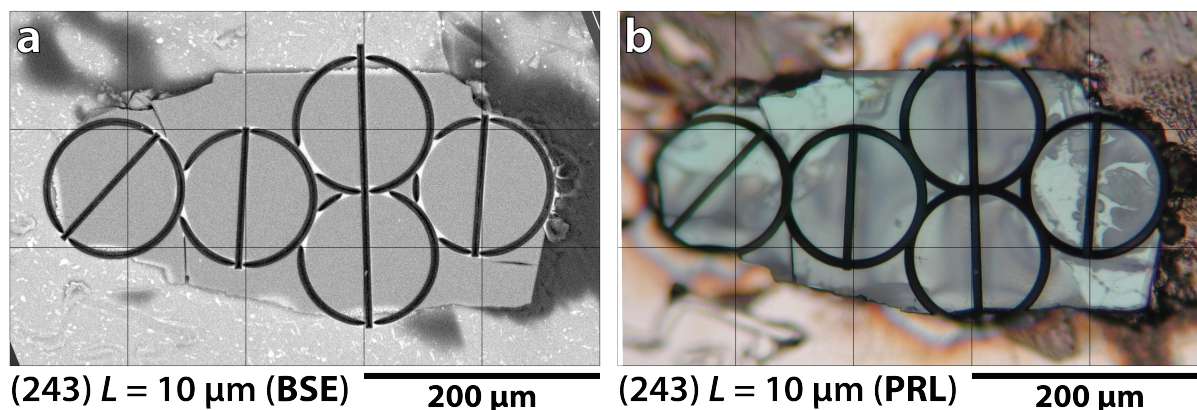


Figure 2.15: Back scatter electron image (a) and reflected light photomicrograph (b) of a wadsleyite single crystal that has been cut into semicircles using a focused ion beam.

of sintered polycrystalline stishovite (Nishiyama et al., 2014) and circles with diameters of 40 μm were cut from the thin section as explained above.

2.3.2 Assembly of the Diamond Anvil Cell

This study focuses on the characterization of elastic properties at high pressures that can be determined using X-ray diffraction (section 2.4.1) and Brillouin spectroscopy (section 2.4.2). Both techniques require a large opening angle of the DAC, i. e. the maximum angle up to which an X-ray or laser beam can be tilted away from the compression axis while still passing through the sample. The BX90 diamond anvil cell (Kantor et al., 2012) was designed with a 90° external opening angle and is well suited for the experiments of this study. To maintain a large opening angle, we used type Ia conical diamond anvils of Boehler Almax¹⁶ design (Boehler and De Hantsetters, 2004; Boehler, 2006) with a nominal opening angle of 80° as constrained by the anvil height and the size of the table. For experiments up to 20 GPa, we chose diamond anvils with culet sizes of 400 or 500 μm . To reach pressures up to about 70 GPa, the culet size was reduced to 200 μm . Diamond anvils were aligned using the optical interference fringes between the culets of opposing anvils and glued to tungsten carbide seats with conical cut-outs using super glue or graphite-based high-temperature glue (Graphi-BondTM 17). Rhenium foils with an initial thickness of 200 μm were used as gaskets. Depending on the culet size, gaskets were preindented to 50–60 μm and to 40 μm for culets with diameters of 400–500 μm and 200 μm , respectively. To create the sample chamber, a hole was drilled in the center of the indentation using either a focused Ga^+ ion beam or an infrared laser. For DACs to be loaded with two crystals, the diameter of the hole varied between 235 and 275 μm . A gasket with a hole of 330 μm in diameter was prepared for a DAC to be loaded with four wadsleyite crystals. For all high-pressure experiments, we loaded neon as pressure-transmitting medium as it creates a quasi-hydrostatic stress environment up to 15 GPa (Meng et al., 1993; Klotz et al., 2009). Even at higher pressures, deviatoric stresses and pressure gradients remain small in neon (Meng et al., 1993; Klotz et al., 2009; Buchen et al., 2017; Buchen et al., 2018a). Precompressed neon was loaded at the gas loading facilities installed at the Bayerisches Geoinstitut (Kurnosov et al., 2008)

¹⁶Almax easyLab Inc., Cambridge, Massachusetts, USA, www.almax-easylab.com

¹⁷Aremco Products Inc., Valley Cottage, New York, USA, www.aremco.com

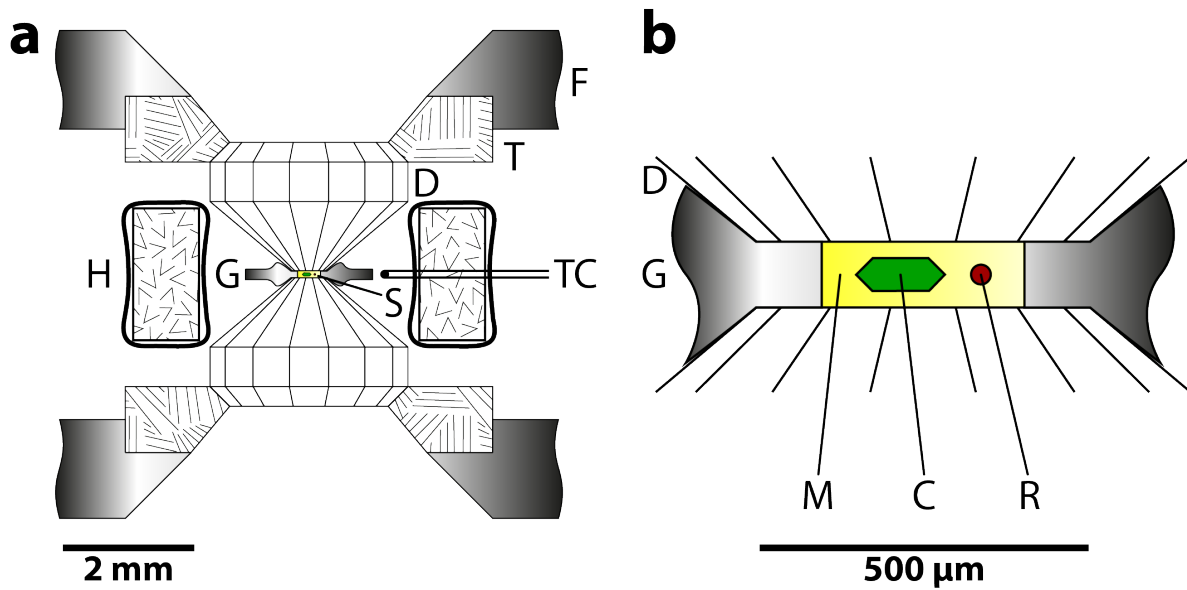


Figure 2.16: Schematic drawing showing the components of a diamond anvil cell (a) and the high-pressure chamber (b). F: metal frame, T: seats (tungsten carbide), D: diamond anvils, G: gasket (rhenium), S: high-pressure sample chamber, H: resistive heater, TC: thermocouple (type S), M: pressure-transmitting medium (neon), C: crystal, R: fluorescent pressure-temperature sensor (ruby, Sm:YAG)

and at PETRA III at the Deutsches Elektronen-Synchrotron (DESY) in Hamburg, Germany (Liermann et al., 2015).

To heat the sample inside the DAC at high pressures, we used a resistive heater that consisted of a platinum wire ($\varnothing = 0.5$ mm) coiled around a MACOR[®] ¹⁸ ceramic ring. With a height of 6 mm, inner and outer diameters of ~ 16 and ~ 22 mm, respectively, the heater fit inside the BX90 metal frame and surrounded the tungsten carbide seats with the diamond anvils at their centers. At room temperature, the heater had an electrical resistance of $\sim 0.4 \Omega$ and was typically powered with 30 to 115 W depending on the temperature to be reached. By comparing the temperature measured with a thermocouple in contact with one of the diamond anvils with the temperature inside the high-pressure chamber of the DAC as estimated by fluorescence spectroscopy, we found that the heater design was able to homogeneously heat the space enclosed by the heater and the tungsten carbide seats including the high-pressure chamber of the DAC and to keep temperatures stable throughout several days. In this study, experiments were performed at a maximum temperature of about 900 K. To prevent oxidation of the rhenium gasket, the DAC was constantly purged with a flow of argon and hydrogen gases mixed in a ratio of $\text{Ar:H}_2 = 99:1$.

2.3.3 Pressure and Temperature Determination by Fluorescence Spectroscopy

During high-pressure experiments, pressure was determined from the calibrated shift of the ruby R_1 fluorescence line to higher wavelengths with increasing pressure (Forman et al., 1972; Mao et al., 1986). Along with the sample, a ruby sphere ($\varnothing = 20 \mu\text{m}$) was loaded into the high-pressure chamber of the DAC. For experiments at combined high pressures

¹⁸Corning Inc., Corning, New York, USA, www.corning.com

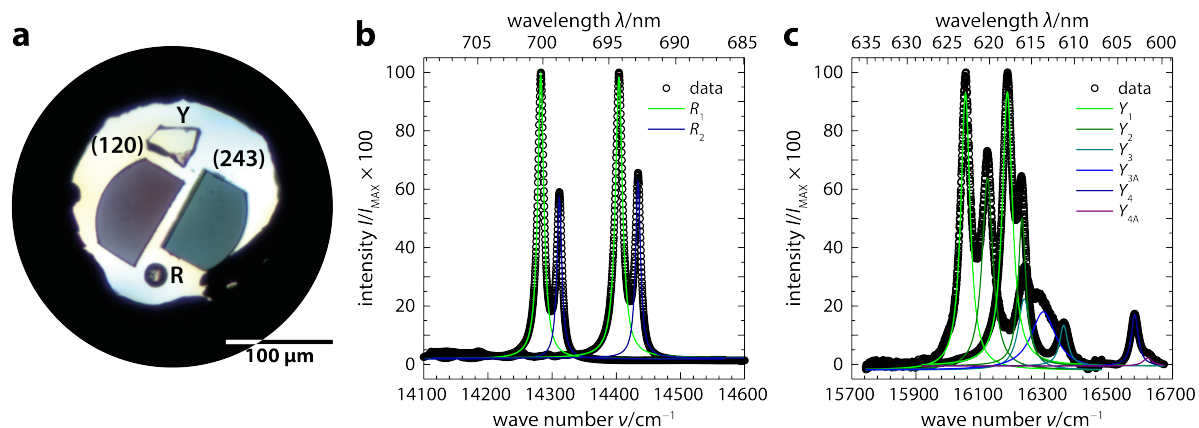


Figure 2.17: **a)** View into a diamond anvil cell loaded with two wadsleyite single crystals, a ruby sphere (R), and a Sm:YAG crystal (Y). The orientations of the wadsleyite crystals are indicated. **b** and **c)** Fluorescence spectra of ruby (**b**) and Sm:YAG (**c**). In **b**) and **c)**, the spectrum at higher wave numbers was recorded at ambient conditions. Lines show peak fitting results.

and high temperatures, we also loaded a chip of a samarium-doped yttrium aluminum garnet (Sm:YAG) crystal with the intention to determine both pressure and temperature inside the high-pressure chamber of the DAC by combining pressure- and temperature-induced shifts of the fluorescence lines of both materials. Fluorescence spectra were recorded either on a HORIBA¹⁹ Jobin Yvon spectrometer, on a Princeton Instruments²⁰ IsoPlane-160 spectrometer (both at the Bayerisches Geoinstitut), on a custom-built spectrometer at PETRA III/DESY in Hamburg (Liermann et al., 2015), or on the online spectrometer at beamline ID15B of the European Synchrotron Radiation Facility (ESRF) in Grenoble. Typically, two fluorescence spectra were collected through each anvil of the DAC, i. e. four in total, before and after X-ray diffraction or Brillouin spectroscopy experiments. Reference spectra of ruby and Sm:YAG at ambient conditions were recorded for each fluorescence spectroscopy session. The Raman spectrum of a silicon standard recorded on the respective spectrometer and for each fluorescence spectroscopy session was used to correct for small shifts in wave numbers assuming a wave number of 521 cm^{-1} for the Raman active mode of silicon (Russell, 1965; Parker et al., 1967; Hart et al., 1970). During synchrotron X-ray diffraction experiments, however, the collection of reference spectra was not possible. To extract the central wave numbers of fluorescence lines, recorded fluorescence spectra were analyzed by fitting Lorentzian peak functions to observed fluorescence lines of ruby and Sm:YAG. After converting the central wave numbers of the ruby R_1 fluorescence line and the Sm:YAG Y_1 fluorescence lines to wavelengths, I calculated pressures according to the calibrations given by Dewaele et al. (2008) for ruby and by Trots et al. (2013) for Sm:YAG. The wavelength of the respective fluorescence line at ambient conditions was taken from the recorded reference spectrum if available. Errors were estimated as the standard deviation of pressures determined before and after X-ray diffraction or Brillouin spectroscopy experiments. Figure 2.17 shows typical ruby and Sm:YAG fluorescence spectra.

In the case of experiments at combined high pressures and high temperatures, the displacements of fluorescence lines from their wave numbers at ambient conditions result from the addition of pressure- and temperature-induced shifts. For both ruby and Sm:YAG, com-

¹⁹HORIBA Ltd., Kyoto, Japan, www.horiba.com

²⁰Princeton Instruments, Trenton, New Jersey, USA, www.princetoninstruments.com

bined pressure- and temperature-induced shifts have been calibrated (Hess and Schiferl, 1990; Rekhi et al., 1999; Sanchez-Valle et al., 2002; Wei et al., 2011). These calibrations can be used to derive pressure and temperature from pairs of ruby and Sm:YAG fluorescence spectra recorded at the same pressures and temperatures. I combined the calibrations for the pressure- and temperature-induced wavelength shifts for the ruby R_1 fluorescence line by Dewaele et al. (2008) and Wei et al. (2011), respectively, with the calibrations for the pressure- and temperature-induced wave number shifts for the Sm:YAG Y_1 fluorescence line by Hess and Schiferl (1992) and Hess and Schiferl (1990), respectively, to numerically solve for the pressure-temperature combinations of experiments at simultaneously high pressures and high temperatures. As the ruby sphere and the Sm:YAG crystal were placed next to the sample, pressures and temperatures derived in this way should reflect the conditions inside the high-pressure chamber of the DAC. As for pressures, errors on temperatures were estimated from the standard deviation of several measurements at the same conditions. Temperatures determined by fluorescence spectroscopy were identical within uncertainties to those read from a thermocouple placed next to one of the diamond anvils. Owing to the strong intensity reduction of the ruby and Sm:YAG fluorescence signal at high temperatures (Hess and Schiferl, 1990; Wei et al., 2011) and the related limited temperature range of available calibrations, the method to derive pressure and temperature from fluorescence spectra as explained above may be applied up to about 800 K. This range coincides with temperatures achievable with the resistive heater used in the present study.

2.4 Determination of Elastic Properties at High Pressures

Minerals and rocks behave elastically for sufficiently small strains and stresses (Karato, 2008). Within the elastic limit, the components of the stress tensor σ_{ij} are linearly related to the components of the strain tensor ε_{ij} (Nye, 1985; Haussühl, 2007):

$$\sigma_{ij} = c_{ijkl}\varepsilon_{kl} \quad \text{and} \quad \varepsilon_{ij} = s_{ijkl}\sigma_{kl} \quad (2.2)$$

The fourth-rank tensors that connect the second-rank tensors of stress and strain are the elastic stiffness tensor with components c_{ijkl} and its inverse, the elastic compliance tensor with components s_{ijkl} . Although the components of the elastic stiffness and compliance tensors vary with pressure and temperature, they are commonly referred to as *elastic constants* and *elastic coefficients*, respectively (Haussühl, 2007). Consequently, I adopted the term *elastic constants* for the components of the elastic stiffness tensor in chapters 4, 6, and 7.

The pressure-volume-temperature (P - V - T) relationship or the equation of state (EOS) of a mineral illustrates how elastic properties are linked to the thermodynamic behavior of the mineral (Eliezer et al., 1986; Poirier, 2000). The Gibbs free energy \mathcal{G} determines the stability of phase assemblages for example in rocks (Philpotts and Ague, 2009) and can be decomposed into the Helmholtz free energy \mathcal{F} and the product of pressure P and volume V (Atkins and de Paula, 2006):

$$\mathcal{G}(P, T) = \mathcal{F}(V, T) + PV \quad (2.3)$$

This Legendre transformation changes the natural variables of the Gibbs free energy $\mathcal{G}(P, T)$, pressure P and temperature T , to the natural variables of the Helmholtz free energy $\mathcal{F}(V, T)$, volume V and temperature T . From an experimental point of view, this has the

advantage that volume can be measured directly, for example by X-ray diffraction (see section 2.4.1). Pressure is defined as the derivative of the Helmholtz free energy with respect to volume at constant temperature (Poirier, 2000):

$$P = -\left(\frac{\partial \mathcal{F}}{\partial V}\right)_T \quad (2.4)$$

The Helmholtz free energy is usually assumed to follow an expansion in terms of volume strain f of the form (Poirier, 2000; Stixrude and Lithgow-Bertelloni, 2005):

$$\mathcal{F}(V, T) = \mathcal{F}_0 + \Delta_{\text{TH}}\mathcal{F}(V, T) + \frac{1}{2}b_2f^2 + \frac{1}{6}b_3f^3 + \frac{1}{24}b_4f^4 + \dots \quad (2.5)$$

with the Helmholtz free energy at the reference state \mathcal{F}_0 and the temperature-dependent (thermal) contribution $\Delta_{\text{TH}}\mathcal{F}(V, T)$. Hydrostatic compression can cause elastic strains that are too high to be described by a linear relation between stress and strain as suggested by equation (2.2) because the elastic properties themselves change as a result of compression. Equation (2.5) therefore expands the Helmholtz free energy in terms of finite volume strains f instead of infinitesimal strains. From the Eulerian definition of finite strain (Poirier, 2000; Stixrude and Lithgow-Bertelloni, 2005)

$$f = f_E = \frac{1}{2} \left[\left(\frac{V_0}{V} \right)^{2/3} - 1 \right] \quad (2.6)$$

and the definition of pressure (2.4), we obtain:

$$P = -\left(\frac{\partial \mathcal{F}}{\partial V}\right)_T = \frac{1}{3}(1 + 2f_E)^{5/2} \left(b_2f_E + \frac{1}{2}b_3f_E^2 + \frac{1}{6}b_4f_E^3 + \dots \right) + P_{\text{TH}} \quad (2.7)$$

with the thermal pressure

$$P_{\text{TH}} = -\left(\frac{\partial \Delta_{\text{TH}}\mathcal{F}}{\partial V}\right)_T \quad (2.8)$$

Equation (2.7) relates pressure to volume and temperature, $P = P(V, T)$, and is called an equation of state. The experimental task consists in determining the numerical values of the coefficients b_2, b_3, b_4, \dots from measurements of volume, pressure, and temperature. Based on the definition (Poirier, 2000)

$$K = -V \left(\frac{\partial P}{\partial V} \right) \quad (2.9)$$

the coefficients b_2, b_3 , and b_4 can be related to the bulk modulus K_0 and its first and second pressure derivatives, $K'_0 = \partial K_0 / \partial P$ and $K''_0 = \partial^2 K_0 / \partial P^2$, at the reference state as (Poirier, 2000; Stixrude and Lithgow-Bertelloni, 2005):

$$b_2 = 9K_0 \quad (2.10)$$

$$b_3 = 27K_0(K'_0 - 4) \quad (2.11)$$

$$b_4 = 81K_0 \left[K_0K''_0 + K'_0(K'_0 - 7) + \frac{143}{9} \right] \quad (2.12)$$

Inserting the expressions for b_2 and b_3 into equation (2.5) and truncating after the term in f^3 yields the third-order Birch-Murnaghan EOS (Birch, 1947; Angel, 2000; Poirier, 2000):

$$P = \frac{1}{3}(1 + 2f_E)^{5/2} \left(9K_0f_E + \frac{27}{2}K_0(K'_0 - 4)f_E^2 \right) \quad (2.13)$$

The truncation to third order implies that (Angel, 2000)

$$K_0'' = \frac{K_0'(7 - K_0') - 143/9}{K_0} \quad (2.14)$$

For second order, we find from equation (2.11) that $K_0' = 4$.

The determination of the EOS parameters therefore facilitates the evaluation of the changes in Helmholtz or Gibbs free energies that arise from compression. At pressures of Earth's mantle, the energetic contribution of compression is substantial and needs to be taken into account when computing phase equilibria. Compressing forsterite at ambient temperature to 10 GPa, for example, increases the Gibbs free energy by about 420 kJ mol^{-1} whereas isobaric heating to 1500°C would decrease the Gibbs free energy by about 390 kJ mol^{-1} . A generalization of finite-strain theory for anisotropic materials and strains has been presented by Stixrude and Lithgow-Bertelloni (2005). For single crystals, a relation between the pressure and the finite strains along individual crystallographic axes can be derived to capture the anisotropy of compressibility (Angel, 2000; Angel et al., 2014).

Elastic properties, i. e. components of the elastic stiffness tensor or combinations of them, can be determined using static or dynamic methods (Haussühl, 2007). Static methods explore the elastic deformation of a sample as a response to a statically applied force. In high-pressure compression experiments, for instance, the change in shape and size of a sample is determined as a function of the applied pressure. Dynamic methods use time- and space-dependent stress fields such as oscillations or elastic waves. Most modern experimental techniques to determine the elastic properties of minerals are based on the propagation of sound waves (Schreuer and Haussühl, 2005; Angel et al., 2009), and some of these techniques have been successfully combined with diamond anvil cells (Whitfield et al., 1976; Zaug et al., 1993; Spetzler et al., 1996; Mao et al., 2001; Fiquet et al., 2004).

Here, I performed X-ray diffraction and Brillouin spectroscopy experiments on samples contained in diamond anvil cells to determine their elastic properties as a function of pressure. X-ray diffraction is sensitive to changes in the size and shape of the crystallographic unit cell. From the evolution of the unit cell dimensions with pressure, volume and axial compressibilities can be derived in addition to the pressure-volume relation known as the equation of state. Brillouin spectroscopy of single crystals allows to determine the full elastic stiffness tensor and hence provides a complete description of elastic properties. When performed on the same sample, X-ray diffraction and Brillouin spectroscopy complement each other as densities derived from X-ray diffraction can be combined with sound wave velocities determined by Brillouin spectroscopy to directly constrain elastic properties at high pressures and high temperatures.

2.4.1 X-Ray Diffraction at High Pressures

X-ray diffraction has evolved to a routine technique in the study of materials at high pressures. A general introduction to X-ray diffraction can be found, for example, in Giacobozzo et al. (2011). High-pressure applications of X-ray diffraction were explained, for example, by Miletich et al. (2005), Angel et al. (2000), and by Boffa Ballaran et al. (2013). Here, I will focus on the experimental details relevant to the present study.

For the quantification of elastic properties, the essential information provided by X-ray diffraction is the size and shape of the unit cell. Unit cell or lattice parameters are derived from the geometry of the diffraction pattern. In an X-ray diffraction experiment, the geometry of the crystal lattice is converted into diffraction angles 2θ of diffracted X-ray beams

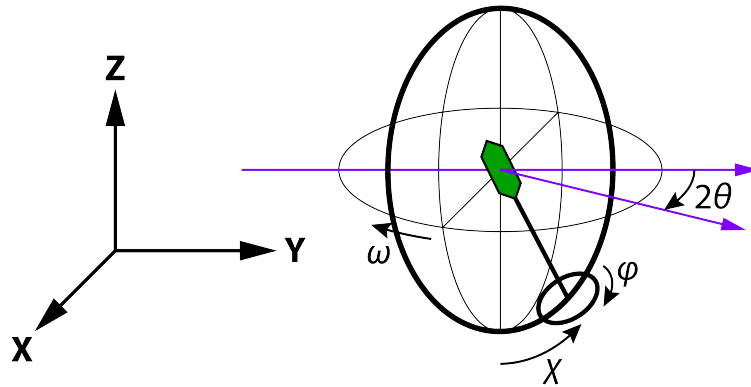


Figure 2.18: Rotation axes of a four-circle Eulerian cradle and the Cartesian diffractometer coordinate system as defined by Busing and Levy (1967).

hkl that are labeled according to the family of crystallographic planes (hkl) on which they were diffracted or reflected. The diffraction angle is related to the spacing d_{hkl} of the corresponding lattice planes by Bragg's law (Bragg, 1914):

$$n\lambda = 2d_{hkl} \sin \theta \quad (2.15)$$

where λ is the wavelength of the X-rays. The order of diffraction (or constructive interference) is conventionally set to $n = 1$ and the indices hkl multiplied by the respective integer. For monoclinic crystal symmetry, for example, the spacing of a given family of planes relates to the lattice parameters as (Massa, 2011):

$$\frac{1}{d_{hkl}^2} = \frac{h^2}{a^2 \sin^2 \beta} + \frac{k^2}{b^2} + \frac{l^2}{c^2 \sin^2 \beta} - \frac{2hl \cos \beta}{ac \sin^2 \beta} \quad (2.16)$$

with the unit cell edge lengths a , b , and c and the monoclinic angle β spanned by the \mathbf{a} and \mathbf{c} axes. By measuring the diffraction angles and hence the lattice spacings of a sufficiently large number of planes, equation (2.16) can be used to refine the lattice parameters by means of a least-squares method. The principles summarized above hold equally true for diffraction of X-rays by single crystals or powders.

2.4.1.1 Single-Crystal X-Ray Diffraction

Different diffractometer systems for single-crystal X-ray diffraction and their modes of operation have been discussed by Angel et al. (2000). Here, I will briefly summarize geometrical conventions and relations relevant for the determination of the crystal orientation as this is of particular interest for the analysis of sound wave velocities determined by Brillouin spectroscopy. Figure 2.18 illustrates the rotation axes of a four-circle Eulerian cradle.

A fixed Cartesian coordinate system is defined following the conventions of Busing and Levy (1967) with the \mathbf{Y} axis along the direct X-ray beam, the \mathbf{Z} axis vertical, and the \mathbf{X} axis completing the right-handed Cartesian coordinate system (Fig. 2.18; Busing and Levy, 1967; Angel et al., 2000). As explained in chapter 5, the crystal-physical coordinate system

(eqn. (5.1) on page 115) is attached to the crystallographic axes \mathbf{a} , \mathbf{b} , and \mathbf{c} of the crystal according to the convention (Haussühl, 2007):

$$\begin{aligned} \mathbf{e}_1 &= \mathbf{e}_2 \times \mathbf{e}_3 \\ \mathbf{e}_2 &= \frac{\mathbf{b}^*}{b^*} \\ \mathbf{e}_3 &= \frac{\mathbf{c}}{c} \end{aligned} \quad (2.17)$$

A vector \mathbf{h} in reciprocal space with components h , k , and l along the reciprocal axes \mathbf{a}^* , \mathbf{b}^* , and \mathbf{c}^* is transformed into the crystal-physical coordinate system by the matrix \mathbf{B} (Haussühl, 2007):

$$\mathbf{h}_e = \mathbf{B}\mathbf{h} \quad \text{with} \quad \mathbf{B} = \begin{pmatrix} c/(Vb^*) & 0 & -a \cos \beta / (Vb^*) \\ a^* \cos \gamma^* & b^* & c^* \cos \alpha^* \\ 0 & 0 & 1/c \end{pmatrix} \quad (2.18)$$

where a , b , c , α , β , γ , and V are the lattice constants and unit cell volume in direct space. Their counterparts in reciprocal space are marked with a star *. The orientation matrix \mathbf{U} transforms the vector \mathbf{h}_e from the crystal-physical system to the Cartesian system of the diffractometer with axes \mathbf{X} , \mathbf{Y} , and \mathbf{Z} as defined above:

$$\mathbf{h}_{XYZ} = \mathbf{U}\mathbf{h}_e \quad (2.19)$$

The orientation matrix \mathbf{U} can be computed from the angle settings of the four-circle Eulerian cradle for a minimum of two reflections with known plane normal vectors \mathbf{h} that have been brought into their reflection positions (Busing and Levy, 1967; Angel et al., 2000). The combined matrix \mathbf{UB} therefore converts the plane normal vector \mathbf{h} from the reciprocal axis system to the diffractometer system.

Once the matrix \mathbf{UB} has been refined from a sufficiently large number of reflections, the orientation of the crystal can be derived from the inverse matrix \mathbf{UB}^{-1} . For the determination of elastic constants by Brillouin spectroscopy, it can be an advantage to know the normal vector of the plane defined by the probed wave vectors. In the symmetric forward scattering geometry (see section 2.4.2.2), the plane of probed wave vectors coincides with the orientation of the plane-parallel surfaces of the crystal section. When the parallel surfaces of the crystal section are oriented perpendicular to the direct X-ray beam, i. e. the \mathbf{Y} axis, the normal vector \mathbf{h} of the crystal section in the reciprocal axis system can be directly read from the inverse matrix \mathbf{UB}^{-1} as the second column vector (Angel et al., 2000):

$$\mathbf{h} = \mathbf{UB}^{-1} \begin{pmatrix} 0 \\ 1 \\ 0 \end{pmatrix} \quad (2.20)$$

The unit normal vector \mathbf{n} in the crystal-physical system as used in chapter 5 is then obtained as:

$$\mathbf{n} = \frac{1}{|\mathbf{h}|} \mathbf{B}\mathbf{h} \quad (2.21)$$

Similarly, the angle χ_0 (see page 115) enclosed by the unit vectors \mathbf{g}_0 (eqn. (5.4)) and \mathbf{p} is calculated from the scalar product:

$$\chi_0 = \cos^{-1}(\mathbf{p} \cdot \mathbf{g}_0) \quad (2.22)$$

with $\mathbf{p} \parallel \mathbf{X}$ or $\mathbf{p} \parallel \mathbf{Z}$ for a horizontal or vertical Brillouin scattering plane, respectively. The plane-parallel surfaces of a crystal section inside a DAC are assumed to be parallel to the culets of the diamond anvils. Aligning the DAC with the compression axis parallel to the direct X-ray beam therefore ensures that $\mathbf{n} \parallel \mathbf{Y}$ for the unit normal vector \mathbf{n} of the crystal section.

After loading two wadsleyite single crystals with complementary orientations into the high-pressure chamber of the same DAC, the DAC was closed and mounted onto the Kappa four-circle goniometer of an XcaliburTM 2²¹ diffractometer. The DAC was aligned with the compression axis parallel to the direct X-ray beam, and the center of the high-pressure chamber was aligned with the center of rotation of the goniometer. Molybdenum $K\alpha$ radiation was generated in an X-ray tube at 40 or 50 kV and 30 or 40 mA, and diffracted X-rays were detected with a CCD area detector. The diffraction pattern was tiled from individual diffraction images that were collected with exposure times of 40 s at diffraction angles $2\theta \leq 60^\circ$ and taking into account the effective opening angle $\psi \leq 45^\circ$ of the DAC. Using the software package CrysAlis^{Pro} 2²¹, the two-dimensional diffraction pattern was indexed and unit cell parameters and orientation matrices extracted for both crystals.

For a precise determination of lattice parameters and crystal orientations, the DAC was transferred to the four-circle Eulerian cradle of a HUBER²² diffractometer and aligned to the center of rotation with the compression axis along the direct X-ray beam as explained above. In contrast to the instrument described earlier, the molybdenum $K\alpha$ radiation generated in an X-ray tube at 50 kV and 40 mA was detected by a scintillation point detector. Point detectors offer advantages over area detectors in terms of signal-to-noise ratio and accuracy of determined lattice parameters (Angel et al., 2000). Based on the lattice parameters and orientation matrices determined in the previous step, individual diffracted X-ray beams or reflections were centered following an 8-position centering procedure that allows correcting for small misalignments of the crystal and the diffractometer (King and Finger, 1979; Angel et al., 2000). Between 10 and 20 reflections were centered for each crystal. The diffractometer was operated with the software SINGLE (Angel and Finger, 2011).

The 8 final ω scans of each centered reflection were individually inspected and refit to Gaussian peak functions using the program WinIntegrStp (Angel, 2003). Some reflection profiles were rejected from the analysis because their low quality did not permit a reliable fit. Lattice parameters and crystal orientations were refined based on the refit reflection positions using the program SINGLE (Angel and Finger, 2011). Once lattice parameters and crystal orientations had been determined inside the DAC, they served as starting parameters for reflection centering after the next compression step without the need to repeat the collection and indexation of two-dimensional diffraction patterns. A similar diffractometer setup, i. e. a HUBER²² four-circle Eulerian cradle combined with a point detector, was used for experiments at combined high pressures and high temperatures. To reduce the scanning time of reflection profiles, however, intense X-rays were generated by a Rigaku²³ FR-E⁺ SuperBright X-ray source with a rotating molybdenum anode operated at 45 kV and 55 mA.

²¹Oxford Diffraction Ltd., Yarnton, Oxfordshire, UK, www.oxford-diffraction.com

²²HUBER Diffractionstechnik GmbH & Co. KG, Rimsting, Germany, www.xhuber.de

²³Rigaku Americas Holding Company Inc., The Woodlands, Texas, USA, www.rigaku.com

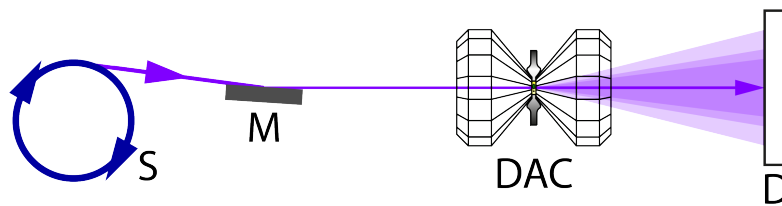


Figure 2.19: Schematic drawing of the experimental setup for a synchrotron powder diffraction experiment at high pressures. S: synchrotron radiation source, M: Si(111) monochromator crystal, DAC: diamond anvil cell, D: area detector.

2.4.1.2 Synchrotron Powder X-Ray Diffraction

The high intensities of X-rays generated by modern synchrotron sources facilitate diffraction experiments on small powder samples contained in DACs. Large area detectors can collect full Debye diffraction rings in exposure times of a few seconds. Synchrotron powder X-ray diffraction has therefore evolved to a standard technique to determine lattice constants as a function of pressure and temperature (Norby and Schwarz, 2008). A general introduction to powder diffraction techniques can be found, for instance, in Dinnebier and Billinge (2008). In axial diffraction geometry, X-rays are guided through one of the diamond anvils onto the powder sample inside the DAC, and those diffracted X-rays that exit the DAC through the opposing diamond anvil are detected. Here, I focus on diffraction experiments on sintered polycrystalline stishovite published in Buchen et al. (2018a) (Chapter 7). Figure 2.19 illustrates the setup for an axial X-ray diffraction experiment.

A circular platelet of sintered polycrystalline stishovite was loaded in the high-pressure chamber of a DAC together with a ruby sphere for pressure determination. Sample and ruby grain were surrounded by neon as pressure-transmitting medium. This setup intended to compress a sintered material in a quasi-hydrostatic way and to investigate how the resulting stresses between grains change the elastic properties of the material.

X-ray diffraction experiments were carried out at beamline ID15B of the European Synchrotron Radiation Facility (ESRF) in Grenoble, France. Radiation generated in a undulator was diffracted on an Si(111) monochromator to obtain X-rays with a wavelength of 0.410768 \AA that were focused down to a spot size of about $30 \times 30 \mu\text{m}^2$. Diffracted X-rays were detected with a mar555²⁴ flatpanel detector with an active area of $430 \times 350 \text{ mm}^2$. A silicon powder standard was used to calibrate the diffraction geometry including the sample-detector distance and detector tilt angles (Hinrichsen et al., 2008; Lutterotti et al., 2014) as well as the instrumental contribution to the profile function (Caglioti et al., 1958; Le Bail, 2008). For the sample inside the DAC, exposure times of 2 to 3 s were long enough to collect diffraction images with complete and continuous Debye rings. Pressures inside the DAC were derived from ruby fluorescence spectra collected with the online fluorescence spectrometer at beamline ID15B. More details about the beamline can be found in Merlini and Hanfland (2013). The FIT2D software (Hammersley, 2016) was used to integrate two-dimensional diffraction patterns to intensity- 2θ profiles. For visualization of diffraction patterns, we used the program DIOPTAS (Prescher and Prakapenka, 2015). Lattice parameters were extracted by whole powder pattern decomposition (Le Bail, 2008), also referred to as Le Bail method (Le Bail et al., 1988), using the program MAUD (Lutterotti et al., 2007;

²⁴marXperts GmbH, Norderstedt, Germany, www.marresearch.com

Lutterotti et al., 2014). Uncertainties on unit cell parameters derived from whole pattern fitting techniques may be underestimated when calculated from statistics only (Bérar and Lelann, 1991). To take into account systematic differences between observed and calculated reflection profiles, Bérar and Lelann (1991) proposed to rescale statistical uncertainties by assigning to each residual intensity the probability to be correlated with the residual intensities of the neighboring steps in the 2θ scan. The uncertainties on lattice parameters derived here from whole powder pattern decomposition were rescaled accordingly. Rescaling factors for uncertainties varied for individual diffraction patterns between 20 and 53.

2.4.2 Brillouin Spectroscopy at High Pressures

The spectroscopic analysis of light that has been inelastically scattered on thermally excited sound waves propagating in a medium allows to derive the propagation velocity of the sound waves and is referred to as Brillouin spectroscopy (Cummins and Schoen, 1972; Dil, 1982). Here, I focus on the principles of Brillouin scattering in crystals and describe experimental aspects relevant for the present study. Reviews on Brillouin scattering in fluids and solids have been presented by Cummins and Schoen (1972) and Dil (1982). A comprehensive introduction into the topic was also given by Speziale et al. (2014) who included a discussion of experimental methods for Brillouin spectroscopy at high pressures and related applications in Earth sciences.

2.4.2.1 Sound Waves and Brillouin Scattering in Crystals

In crystals, thermally excited sound waves correspond to acoustic phonons with wavelengths typically 100 to 1000 times longer than the dimensions of the unit cell. In the long-wavelength approximation, acoustic phonons can be treated as waves in an elastic continuum (Cummins and Schoen, 1972; Dil, 1982). In a non-piezoelectric crystal of density ρ , the propagation of elastic plane waves is described by the equation (Auld, 1973; Haussühl, 2007):

$$(c_{ijkl}g_jg_l - \rho v^2\delta_{ik})u_k = 0 \quad (2.23)$$

In the most general case, the solution of this equation yields three different sound wave velocities $\mathbf{v} = v\mathbf{g}$ with speeds v , propagation directions \mathbf{g} , and associated displacement vectors \mathbf{u} . The displacement vectors are mutually perpendicular and are used to distinguish the longitudinal wave with $\mathbf{u} \parallel \mathbf{g}$ from the two transverse waves with $\mathbf{u} \perp \mathbf{g}$. Pure longitudinal and pure transverse waves, however, propagate only along specific directions in a crystal, and the waves are instead classified into quasi-longitudinal and quasi-transverse waves according to the orientation relation between \mathbf{u} and \mathbf{g} . In analogy to seismic waves, quasi-longitudinal sound waves are often referred to as P waves and quasi-transverse waves as shear waves or S waves. I adopt this notation here with the convention that $v_{S1} \leq v_{S2} < v_P$. A solution of equation (2.23) in terms of velocities is presented in section 5.2.2.

Scattering of light by acoustic phonons arises from periodic perturbations in polarizability that result from the collective displacement of atoms from their mean positions. The space- and time-dependent polarizability of the crystal can be described by the dielectric constant (or permittivity) tensor $\epsilon_{ij}(\mathbf{r}, t)$ at location \mathbf{r} and time t (Dil, 1982):

$$\epsilon_{ij}(\mathbf{r}, t) = \epsilon_{ij} + \Delta\epsilon_{ij}(\mathbf{r}, t) \quad (2.24)$$

with the unperturbed and perturbed contributions ϵ_{ij} and $\Delta\epsilon_{ij}(\mathbf{r}, t)$, respectively. The perturbation $\Delta\epsilon_{ij}$ is related to the symmetric (strain) ϵ_{kl} and anti-symmetric (rotation) r_{kl}

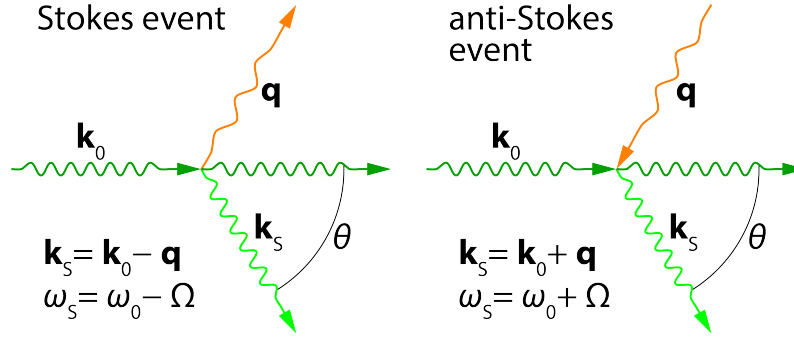


Figure 2.20: Illustration of inelastic photon-phonon scattering and the scattering geometry defined by the angle θ .

parts of the displacement gradient through the associated photoelastic tensors p_{mnl} and q_{mnl} (Nelson and Lax, 1971; Dil, 1982):

$$\Delta\epsilon_{ij} = -\epsilon_{im}\epsilon_{jn}(p_{mnl}\epsilon_{kl} + q_{mnl}r_{kl}) \quad (2.25)$$

The interaction of the perturbation $\Delta\epsilon_{ij}(\mathbf{q}, \Omega) = \Delta\epsilon_{ij} \exp 2\pi i[\mathbf{q} \cdot \mathbf{r} - \Omega t]$ generated by an elastic plane wave with wave vector \mathbf{q} and frequency Ω with an electromagnetic plane wave $\mathbf{E}(\mathbf{k}_0, \omega_0) = \mathbf{E}_0 \exp 2\pi i[\mathbf{k}_0 \cdot \mathbf{r} - \omega_0 t]$ with wave vector \mathbf{k}_0 and frequency ω_0 results in an excess polarization $\Delta\mathbf{P} = \Delta\epsilon(\mathbf{q}, \Omega)\mathbf{E}(\mathbf{k}_0, \omega_0)$ (Cummins and Schoen, 1972) with components:

$$\begin{aligned} \Delta P_i &= \Delta\epsilon_{ij}(\mathbf{q}, \Omega)E_j(\mathbf{k}_0, \omega_0) \\ &= \Delta\epsilon_{ij} \exp 2\pi i[\mathbf{q} \cdot \mathbf{r} - \Omega t]E_{j0} \exp 2\pi i[\mathbf{k}_0 \cdot \mathbf{r} - \omega_0 t] \\ &= \Delta\epsilon_{ij}E_{j0} \exp 2\pi i[(\mathbf{k}_0 \pm \mathbf{q}) \cdot \mathbf{r} - (\omega_0 \pm \Omega)t] \end{aligned} \quad (2.26)$$

The excess polarization $\Delta\mathbf{P}$ irradiates an electric field $\mathbf{E}_s(\mathbf{k}_s, \omega_s)$ of inelastically scattered radiation with wave vector $\mathbf{k}_s = \mathbf{k}_0 \pm \mathbf{q}$ and frequency $\omega_s = \omega_0 \pm \Omega$. The \pm sign in the last line of equation (2.26) can be understood from a quantum mechanical point of view that includes both the creation and annihilation of a phonon in the scattering process (Cummins and Schoen, 1972). The spectrum of the scattered light is therefore symmetric with respect to the incident light frequency. Energy loss, $\omega_s = \omega_0 - \Omega$, is referred to as Stokes event and energy gain, $\omega_s = \omega_0 + \Omega$, as anti-Stokes event.

Figure 2.20 illustrates the inelastic scattering process and geometry. Because of the small frequencies of acoustic phonons (see below), the wavelengths of the incident and scattered photons can be assumed to be approximately equal, i. e. $|\mathbf{k}_0| = 1/\lambda_0 \approx 1/\lambda_s = |\mathbf{k}_s|$. It follows from the scattering geometry that (Speziale et al., 2014):

$$|\mathbf{q}| = 2|\mathbf{k}_0| \sin(\theta/2) \quad (2.27)$$

The use of visible light as incident radiation therefore restricts the phonon wave vectors \mathbf{q} to values below $2|\mathbf{k}_0| = 37600 \text{ cm}^{-1}$ for $\lambda_0 = 532 \text{ nm}$ with corresponding phonon wavelengths on the order of 100 to 1000 nm. In comparison to wave vectors on the edge of the first Brillouin zone with $|\mathbf{q}| \approx 10^7 \text{ cm}^{-1}$ for a crystal with unit cell dimensions on the order of 10 \AA , phonon wave vectors probed by Brillouin spectroscopy stay close to the Brillouin zone center. The relation between wave vector and frequency of acoustic phonons is illustrated by the schematic dispersion curves shown in Figure 2.21. As most other experimental techniques used to measure sound wave velocities in crystals, Brillouin spectroscopy samples the

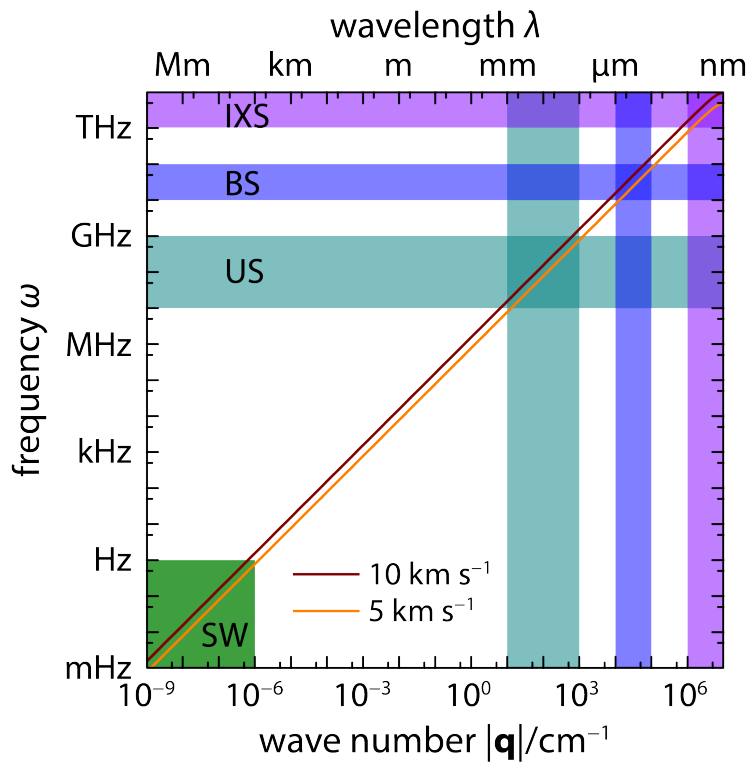


Figure 2.21: Schematic (sinusoidal) dispersion curves for acoustic waves traveling at 5 and 10 km s⁻¹ in a crystal with a 10 Å translation period. Color shadings indicate frequencies, wave vectors, and wavelengths of acoustic waves probed with different experimental techniques and those relevant for seismic waves (SW). IXS: inelastic X-ray scattering techniques, BS: Brillouin spectroscopy, US: ultrasonic techniques.

dispersion curves of acoustic phonons in the linear regime where the sound wave velocity is given by $v = \Omega/|\mathbf{q}|$. Brillouin spectroscopy bears the advantage to probe sound waves with wavelengths short enough not to be affected by grain boundaries for crystals larger than about 50 μm. At frequencies below 1 GHz as typically employed in ultrasonic techniques (Angel et al., 2009), the wavelength of sound waves increases to several micrometers and might be more sensitive to grain boundary effects, in particular in the case of polycrystalline samples with small grain sizes (Marquardt et al., 2011). The frequencies of seismic waves, however, are on the order of 1 mHz to 1 Hz with corresponding wavelengths of several kilometers (Stein and Wysession, 2003). Measurements at higher frequencies therefore neglect contributions that may arise from processes operating at seismic frequencies such as attenuation and dispersion of seismic waves by anelastic relaxation (Jackson, 2007; Karato, 2008).

2.4.2.2 Determination of Sound Wave Velocities at High Pressures

In an elastically anisotropic medium, the sound wave velocity \mathbf{v} is defined by the unit propagation vector \mathbf{g} of the sound wave and the magnitude, i. e. the speed $|\mathbf{v}| = v = \Omega/|\mathbf{q}|$ with the oscillation frequency Ω and the wave vector $\mathbf{q} \parallel \mathbf{g}$. Direction and magnitude of the wave vector are defined by the scattering geometry according to equation (2.27) (see also Figs.

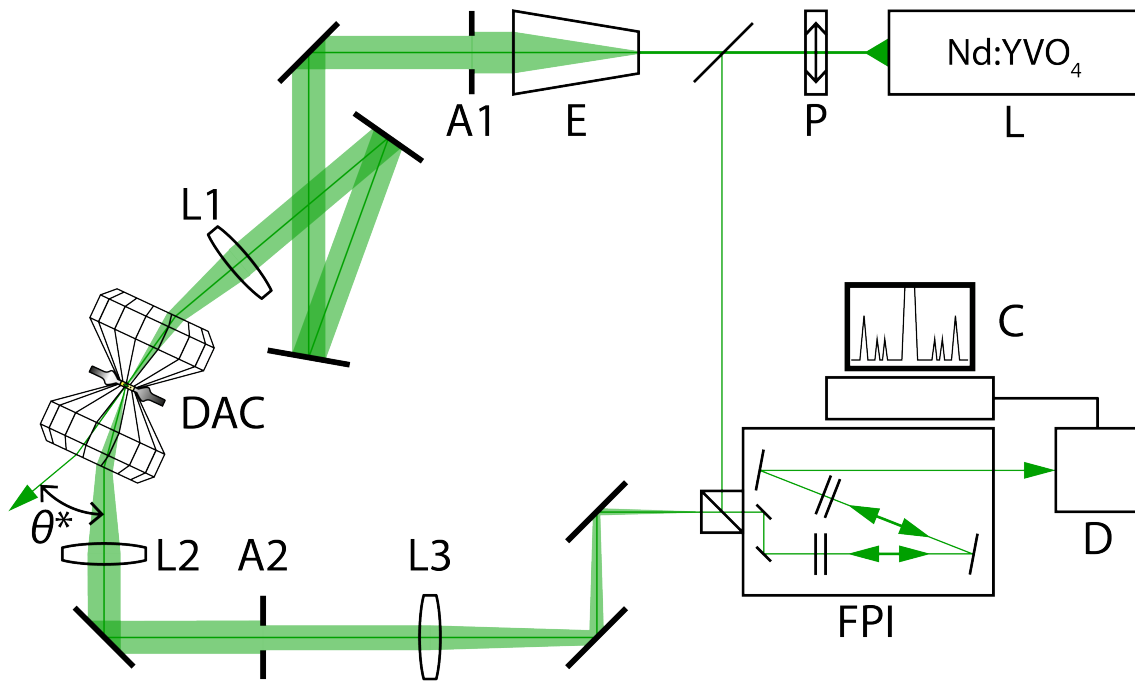


Figure 2.22: Schematic drawing of the experimental setup for Brillouin spectroscopy at high pressures. L: laser (Nd:YVO₄), P: polarizer, E: beam expander, A1: aperture, L1: focusing lens, DAC: diamond anvil cell, external scattering angle θ^* , L2: collecting lens, A2: collecting aperture, L3: lens, FPI: Fabry-Perot interferometer, D: detector, C: interferometer controls.

2.20 and 2.22). The oscillation frequency can be obtained from the spectroscopic analysis of the scattered light as $\Omega = \omega_s - \omega_0$. For the sound wave velocity, we then have:

$$\mathbf{v} = \mathbf{g}v = \mathbf{g} \frac{\Omega}{|\mathbf{q}|} = \mathbf{g} \frac{\Omega \lambda_0}{2 \sin(\theta/2)} \quad (2.28)$$

with the wavelength λ_0 of the incident light and the scattering angle θ .

The wavelengths and wave vectors of the incident and scattered photons are modified by the refractive index of the medium. In addition, refraction of incident and scattered light beams at the surfaces of the sample may distort the scattering angle away from its value inside the crystal. When the light enters and leaves the sample through opposing plane-parallel surfaces, the scattering geometry can be adjusted to bring the surface normal vector \mathbf{n} into the plane spanned by the incident and scattered light beams so as to bisect the scattering angle θ . In this forward symmetric scattering geometry, the effects of refraction cancel out (Speziale et al., 2014). This holds true even when the crystal section resides in a DAC as long as tables and culets of both diamond anvils are aligned to be exactly parallel to each other and to the plane-parallel sample surfaces (Whitfield et al., 1976). In this case, the scattering angle θ in equation (2.28) can be replaced by the external scattering angle θ^* (Fig. 2.22). Systematic errors that may result from non-parallel surfaces of the sample and diamond anvils have been analyzed by Zha et al. (1996) and by Sinogeikin and Bass (2000) and were estimated to remain below 1% of the derived sound wave velocities for reasonable ranges of surface inclination angles.

Figure 2.22 shows a schematic drawing of the experimental setup used in the present study to measure sound wave velocities at high pressures. The Brillouin spectroscopy setup

is installed at PETRA III/DESY in Hamburg/Germany and resembles the one presented by Speziale and Duffy (2002). The DAC was mounted onto a Eulerian cradle and aligned to the center of rotation. The reflections of the laser beam on the tables of both diamond anvils were used to align the DAC according to the forward symmetric scattering geometry as explained above. The sample was aligned with the laser beam and the collecting optics by moving the Eulerian cradle on a motorized stage. Different propagation directions \mathbf{g} of sound waves in the crystal were selected by rotating the DAC around the compression axis, i. e. by changing the angle χ of the goniometer (Fig. 2.18). Coherent monochromatic light with a wavelength of $\lambda_0 = 532$ nm was generated in a Verdi²⁵ 2 W laser by doubling the frequency of the radiation emitted from a diode-pumped neodymium-doped YVO₄ crystal. A polarizer was used to control the polarization of the laser light. The laser beam was expanded from an initial diameter of about 3 mm to about 15 mm by sending it through a beam expander followed by a circular aperture. A lens with 200 mm focal length focused the light onto the sample inside the DAC. The laser output power was adjusted to keep the effective power of the light incident onto the DAC around 190 mW and around 90 mW for measurements without pressure-transmitting medium. Scattered light was collected by a lens with 200 mm focal length and sent through a circular aperture with a diameter of 12 mm to select the central part of the light cone captured by the collecting lens. The effective external scattering angle θ^* was calibrated for each scattering geometry as defined by the opening of circular apertures. I used sound wave velocities collected at ambient conditions on an oriented MgO single crystal to refine the external scattering angle θ^* based on the measured density ($3.5819(1)$ g cm⁻³) of the MgO crystal and the elastic stiffness tensor of MgO reported by Spetzler (1970). The external scattering angle was close to 50° but varied by about 1° between different measurement sessions.

The selected part of the scattered light was focused onto the entrance pinhole ($\varnothing = 200$ μm) of a multi-pass TFP-1²⁶ tandem Fabry-Perot interferometer (Lindsay et al., 1981). Details on the working principle and operation of a tandem Fabry-Perot interferometer can be found in Lindsay et al. (1981) and Speziale et al. (2014). The interferometer operated with a spacing of 8.000(5) mm between the first pair of mirrors at a nominal scanning amplitude of 600 nm. Photons transmitted through the interferometer were detected with a photomultiplier tube or a COUNT[®]-10B²⁷ avalanche photodiode. The recorded signal was sent through a multi-channel analyzer that was synchronized with the scanning motion of the mirror pairs. For wadsleyite single crystals inside the DAC, typical collection times for individual spectra varied between 1 and 8 h depending on crystal orientation and laser polarization. The use of the avalanche photodiode reduced collection times to about half of those required with the photomultiplier tube with the disadvantage of a stronger background.

The actual scanning amplitude and frequency scale were calibrated for each spectrum based on the separation of the inner pair of ghost peaks. The inner pair of ghost peaks arises from interferences of orders $h \pm 1$ of the (unchanged) laser light between the first pair of mirrors when the h th order of interference is located at the center of the spectrum with frequency shift $\Delta\omega = 0$. The separation between the inner ghost peaks (in channel numbers) corresponds to twice the free spectral range $2\Delta_{\text{FSR}}\omega$ (in wave numbers) with the free spectral range defined by the mirror spacing d as $\Delta_{\text{FSR}}\omega = 1/(2nd)$ and the refractive index of air assumed to be $n = 1$ (Kuzmany, 2009; Speziale et al., 2014). The center of the spectrum at which $\Delta\omega = 0$ was determined by calculating the mean position of pairs of well

²⁵Coherent Inc., Santa Clara, California, USA, www.coherent.com

²⁶The Table Stable Ltd., Mettmenstetten, Switzerland, www.tablestable.com

²⁷LASER COMPONENTS GmbH, Olching, Germany, www.lasercomponents.com

Table 2.4: Components and technical parameters for Brillouin spectroscopy setups

Setup at	PETRA III/DESY ^a	BGI ^b
Incident beam optics		
Light source	Verdi ^c 2 W laser	Verdi ^c 2 W laser
Wavelength (nm)	532	532
Polarizer	polymer film	polymer film
Beam expander	Keplerian 10×	none
Beam diameter (mm)	15	3
Focal length (mm)	200	100
Collecting optics		
Scattering angle (°)	50	80
Focal length (mm)	200	100
Beam diameter (mm)	12	7
Interferometer		
Type (model)	multi-pass tandem Fabry-Perot (TFP-1 ^d)	multi-pass tandem Fabry-Perot (TFP-1 ^d)
Mirror spacing (mm)	8.000(5)	4.000(5)
Free spectral range (cm ⁻¹)	0.6250(4)	1.250(2)
Scanning amplitude (nm)	600	600
Detector	photomultiplier tube, avalanche photodiode	photomultiplier tube, avalanche photodiode

^aPETRA III, Deutsches Elektronen-Synchrotron, Hamburg, Germany.

^bBayerisches Geoinstitut, Universität Bayreuth, Bayreuth, Germany.

^cCoherent Inc., Santa Clara, California, USA.

^dThe Table Stable Ltd., Mettmenstetten, Switzerland.

resolved peaks. This internal calibration approach revealed that the true scanning amplitude was around 593 nm, i. e. substantially smaller than the scanning amplitude suggested by the instrument controls. Using the nominal scanning amplitude of 600 nm to convert channel numbers to frequency shifts would result in an overestimation of sound wave velocities by more than 1 %.

Sound wave velocity measurements at combined high pressures and high temperatures were performed on a similar Brillouin spectroscopy setup installed at the Bayerisches Geoinstitut. Table 2.4 compares both setups and their technical parameters. The setup at Bayerisches Geoinstitut is combined with an intense X-ray source to facilitate X-ray diffraction experiments on the sample at the same combination of pressure and temperature at which Brillouin spectra were collected (see also section 2.4.1.1). Instead of using the reflections of the laser beam, the DAC was aligned with the compression axis along the direct X-ray beam using a water bubble. After taking into account calibrations of effective external scattering angles and scanning amplitudes, both setups gave identical sound wave velocities within uncertainties.

To extract peak positions from a recorded Brillouin spectrum, a manually adjusted baseline was subtracted from the raw spectrum that was subsequently divided into regions. The channel interval of each region was chosen to contain a single peak or, if close to each other, several peaks and was linked to its symmetric counterpart on the opposite site of the strong central peak due to elastic scattering. The intensities of peaks in symmetric pairs of regions

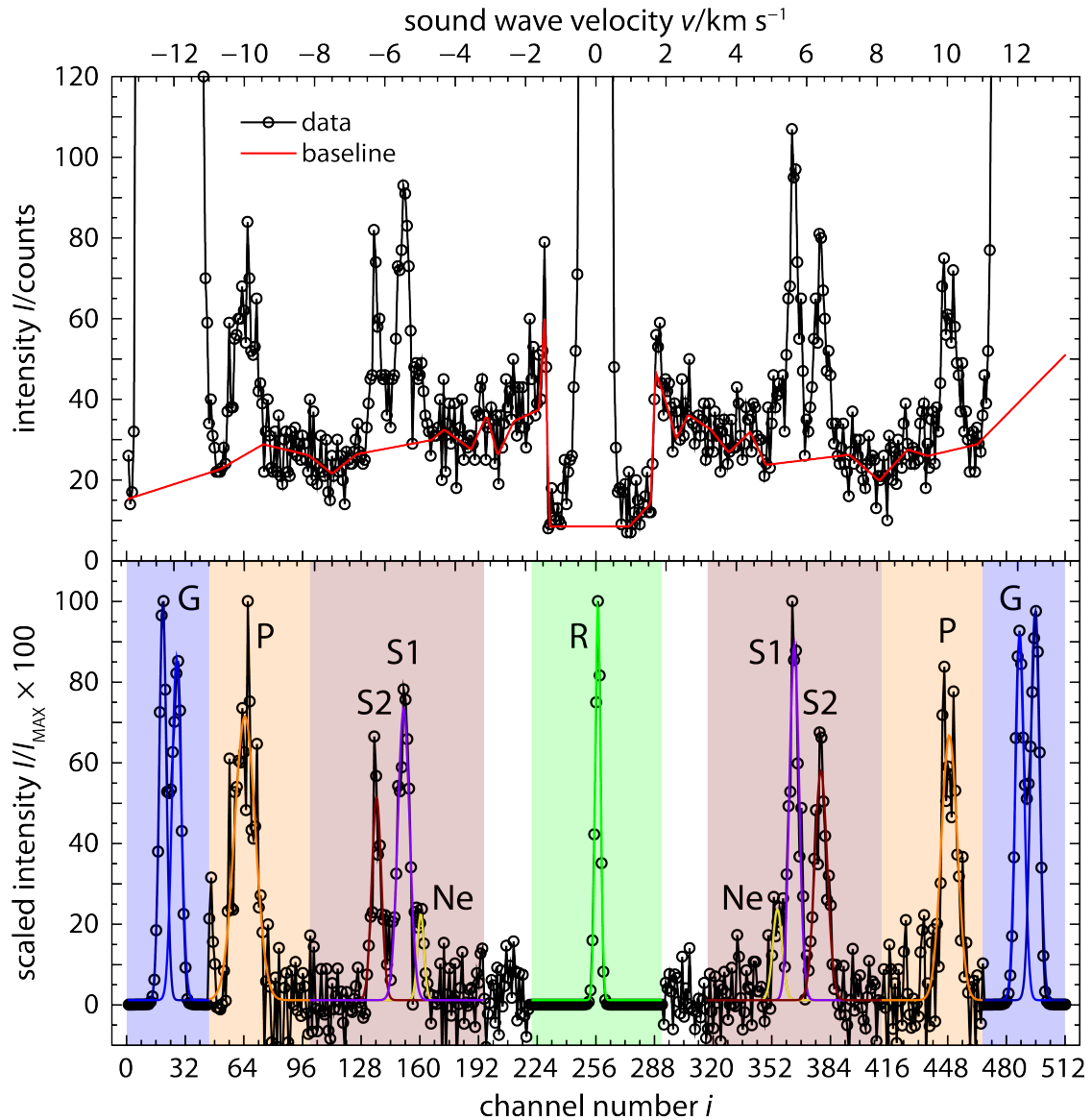


Figure 2.23: Analysis of Brillouin spectra. Upper panel shows raw spectrum with baseline. Lower panel shows rescaled intensities and peak fitting results. Color shading indicates associated scaling regions. Scattered intensity arises from inelastic scattering on quasi-longitudinal (P) and quasi-transverse (S1 and S2) acoustic waves in the sample and the pressure-transmitting medium (Ne). R: elastic (Rayleigh) scattering, G: ghost peaks (interferometric repetitions of the central elastic line).

were scaled by assigning a relative intensity of 100% to the highest peak within each pair of regions. When defining the channel intervals of scaling regions, it is important to include sufficient channels on either side of the peaks to not distort their original signal-to-noise ratio. All peaks in the scaled spectrum could then simultaneously be fit to Gaussian peak functions to obtain their central positions in channel numbers. The analysis of a Brillouin spectrum is illustrated in Figure 2.23. Based on the calibration explained above, channel numbers were converted to frequency shifts or, via equation (2.28), to sound wave velocities. In estimating the errors on sound wave velocities, I propagated uncertainties on the

external scattering angle, the channel number-to-frequency shift conversion, fitted peak positions, and differences in frequency shifts between Stokes and anti-Stokes components. Estimated relative errors $\Delta v/v$ on sound wave velocities ranged between 0.1 and 4.9% mainly depending on the signal-to-noise ratio of individual peaks. The mean value of $\Delta v/v$ around 0.7(5)% reflects the expected precision ($\sim 0.5\%$) and accuracy ($\sim 1\%$) of sound wave velocities determined by Brillouin spectroscopy (Speziale and Duffy, 2002; Speziale et al., 2014).

Chapter 3

Results and Discussion

This chapter aims at highlighting how the findings presented in the following chapters link to key questions defined in chapter 1. Chapters 4, 6, and 7 have been published as Buchen et al. (2017), Buchen et al. (2018b), and Buchen et al. (2018a), respectively, and present experimental results on the high-pressure elastic properties of wadsleyite and stishovite together with implications for the seismic detection of water and silica-rich rocks in Earth's mantle. Chapter 5 has been prepared for publication and describes and compares different approaches to derive a self-consistent description of anisotropic elastic properties at high pressures from sound wave velocity measurements. In section 3.4, I present the results of Brillouin spectroscopy and X-ray diffraction experiments on wadsleyite single crystals at combined high pressures and high temperatures that include the first elastic stiffness tensors of wadsleyite at simultaneously high pressures and high temperatures.

3.1 The Equation of State of Wadsleyite

In chapter 4, we derive the volume and axial equations of state for wadsleyite with a composition relevant for the transition zone. The chemical composition was characterized in terms of the $\text{Fe}/(\text{Mg}+\text{Fe})$ ratio, the hydrogen content, and the $\text{Fe}^{3+}/\Sigma\text{Fe}$ ratio. We measured the changes in unit cell volume and unit cell edge lengths as a function of pressure on two wadsleyite single crystals using X-ray diffraction and, among other parameters, extracted the bulk modulus from the compression curves. The two wadsleyite crystals were compressed together inside the same DAC but had different orientations with respect to the compression axis. Despite the anisotropic compression behavior of wadsleyite, both crystals followed identical compression curves indicating quasi-hydrostatic stress conditions during compression.

Wadsleyite compositions span solid solutions between the end members Mg_2SiO_4 , Fe_2SiO_4 , MgH_2SiO_4 , and Fe_3O_4 . However, only the magnesian end member Mg_2SiO_4 crystallizes in the wadsleyite crystal structure as a pure compound while all other end members are hypothetical in the sense that they do not adopt the wadsleyite crystal structure or are not stable as pure compounds. Defined in this way, wadsleyite solid solutions include the spinelloid III solid solution $(\text{Mg},\text{Fe}^{2+},\text{Fe}^{3+})_2(\text{Si},\text{Fe}^{3+})\text{O}_4$ (Woodland and Angel, 1998; Woodland and Angel, 2000; Koch et al., 2004) even though this solid solution is stable only at pressures below 9 GPa (Koch et al., 2004; Woodland et al., 2012). We show in chapter 4 that ferric iron has a resolvable effect on the compressibility when dissolved into the wadsleyite crystal structure and that this effect differs from the effect of ferrous iron.

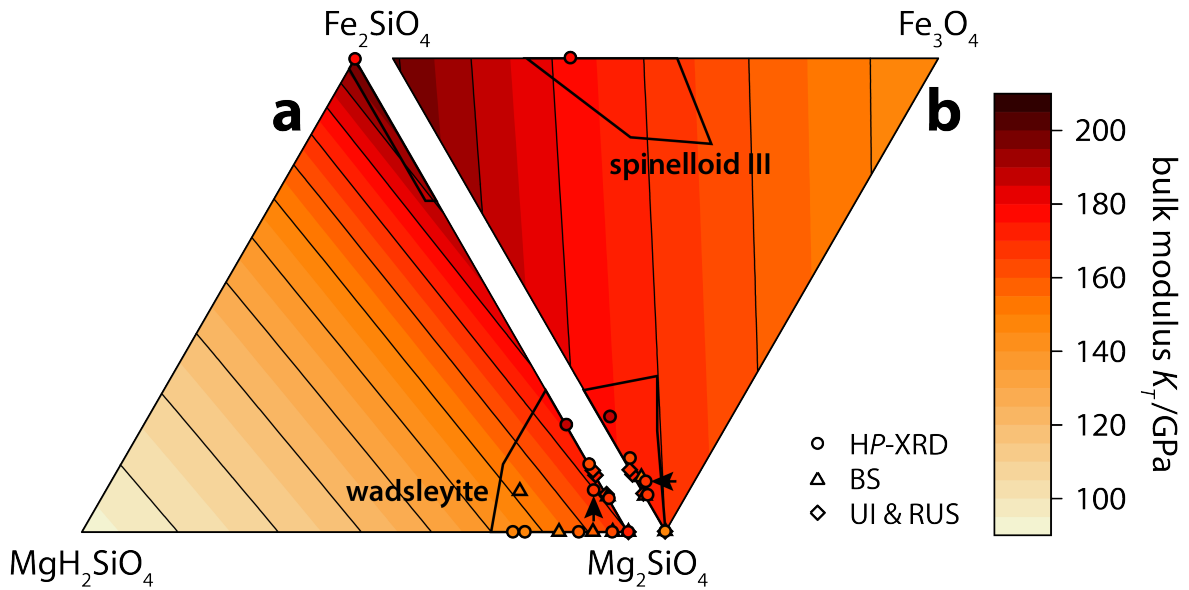


Figure 3.1: Isothermal bulk modulus of wadsleyite solid solutions. Chemical compositions are projected into ternary diagrams spanned by the end members Mg_2SiO_4 - Fe_2SiO_4 - MgH_2SiO_4 (a) and Mg_2SiO_4 - Fe_2SiO_4 - Fe_3O_4 (b). The color map was generated based on the four-end-member model reported in Buchen et al. (2017) (Table 4.3). The compositional ranges of wadsleyite and spinelloid III solid solutions are marked. Black arrows indicate the here-studied wadsleyite composition. See Table A.7 for references. HP-XRD: high-pressure X-ray diffraction, BS: Brillouin spectroscopy, UI: ultrasonic interferometry, RUS: resonant ultrasound spectroscopy.

In Table A.6 (page 188), we compiled available literature data on the unit cell parameters for different wadsleyite compositions at ambient conditions. We inverted this data set for the unit cell volumes of the four end members assuming an ideal mixing behavior to describe the variation of unit cell volume with chemical composition. Table A.7 (page 190) lists equation of state parameters based on a reanalysis of available compression data for different wadsleyite compositions together with bulk and linear moduli determined by ultrasonic measurements and Brillouin spectroscopy. This comprehensive data set on the compression behavior of wadsleyite solid solutions was analyzed assuming Reuss and Voigt averaging schemes (Hill, 1963; Watt et al., 1976) to extract bulk and linear moduli for each end member. In combination with the variation of the unit cell volume, the resulting model allows constructing an EOS for members of wadsleyite solid solutions within the analyzed composition space. Figure 3.1 shows the variation of the bulk modulus at ambient conditions within the system Mg_2SiO_4 - Fe_2SiO_4 - MgH_2SiO_4 - Fe_3O_4 .

Via the Helmholtz and Gibbs free energies (eqns. (2.3) and (2.5)), the multi-end-member EOS for wadsleyite solid solutions can be integrated into phase equilibria computations. Our multi-end-member model bears the advantage that it includes the effect of hydrogen and ferric iron on the EOS. Both hydrogen and ferric iron were shown to stabilize wadsleyite to lower pressures and to expand the two-phase region defined by coexisting olivine and wadsleyite (Chen et al., 2002; Smyth and Frost, 2002; Frost and Dolejš, 2007; Frost and McCammon, 2009). In Earth's mantle, this translates to a shift of the 410-km discontinuity to shallower depths while, at the same time, reducing the sharpness of the discontinuity (Wood, 1995; Smyth and Frost, 2002; Litasov et al., 2006; Hirschmann et al., 2006; Frost and Dolejš, 2007; Frost and McCammon, 2009). Depth and sharpness of the 410-km

discontinuity can be derived from seismic observations (Benz and Vidale, 1993; Helffrich and Wood, 1996; Melbourne and Helmberger, 1998; Chambers et al., 2005b; Schmerr and Garnero, 2007; Saki et al., 2015; Houser, 2016) with the potential to detect lateral variations of the hydration and oxidation state of the deep upper mantle.

3.2 From Sound Wave Velocities to Single-Crystal Elasticity

A rock in Earth's mantle can be thought of as an aggregate of individual crystals tightly packed together. Each crystal has anisotropic elastic properties that change systematically with pressure and temperature. One approach to constrain the elastic properties of the rock consists in combining the elastic properties of individual crystals in a way that reflects the mineralogical composition and fabric of the rock. In a deformed rock, for example, crystals might be aligned to form a crystallographic preferred orientation. The anisotropy of the crystals is then at least partly transferred to the rock. Knowledge of the elastic properties, or more precisely, the elastic stiffness tensors of minerals therefore allows to assemble hypothetical rocks and to derive their elastic properties. Once descriptions for the elastic stiffness tensors of sufficient minerals are available as a function of pressure and temperature, this single-crystal based approach to rock elasticity becomes very flexible in combining petrological and textural constraints to explain geophysical observations such as seismic anisotropy in Earth's mantle. In chapter 5, we explain in detail how to derive a self-consistent description of the elastic stiffness tensor as a function of pressure and temperature from sound wave velocity measurements on single crystals. Here, self-consistency refers on one hand to the use of the thermodynamically self-consistent finite-strain approach to single-crystal elasticity developed by Stixrude and Lithgow-Bertelloni (2005) and on the other hand to the self-consistent calculation of pressure and aggregate elastic moduli.

In the calculation of sound wave velocities, poly-mineralic rocks are often assumed to be isotropic aggregates of the constituent minerals. Similarly, sound wave velocities of different minerals or minerals with different chemical compositions are best compared based on the sound wave velocities of isotropic aggregates. The elastic properties of polycrystalline aggregates, however, are complex and best captured by defining bounds on the bulk and shear moduli of the aggregate (Watt et al., 1976). The Voigt and Reuss averages of components of the elastic stiffness and compliance tensors, respectively (Voigt, 1928; Reuss, 1929), give the most extreme bounds on the bulk and shear moduli of isotropic aggregates (Hill, 1952; Watt et al., 1976). For materials of moderate elastic anisotropy and for many minerals in particular, the separation of the Voigt and Reuss bounds is on the order of the uncertainties on experimentally determined moduli providing a realistic and readily accessible bounding scheme (Chung and Buessem, 1967; Thomsen, 1972; Angel et al., 2009). In deriving bounds on aggregate moduli and their pressure derivatives, we ensured that the relations between components of the elastic stiffness and compliance tensors and the respective bounds remain valid when computing elastic properties at high pressures based on derived finite-strain parameters. Similarly, the coefficients of equation (2.7) can be derived from the results to calculate pressure in a self-consistent way and with the possibility to allow for assumptions on the stress conditions during compression.

As a novelty, we present and test an inversion procedure that simultaneously inverts sound wave velocities measured at different pressures (and temperatures) directly to single-crystal finite-strain parameters, i. e. the components of the elastic stiffness tensor and their pressure derivatives at ambient conditions, without need to derive elastic stiffness tensors

at individual pressure-temperature combinations. As long as each sound wave velocity is linked to a propagation direction \mathbf{g} in the crystal and to the conditions of the measurement as defined by pressure P or finite strain (or volume V) and temperature T , sound wave velocities spread out in P - T - \mathbf{g} (V - T - \mathbf{g}) space can be jointly inverted. In reverse, the presented formalism can be used to design the experimental strategy in order to optimize the number, directions, and conditions of sound wave velocities required to constrain a given set of parameters. This global inversion procedure is perfectly compatible with the multi-sample approach (Schulze et al., 2017) and was successfully applied to invert sound wave velocities determined at high pressures on (Al,Fe)-bearing bridgmanite (Kurnosov et al., 2017) and wadsleyite (Buchen et al., 2018b; see also chapter 6).

3.3 High-Pressure Single-Crystal Elasticity of Wadsleyite

The elastic stiffness tensor can be derived from sound wave velocities that were measured on a single crystal at a given pressure-temperature combination and cover sufficient propagation directions. As explained in section 5.2.2, sound wave velocities are conventionally inverted to elastic stiffness tensors using equation (5.10) in a least-squares procedure. In addition, we used the global inversion procedure explained in the previous section to derive the components of the elastic stiffness tensor of iron-bearing wadsleyite together with their pressure derivatives at ambient conditions (Table 6.1 on page 139). From the components of the elastic stiffness and compliance tensors, bounds on the bulk and shear moduli for an isotropic aggregate can be computed as described in section 5.3.4.

Elastic stiffness tensors and Voigt-Reuss-Hill averages (Hill, 1952; Watt et al., 1976) of the bounds on bulk and shear moduli for isotropic aggregates of different wadsleyite compositions are compiled in Table 3.1 and arranged according to the number of H_2O molecules per formula unit in Figure 3.2. I included data from previous Brillouin spectroscopy studies on different wadsleyite compositions as well as our own results on slightly hydrous iron-bearing wadsleyite (Buchen et al., 2018b) and unpublished results on hydrous iron-bearing wadsleyite with 0.7(1) wt-% H_2O (see Table 2.3 on page 29). Figure 3.2 clearly shows that the incorporation of hydrogen into iron-free and iron-bearing wadsleyite reduces both bulk and shear moduli at ambient conditions. The elastic moduli of iron-free wadsleyite appear to decrease linearly with the number of H_2O molecules per formula unit (Mao et al., 2008b). For iron-bearing wadsleyite, the reduction of elastic moduli upon hydrogen incorporation is less well defined but still evident. Some spread in the data may result from the use of different methods to quantify hydrogen contents (Chang et al., 2015; Buchen et al., 2017; see also section A.1.1) and from differences in the way hydroxyl groups enter the crystal structure of wadsleyite (Inoue et al., 1995; Jacobsen et al., 2005; Bolfan-Casanova et al., 2012; Kawazoe et al., 2016).

The reduction of elastic moduli with increasing hydrogen content at ambient conditions as observed for iron-free wadsleyite (Mao et al., 2008b) has led to the conclusion that sound wave velocities of hydrous wadsleyite might remain lower than those of anhydrous wadsleyite at conditions of the transition zone (Smyth and Jacobsen, 2006; Holl et al., 2008; Mao et al., 2008b). Sound wave velocity measurements on wadsleyite single crystals and polycrystalline wadsleyite at high pressures seemingly supported this conclusion (Mao et al., 2008a; Liu et al., 2009; Mao et al., 2011) though experimental pressures did not reach those of the transition zone. Moreover, supposedly anhydrous iron-bearing wadsleyite samples were not fully characterized in terms of hydrogen and ferric iron contents (Li and Lieber-

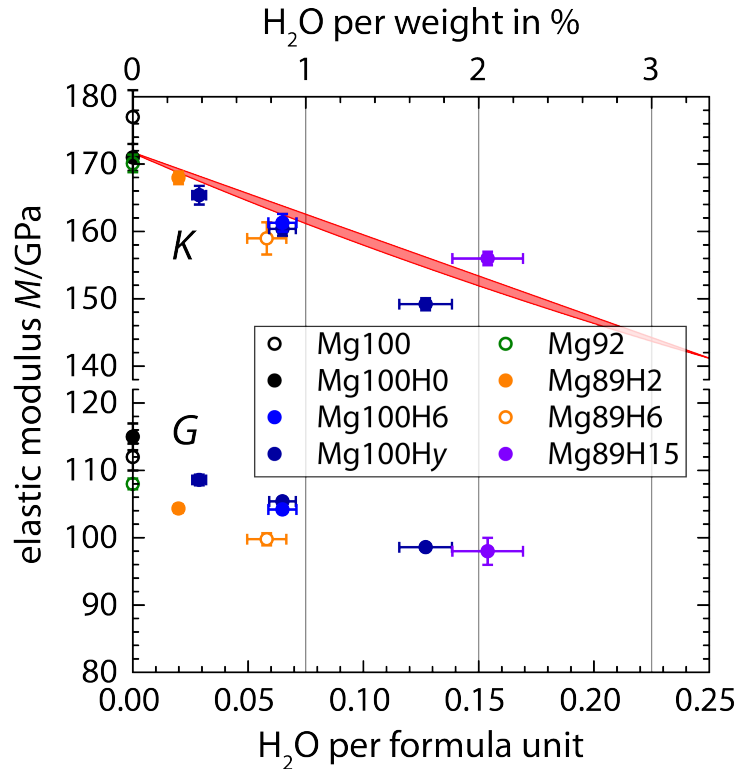


Figure 3.2: Bulk (K) and shear (G) moduli of wadsleyite determined by Brillouin spectroscopy on single crystals as a function of H_2O molecular equivalents per formula unit. Open symbols indicate compositions with unknown hydrogen, iron, or ferric iron contents. Red lines and shading show the variation of the bulk modulus calculated from the three-end-member model reported in Buchen et al. (2017) (Table 4.3). Mg100: Sawamoto et al. (1984), Mg100H0: Zha et al. (1997), Mg100H6: Mao et al. (2008a), Mg100Hy: Mao et al. (2008b), Mg92: Sinogeikin et al. (1998) and Wang et al. (2014), Mg89H2: Buchen et al. (2018b), Mg89H6: this study (unpublished), Mg89H15: Mao et al. (2011).

mann, 2000; Liu et al., 2009; Wang et al., 2014) impeding a reliable quantification of the effect of structurally bonded hydrogen on the elastic properties of iron-bearing wadsleyite. The sound wave velocities of ringwoodite have also been found to decrease with increasing hydrogen content (Jacobsen et al., 2004; Mao et al., 2012; Schulze et al., 2018). As a consequence, slow seismic velocities observed in the transition zone have been related to the presence of water dissolved in wadsleyite and ringwoodite with partly contradicting results (Smyth and Jacobsen, 2006; Suetsugu et al., 2006; Meier et al., 2009; Houser, 2016; Thio et al., 2016).

Based on a comparison of our results on the high-pressure elasticity of iron-bearing wadsleyite with literature data on strongly hydrous iron-bearing wadsleyite (Mao et al., 2011), we argue in chapter 6 that hydration of iron-bearing wadsleyite raises the pressure derivatives of bulk and shear moduli. We show that, as a consequence, P and S wave velocities of hydrous iron-bearing wadsleyite overtake those of anhydrous wadsleyite at pressures relevant for the transition zone. The idea that structural incorporation of hydroxyl groups raises the pressure derivatives of elastic moduli of nominally anhydrous minerals, including wadsleyite and ringwoodite, has been discussed earlier (Jacobsen, 2006; Smyth and Jacobsen, 2006; Holl et al., 2008; Chang et al., 2015), and the effect might be related to changes in

Table 3.1: Elastic properties for different wadsleyite compositions at ambient conditions

Fe/(Mg+Fe) x	H ₂ O (mpu) ^a		Fe ³⁺ /ΣFe z	Density (g cm ⁻³)	Components of the adiabatic elastic stiffness tensor and aggregate elastic moduli ^b (GPa)												Reference ^c
	y	z			C ₁₁	C ₂₂	C ₃₃	C ₄₄	C ₅₅	C ₆₆	C ₁₂	C ₁₃	C ₂₃	K _S	G		
0	0	0	0	3.474	360(6)	383(4)	273(5)	112(2)	118(4)	98(4)	75(9)	110(6)	105(9)	177(4)	112(2)	Mg100	
0	0	0	0	3.488(1)	370.5(78)	367.7(65)	272.4(58)	111.2(36)	122.5(40)	103.1(39)	65.6(45)	95.2(52)	105.1(44)	171(2)	115(2)	Mg100H0	
0	0.0649(61)	0	0	3.435(4)	341(2)	343(2)	256(3)	101.9(12)	105.6(11)	93(1)	68(2)	96(1)	95(1)	161.3(13)	104.2(5)	Mg100H6	
0	0.0288(30)	0	0	3.453(2)	356.9(29)	358.4(29)	255.6(17)	106.5(8)	112.4(8)	96.3(32)	68.7(43)	97.4(25)	97.7(20)	165.4(14)	108.6(8)	Mg100H4	
0	0.0649(58)	0	0	3.435(7)	337.5(24)	345.8(20)	251.5(17)	103.5(8)	110.5(8)	93.8(12)	70.9(23)	96.5(19)	91.2(23)	160.4(10)	105.4(4)	Mg100H4	
0	0.1270(114)	0	0	3.395(10)	321.9(24)	321(2)	232(18)	96.4(7)	101.4(8)	89.3(9)	62.7(24)	90.8(18)	84.8(20)	149.2(9)	98.6(4)	Mg100H4	
0.075(10)				3.57(3)	348(3)	372(3)	254(3)	106(2)	115(2)	97(2)	78(3)	102(3)	105(3)	170.1(13)	108.0(9)	Mg92	
0.112(2)	0.0198(18)	0.15(3)	0.15(3)	3.598(11)	356(2)	357(2)	256(1)	107(1)	108(1)	85(1)	77(2)	107(2)	94(2)	168.0(9)	104.3(5)	Mg89H2	
0.11(2) ^d	0.0581(85)	0.30(6) ^d	0.30(6) ^d	3.57(6)	339(5)	341(5)	235(1)	100(1)	106(2)	86(3)	64(4)	109(4)	90(4)	159.0(24)	99.8(9)	Mg89H6	
0.11(1)	0.1539(153)	0.11(6)	0.11(6)	3.513(3)	334(2)	319(2)	242(1)	95.2(5)	102.4(6)	86.9(7)	68.5(20)	102(2)	89(2)	156(1)	98(2)	Mg89H15	

No entry implies that the respective information was not available.

^aH₂O molecules per formula unit.

^bVoigt-Reuss-Hill averages.

^cReferences: Mg100: Sawamoto et al. (1984), Mg100H0: Zha et al. (1997), Mg100H6: Mao et al. (2008a), Mg100H4: Mao et al. (2008b), Mg92: Sinogekin et al. (1998) and Wang et al. (2014), Mg89H2: Buchen et al. (2018b), Mg89H6: this study (unpublished), Mg89H15: Mao et al. (2011).

^dValues estimated based on synthesis conditions (see Table 2.1).

Table 3.2: Elastic properties of iron-bearing wadsleyite at high pressures and high temperatures

Pressure ^a (GPa)	Temperature ^b (K)	Unit cell volume (Å ³)	Density (g cm ⁻³)	Components of the adiabatic elastic stiffness tensor ^c (GPa)												Aggregate elastic properties ^c			
				C ₁₁	C ₂₂	C ₃₃	C ₄₄	C ₅₅	C ₆₆	C ₁₂	C ₁₃	C ₂₃	K _S (GPa)	G (GPa)	V _p (km s ⁻¹)	V _S (km s ⁻¹)			
0.00(2)	298(5)	542.12(4)	3.598(11)	356(2)	357(2)	256(1)	107(1)	108(1)	85(1)	77(2)	107(2)	94(2)	168.0(9)	104.3(5)	9.239(22)	5.385(14)			
11.6(2)	500(25)	511.60(13)	3.812(11)	424(4)	411(3)	335(2)	115(1)	118(2)	114(2)	117(2)	135(3)	131(2)	214.4(12)	121.0(6)	9.928(24)	5.634(17)			
11.8(3)	640(25)	512.63(13)	3.804(11)	406(3)	408(3)	332(1)	111(1)	121(1)	117(2)	112(2)	129(2)	140(2)	211.4(11)	119.8(5)	9.877(22)	5.612(14)			
18.7(3)	460(25)	495.34(24)	3.937(12)	462(6)	475(5)	389(2)	123(1)	129(2)	130(3)	143(3)	157(3)	165(3)	250.0(18)	132.9(8)	10.417(30)	5.811(20)			

^aCalculated from Reuss Thermal EOS with thermoelastic parameters from Stixrude and Lithgow-Bertelloni (2011).

^bBased on fluorescence spectroscopy.

^cVoigt-Reuss-Hill averages.

hydrogen bonding at high pressures (Liu et al., 1998; Kleppe et al., 2001; Kleppe et al., 2006; Yang et al., 2014). We extrapolated the velocity cross-over points to realistic mantle temperatures using tabulated thermoelastic parameters (Stixrude and Lithgow-Bertelloni, 2011) and conclude that the changes in seismic wave speeds induced by hydration of wadsleyite potentially remain too small to identify hydrated regions in the shallow transition zone by seismic tomography.

As an alternative to seismic tomography, we assessed the seismic properties of the 410-km discontinuity as a function of water distribution between olivine and wadsleyite. In a first step, we combined the high-pressure elastic properties of the here-studied wadsleyite crystals with those determined on complementary wadsleyite compositions (Zha et al., 1997; Mao et al., 2011) to map the effect of chemical composition on P and S wave velocities as well as on the density of wadsleyite. Similarly, we combined elastic properties for different olivine compositions to span compositions relevant for Earth’s mantle (Zha et al., 1996; Mao et al., 2010; Mao et al., 2015; Zhang and Bass, 2016). For consistency, we only included elastic properties derived from high-pressure Brillouin spectroscopy experiments on single crystals of wadsleyite or olivine in conjunction with tabulated thermoelastic parameters (Stixrude and Lithgow-Bertelloni, 2011). We then computed the contrasts in P and S wave velocities and density between wadsleyite and olivine at pressures and temperatures of the 410-km discontinuity. While contrasts in sound wave velocities become sensitive to hydration only at high temperatures, combining velocity and density contrasts suggests that acoustic impedance contrasts are significantly reduced by hydration at all relevant temperatures. As explained in section 1.2, the impedance contrast across a seismic discontinuity is related to the reflectivity of the discontinuity and can be constrained from polarities and amplitudes of seismic waves reflected at the discontinuity. Lateral variations in reflectivity of the 410-km discontinuity can be inferred by analyzing waveforms of PP and SS precursors (Chambers et al., 2005a) or ScS reverberations (Revenaugh and Jordan, 1991; Bagley and Revenaugh, 2008). We therefore propose that mapping regions with a reduced reflectivity of the 410-km discontinuity may contribute to detect hydrated regions in the deep upper mantle and to understand cycling of water through the transition zone in Earth’s mantle.

3.4 Single-Crystal Elasticity of Wadsleyite at High Pressures and High Temperatures

Brillouin spectroscopy experiments on wadsleyite were also performed at combined high pressures and high temperatures. As explained in section 2.3.2, we used a resistive heater placed around the diamond anvils to heat the high-pressure chamber of the DAC. As with room temperature experiments, sound wave velocities were measured on two crystals that were loaded together inside the high-pressure chamber of the same DAC. The orientations of the crystals were chosen to complement each other so as to provide sufficient propagation directions of sound waves to constrain the full elastic stiffness tensor. At combined high pressures and high temperatures, this is of great advantage as all sound wave velocities can be determined at the same conditions. Otherwise, identical conditions of pressure and temperature would have to be inferred for separated experiments indirectly based on measurements that might be biased, for instance, by thermal gradients. Pressure and temperature were determined from fluorescence spectra of standard materials that were placed next to the crystals inside the high-pressure chamber of the DAC (see section 2.3.3). Densities of the crystals were calculated from unit cell volumes determined by X-ray diffraction

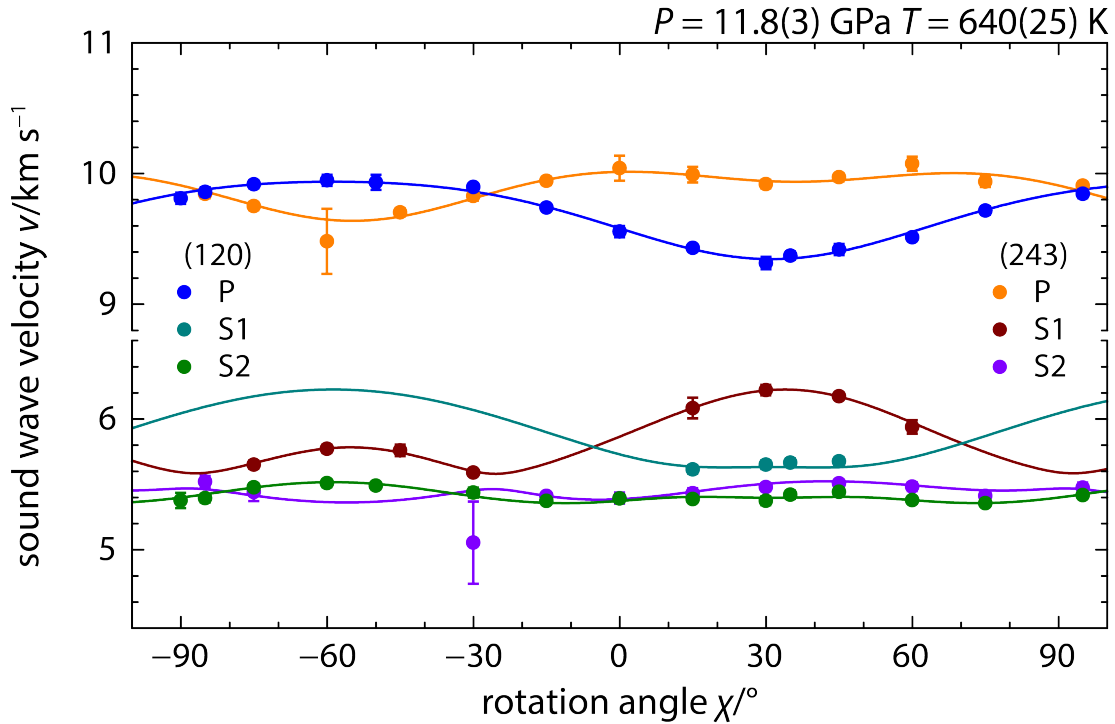


Figure 3.3: Sound wave velocities of wadsleyite single crystals with propagation directions within the (120) and (243) crystallographic planes. Solid circles show sound wave velocities determined by Brillouin spectroscopy at 11.8(3) GPa and 640(25) K as a function of rotation angle. Lines show fitted angular dispersion curves.

at the same pressures and temperatures were Brillouin spectra were recorded. While the approach used here allows deriving complete elastic stiffness tensors at individual combinations of pressure and temperature, sound wave velocities collected at various pressures and temperatures and for different propagation directions can also be analyzed using the global inversion procedure outlined in chapter 5. Isolated sound wave velocity measurements may result from failure of components of the DAC during high-pressure high-temperature experiments. By applying the global inversion procedure, their information can still contribute to the description of elastic properties even though it may not be possible to derive the complete elastic stiffness tensor directly from the sound wave velocities determined at the respective conditions.

Figure 3.3 illustrates the analysis of sound wave velocities collected at 11.8(3) GPa and 640(25) K. Elastic stiffness tensors of iron-bearing wadsleyite determined at combined high pressures and high temperatures are compiled in Table 3.2. Following the lines in the previous section, I calculated bulk and shear moduli of isotropic wadsleyite aggregates. Figure 3.4 compares the corresponding P and S wave velocities with velocities predicted based on the results of chapter 6 (Buchen et al., 2018b) and tabulated thermoelastic parameters (Stixrude and Lithgow-Bertelloni, 2011; see also Table 6.2 on page 145). While the direct experimental results at pressures around 12 GPa indicate a reduction of sound wave velocities with increasing temperature, more measurements at combined high pressures and high temperatures are needed to refine tabulated thermoelastic parameters. In view of the uncertainties as indicated by the experimental scatter of results at room temperature, I conclude that tabulated thermoelastic parameters are consistent with the here-presented measure-

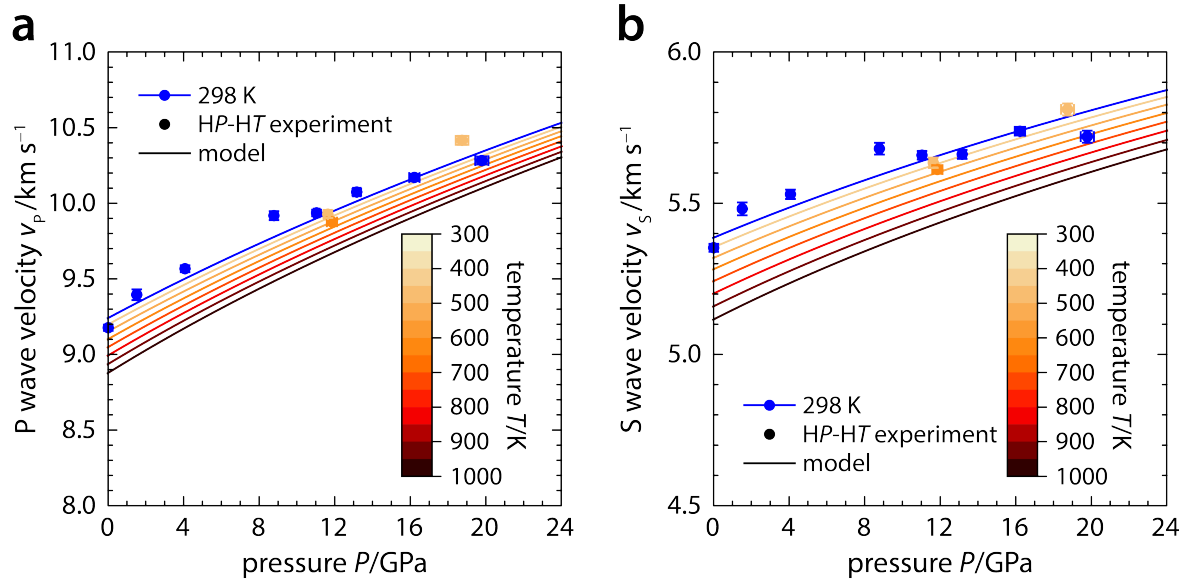


Figure 3.4: P wave (a) and S wave (b) velocities for isotropic aggregates of iron-bearing wadsleyite as a function of pressure at different temperatures. Solid circles show experimental results at ambient temperature (blue) and at high temperatures (Table 3.2). Lines were calculated based on finite-strain parameters reported in Buchen et al. (2018b) (Table 6.1) and tabulated thermoelastic parameters (Stixrude and Lithgow-Bertelloni, 2011).

ments at combined high pressures and high temperatures. This finding also justifies the use of tabulated thermoelastic parameters in modeling sound wave velocities of wadsleyite at conditions of the transition zone in chapter 6.

In addition to P and S wave velocities of isotropic aggregates, the acoustic anisotropy of wadsleyite single crystals can be computed from elastic stiffness tensors using the solutions to equation (5.10) as derived in section 5.2.2. Figure 3.5 displays the variation in propagation velocities of quasi-longitudinal (P) waves and quasi-transverse waves (S1 and S2) with propagation direction for a wadsleyite single crystal at ambient conditions and at 11.8(3) GPa and 640(25) K. For all three types of waves, the anisotropy of their propagation velocity decreases from ambient conditions to 11.8 GPa and 640 K as can be read from the range of velocities covered at each set of conditions. For quasi-transverse waves, the anisotropy can be expressed in terms of the relative difference in propagation velocities of perpendicularly polarized waves propagating in the same direction (Mainprice, 2015) (in %):

$$A_s = \frac{v_{S2} - v_{S1}}{v_{S1} + v_{S2}} \times 200 \quad (3.1)$$

with the velocities v_{S1} and v_{S2} of S1 and S2 waves, respectively. The maximum anisotropy A_s decreases from about 18 % at ambient conditions to about 12 % at 11.8 GPa and 640 K. This reduction is accompanied by a shift of the propagation direction with maximal A_s from a direction that makes nearly equal angles to all three crystallographic axes to a direction in the **a-b** plane with nearly equal angles to these two crystallographic axes. These changes in the pattern of acoustic anisotropy are similar to pressure-induced changes observed for Mg_2SiO_4 wadsleyite (Zha et al., 1997).

Information on the acoustic anisotropy of single crystals can be integrated with microstructural observations on natural rocks or on synthetic polycrystalline aggregates de-

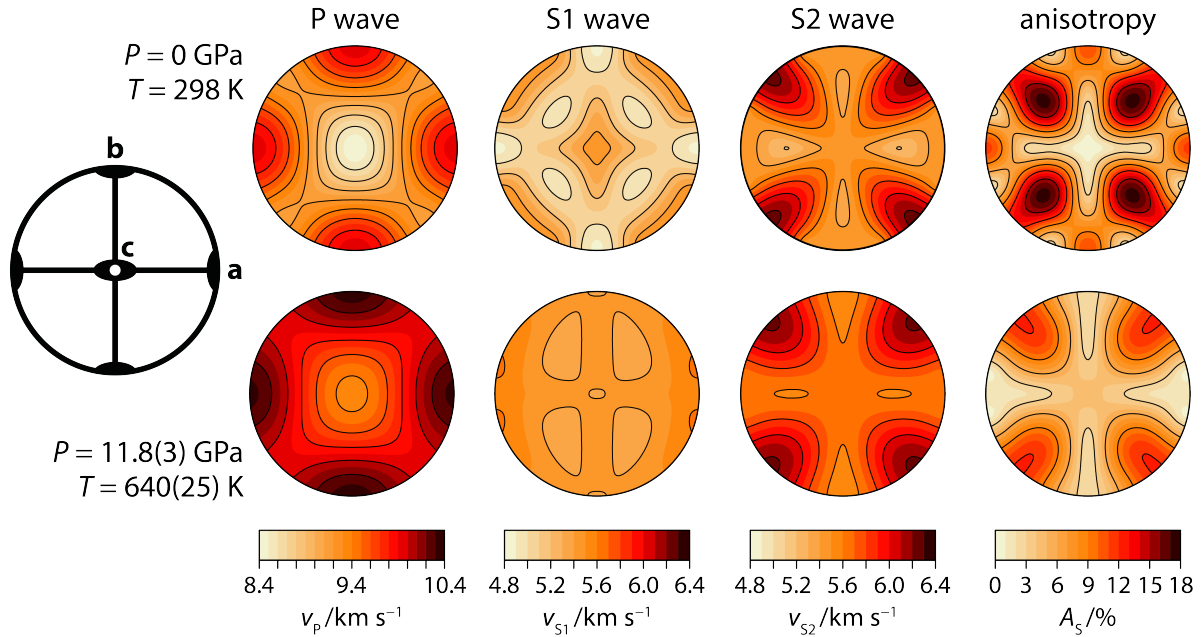


Figure 3.5: Equal-area projections showing the sound wave velocities and acoustic anisotropy of a wadsleyite single crystal at ambient conditions (upper row) and at 11.8(3) GPa and 640(25) K (lower row) for quasi-longitudinal (P) waves and quasi-transverse waves (S1 and S2). The shear wave anisotropy A_S is defined in equation (3.1).

formed at high pressures and high temperatures to predict the anisotropic seismic properties of deformed rocks (Mainprice, 2015; Almqvist and Mainprice, 2017). Viscoplastic self-consistent modeling and deformation experiments on polycrystalline wadsleyite aggregates suggest that wadsleyite grains tend to align in a crystallographic preferred orientation under shear deformation (Tommasi et al., 2004; Kawazoe et al., 2013; Ohuchi et al., 2014; Farla et al., 2015). The orientation distribution function describing the crystallographic preferred orientation can be combined with the elastic stiffness tensor of a wadsleyite single crystal to calculate the elastic stiffness tensor and the acoustic anisotropy of a polycrystalline wadsleyite aggregate (Mainprice et al., 2000; Tommasi et al., 2004; Kawazoe et al., 2013; Ohuchi et al., 2014; Mainprice, 2015).

Evidence for azimuthal and radial seismic anisotropy within the transition zone comes from the analysis of higher mode surface waves (Trampert and van Heijst, 2002; Visser et al., 2008). Seismic anisotropy at depths relevant to wadsleyite has also been inferred from observations of shear wave splitting (Fouch and Fischer, 1996; Foley and Long, 2011; Long, 2013). In comparison to other transition zone minerals, wadsleyite shows the strongest acoustic anisotropy (Mainprice, 2015) and can therefore be expected to contribute most to seismic anisotropy in the transition zone if the observed anisotropy reflects crystallographic preferred orientation of minerals. Since deformation and plastic flow of rock leads to the development of crystallographic preferred orientation (Karato, 2008), seismic anisotropy may contain information about material flow patterns in the transition zone. To translate seismically observed anisotropy to flow patterns, however, more information about the deformation behavior and the elastic properties of wadsleyite at realistic pressures, temperatures, and time scales is needed. The elastic stiffness tensors of wadsleyite compiled in Table 3.2 are the first ones determined at combined high pressures and high temperatures

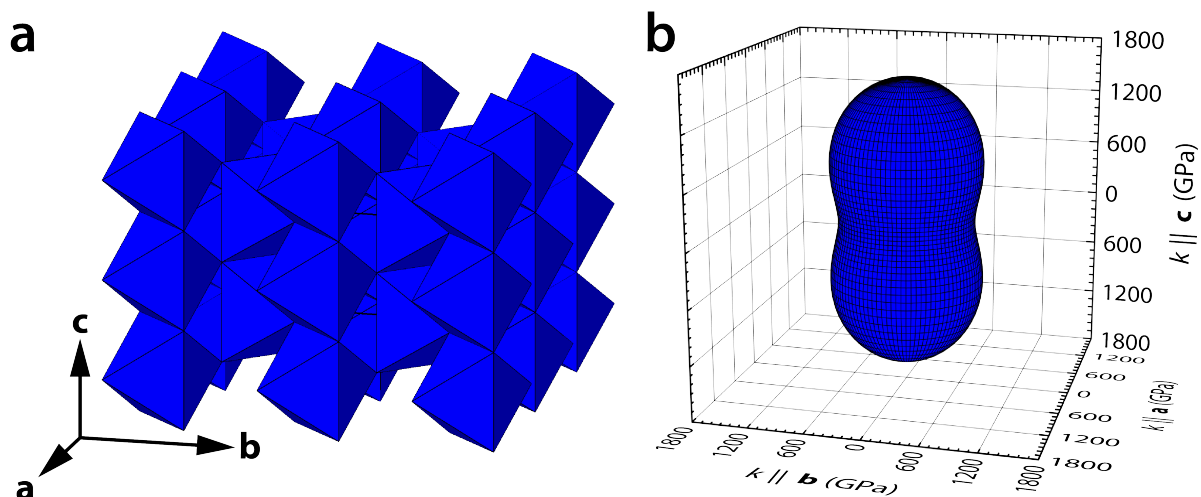


Figure 3.6: Perspective view of the crystal structure of stishovite (a) and the linear compression modulus surface (b) in the same orientation. Linear compression moduli in (b) were calculated from the elastic stiffness tensor of stishovite at ambient conditions (Jiang et al., 2009). Note that the stiffest direction points along ribbons of edge-sharing octahedra parallel to the *c* axis.

and may be used to improve estimates of anisotropic seismic properties of transition zone rocks.

3.5 High-Pressure Elasticity of Stishovite

The ferroelastic phase transition from stishovite to CaCl_2 -type SiO_2 provides another example of how processes operating on the atomic scale may affect physical properties of minerals and rocks in a way that is perceivable by geophysical observations on Earth's mantle. In scaling properties from a microscopic to a macroscopic scale, however, processes that operate at intermediate scales can modify the way in which a microscopic property translates into a macroscopic property. Considering the elastic properties of rocks, the elastic properties of individual grains or crystals combine to the overall elastic response of the rock depending on the geometry of the grains and how they are connected and arranged relative to each other (Thomsen, 1972; Watt et al., 1976). In a straightforward approach, bounds on the elastic moduli of the rock can be computed that reflect different assumptions about the stress and strain states of individual grains (Voigt, 1928; Reuss, 1929; Hill, 1952; Hashin and Shtrikman, 1962). The actual elastic response of the rock is assumed to fall between these theoretical bounds. For monomineralic rocks or single-phase polycrystalline aggregates, the separation of the bounds essentially reflects the magnitude of the elastic anisotropy of the component grains or crystals.

In chapter 7, we investigate the elastic response of sintered polycrystalline stishovite to quasi-hydrostatic compression. Stishovite displays a strong compressional anisotropy (Ross et al., 1990; Andrault et al., 2003; Jiang et al., 2009) as illustrated by the directional variation of the linear compression modulus shown in Figure 3.6. Table 3.3 lists linear compression moduli k_i along each crystallographic axis together with bulk moduli for both Voigt and Reuss bounds calculated based on the elastic stiffness tensor of stishovite at ambient conditions reported by Jiang et al. (2009). I also included compression moduli derived from compression curves of a stishovite single crystal and stishovite powder (Andrault et

Table 3.3: Compression moduli of stishovite at ambient conditions

	Voigt bound^a	Reuss bound^a	Powder & SX^b	SPX^c
Linear moduli (GPa)				
$k_1 = k_2$	846(2)	745(7)	808(10)	867(44)
k_3	1146(2)	1573(2)	1459(17)	1467(15)
Bulk modulus (GPa)				
K	315(1)	301(2)	320(2)	344(25)

^aElastic stiffness tensor from Jiang et al. (2009).

^bCompression data from Andraut et al. (2003);

SX: single-crystal data for $P < 10$ GPa.

^cSPX: sintered polycrystalline stishovite.

al., 2003) as well as our own results on sintered polycrystalline stishovite (Buchen et al., 2018a). The strong compressional anisotropy of stishovite enhances stresses between grains that are expected to arise upon compression in a sintered polycrystalline material because grain boundaries are locked to each other. Therefore, sintered polycrystalline stishovite appears to be an ideal material to study the effect of grain-grain interactions on the overall elastic response of a polycrystalline aggregate. Moreover, the transition pressure of the ferroelastic phase transition shifts to lower pressures upon nonhydrostatic compression (Singh et al., 2012; Asahara et al., 2013) providing a sensor for deviatoric stresses that arise from nonhydrostatic compression.

By comparing the compression behavior of sintered polycrystalline stishovite and stishovite powder (Andraut et al., 2003; Nisir et al., 2017), we found that sintered polycrystalline stishovite is significantly less compressible than stishovite powder, in particular along the **a** axis (Fig. 7.2 on page 161). The transition pressures to CaCl_2 -type SiO_2 are similar for both materials when derived from an analysis of spontaneous strains (Fig. 7.3a on page 166). After the phase transition to CaCl_2 -type SiO_2 , the compression curves suggest similar compressibilities for the sintered polycrystalline material and silica powder (see also Table 7.2 on page 162). These observations led us to conclude that the initial stiffening of sintered polycrystalline stishovite is related to stresses between grains arising from the strong compressional anisotropy of stishovite. These stresses are partially released at the phase transition from stishovite to CaCl_2 -type SiO_2 as the grains in the sintered material become free to distort from tetragonal to orthorhombic symmetry.

The intersection of the equations of state of sintered polycrystalline stishovite and CaCl_2 -type SiO_2 at the phase transition suggests a sharp drop of the bulk modulus as both EOS have different slopes at the transition pressure (Figs. 7.2c and 7.4c). We used a Landau theory approach (Carpenter et al., 2000; Carpenter, 2006) to predict the changes in individual components of the elastic stiffness tensor across the phase transition based on the experimentally observed evolution of unit cell parameters with pressure and previously determined elastic stiffness tensors at lower pressures (Jiang et al., 2009). From the predicted elastic stiffness tensors, we calculated the shear modulus as a function of pressure and found substantial softening of the shear modulus at pressures close to the phase transition. While a reduction of the shear modulus has been inferred earlier (Karki et al., 1997a; Carpenter et al., 2000; Shieh et al., 2002; Asahara et al., 2013), the sharp drop in bulk modulus appears to be particularly pronounced in sintered polycrystalline silica (Fig. 7.4c on page 168).

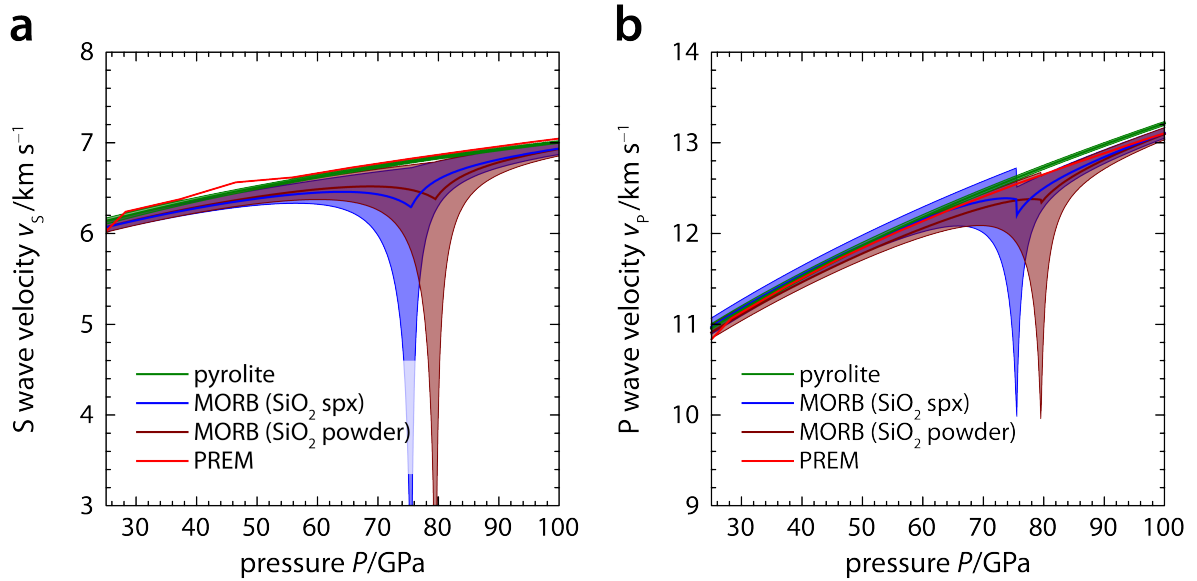


Figure 3.7: P wave (a) and S wave (b) velocities of pyrolite and a basaltic rock (MORB) along an adiabatic geotherm. For the basaltic rock, either the EOS and elastic properties of sintered polycrystalline silica (SiO_2 spx) or of silica powder (SiO_2 powder) were used to calculate sound wave velocities. Shading indicates Voigt (upper) and Reuss (lower) bounds; central bold lines show Voigt-Reuss-Hill averages. Red curves show the velocities of PREM (Dziewonski and Anderson, 1981). Note the sharp drop in P wave velocities of a basaltic rock (b) when computed based on the EOS and elastic properties of sintered polycrystalline silica (SiO_2 spx).

To illustrate a potential application of our results on sintered polycrystalline silica, I computed sound wave velocities for simplified pyrolite and MORB compositions along a mantle geotherm. For pyrolite (45.53 wt-% SiO_2 , 4.50 wt-% Al_2O_3 , 8.14 wt-% FeO , 38.24 wt-% MgO , 3.59 wt-% CaO ; McDonough and Sun, 1995), I used elastic and thermoelastic parameters for bridgmanite, ferropericlase, and Ca-silicate perovskite as given by Stixrude and Lithgow-Bertelloni (2011) and Kurnosov et al. (2017). I assumed a constant Fe-Mg partitioning coefficient of $K_{\text{br}/\text{fp}}^{\text{Fe}/\text{Mg}} = 0.5$ between bridgmanite and ferropericlase (Murakami et al., 2005; Irifune et al., 2010; Sinmyo and Hirose, 2013) and, for simplicity, neglected the effect of ferric iron on the sound wave velocities of bridgmanite that has been constrained by experiments only at pressures below 40 GPa (Kurnosov et al., 2017). For MORB (51.62 wt-% SiO_2 , 15.66 wt-% Al_2O_3 , 10.56 wt-% FeO , 7.63 wt-% MgO , 11.74 wt-% CaO , 2.7 wt-% Na_2O ; Anderson, 2007), I used tabulated elastic and thermoelastic parameters for the same mineral species as for pyrolite and added the Ca-ferrite phase (Stixrude and Lithgow-Bertelloni, 2011). The properties of stishovite and CaCl_2 -type SiO_2 were calculated from the EOS and the Landau theory descriptions for either sintered polycrystalline silica or silica powder as derived in chapter 7 (Tables 7.2 and 7.3) in combination with tabulated thermoelastic parameters (Stixrude and Lithgow-Bertelloni, 2011). I used the Clapeyron slope of $dP/dT = 15.5 \text{ MPa K}^{-1}$ for the stishovite– CaCl_2 -type SiO_2 phase transition recently determined by Fischer et al. (2018). To compute the volume fractions of phases, I assumed $K_{\text{br}/\text{cf}}^{\text{Fe}/\text{Mg}} = 0.7$ between bridgmanite and the Ca-ferrite phase and a stishovite volume fraction of 15 vol-% (Ricolleau et al., 2010). For each species, physical properties were computed as described by Stixrude and Lithgow-Bertelloni (2005). Debye functions (Ita and Stixrude, 1992) were integrated numerically for each species and the properties of all species com-

bined after each calculation step according to either the Voigt or Reuss bound or the Voigt-Reuss-Hill average. An adiabatic geotherm starting at 23.5 GPa and 1900 K was computed for pyrolite and used in all subsequent calculations. The results are shown in Figure 3.7 together with P and S wave velocities of PREM (Dziewonski and Anderson, 1981).

The ferroelastic phase transition appears to perturb the elastic properties of silica strong enough to affect the sound wave velocities of a basaltic rock in Earth's mantle. For shear wave velocities, the difference in using the EOS and Landau theory descriptions of sintered polycrystalline silica or silica powder merely consists in a shift of the transition pressure. P wave velocities based on the Voigt-Reuss-Hill average and the elastic properties of sintered polycrystalline silica, however, drop abruptly at the phase transition. Based on these preliminary modeling results, the ferroelastic phase transition in silica bears the potential to be seismically detectable in Earth's lower mantle, for example, by scattering of seismic waves on kilometer-sized fragments of subducted oceanic crust. In general, S waves appear to be more affected in agreement with seismic observations of S-to-P scattered waves (Kaneshima and Helffrich, 1998; Kaneshima and Helffrich, 2009; Kaneshima and Helffrich, 2010). Our results on sintered polycrystalline silica, however, indicate that P waves might also be scattered, especially at conditions close to the phase transition where the P wave velocity contrast between pyrolite or PREM and a basaltic rock is amplified by the sharp drop in P wave velocities.

Whether the sharp drop of the bulk modulus at the phase transition from stishovite to CaCl_2 -type SiO_2 can affect P wave waves in Earth's mantle depends on the extent of stresses that can accumulate between grains during the passage of a seismic wave. At mantle temperatures and low oscillation frequencies, stresses between grains can relax, and the rock would be expected to follow the velocity curves computed based on the EOS of silica powder. Oscillation frequencies that are high enough to impede complete relaxation of stresses between grains, however, could shift the elastic response towards the behavior of sintered polycrystalline silica. The actual response of a stishovite-bearing rock might fall in between the completely relaxed and unrelaxed situations. The frequency range above which stresses between grains cannot relax efficiently by anelastic processes depends on the relaxation processes (Jackson, 2007; Karato, 2008). To constrain the elastic and anelastic response of polycrystalline stishovite or mantle rocks in general, experiments at seismic frequencies are required, ideally at pressures and temperatures relevant to Earth's mantle. Recently, the spin transition of $(\text{Mg,Fe})\text{O}$ ferropericlase has been probed at pressures of the lower mantle and at seismic frequencies using a dynamically-driven diamond anvil cell (dDAC) (Marquardt et al., 2018). The dDAC can generate pressure oscillations similar to those of a P wave and would therefore be ideally suited to test whether the drop of the bulk modulus at the phase transition from stishovite to CaCl_2 -type SiO_2 shows a frequency dependence. Using stishovite as an example, we showed that the elastic response of sintered polycrystalline materials may be complex and deviate from powder, in particular in the vicinity of phase transitions. Future studies might aim at constraining the elastic and anelastic properties of polycrystalline materials composed of phases of geophysical interest at seismic frequencies and at simultaneously high pressures and high temperatures.

References

- Ackermann, L., L. Cemič, and K. Langer (1983). Hydrogarnet substitution in pyrope: a possible location for “water” in the mantle. *Earth Planet. Sci. Lett.* **62**, 208–214.
- Agee, C. B. (1998). Phase transformations and seismic structure in the upper mantle and transition zone. *Rev. Mineral.* **37**, 165–203.
- Akaogi, M., E. Ito, and A. Navrotsky (1989). Olivine-modified spinel-spinel transitions in the system $\text{Mg}_2\text{SiO}_4 - \text{Fe}_2\text{SiO}_4$: Calorimetric measurements, thermochemical calculation, and geophysical application. *J. Geophys. Res.: Solid Earth* **94**, 15671–15685.
- Akaogi, M., H. Yusa, K. Shiraishi, and T. Suzuki (1995). Thermodynamic properties of α -quartz, coesite, and stishovite and equilibrium phase relations at high pressures and high temperatures. *J. Geophys. Res.: Solid Earth* **100**, 22337–22347.
- Almqvist, B. S. G. and D. Mainprice (2017). Seismic properties and anisotropy of the continental crust: Predictions based on mineral texture and rock microstructure. *Rev. Geophys.* **55**, 367–433.
- Anderson, D. L. (1979). The upper mantle transition region: Eclogite? *Geophys. Res. Lett.* **6**, 433–436.
- (2007). *New Theory of the Earth*. Cambridge University Press, Cambridge, 384 pp.
- Anderson, D. L. and J. D. Bass (1984). Mineralogy and composition of the upper mantle. *Geophys. Res. Lett.* **11**, 637–640.
- (1986). Transition region of the Earth’s upper mantle. *Nature* **320**, 321–328.
- Andrault, D., G. Fiquet, F. Guyot, and M. Hanfland (1998). Pressure-induced Landau-type transition in stishovite. *Science* **282**, 720–724.
- Andrault, D., R. J. Angel, J. L. Mosenfelder, and T. Le Bihan (2003). Equation of state of stishovite to lower mantle pressures. *Am. Mineral.* **88**, 301–307.
- Angel, R. J. (2000). Equations of state. *Rev. Mineral. Geochem.* **41**, 35–59.
- (2003). Automated profile analysis for single-crystal diffraction data. *J. Appl. Crystallogr.* **36**, 295–300.
- Angel, R. J. and L. W. Finger (2011). *SINGLE*: a program to control single-crystal diffractometers. *J. Appl. Crystallogr.* **44**, 247–251.
- Angel, R. J., R. T. Downs, and L. W. Finger (2000). High-temperature–high-pressure diffraction. *Rev. Mineral. Geochem.* **41**, 559–597.
- Angel, R. J., J. M. Jackson, H. J. Reichmann, and S. Speziale (2009). Elasticity measurements on minerals: a review. *Eur. J. Mineral.* **21**, 525–550.
- Angel, R. J., M. Alvaro, and J. Gonzalez-Platas (2014). EosFit7c and a Fortran module (library) for equation of state calculations. *Z. Kristallogr. - Cryst. Mater.* **229**, 405–419.
- Antonangeli, D., J. Siebert, C. M. Aracne, D. L. Farber, A. Bosak, M. Hoesch, M. Krisch, F. J. Ryerson, G. Fiquet, and J. Badro (2011). Spin crossover in ferropericlae at high pressure: a seismologically transparent transition? *Science* **331**, 64–67.

- Asahara, Y., K. Hirose, Y. Ohishi, N. Hirao, H. Ozawa, and M. Murakami (2013). Acoustic velocity measurements for stishovite across the post-stishovite phase transition under deviatoric stress: Implications for the seismic features of subducting slabs in the mid-mantle. *Am. Mineral.* **98**, 2053–2062.
- Asimow, P. D. and C. H. Langmuir (2003). The importance of water to oceanic mantle melting regimes. *Nature* **421**, 815–820.
- Asimow, P. D., J. E. Dixon, and C. H. Langmuir (2004). A hydrous melting and fractionation model for mid-ocean ridge basalts: Application to the Mid-Atlantic Ridge near the Azores. *Geochem., Geophys., Geosyst.* **5**.
- Atkins, P and J. de Paula (2006). *Physical Chemistry*. 8th edition. Oxford University Press, Oxford, 1064 pp.
- Auld, B. A. (1973). *Acoustic Fields and Waves in Solids I & II*. John Wiley & Sons, New York, 423 pp. & 414 pp.
- Bach, W., C. J. Garrido, H. Paulick, J. Harvey, and M. Rosner (2004). Seawater-peridotite interactions: First insights from ODP Leg 209, MAR 15°N. *Geochem., Geophys., Geosyst.* **5**.
- Bagley, B. and J. Revenaugh (2008). Upper mantle seismic shear discontinuities of the Pacific. *J. Geophys. Res.: Solid Earth* **113**, B12301.
- Baker, V. R., R. G. Strom, V. C. Gulick, J. S. Kargel, G. Komatsu, and V. S. Kale (1991). Ancient oceans, ice sheets and the hydrological cycle on Mars. *Nature* **352**, 589–594.
- Ballmer, M. D., C. Houser, J. W. Hernlund, R. M. Wentzcovitch, and K. Hirose (2017). Persistence of strong silica-enriched domains in the Earth's lower mantle. *Nat. Geosci.* **10**, 236–240.
- Bass, J. D. and D. L. Anderson (1984). Composition of the upper mantle: Geophysical tests of two petrological models. *Geophys. Res. Lett.* **11**, 229–232.
- Bearden, J. A. (1967). X-ray wavelengths. *Rev. Mod. Phys.* **39**, 78–124.
- Benz, H. M. and J. E. Vidale (1993). Sharpness of upper-mantle discontinuities determined from high-frequency reflections. *Nature* **365**, 147–150.
- Bérar, J.-F. and P. Lelann (1991). E.s.d.'s and estimated probable error obtained in Rietveld refinements with local correlations. *J. Appl. Crystallogr.* **24**, 1–5.
- Bercovici, D. and S.-i. Karato (2003). Whole-mantle convection and the transition-zone water filter. *Nature* **425**, 39–44.
- Bina, C. R. and B. J. Wood (1987). Olivine-spinel transitions: Experimental and thermodynamic constraints and implications for the nature of the 400-km seismic discontinuity. *J. Geophys. Res.: Solid Earth* **92**, 4853–4866.
- Birch, F. (1947). Finite elastic strain of cubic crystals. *Phys. Rev.* **71**, 809–824.
- Blichert-Toft, J. and F. Albarède (1997). The Lu–Hf isotope geochemistry of chondrites and the evolution of the mantle-crust system. *Earth Planet. Sci. Lett.* **148**, 243–258.
- Boehler, R. (2006). New diamond cell for single-crystal x-ray diffraction. *Rev. Sci. Instrum.* **77**, 115103.
- Boehler, R. and K. De Hantsetters (2004). New anvil designs in diamond-cells. *High Pressure Res.* **24**, 391–396.
- Boffa Ballaran, T., A. Kurnosov, and D. Trots (2013). Single-crystal X-ray diffraction at extreme conditions: a review. *High Pressure Res.* **33**, 453–465.
- Bolfan-Casanova, N. (2005). Water in the Earth's mantle. *Mineral. Mag.* **69**, 229–257.
- Bolfan-Casanova, N., C. A. McCammon, and S. J. Mackwell (2006). Water in transition zone and lower mantle minerals. In: *Earth's Deep Water Cycle*. Ed. by S. D. Jacobsen and S. van der Lee. American Geophysical Union, Washington, DC, 57–68.

- Bolfan-Casanova, N., D. Andrault, E. Amiguet, and N. Guignot (2009). Equation of state and post-stishovite transformation of Al-bearing silica up to 100 GPa and 3000 K. *Phys. Earth Planet. Inter.* **174**, 70–77.
- Bolfan-Casanova, N., M. Muñoz, C. McCammon, E. Deloule, A. Férot, S. Demouchy, L. France, D. Andrault, and S. Pascarelli (2012). Ferric iron and water incorporation in wadsleyite under hydrous and oxidizing conditions: A XANES, Mössbauer, and SIMS study. *Am. Mineral.* **97**, 1483–1493.
- Bolfan-Casanova, N., F. Schiavi, C. Raepsaet, D. Novella, H. Bureau, H. Khodja, and S. Demouchy (2018). Examination of water quantification and incorporation in transition zone minerals: Wadsleyite, ringwoodite and phase D using ERDA (Elastic Recoil Detection analysis). *Front. Earth Sci.* **6**, 75.
- Bragg, W. L. (1914). The Analysis of Crystals by the X-Ray Spectrometer. *Proc. R. Soc. London, Ser. A* **89**, 468–489.
- Brandenburg, J. P. and P. E. van Keken (2007). Deep storage of oceanic crust in a vigorously convecting mantle. *J. Geophys. Res.: Solid Earth* **112**.
- Brazhkin, V. V., L. E. McNeil, M. Grimsditch, N. A. Bendeliani, T. I. Dyuzheva, and L. M. Lityagina (2005). Elastic constants of stishovite up to its amorphization temperature. *J. Phys.: Condens. Matter* **17**, 1869.
- Bromiley, G. D., F. A. Bromiley, and D. W. Bromiley (2006). On the mechanisms for H and Al incorporation in stishovite. *Phys. Chem. Miner.* **33**, 613–621.
- Buchen, J., H. Marquardt, T. Boffa Ballaran, T. Kawazoe, and C. McCammon (2017). The equation of state of wadsleyite solid solutions: Constraining the effects of anisotropy and crystal chemistry. *Am. Mineral.* **102**, 2494–2504.
- Buchen, J., H. Marquardt, K. Schulze, S. Speziale, T. Boffa Ballaran, N. Nishiyama, and M. Hanfland (2018a). Equation of state of polycrystalline stishovite across the tetragonal-orthorhombic phase transition. *J. Geophys. Res.: Solid Earth* **123**, 7347–7360.
- Buchen, J., H. Marquardt, S. Speziale, T. Kawazoe, T. Boffa Ballaran, and A. Kurnosov (2018b). High-pressure single-crystal elasticity of wadsleyite and the seismic signature of water in the shallow transition zone. *Earth Planet. Sci. Lett.* **498**, 77–87.
- Busing, W. R. and H. A. Levy (1967). Angle calculations for 3- and 4-Circle X-ray and neutron diffractometers. *Acta Crystallogr.* **22**, 457–464.
- Caglioti, G., A. Paoletti, and F. P. Ricci (1958). Choice of collimators for a crystal spectrometer for neutron diffraction. *Nucl. Instrum.* **3**, 223–228.
- Carpenter, M. A. (2006). Elastic properties of minerals and the influence of phase transitions. *Am. Mineral.* **91**, 229–246.
- Carpenter, M. A. and E. K. H. Salje (1998). Elastic anomalies in minerals due to structural phase transitions. *Eur. J. Mineral.* **10**, 693–812.
- Carpenter, M. A., R. J. Hemley, and H.-k. Mao (2000). High-pressure elasticity of stishovite and the $P4_2/mnm \rightleftharpoons Pnnm$ phase transition. *J. Geophys. Res.: Solid Earth* **105**, 10807–10816.
- Chambers, K., A. Deuss, and J. H. Woodhouse (2005a). Reflectivity of the 410-km discontinuity from PP and SS precursors. *J. Geophys. Res.: Solid Earth* **110**, B02301.
- Chambers, K., J. H. Woodhouse, and A. Deuss (2005b). Topography of the 410-km discontinuity from PP and SS precursors. *Earth Planet. Sci. Lett.* **235**, 610–622.
- Chang, Y.-Y., S. D. Jacobsen, C. R. Bina, S.-M. Thomas, J. R. Smyth, D. J. Frost, T. Boffa Ballaran, C. A. McCammon, E. H. Hauri, T. Inoue, et al. (2015). Comparative compressibility of hydrous wadsleyite and ringwoodite: Effect of H₂O and implications for detecting water in the transition zone. *J. Geophys. Res.: Solid Earth* **120**, 8259–8280.

- Chase, C. G. and P. J. Patchett (1988). Stored mafic/ultramafic crust and early Archean mantle depletion. *Earth Planet. Sci. Lett.* **91**, 66–72.
- Chen, J., T. Inoue, H. Yurimoto, and D. J. Weidner (2002). Effect of water on olivine-wadsleyite phase boundary in the (Mg, Fe)₂SiO₄ system. *Geophys. Res. Lett.* **29**, 1875.
- Christensen, U. (1989). Mixing by time-dependent convection. *Earth Planet. Sci. Lett.* **95**, 382–394.
- Christensen, U. R. and A. W. Hofmann (1994). Segregation of subducted oceanic crust in the convecting mantle. *J. Geophys. Res.: Solid Earth* **99**, 19867–19884.
- Chung, D. H. and W. R. Buessem (1967). The Voigt–Reuss–Hill approximation and elastic moduli of polycrystalline MgO, CaF₂, β-ZnS, ZnSe, and CdTe. *J. Appl. Phys.* **38**, 2535–2540.
- Chung, J. I. and H. Kagi (2002). High concentration of water in stishovite in the MORB system. *Geophys. Res. Lett.* **29**, 2020.
- Condie, K. C. and V. Pease, eds. (2008). *When Did Plate Tectonics Begin on Planet Earth?* Geological Society of America, Boulder, CO.
- Crowhurst, J. C., J. M. Brown, A. F. Goncharov, and S. D. Jacobsen (2008). Elasticity of (Mg,Fe)O through the spin transition of iron in the lower mantle. *Science* **319**, 451–453.
- Cummins, H. Z. and P. E. Schoen (1972). Linear scattering from thermal fluctuations. In: *Laser Handbook*. Ed. by F. T. Arecchi and E. O. Schulz-DuBois. Vol. 2. North-Holland Publishing Company, Amsterdam, 1029–1075.
- Demouchy, S., E. Deloule, D. J. Frost, and H. Keppler (2005). Pressure and temperature-dependence of water solubility in Fe-free wadsleyite. *Am. Mineral.* **90**, 1084–1091.
- Deon, F., M. Koch-Müller, D. Rhede, M. Gottschalk, R. Wirth, and S.-M. Thomas (2010). Location and quantification of hydroxyl in wadsleyite: New insights. *Am. Mineral.* **95**, 312–322.
- Dewaele, A., M. Torrent, P. Loubeyre, and M. Mezouar (2008). Compression curves of transition metals in the Mbar range: Experiments and projector augmented-wave calculations. *Phys. Rev. B* **78**, 104102.
- Dil, J. G. (1982). Brillouin scattering in condensed matter. *Rep. Prog. Phys.* **45**, 285–334.
- Dinnebier, R. E. and S. J. L. Billinge, eds. (2008). *Powder Diffraction: Theory and Practice*. Royal Society of Chemistry, Cambridge, 582 pp.
- Downs, J. W. (1989). Possible sites for protonation in β-Mg₂SiO₄ from an experimentally derived electrostatic potential. *Am. Mineral.* **74**, 1124–1129.
- Dziewonski, A. M. and D. L. Anderson (1981). Preliminary reference Earth model. *Phys. Earth Planet. Inter.* **25**, 297–356.
- Eiler, J., ed. (2003). *Inside the Subduction Factory*. American Geophysical Union, Washington, DC.
- El Goresy, A., P. Dera, T. G. Sharp, C. T. Prewitt, M. Chen, L. Dubrovinsky, B. Wopenka, N. Z. Boctor, and R. J. Hemley (2008). Seifertite, a dense orthorhombic polymorph of silica from the Martian meteorites Shergotty and Zagami. *Eur. J. Mineral.* **20**, 523–528.
- Eliezer, S., A. Ghatak, and H. Hora (1986). *An Introduction to Equations of State: Theory and Applications*. Cambridge University Press, Cambridge, 384 pp.
- Evans, B. W. (1977). Metamorphism of alpine peridotite and serpentinite. *Annu. Rev. Earth Planet. Sci.* **5**, 397–447.
- Farla, R., G. Amulele, J. Girard, N. Miyajima, and S.-i. Karato (2015). High-pressure and high-temperature deformation experiments on polycrystalline wadsleyite using the rotational Drickamer apparatus. *Phys. Chem. Miner.* **42**, 541–558.

- Fei, H., D. Yamazaki, M. Sakurai, N. Miyajima, H. Ohfuji, T. Katsura, and T. Yamamoto (2017). A nearly water-saturated mantle transition zone inferred from mineral viscosity. *Sci. Adv.* **3**, e1603024.
- Finger, L. W., R. M. Hazen, J. Zhang, J. Ko, and A. Navrotsky (1993). The effect of Fe on the crystal structure of wadsleyite β - $(\text{Mg}_{1-x}\text{Fe}_x)_2\text{SiO}_4$, $0.00 \leq x \leq 0.40$. *Phys. Chem. Miner.* **19**, 361–368.
- Fiquet, G., J. Badro, F. Guyot, C. Bellin, M. Krisch, D. Antonangeli, H. Requardt, A. Mermet, D. Farber, C. Aracne-Ruddle, et al. (2004). Application of inelastic X-ray scattering to the measurements of acoustic wave velocities in geophysical materials at very high pressure. *Phys. Earth Planet. Inter.* **143–144**, 5–18.
- Fiquet, G., F. Guyot, and J. Badro (2008). The Earth's lower mantle and core. *Elements* **4**, 177–182.
- Fischer, R. A., A. J. Campbell, B. A. Chidester, D. M. Reaman, E. C. Thompson, J. S. Pigott, V. B. Prakapenka, and J. S. Smith (2018). Equations of state and phase boundary for stishovite and CaCl_2 -type SiO_2 . *Am. Mineral.* **103**, 792–802.
- Foley, B. J. and M. D. Long (2011). Upper and mid-mantle anisotropy beneath the Tonga slab. *Geophys. Res. Lett.* **38**, L02303.
- Foley, S. (2008). A trace element perspective on Archean crust formation and on the presence or absence of Archean subduction. In: *When Did Plate Tectonics Begin on Planet Earth?* Ed. by K. C. Condie and V. Pease. Geological Society of America, Boulder, CO, 31–50.
- Foley, S., M. Tiepolo, and R. Vannucci (2002). Growth of early continental crust controlled by melting of amphibolite in subduction zones. *Nature* **417**, 837–840.
- Foley, S. E., S. Buhre, and D. E. Jacob (2003). Evolution of the Archaean crust by delamination and shallow subduction. *Nature* **421**, 249–252.
- Forman, R. A., G. J. Piermarini, J. D. Barnett, and S. Block (1972). Pressure measurement made by the utilization of ruby sharp-line luminescence. *Science* **176**, 284–285.
- Fouch, M. J. and K. M. Fischer (1996). Mantle anisotropy beneath northwest Pacific subduction zones. *J. Geophys. Res.: Solid Earth* **101**, 15987–16002.
- Freitas, D., G. Manthilake, F. Schiavi, J. Chantel, N. Bolfan-Casanova, M. A. Bouhifd, and D. Andrault (2017). Experimental evidence supporting a global melt layer at the base of the Earth's upper mantle. *Nat. Commun.* **8**, 2186.
- Frigo, C., R. Stalder, and T. Ludwig (2018). OH defects in coesite and stishovite during ultrahigh-pressure metamorphism of continental crust. *Phys. Chem. Miner.* 1–13.
- Frost, D. J. (2003a). Fe^{2+} -Mg partitioning between garnet, magnesio-wüstite, and $(\text{Mg,Fe})_2\text{SiO}_4$ phases of the transition zone. *Am. Mineral.* **88**, 387–397.
- (2003b). The structure and sharpness of $(\text{Mg,Fe})_2\text{SiO}_4$ phase transformations in the transition zone. *Earth Planet. Sci. Lett.* **216**, 313–328.
- (2008). The upper mantle and transition zone. *Elements* **4**, 171–176.
- Frost, D. J. and D. Dolejš (2007). Experimental determination of the effect of H_2O on the 410-km seismic discontinuity. *Earth Planet. Sci. Lett.* **256**, 182–195.
- Frost, D. J. and C. A. McCammon (2008). The redox state of Earth's mantle. *Annu. Rev. Earth Planet. Sci.* **36**, 389–420.
- (2009). The effect of oxygen fugacity on the olivine to wadsleyite transformation: Implications for remote sensing of mantle redox state at the 410 km seismic discontinuity. *Am. Mineral.* **94**, 872–882.

- Frost, D. J., F. Langenhorst, and P. A. van Aken (2001). Fe–Mg partitioning between ringwoodite and magnesiowüstite and the effect of pressure, temperature and oxygen fugacity. *Phys. Chem. Miner.* **28**, 455–470.
- Fukao, Y. and M. Obayashi (2013). Subducted slabs stagnant above, penetrating through, and trapped below the 660 km discontinuity. *J. Geophys. Res.: Solid Earth* **118**, 5920–5938.
- Fukao, Y., M. Obayashi, and T. Nakakuki (2009). Stagnant slab: a review. *Annu. Rev. Earth Planet. Sci.* **37**, 19–46.
- Giacovazzo, C., H. L. Monaco, G. Artioli, D. Viterbo, M. Milanesio, G. Gilli, P. Gilli, G. Zanotti, G. Ferraris, and M. Catti, eds. (2011). *Fundamentals of Crystallography*. 3rd edition. International Union of Crystallography Texts on Crystallography. Oxford University Press, Oxford, 864 pp.
- Gibbs, G. V., D. F. Cox, and N. L. Ross (2004). A modeling of the structure and favorable H-docking sites and defects for the high-pressure silica polymorph stishovite. *Phys. Chem. Miner.* **31**, 232–239.
- Goldstein, J. I., D. E. Newbury, J. R. Michael, N. W. M. Ritchie, J. H. J. Scott, and D. C. Joy (2018). *Scanning Electron Microscopy and X-Ray Microanalysis*. 4th edition. Springer-Verlag, New York, 550 pp.
- Goncharov, A. F., V. V. Struzhkin, and S. D. Jacobsen (2006). Reduced radiative conductivity of low-spin (Mg,Fe)O in the lower mantle. *Science* **312**, 1205–1208.
- Grand, S. P. (2002). Mantle shear-wave tomography and the fate of subducted slabs. *Philos. Trans. R. Soc., A* **360**, 2475–2491.
- Griffin, J. M., A. J. Berry, D. J. Frost, S. Wimperis, and S. E. Ashbrook (2013). Water in the Earth's mantle: a solid-state NMR study of hydrous wadsleyite. *Chem. Sci.* **4**, 1523–1538.
- Grocholski, B., S.-H. Shim, and V. B. Prakapenka (2013). Stability, metastability, and elastic properties of a dense silica polymorph, seifertite. *J. Geophys. Res.: Solid Earth* **118**, 4745–4757.
- Grotzinger, J. (2009). Beyond Water on Mars. *Nat. Geosci.* **2**, 231–233.
- Gurnis, M. and G. F. Davies (1986). Mixing in numerical models of mantle convection incorporating plate kinematics. *J. Geophys. Res.: Solid Earth* **91**, 6375–6395.
- Hammersley, A. P. (2016). *FIT2D*: a multi-purpose data reduction, analysis and visualization program. *J. Appl. Crystallogr.* **49**, 646–652.
- Hart, S. R. and A. Zindler (1986). In search of a bulk-Earth composition. *Chem. Geol.* **57**, 247–267.
- Hart, T. R., R. L. Aggarwal, and B. Lax (1970). Temperature dependence of Raman scattering in silicon. *Phys. Rev. B* **1**, 638–642.
- Hashin, Z. and S. Shtrikman (1962). A variational approach to the theory of the elastic behaviour of polycrystals. *J. Mech. Phys. Solids* **10**, 343–352.
- Haussühl, S. (2007). *Physical Properties of Crystals: An Introduction*. Wiley-VCH, Weinheim, 439 pp.
- Hazen, R. M., M. B. Weinberger, H. Yang, and C. T. Prewitt (2000). Comparative high-pressure crystal chemistry of wadsleyite, β -(Mg_{1-x}Fe_x)₂SiO₄, with $x = 0$ and 0.25. *Am. Mineral.* **85**, 770–777.
- Hedlin, M. A. H., P. M. Shearer, and P. S. Earle (1997). Seismic evidence for small-scale heterogeneity throughout the Earth's mantle. *Nature* **387**, 145.
- Helfrich, G., M. D. Ballmer, and K. Hirose (2018). Core-exsolved SiO₂ dispersal in the Earth's mantle. *J. Geophys. Res.: Solid Earth* **123**, 176–188.

- Helfrich, G. R. and B. J. Wood (1996). 410 km discontinuity sharpness and the form of the olivine α - β phase diagram: resolution of apparent seismic contradictions. *Geophys. J. Int.* **126**, F7–F12.
- Hemley, R. J., C. T. Prewitt, and K. J. Kingma (1994). High-pressure behavior of silica. *Rev. Mineral.* **29**, 41–81.
- Hemley, R. J., J. Shu, M. A. Carpenter, J. Hu, H. K. Mao, and K. J. Kingma (2000). Strain/order parameter coupling in the ferroelastic transition in dense SiO₂. *Solid State Commun.* **114**, 527–532.
- Herzberg, C. and R. Rudnick (2012). Formation of cratonic lithosphere: An integrated thermal and petrological model. *Lithos* **149**, 4–15.
- Hess, N. J. and D. Schiferl (1990). Pressure and temperature dependence of laser-induced fluorescence of Sm:YAG to 100 kbar and 700 °C and an empirical model. *J. Appl. Phys.* **68**, 1953–1960.
- (1992). Comparison of the pressure-induced frequency shift of Sm:YAG to the ruby and nitrogen vibron pressure scales from 6 to 820 K and 0 to 25 GPa and suggestions for use as a high-temperature pressure calibrant. *J. Appl. Phys.* **71**, 2082–2086.
- Hill, R. (1952). The elastic behaviour of a crystalline aggregate. *Proc. Phys. Soc., London, Sect. A* **65**, 349–354.
- (1963). Elastic properties of reinforced solids: Some theoretical principles. *J. Mech. Phys. Solids* **11**, 357–372.
- Hinrichsen, B., R. E. Dinnebier, and M. Jansen (2008). Two-dimensional diffraction using area detectors. In: *Powder Diffraction: Theory and Practice*. Ed. by R. E. Dinnebier and S. J. L. Billinge. Royal Society of Chemistry, Cambridge, 414–438.
- Hirose, K., Y. Fei, Y. Ma, and H.-K. Mao (1999). The fate of subducted basaltic crust in the Earth's lower mantle. *Nature* **397**, 53.
- Hirose, K., N. Takafuji, N. Sata, and Y. Ohishi (2005). Phase transition and density of subducted MORB crust in the lower mantle. *Earth Planet. Sci. Lett.* **237**, 239–251.
- Hirose, K., G. Morard, R. Sinmyo, K. Umemoto, J. Hernlund, G. Helffrich, and S. Labrosse (2017). Crystallization of silicon dioxide and compositional evolution of the Earth's core. *Nature* **543**, 99–102.
- Hirschmann, M. M., A. C. Withers, and C. Aubaud (2006). Petrologic structure of a hydrous 410 km discontinuity. In: *Earth's Deep Water Cycle*. Ed. by S. D. Jacobsen and S. van der Lee. American Geophysical Union, Washington, DC, 277–287.
- Hirth, G. and S. Guillot (2013). Rheology and tectonic significance of serpentinite. *Elements* **9**, 107–113.
- Hirth, G. and D. L. Kohlstedt (1996). Water in the oceanic upper mantle: implications for rheology, melt extraction and the evolution of the lithosphere. *Earth Planet. Sci. Lett.* **144**, 93–108.
- Hofmann, A. W. (1997). Mantle geochemistry: the message from oceanic volcanism. *Nature* **385**, 219–229.
- Hofmann, A. W. and W. M. White (1982). Mantle plumes from ancient oceanic crust. *Earth Planet. Sci. Lett.* **57**, 421–436.
- Holl, C. M., J. R. Smyth, S. D. Jacobsen, and D. J. Frost (2008). Effects of hydration on the structure and compressibility of wadsleyite, β -(Mg₂SiO₄). *Am. Mineral.* **93**, 598–607.
- Holland, T. J. B. and R. Powell (1998). An internally consistent thermodynamic data set for phases of petrological interest. *J. Metamorph. Geol.* **16**, 309–343.
- Holzappel, C., D. C. Rubie, S. Mackwell, and D. J. Frost (2003). Effect of pressure on Fe–Mg interdiffusion in (Fe_xMg_{1-x})O, ferropericlase. *Phys. Earth Planet. Inter.* **139**, 21–34.

- Horiuchi, H. and H. Sawamoto (1981). β - Mg_2SiO_4 : Single-crystal X-ray diffraction study. *Am. Mineral.* **66**, 568–575.
- Houser, C. (2016). Global seismic data reveal little water in the mantle transition zone. *Earth Planet. Sci. Lett.* **448**, 94–101.
- Huang, X., Y. Xu, and S.-i. Karato (2005). Water content in the transition zone from electrical conductivity of wadsleyite and ringwoodite. *Nature* **434**, 746–749.
- Humphris, S. E. and G. Thompson (1978). Hydrothermal alteration of oceanic basalts by seawater. *Geochim. Cosmochim. Acta* **42**, 107–125.
- Hutko, A. R., T. Lay, E. J. Garnero, and J. Revenaugh (2006). Seismic detection of folded, subducted lithosphere at the core–mantle boundary. *Nature* **441**, 333–336.
- Hyndman, R. D. and S. M. Peacock (2003). Serpentinization of the forearc mantle. *Earth Planet. Sci. Lett.* **212**, 417–432.
- Ichiki, M., M. Uyeshima, H. Utada, Z. Guoze, T. Ji, and M. Mingzhi (2001). Upper mantle conductivity structure of the back-arc region beneath northeastern China. *Geophys. Res. Lett.* **28**, 3773–3776.
- Immoor, J., H. Marquardt, L. Miyagi, F. Lin, S. Speziale, S. Merkel, J. Buchen, A. Kurnosov, and H.-P. Liermann (2018). Evidence for {100}<100> slip in ferropicicase in Earth's lower mantle from high-pressure/high-temperature experiments. *Earth Planet. Sci. Lett.* **489**, 251–257.
- Inoue, T., H. Yurimoto, and Y. Kudoh (1995). Hydrous modified spinel, $\text{Mg}_{1.75}\text{SiH}_{0.5}\text{O}_4$: A new water reservoir in the mantle transition region. *Geophys. Res. Lett.* **22**, 117–120.
- Inoue, T., T. Wada, R. Sasaki, and H. Yurimoto (2010). Water partitioning in the Earth's mantle. *Phys. Earth Planet. Inter.* **183**, 245–251.
- Irifune, T. and M. Isshiki (1998). Iron partitioning in a pyrolite mantle and the nature of the 410-km seismic discontinuity. *Nature* **392**, 702–705.
- Irifune, T. and A. E. Ringwood (1987). Phase transformations in primitive MORB and pyrolite compositions to 25 GPa and some geophysical implications. In: *High-Pressure Research in Mineral Physics: A Volume in Honor of Syun-iti Akimoto*. Ed. by M. H. Manghnani and Y. Syono. American Geophysical Union, Washington, DC, 231–242.
- (1993). Phase transformations in subducted oceanic crust and buoyancy relationships at depths of 600–800 km in the mantle. *Earth Planet. Sci. Lett.* **117**, 101–110.
- Irifune, T., T. Sekine, A. E. Ringwood, and W. O. Hibberson (1986). The eclogite-garnetite transformation at high pressure and some geophysical implications. *Earth Planet. Sci. Lett.* **77**, 245–256.
- Irifune, T., T. Shinmei, C. A. McCammon, N. Miyajima, D. C. Rubie, and D. J. Frost (2010). Iron partitioning and density changes of pyrolite in Earth's lower mantle. *Science* **327**, 193–195.
- Ishii, T., R. Huang, H. Fei, I. Koemets, Z. Liu, F. Maeda, L. Yuan, L. Wang, D. Druzhbin, T. Yamamoto, et al. (2018). Complete agreement of the post-spinel transition with the 660-km seismic discontinuity. *Sci. Rep.* **8**, 6358.
- Ita, J. and L. Stixrude (1992). Petrology, elasticity, and composition of the mantle transition zone. *J. Geophys. Res.: Solid Earth* **97**, 6849–6866.
- Ito, E. and E. Takahashi (1989). Postspinel transformations in the system Mg_2SiO_4 - Fe_2SiO_4 and some geophysical implications. *J. Geophys. Res.: Solid Earth* **94**, 10637–10646.
- Jackson, I. (2007). Properties of rocks and minerals – Physical origins of anelasticity and attenuation in rock. In: *Treatise on Geophysics*. Ed. by G. Schubert. Elsevier, Amsterdam, 493–525.

- Jacobsen, S. D. (2006). Effect of water on the equation of state of nominally anhydrous minerals. *Rev. Mineral. Geochem.* **62**, 321–342.
- Jacobsen, S. D., H.-J. Reichmann, H. A. Spetzler, S. J. Mackwell, J. R. Smyth, R. J. Angel, and C. A. McCammon (2002). Structure and elasticity of single-crystal (Mg,Fe)O and a new method of generating shear waves for gigahertz ultrasonic interferometry. *J. Geophys. Res.: Solid Earth* **107**, ECV 4–1–ECV 4–14.
- Jacobsen, S. D., J. R. Smyth, H. Spetzler, C. M. Holl, and D. J. Frost (2004). Sound velocities and elastic constants of iron-bearing hydrous ringwoodite. *Phys. Earth Planet. Inter.* **143–144**, 47–56.
- Jacobsen, S. D., S. Demouchy, D. J. Frost, T. Boffa Ballaran, and J. Kung (2005). A systematic study of OH in hydrous wadsleyite from polarized FTIR spectroscopy and single-crystal X-ray diffraction: Oxygen sites for hydrogen storage in Earth's interior. *Am. Mineral.* **90**, 61–70.
- Jayaraman, A. (1983). Diamond anvil cell and high-pressure physical investigations. *Rev. Mod. Phys.* **55**, 65–108.
- Jiang, F., G. D. Gwanmesia, T. I. Dyuzheva, and T. S. Duffy (2009). Elasticity of stishovite and acoustic mode softening under high pressure by Brillouin scattering. *Phys. Earth Planet. Inter.* **172**, 235–240.
- Johnson, T. E., M. Brown, B. J. P. Kaus, and J. A. VanTongeren (2014). Delamination and recycling of Archaean crust caused by gravitational instabilities. *Nat. Geosci.* **7**, 47–52.
- Johnson, T. E., M. Brown, N. J. Gardiner, C. L. Kirkland, and R. H. Smithies (2017). Earth's first stable continents did not form by subduction. *Nature* **543**, 239–242.
- Kaneshima, S. (2009). Seismic scatterers at the shallowest lower mantle beneath subducted slabs. *Earth Planet. Sci. Lett.* **286**, 304–315.
- Kaneshima, S. and G. Helffrich (1998). Detection of lower mantle scatterers northeast of the Marianna subduction zone using short-period array data. *J. Geophys. Res.: Solid Earth* **103**, 4825–4838.
- (1999). Dipping low-velocity layer in the mid-lower mantle: Evidence for geochemical heterogeneity. *Science* **283**, 1888–1892.
- (2003). Subparallel dipping heterogeneities in the mid-lower mantle. *J. Geophys. Res.: Solid Earth* **108**, 2272.
- (2009). Lower mantle scattering profiles and fabric below Pacific subduction zones. *Earth Planet. Sci. Lett.* **282**, 234–239.
- (2010). Small scale heterogeneity in the mid-lower mantle beneath the circum-Pacific area. *Phys. Earth Planet. Inter.* **183**, 91–103.
- Kantor, I., V. Prakapenka, A. Kantor, P. Dera, A. Kurnosov, S. Sinogeikin, N. Dubrovinskaia, and L. Dubrovinsky (2012). BX90: A new diamond anvil cell design for X-ray diffraction and optical measurements. *Rev. Sci. Instrum.* **83**, 125102.
- Karato, S.-i. (2008). *Deformation of Earth Materials: An Introduction to the Rheology of Solid Earth*. Cambridge University Press, Cambridge, 463 pp.
- (2011). Water distribution across the mantle transition zone and its implications for global material circulation. *Earth Planet. Sci. Lett.* **301**, 413–423.
- Karato, S.-I., M. S. Paterson, and J. D. FitzGerald (1986). Rheology of synthetic olivine aggregates: Influence of grain size and water. *J. Geophys. Res.: Solid Earth* **91**, 8151–8176.
- Karato, S.-I., D. Bercovici, G. Leahy, G. Richard, and Z. Jing (2006). The transition-zone water filter model for global material circulation: where do we stand? In: *Earth's Deep*

- Water Cycle*. Ed. by S. D. Jacobsen and S. van der Lee. American Geophysical Union, Washington, DC, 289–313.
- Karki, B. B., L. Stixrude, and J. Crain (1997a). Ab initio elasticity of three high-pressure polymorphs of silica. *Geophys. Res. Lett.* **24**, 3269–3272.
- Karki, B. B., M. C. Warren, L. Stixrude, G. J. Ackland, and J. Crain (1997b). Ab initio studies of high-pressure structural transformations in silica. *Phys. Rev. B* **55**, 3465–3471.
- Katsura, T. and E. Ito (1989). The system $\text{Mg}_2\text{SiO}_4\text{-Fe}_2\text{SiO}_4$ at high pressures and temperatures: Precise determination of stabilities of olivine, modified spinel, and spinel. *J. Geophys. Res.: Solid Earth* **94**, 15663–15670.
- Katsura, T., A. Yoneda, D. Yamazaki, T. Yoshino, and E. Ito (2010). Adiabatic temperature profile in the mantle. *Phys. Earth Planet. Inter.* **183**, 212–218.
- Kawai, N. and S. Endo (1970). The generation of ultrahigh hydrostatic pressures by a split sphere apparatus. *Rev. Sci. Instrum.* **41**, 1178–1181.
- Kawazoe, T., T. Ohuchi, Y. Nishihara, N. Nishiyama, K. Fujino, and T. Irifune (2013). Seismic anisotropy in the mantle transition zone induced by shear deformation of wadsleyite. *Phys. Earth Planet. Inter.* **216**, 91–98.
- Kawazoe, T., J. Buchen, and H. Marquardt (2015). Synthesis of large wadsleyite single crystals by solid-state recrystallization. *Am. Mineral.* **100**, 2336–2339.
- Kawazoe, T., A. Chaudhari, J. R. Smyth, and C. McCammon (2016). Coupled substitution of Fe^{3+} and H^+ for Si in wadsleyite: A study by polarized infrared and Mössbauer spectroscopies and single-crystal X-ray diffraction. *Am. Mineral.* **101**, 1236–1239.
- Kelbert, A., A. Schultz, and G. Egbert (2009). Global electromagnetic induction constraints on transition-zone water content variations. *Nature* **460**, 1003–1006.
- Kellogg, L. H. and D. L. Turcotte (1990). Mixing and the distribution of heterogeneities in a chaotically convecting mantle. *J. Geophys. Res.: Solid Earth* **95**, 421–432.
- Kennett, B. L. N. and E. R. Engdahl (1991). Traveltimes for global earthquake location and phase identification. *Geophys. J. Int.* **105**, 429–465.
- Kennett, B. L. N., E. R. Engdahl, and R. Buland (1995). Constraints on seismic velocities in the Earth from traveltimes. *Geophys. J. Int.* **122**, 108–124.
- Keppler, H. and D. J. Frost (2005). Introduction to minerals under extreme conditions. In: *Mineral Behaviour at Extreme Conditions*. Ed. by R. Miletich. Vol. 7. European Mineralogical Union Notes in Mineralogy. Eötvös University Press, Budapest, 1–30.
- Keppler, H., I. Kantor, and L. S. Dubrovinsky (2007). Optical absorption spectra of ferropericlase to 84 GPa. *Am. Mineral.* **92**, 433–436.
- Kesson, S. E., J. D. Fitz Gerald, and J. M. G. Shelley (1994). Mineral chemistry and density of subducted basaltic crust at lower-mantle pressures. *Nature* **372**, 767–769.
- King, H. E. and L. W. Finger (1979). Diffracted beam crystal centering and its application to high-pressure crystallography. *J. Appl. Crystallogr.* **12**, 374–378.
- Kingma, K. J., R. E. Cohen, R. J. Hemley, and H.-k. Mao (1995). Transformation of stishovite to a denser phase at lower-mantle pressures. *Nature* **374**, 243.
- Kleppe, A. K., A. P. Jephcoat, H. Olijnyk, A. E. Slesinger, S. C. Kohn, and B. J. Wood (2001). Raman spectroscopic study of hydrous wadsleyite ($\beta\text{-Mg}_2\text{SiO}_4$) to 50 GPa. *Phys. Chem. Miner.* **28**, 232–241.
- Kleppe, A. K., A. P. Jephcoat, and J. R. Smyth (2006). High-pressure Raman spectroscopic study of Fo_{90} hydrous wadsleyite. *Phys. Chem. Miner.* **32**, 700–709.
- Klotz, S., J.-C. Chervin, P. Munsch, and G. Le Marchand (2009). Hydrostatic limits of 11 pressure transmitting media. *J. Phys. D: Appl. Phys.* **42**, 075413.

- Koch, M., A. B. Woodland, and R. J. Angel (2004). Stability of spinelloid phases in the system $\text{Mg}_2\text{SiO}_4\text{--Fe}_2\text{SiO}_4\text{--Fe}_3\text{O}_4$ at 1100 °C and up to 10.5 GPa. *Phys. Earth Planet. Inter.* **143–144**, 171–183.
- Kohlstedt, D. L., H. Keppler, and D. C. Rubie (1996). Solubility of water in the α , β and γ phases of $(\text{Mg,Fe})_2\text{SiO}_4$. *Contrib. Mineral. Petrol.* **123**, 345–357.
- Kohn, S. C., R. A. Brooker, D. J. Frost, A. E. Slesinger, and B. J. Wood (2002). Ordering of hydroxyl defects in hydrous wadsleyite ($\beta\text{-Mg}_2\text{SiO}_4$). *Am. Mineral.* **87**, 293–301.
- Komabayashi, T. (2006). Phase relations of hydrous peridotite: Implications for water circulation in the Earth's mantle. In: *Earth's Deep Water Cycle*. Ed. by S. D. Jacobsen and S. van der Lee. American Geophysical Union, Washington, DC, 29–43.
- Kubo, T., E. Ohtani, and K.-i. Funakoshi (2004). Nucleation and growth kinetics of the α - β transformation in Mg_2SiO_4 determined by in situ synchrotron powder X-ray diffraction. *Am. Mineral.* **89**, 285–293.
- Kudoh, Y. and T. Inoue (1999). Mg-vacant structural modules and dilution of the symmetry of hydrous wadsleyite, $\beta\text{-Mg}_{2-x}\text{SiH}_{2x}\text{O}_4$ with $0.00 \leq x \leq 0.25$. *Phys. Chem. Miner.* **26**, 382–388.
- Kudoh, Y., T. Inoue, and H. Arashi (1996). Structure and crystal chemistry of hydrous wadsleyite, $\text{Mg}_{1.75}\text{SiH}_{0.5}\text{O}_4$: possible hydrous magnesium silicate in the mantle transition zone. *Phys. Chem. Miner.* **23**, 461–469.
- Kudoh, Y., T. Kuribayashi, H. Mizobata, and E. Ohtani (2000). Structure and cation disorder of hydrous ringwoodite, $\gamma\text{-Mg}_{1.89}\text{Si}_{0.98}\text{H}_{0.30}\text{O}_4$. *Phys. Chem. Miner.* **27**, 474–479.
- Kurnosov, A., I. Kantor, T. Boffa-Ballaran, S. Lindhardt, L. Dubrovinsky, A. Kuznetsov, and B. H. Zehnder (2008). A novel gas-loading system for mechanically closing of various types of diamond anvil cells. *Rev. Sci. Instrum.* **79**, 045110.
- Kurnosov, A., H. Marquardt, D. J. Frost, T. Boffa Ballaran, and L. Ziberna (2017). Evidence for a Fe^{3+} -rich pyrolitic lower mantle from (Al,Fe)-bearing bridgmanite elasticity data. *Nature* **543**, 543–546.
- Kuzmany, H. (2009). *Solid-State Spectroscopy*. 2nd edition. Springer, Heidelberg, 554 pp.
- Lakshtanov, D. L., S. V. Sinogeikin, K. D. Litasov, V. B. Prakapenka, H. Hellwig, J. Wang, C. Sanches-Valle, J.-P. Perrillat, B. Chen, M. Somayazulu, et al. (2007). The post-stishovite phase transition in hydrous alumina-bearing SiO_2 in the lower mantle of the earth. *Proc. Natl. Acad. Sci. U. S. A.* **104**, 13588–13590.
- Le Bail, A. (2008). The profile of a Bragg reflection for extracting intensities. In: *Powder Diffraction: Theory and Practice*. Ed. by R. E. Dinnebier and S. J. L. Billinge. Royal Society of Chemistry, Cambridge, 134–165.
- Le Bail, A., H. Duroy, and J. L. Fourquet (1988). Ab-initio structure determination of LiSbWO_6 by X-ray powder diffraction. *Mater. Res. Bull.* **23**, 447–452.
- Li, B. and R. C. Liebermann (2000). Sound velocities of wadsleyite $\beta\text{-(Mg}_{0.88}\text{Fe}_{0.12})_2\text{SiO}_4$ to 10 GPa. *Am. Mineral.* **85**, 292–295.
- Libowitzky, E. (1999). Correlation of O–H stretching frequencies and O–H \cdots O hydrogen bond lengths in minerals. *Monatsh. Chem.* **130**, 1047–1059.
- (2006). The structure of hydrous species in nominally anhydrous minerals: Information from polarized IR spectroscopy. *Rev. Mineral. Geochem.* **62**, 29–52.
- Libowitzky, E. and G. R. Rossman (1996). Principles of quantitative absorbance measurements in anisotropic crystals. *Phys. Chem. Miner.* **23**, 319–327.
- (1997). An IR absorption calibration for water in minerals. *Am. Mineral.* **82**, 1111–1115.
- Liermann, H.-P., Z. Konôpková, W. Morgenroth, K. Glazyrin, J. Bednarčík, E. E. McBride, S. Petitgirard, J. T. Delitz, M. Wendt, Y. Bican, et al. (2015). The Extreme Conditions

- Beamline P02.2 and the Extreme Conditions Science Infrastructure at PETRA III. *J. Synchrotron Radiat.* **22**, 908–924.
- Lindsay, S. M., M. W. Anderson, and J. R. Sandercock (1981). Construction and alignment of a high performance multipass vernier tandem Fabry–Perot interferometer. *Rev. Sci. Instrum.* **52**, 1478–1486.
- Litasov, K. D., E. Ohtani, and A. Sano (2006). Influence of water on major phase transitions in the Earth’s mantle. In: *Earth’s Deep Water Cycle*. Ed. by S. D. Jacobsen and S. van der Lee. American Geophysical Union, Washington, DC, 95–111.
- Litasov, K. D., H. Kagi, A. Shatskiy, E. Ohtani, D. L. Lakshtanov, J. D. Bass, and E. Ito (2007). High hydrogen solubility in Al-rich stishovite and water transport in the lower mantle. *Earth Planet. Sci. Lett.* **262**, 620–634.
- Litasov, K. D., A. Shatskiy, E. Ohtani, and T. Katsura (2011). Systematic study of hydrogen incorporation into Fe-free wadsleyite. *Phys. Chem. Miner.* **38**, 75–84.
- Liu, L.-g., T. P. Mernagh, C.-C. Lin, J.-a. Xu, and T. Inoue (1998). Raman spectra of hydrous β - Mg_2SiO_4 at various pressures and temperatures. In: *Properties of Earth and Planetary Materials at High Pressure and Temperature*. Ed. by M. H. Manghnani and T. Yagi. American Geophysical Union, Washington, DC, 523–530.
- Liu, W., J. Kung, B. Li, N. Nishiyama, and Y. Wang (2009). Elasticity of $(\text{Mg}_{0.87}\text{Fe}_{0.13})_2\text{SiO}_4$ wadsleyite to 12 GPa and 1073 K. *Phys. Earth Planet. Inter.* **174**, 98–104.
- Liu, X., N. Nishiyama, T. Sanehira, T. Inoue, Y. Higo, and S. Sakamoto (2006). Decomposition of kyanite and solubility of Al_2O_3 in stishovite at high pressure and high temperature conditions. *Phys. Chem. Miner.* **33**, 711–721.
- Long, M. D. (2013). Constraints on subduction geodynamics from seismic anisotropy: Subduction zone anisotropy. *Rev. Geophys.* **51**, 76–112.
- Long, M. D., X. Xiao, Z. Jiang, B. Evans, and S.-i. Karato (2006). Lattice preferred orientation in deformed polycrystalline $(\text{Mg,Fe})\text{O}$ and implications for seismic anisotropy in D'' . *Phys. Earth Planet. Inter.* **156**, 75–88.
- Longo, M., C. A. McCammon, and S. D. Jacobsen (2011). Microanalysis of the iron oxidation state in $(\text{Mg,Fe})\text{O}$ and application to the study of microscale processes. *Contrib. Mineral. Petrol.* **162**, 1249–1257.
- Lutterotti, L., M. Bortolotti, G. Ischia, I. Lonardelli, and H. R. Wenk (2007). Rietveld texture analysis from diffraction images. *Z. Kristallogr. Suppl.* **26**, 125–130.
- Lutterotti, L., R. Vasin, and H.-R. Wenk (2014). Rietveld texture analysis from synchrotron diffraction images. I. Calibration and basic analysis. *Powder Diffr.* **29**, 76–84.
- Mackwell, S., M. Bystricky, and C. Sproni (2005). Fe–Mg interdiffusion in $(\text{Mg,Fe})\text{O}$. *Phys. Chem. Miner.* **32**, 418–425.
- Mainprice, D. (2015). Seismic anisotropy of the deep Earth from a mineral and rock physics perspective. In: *Treatise on Geophysics*. Ed. by G. Schubert. 2nd edition. Vol. 2. Elsevier, Amsterdam, 487–538.
- Mainprice, D., G. Barruol, and W. Ben Ismail (2000). The seismic anisotropy of the Earth’s mantle: from single crystal to polycrystal. In: *Earth’s Deep Interior: Mineral Physics and Tomography From the Atomic to the Global Scale*. Ed. by S.-I. Karato, A. Forte, R. Liebermann, G. Masters, and L. Stixrude. American Geophysical Union, Washington, DC, 237–264.
- Manthilake, M. A. G. M., T. Matsuzaki, T. Yoshino, S. Yamashita, E. Ito, and T. Katsura (2009). Electrical conductivity of wadsleyite as a function of temperature and water content. *Phys. Earth Planet. Inter.* **174**, 10–18.

- Mao, H.-k. and R. J. Hemley (1996). Experimental studies of Earth's deep interior: accuracy and versatility of diamond-anvil cells. *Philos. Trans. R. Soc., A* **354**, 1315–1332.
- Mao, H. K., J. Xu, and P. M. Bell (1986). Calibration of the ruby pressure gauge to 800 kbar under quasi-hydrostatic conditions. *J. Geophys. Res.: Solid Earth* **91**, 4673–4676.
- Mao, H. K., J. Xu, V. V. Struzhkin, J. Shu, R. J. Hemley, W. Sturhahn, M. Y. Hu, E. E. Alp, L. Vocadlo, D. Alfè, et al. (2001). Phonon density of states of iron up to 153 gigapascals. *Science* **292**, 914–916.
- Mao, Z., S. D. Jacobsen, F. Jiang, J. R. Smyth, C. M. Holl, and T. S. Duffy (2008a). Elasticity of hydrous wadsleyite to 12 GPa: Implications for Earth's transition zone. *Geophys. Res. Lett.* **35**, L21305.
- Mao, Z., S. D. Jacobsen, F. M. Jiang, J. R. Smyth, C. M. Holl, D. J. Frost, and T. S. Duffy (2008b). Single-crystal elasticity of wadsleyites, β -Mg₂SiO₄, containing 0.37–1.66 wt.% H₂O. *Earth Planet. Sci. Lett.* **268**, 540–549.
- Mao, Z., S. D. Jacobsen, F. Jiang, J. R. Smyth, C. M. Holl, D. J. Frost, and T. S. Duffy (2010). Velocity crossover between hydrous and anhydrous forsterite at high pressures. *Earth Planet. Sci. Lett.* **293**, 250–258.
- Mao, Z., S. D. Jacobsen, D. J. Frost, C. A. McCammon, E. H. Hauri, and T. S. Duffy (2011). Effect of hydration on the single-crystal elasticity of Fe-bearing wadsleyite to 12 GPa. *Am. Mineral.* **96**, 1606–1612.
- Mao, Z., J.-F. Lin, S. D. Jacobsen, T. S. Duffy, Y.-Y. Chang, J. R. Smyth, D. J. Frost, E. H. Hauri, and V. B. Prakapenka (2012). Sound velocities of hydrous ringwoodite to 16 GPa and 673 K. *Earth Planet. Sci. Lett.* **331–332**, 112–119.
- Mao, Z., D. Fan, J.-F. Lin, J. Yang, S. N. Tkachev, K. Zhuravlev, and V. B. Prakapenka (2015). Elasticity of single-crystal olivine at high pressures and temperatures. *Earth Planet. Sci. Lett.* **426**, 204–215.
- Marquardt, H. and K. Marquardt (2012). Focused ion beam preparation and characterization of single-crystal samples for high-pressure experiments in the diamond-anvil cell. *Am. Mineral.* **97**, 299–304.
- Marquardt, H., S. Speziale, H. J. Reichmann, D. J. Frost, and F. R. Schilling (2009b). Single-crystal elasticity of (Mg_{0.9}Fe_{0.1})O to 81 GPa. *Earth Planet. Sci. Lett.* **287**, 345–352.
- Marquardt, H., S. Speziale, H. J. Reichmann, D. J. Frost, F. R. Schilling, and E. J. Garnero (2009a). Elastic shear anisotropy of ferropericlase in Earth's lower mantle. *Science* **324**, 224–226.
- Marquardt, H., A. Gleason, K. Marquardt, S. Speziale, L. Miyagi, G. Neusser, H.-R. Wenk, and R. Jeanloz (2011). Elastic properties of MgO nanocrystals and grain boundaries at high pressures by Brillouin scattering. *Phys. Rev. B* **84**, 064131.
- Marquardt, H., J. Buchen, A. S. J. Mendez, A. Kurnosov, M. Wendt, A. Rothkirch, D. Pennicard, and H.-P. Liermann (2018). Elastic softening of (Mg_{0.8}Fe_{0.2})O ferropericlase across the iron spin crossover measured at seismic frequencies. *Geophys. Res. Lett.* **45**, 6862–6868.
- Massa, W. (2011). Kristallstrukturbestimmung. 7th edition. Vieweg & Teubner, Wiesbaden, 269 pp. (in German).
- Matsuzaka, K., M. Akaogi, T. Suzuki, and T. Suda (2000). Mg-Fe partitioning between silicate spinel and magnesiowüstite at high pressure: experimental determination and calculation of phase relations in the system Mg₂SiO₄-Fe₂SiO₄. *Phys. Chem. Miner.* **27**, 310–319.
- McCammon, C., J. Peyronneau, and J.-P. Poirier (1998). Low ferric iron content of (Mg,Fe)O at high pressures and temperatures. *Geophys. Res. Lett.* **25**, 1589–1592.

- McDonough, W. F. and S.-s. Sun (1995). The composition of the Earth. *Chem. Geol.* **120**, 223–253.
- McMillan, P. F. and A. M. Hofmeister (1988). Infrared and Raman spectroscopy. *Rev. Mineral.* **18**, 99–159.
- McMillan, P. F., M. Akaogi, R. K. Sato, B. Poe, and J. Foley (1991). Hydroxyl groups in β - Mg_2SiO_4 . *Am. Mineral.* **76**, 354–360.
- Mei, S. and D. L. Kohlstedt (2000). Influence of water on plastic deformation of olivine aggregates: 1. Diffusion creep regime. *J. Geophys. Res.: Solid Earth* **105**, 21457–21469.
- Meier, U., J. Trampert, and A. Curtis (2009). Global variations of temperature and water content in the mantle transition zone from higher mode surface waves. *Earth Planet. Sci. Lett.* **282**, 91–101.
- Melbourne, T. and D. Helmberger (1998). Fine structure of the 410-km discontinuity. *J. Geophys. Res.: Solid Earth* **103**, 10091–10102.
- Meng, Y., D. J. Weidner, and Y. Fei (1993). Deviatoric stress in a quasi-hydrostatic diamond anvil cell: Effect on the volume-based pressure calibration. *Geophys. Res. Lett.* **20**, 1147–1150.
- Merlini, M. and M. Hanfland (2013). Single-crystal diffraction at megabar conditions by synchrotron radiation. *High Pressure Res.* **33**, 511–522.
- Mével, C. (2003). Serpentinization of abyssal peridotites at mid-ocean ridges. *C. R. Geosci.* **335**, 825–852.
- Miletich, R., D. R. Allan, and W. F. Kuhs (2000). High-pressure single-crystal techniques. *Rev. Mineral. Geochem.* **41**, 445–519.
- Miletich, R., C. Hejny, G. Krauss, and A. Ullrich (2005). Diffraction techniques: Shedding light on structural changes at extreme conditions. In: *Mineral Behaviour at Extreme Conditions*. Ed. by R. Miletich. Vol. 7. European Mineralogical Union Notes in Mineralogy. Eötvös University Press, Budapest, 281–338.
- Mitrovica, J. X. and A. M. Forte (2004). A new inference of mantle viscosity based upon joint inversion of convection and glacial isostatic adjustment data. *Earth Planet. Sci. Lett.* **225**, 177–189.
- Montagner, J.-P. and B. L. N. Kennett (1996). How to reconcile body-wave and normal-mode reference earth models. *Geophys. J. Int.* **125**, 229–248.
- Moore, P. B. and J. V. Smith (1970). Crystal structure of β - Mg_2SiO_4 : crystal-chemical and geophysical implications. *Phys. Earth Planet. Inter.* **3**, 166–177.
- Morimoto, N., S. Akimoto, K. Koto, and M. Tokonami (1970). Crystal structures of high pressure modifications of Mn_2GeO_4 and Co_2SiO_4 . *Phys. Earth Planet. Inter.* **3**, 161–165.
- Murakami, M., K. Hirose, S. Ono, and Y. Ohishi (2003). Stability of CaCl_2 -type and α - PbO_2 -type SiO_2 at high pressure and temperature determined by in-situ X-ray measurements. *Geophys. Res. Lett.* **30**, 1207.
- Murakami, M., K. Hirose, N. Sata, and Y. Ohishi (2005). Post-perovskite phase transition and mineral chemistry in the pyrolitic lowermost mantle. *Geophys. Res. Lett.* **32**, L03304.
- Nakagawa, T. and B. A. Buffett (2005). Mass transport mechanism between the upper and lower mantle in numerical simulations of thermochemical mantle convection with multicomponent phase changes. *Earth Planet. Sci. Lett.* **230**, 11–27.
- Nakamoto, K., M. Margoshes, and R. E. Rundle (1955). Stretching frequencies as a function of distances in hydrogen bonds. *J. Am. Chem. Soc.* **77**, 6480–6486.
- Nelson, D. F. and M. Lax (1971). Theory of the photoelastic interaction. *Phys. Rev. B* **3**, 2778–2794.

- Nishi, M., T. Irifune, J. Tsuchiya, Y. Tange, Y. Nishihara, K. Fujino, and Y. Higo (2014). Stability of hydrous silicate at high pressures and water transport to the deep lower mantle. *Nat. Geosci.* **7**, 224–227.
- Nishihara, Y., T. Shinmei, and S.-i. Karato (2006). Grain-growth kinetics in wadsleyite: Effects of chemical environment. *Phys. Earth Planet. Inter.* **154**, 30–43.
- Nishiyama, N., S. Seike, T. Hamaguchi, T. Irifune, M. Matsushita, M. Takahashi, H. Ohfuji, and Y. Kono (2012). Synthesis of nanocrystalline bulk SiO₂ stishovite with very high toughness. *Scr. Mater.* **67**, 955–958.
- Nishiyama, N., F. Wakai, H. Ohfuji, Y. Tamenori, H. Murata, T. Taniguchi, M. Matsushita, M. Takahashi, E. Kulik, K. Yoshida, et al. (2014). Fracture-induced amorphization of polycrystalline SiO₂ stishovite: a potential platform for toughening in ceramics. *Sci. Rep.* **4**, 6558.
- Nisr, C., K. Leinenweber, V. Prakapenka, C. Prescher, S. Tkachev, and S.-H. D. Shim (2017). Phase transition and equation of state of dense hydrous silica up to 63 GPa. *J. Geophys. Res.: Solid Earth* **122**, 6972–6983.
- Niu, F., H. Kawakatsu, and Y. Fukao (2003). Seismic evidence for a chemical heterogeneity in the midmantle: A strong and slightly dipping seismic reflector beneath the Mariana subduction zone. *J. Geophys. Res.: Solid Earth* **108**, 2419.
- Nomura, R., K. Hirose, N. Sata, and Y. Ohishi (2010). Precise determination of post-stishovite phase transition boundary and implications for seismic heterogeneities in the mid-lower mantle. *Phys. Earth Planet. Inter.* **183**, 104–109.
- Norby, P. and U. Schwarz (2008). Powder diffraction under non-ambient conditions. In: *Powder Diffraction: Theory and Practice*. Ed. by R. E. Dinnebier and S. J. L. Billinge. Royal Society of Chemistry, Cambridge, 439–463.
- Nye, J. F. (1985). *Physical Properties of Crystals: Their Representation by Tensors and Matrices*. Oxford University Press, Oxford, 329 pp.
- Ohira, I., E. Ohtani, T. Sakai, M. Miyahara, N. Hirao, Y. Ohishi, and M. Nishijima (2014). Stability of a hydrous δ -phase, AlOOH–MgSiO₂(OH)₂, and a mechanism for water transport into the base of lower mantle. *Earth Planet. Sci. Lett.* **401**, 12–17.
- Ohtani, E., K. Litasov, T. Hosoya, T. Kubo, and T. Kondo (2004). Water transport into the deep mantle and formation of a hydrous transition zone. *Phys. Earth Planet. Inter. New Developments in High-Pressure Mineral Physics and Applications to the Earth's Interior* **143–144**, 255–269.
- Ohuchi, T., K. Fujino, T. Kawazoe, and T. Irifune (2014). Crystallographic preferred orientation of wadsleyite and ringwoodite: Effects of phase transformation and water on seismic anisotropy in the mantle transition zone. *Earth Planet. Sci. Lett.* **397**, 133–144.
- Ojha, L., M. B. Wilhelm, S. L. Murchie, A. S. McEwen, J. J. Wray, J. Hanley, M. Massé, and M. Chojnacki (2015). Spectral evidence for hydrated salts in recurring slope lineae on Mars. *Nat. Geosci.* **8**, 829–832.
- O'Neill, H. St. C. (1987). Quartz-fayalite-iron and quartz-fayalite-magnetite equilibria and the free energy of formation of fayalite (Fe₂SiO₄) and magnetite (Fe₃O₄). *Am. Mineral.* **72**, 67–75.
- O'Neill, H. St. C. and M. I. Pownceby (1993). Thermodynamic data from redox reactions at high temperatures. I. An experimental and theoretical assessment of the electrochemical method using stabilized zirconia electrolytes, with revised values for the Fe–“FeO”, Co–CoO, Ni–NiO and Cu–Cu₂O oxygen buffers, and new data for the W–WO₂ buffer. *Contrib. Mineral. Petrol.* **114**, 296–314.

- Ono, S. (1998). Stability limits of hydrous minerals in sediment and mid-ocean ridge basalt compositions: Implications for water transport in subduction zones. *J. Geophys. Res.: Solid Earth* **103**, 18253–18267.
- (1999). High temperature stability limit of phase egg, $\text{AlSiO}_3(\text{OH})$. *Contrib. Mineral. Petrol.* **137**, 83–89.
- Ono, S., E. Ito, and T. Katsura (2001). Mineralogy of subducted basaltic crust (MORB) from 25 to 37 GPa, and chemical heterogeneity of the lower mantle. *Earth Planet. Sci. Lett.* **190**, 57–63.
- Orosei, R., S. E. Lauro, E. Pettinelli, A. Cichetti, M. Coradini, B. Cosciotti, F. Di Paolo, E. Flamini, E. Mattei, M. Pajola, et al. (2018). Radar evidence of subglacial liquid water on Mars. *Science* **361**, 490–493.
- Otsuka, K., C. A. McCammon, and S.-i. Karato (2010). Tetrahedral occupancy of ferric iron in $(\text{Mg,Fe})\text{O}$: Implications for point defects in the Earth's lower mantle. *Phys. Earth Planet. Inter.* **180**, 179–188.
- Otsuka, K., M. Longo, C. A. McCammon, and S.-i. Karato (2013). Ferric iron content of ferropicrinite as a function of composition, oxygen fugacity, temperature and pressure: Implications for redox conditions during diamond formation in the lower mantle. *Earth Planet. Sci. Lett.* **365**, 7–16.
- Pamato, M. G., R. Myhill, T. Boffa Ballaran, D. J. Frost, F. Heidelbach, and N. Miyajima (2015). Lower-mantle water reservoir implied by the extreme stability of a hydrous aluminosilicate. *Nat. Geosci.* **8**, 75–79.
- Panero, W. R. and L. P. Stixrude (2004). Hydrogen incorporation in stishovite at high pressure and symmetric hydrogen bonding in $\delta\text{-AlOOH}$. *Earth Planet. Sci. Lett.* **221**, 421–431.
- Panero, W. R., L. R. Benedetti, and R. Jeanloz (2003). Transport of water into the lower mantle: Role of stishovite. *J. Geophys. Res.: Solid Earth* **108**, 2039.
- Panning, M. and B. Romanowicz (2006). A three-dimensional radially anisotropic model of shear velocity in the whole mantle. *Geophys. J. Int.* **167**, 361–379.
- Parker, J. H., D. W. Feldman, and M. Ashkin (1967). Raman scattering by silicon and germanium. *Phys. Rev.* **155**, 712–714.
- Paterson, M. S. (1982). The determination of hydroxyl by infrared absorption in quartz, silicate glasses and similar materials. *Bull. Mineral.* **105**, 20–29.
- Pawley, A. R. and J. R. Holloway (1993). Water sources for subduction zone volcanism: new experimental constraints. *Science* **260**, 664–667.
- Pawley, A. R., P. F. McMillan, and J. R. Holloway (1993). Hydrogen in stishovite, with implications for mantle water content. *Science* **261**, 1024–1026.
- Pearson, D. G., F. E. Brenker, F. Nestola, J. McNeill, L. Nasdala, M. T. Hutchison, S. Matveev, K. Mather, G. Silversmit, S. Schmitz, et al. (2014). Hydrous mantle transition zone indicated by ringwoodite included within diamond. *Nature* **507**, 221–224.
- Peltier, W. R. (1998). Postglacial variations in the level of the sea: Implications for climate dynamics and solid-Earth geophysics. *Rev. Geophys.* **36**, 603–689.
- Perrillat, J.-P., A. Ricolleau, I. Daniel, G. Fiquet, M. Mezouar, N. Guignot, and H. Cardon (2006). Phase transformations of subducted basaltic crust in the uppermost lower mantle. *Phys. Earth Planet. Inter.* **157**, 139–149.
- Philpotts, A. and J. Ague (2009). Principles of Igneous and Metamorphic Petrology. 2nd edition. Cambridge University Press, Cambridge, 667 pp.
- Poirier, J.-P. (2000). Introduction to the Physics of the Earth's Interior. 2nd edition. Cambridge University Press, Cambridge, 312 pp.

- Poli, S. and M. W. Schmidt (1995). H₂O transport and release in subduction zones: Experimental constraints on basaltic and andesitic systems. *J. Geophys. Res.: Solid Earth* **100**, 22299–22314.
- (2002). Petrology of subducted slabs. *Annu. Rev. Earth Planet. Sci.* **30**, 207–235.
- Prescher, C. and V. B. Prakapenka (2015). *DIOPTAS*: a program for reduction of two-dimensional X-ray diffraction data and data exploration. *High Pressure Res.* **35**, 223–230.
- Rapp, R. P. and E. B. Watson (1995). Dehydration melting of metabasalt at 8–32 kbar: Implications for continental growth and crust-mantle recycling. *J. Petrol.* **36**, 891–931.
- Rekhi, S., L. Dubrovinsky, and S. K. Saxena (1999). Temperature-induced ruby fluorescence shifts up to a pressure of 15 GPa in an externally heated diamond anvil cell. *High Temp. - High Pressures* **31**, 299–305.
- Reuss, A. (1929). Berechnung der Fließgrenze von Mischkristallen auf Grund der Plastizitätsbedingung für Einkristalle. *Z. Angew. Math. Mech.* **9**, 49–58 (in German).
- Revenaugh, J. and T. H. Jordan (1991). Mantle layering from ScS reverberations: 2. The transition zone. *J. Geophys. Res.: Solid Earth* **96**, 19763–19780.
- Revenaugh, J. and S. A. Sipkin (1994). Seismic evidence for silicate melt atop the 410-km mantle discontinuity. *Nature* **369**, 474–476.
- Ricolleau, A., J.-P. Perrillat, G. Fiquet, I. Daniel, J. Matas, A. Addad, N. Menguy, H. Cardon, M. Mezouar, and N. Guignot (2010). Phase relations and equation of state of a natural MORB: Implications for the density profile of subducted oceanic crust in the Earth's lower mantle. *J. Geophys. Res.: Solid Earth* **115**, B08202.
- Ringwood, A. E. (1991). Phase transformations and their bearing on the constitution and dynamics of the mantle. *Geochim. Cosmochim. Acta* **55**, 2083–2110.
- Ringwood, A. E. and A. Major (1966). Synthesis of Mg₂SiO₄-Fe₂SiO₄ spinel solid solutions. *Earth Planet. Sci. Lett.* **1**, 241–245.
- (1970). The system Mg₂SiO₄-Fe₂SiO₄ at high pressures and temperatures. *Phys. Earth Planet. Inter.* **3**, 89–108.
- Ritsema, J., A. Deuss, H. J. van Heijst, and J. H. Woodhouse (2011). S40RTS: a degree-40 shear-velocity model for the mantle from new Rayleigh wave dispersion, teleseismic traveltimes and normal-mode splitting function measurements. *Geophys. J. Int.* **184**, 1223–1236.
- Romanowicz, B. (2003). Global mantle tomography: Progress status in the past 10 years. *Annu. Rev. Earth Planet. Sci.* **31**, 303–328.
- Ross, N. L., J. Shu, and R. M. Hazen (1990). High-pressure crystal chemistry of stishovite. *Am. Mineral.* **75**, 739–747.
- Rossmann, G. R. (1988). Vibrational spectroscopy of hydrous components. *Rev. Mineral.* **18**, 193–206.
- (2006). Analytical methods for measuring water in nominally anhydrous minerals. *Rev. Mineral. Geochem.* **62**, 1–28.
- Rost, S. and M. Weber (2002). The upper mantle transition zone discontinuities in the Pacific as determined by short-period array data. *Earth Planet. Sci. Lett.* **204**, 347–361.
- Russell, J. P. (1965). Raman scattering in silicon. *Appl. Phys. Lett.* **6**, 223–224.
- Saki, M., C. Thomas, S. E. J. Nippres, and S. Lessing (2015). Topography of upper mantle seismic discontinuities beneath the North Atlantic: The Azores, Canary and Cape Verde plumes. *Earth Planet. Sci. Lett.* **409**, 193–202.

- Sanchez-Valle, C., I. Daniel, B. Reynard, R. Abraham, and C. Goutaudier (2002). Optimization of Sm^{3+} fluorescence in Sm-doped yttrium aluminum garnet: Application to pressure calibration in diamond-anvil cell at high temperature. *J. Appl. Phys.* **92**, 4349–4353.
- Sano-Furukawa, A., T. Kuribayashi, K. Komatsu, T. Yagi, and E. Ohtani (2011). Investigation of hydrogen sites of wadsleyite: A neutron diffraction study. *Phys. Earth Planet. Inter.* **189**, 56–62.
- Sawamoto, H. (1986). Single crystal growth of the modified spinel (β) and Spinel (γ) phases of $(\text{Mg,Fe})_2\text{SiO}_4$ and some geophysical implications. *Phys. Chem. Miner.* **13**, 1–10.
- Sawamoto, H. and H. Horiuchi (1990). β $(\text{Mg}_{0.9}, \text{Fe}_{0.1})_2\text{SiO}_4$: Single crystal structure, cation distribution, and properties of coordination polyhedra. *Phys. Chem. Miner.* **17**, 293–300.
- Sawamoto, H., D. J. Weidner, S. Sasaki, and M. Kumazawa (1984). Single-crystal elastic properties of the modified spinel (beta) phase of magnesium orthosilicate. *Science* **224**, 749–751.
- Schmerr, N. (2015). Imaging mantle heterogeneity with upper mantle seismic discontinuities. In: *The Earth's Heterogeneous Mantle*. Ed. by A. Khan and F. Deschamps. Springer, Cham, 79–104.
- Schmerr, N. and E. J. Garnero (2007). Upper mantle discontinuity topography from thermal and chemical heterogeneity. *Science* **318**, 623–626.
- Schmidt, M. W. and S. Poli (1998). Experimentally based water budgets for dehydrating slabs and consequences for arc magma generation. *Earth Planet. Sci. Lett.* **163**, 361–379.
- Schreuer, J. and S. Haussühl (2005). Elastic and piezoelectric properties of minerals I. Principles and experimental approaches. In: *Mineral Behaviour at Extreme Conditions*. Ed. by R. Miletich. Vol. 7. European Mineralogical Union Notes in Mineralogy. Eötvös University Press, Budapest, 95–116.
- Schulze, K., J. Buchen, K. Marquardt, and H. Marquardt (2017). Multi-sample loading technique for comparative physical property measurements in the diamond-anvil cell. *High Pressure Res.* **37**, 159–169.
- Schulze, K., H. Marquardt, T. Kawazoe, T. Boffa Ballaran, C. McCammon, M. Koch-Müller, A. Kurnosov, and K. Marquardt (2018). Seismically invisible water in Earth's transition zone? *Earth Planet. Sci. Lett.* **498**, 9–16.
- Shatskiy, A., K. D. Litasov, T. Matsuzaki, K. Shinoda, D. Yamazaki, A. Yoneda, E. Ito, and T. Katsura (2009). Single crystal growth of wadsleyite. *Am. Mineral.* **94**, 1130–1136.
- Shearer, P. M. and M. P. Flanagan (1999). Seismic velocity and density jumps across the 410- and 660-kilometer discontinuities. *Science* **285**, 1545–1548.
- Shieh, S. R., T. S. Duffy, and B. Li (2002). Strength and elasticity of SiO_2 across the stishovite– CaCl_2 -type structural phase boundary. *Phys. Rev. Lett.* **89**, 255507.
- Shim, S.-H., T. S. Duffy, and G. Shen (2001). The post-spinel transformation in Mg_2SiO_4 and its relation to the 660-km seismic discontinuity. *Nature* **411**, 571–574.
- Sinclair, W. and A. E. Ringwood (1978). Single crystal analysis of the structure of stishovite. *Nature* **272**, 714–715.
- Singh, A. K., D. Andrault, and P. Bouvier (2012). X-ray diffraction from stishovite under nonhydrostatic compression to 70 GPa: Strength and elasticity across the tetragonal \rightarrow orthorhombic transition. *Phys. Earth Planet. Inter.* **208**, 1–10.
- Sinmyo, R. and K. Hirose (2013). Iron partitioning in pyrolytic lower mantle. *Phys. Chem. Miner.* **40**, 107–113.
- Sinogeikin, S. V. and J. D. Bass (2000). Single-crystal elasticity of pyrope and MgO to 20 GPa by Brillouin scattering in the diamond cell. *Phys. Earth Planet. Inter.* **120**, 43–62.

- Sinogeikin, S. V., T. Katsura, and J. D. Bass (1998). Sound velocities and elastic properties of Fe-bearing wadsleyite and ringwoodite. *J. Geophys. Res.: Solid Earth* **103**, 20819–20825.
- Smyth, J. R. (1987). β -Mg₂SiO₄: A potential host for water in the mantle? *Am. Mineral.* **72**, 1051–1055.
- (1994). A crystallographic model for hydrous wadsleyite (β -Mg₂SiO₄): An ocean in the Earth's interior? *Am. Mineral.* **79**, 1021–1024.
- Smyth, J. R. and D. J. Frost (2002). The effect of water on the 410-km discontinuity: An experimental study. *Geophys. Res. Lett.* **29**, 123.
- Smyth, J. R. and S. D. Jacobsen (2006). Nominally anhydrous minerals and Earth's deep water cycle. In: *Earth's Deep Water Cycle*. Ed. by S. D. Jacobsen and S. van der Lee. American Geophysical Union, Washington, DC, 1–11.
- Smyth, J. R., R. J. Swope, and A. R. Pawley (1995). H in rutile-type Compounds: II. Crystal chemistry of Al substitution in H-bearing stishovite. *Am. Mineral.* **80**, 454–456.
- Smyth, J. R., T. Kawamoto, S. D. Jacobsen, R. J. Swope, R. L. Hervig, and J. R. Holloway (1997). Crystal structure of monoclinic hydrous wadsleyite [β -(Mg,Fe)₂SiO₄]. *Am. Mineral.* **82**, 270–275.
- Smyth, J. R., N. Bolfan-Casanova, D. Avignant, M. El-Ghozzi, and S. M. Hirner (2014). Tetrahedral ferric iron in oxidized hydrous wadsleyite. *Am. Mineral.* **99**, 458–466.
- Soldati, G., L. Boschi, F. Deschamps, and D. Giardini (2009). Inferring radial models of mantle viscosity from gravity (GRACE) data and an evolutionary algorithm. *Phys. Earth Planet. Inter.* **176**, 19–32.
- Spektor, K., J. Nylén, E. Stoyanov, A. Navrotsky, R. L. Hervig, K. Leinenweber, G. P. Holland, and U. Häussermann (2011). Ultrahydrous stishovite from high-pressure hydrothermal treatment of SiO₂. *Proc. Natl. Acad. Sci. U. S. A.* **108**, 20918–20922.
- Spektor, K., J. Nylén, R. Mathew, M. Edén, E. Stoyanov, A. Navrotsky, K. Leinenweber, and U. Häussermann (2016). Formation of hydrous stishovite from coesite in high-pressure hydrothermal environments. *Am. Mineral.* **101**, 2514–2524.
- Spetzler, H. (1970). Equation of state of polycrystalline and single-crystal MgO to 8 kilobars and 800°K. *J. Geophys. Res.* **75**, 2073–2087.
- Spetzler, H., A. Shen, G. Chen, G. Herrmannsdoerfer, H. Schulze, and R. Weigel (1996). Ultrasonic measurements in a diamond anvil cell. *Phys. Earth Planet. Inter.* **98**, 93–99.
- Speziale, S. and T. S. Duffy (2002). Single-crystal elastic constants of fluorite (CaF₂) to 9.3 GPa. *Phys. Chem. Miner.* **29**, 465–472.
- Speziale, S., H. Marquardt, and T. S. Duffy (2014). Brillouin scattering and its application in geosciences. *Rev. Mineral. Geochem.* **78**, 543–603.
- Staudigel, H. (2003). Hydrothermal alteration processes in the oceanic crust. In: *Treatise on Geochemistry*. Ed. by H. D. Holland and K. K. Turekian. Pergamon, Oxford, 511–535.
- Stebbins, J. F., J. R. Smyth, W. R. Panero, and D. J. Frost (2009). Forsterite, hydrous and anhydrous wadsleyite and ringwoodite (Mg₂SiO₄): ²⁹Si NMR results for chemical shift anisotropy, spin-lattice relaxation, and mechanism of hydration. *Am. Mineral.* **94**, 905–915.
- Stein, S. and M. Wysession (2003). *An Introduction to Seismology, Earthquakes, and Earth Structure*. Blackwell Publishing, Oxford, 498 pp.
- Stern, R. J. (2008). Modern-style plate tectonics began in Neoproterozoic time: An alternative interpretation of Earth's tectonic history. In: *When Did Plate Tectonics Begin on Planet Earth?* Ed. by K. C. Condie and V. Pease. Geological Society of America, Boulder, CO, 265–280.

- Stishov, S. M. and N. V. Belov (1962). Crystalline structure of the new close-grained modification of silica, SiO₂. *Dokl. Akad. Nauk SSSR* **143**, 951–954 (in Russian).
- Stixrude, L. and C. Lithgow-Bertelloni (2005). Thermodynamics of mantle minerals – I. Physical properties. *Geophys. J. Int.* **162**, 610–632.
- (2011). Thermodynamics of mantle minerals – II. Phase equilibria. *Geophys. J. Int.* **184**, 1180–1213.
- Suetsugu, D., T. Inoue, A. Yamada, D. Zhao, and M. Obayashi (2006). Towards mapping the three-dimensional distribution of water in the transition zone from P-velocity tomography and 660-km discontinuity depths. In: *Earth's Deep Water Cycle*. Ed. by S. D. Jacobsen and S. van der Lee. American Geophysical Union, Washington, DC, 237–249.
- Tackley, P. J. (2000). Mantle convection and plate tectonics: toward an integrated physical and chemical theory. *Science* **288**, 2002–2007.
- Tauzin, B., R. D. van der Hilst, G. Wittlinger, and Y. Ricard (2013). Multiple transition zone seismic discontinuities and low velocity layers below western United States. *J. Geophys. Res.: Solid Earth* **118**, 2307–2322.
- Thio, V., L. Cobden, and J. Trampert (2016). Seismic signature of a hydrous mantle transition zone. *Phys. Earth Planet. Inter.* **250**, 46–63.
- Thomsen, L. (1972). Elasticity of polycrystals and rocks. *J. Geophys. Res.* **77**, 315–327.
- Tommasi, A., D. Mainprice, P. Cordier, C. Thoraval, and H. Couvy (2004). Strain-induced seismic anisotropy of wadsleyite polycrystals and flow patterns in the mantle transition zone. *J. Geophys. Res.: Solid Earth* **109**, B12405.
- Trampert, J. and H. J. van Heijst (2002). Global azimuthal anisotropy in the transition zone. *Science* **296**, 1297–1299.
- Trots, D. M., A. Kurnosov, T. Boffa Ballaran, S. Tkachev, K. Zhuravlev, V. Prakapenka, M. Berkowski, and D. J. Frost (2013). The Sm:YAG primary fluorescence pressure scale. *J. Geophys. Res.: Solid Earth* **118**, 5805–5813.
- Tschauner, O., S. Huang, E. Greenberg, V. B. Prakapenka, C. Ma, G. R. Rossman, A. H. Shen, D. Zhang, M. Newville, A. Lanzirrotti, et al. (2018). Ice-VII inclusions in diamonds: Evidence for aqueous fluid in Earth's deep mantle. *Science* **359**, 1136–1139.
- Tsuchiya, J. and T. Tsuchiya (2009). First principles investigation of the structural and elastic properties of hydrous wadsleyite under pressure. *J. Geophys. Res.: Solid Earth* **114**, B02206.
- Tsuchiya, T. (2011). Elasticity of subducted basaltic crust at the lower mantle pressures: Insights on the nature of deep mantle heterogeneity. *Phys. Earth Planet. Inter.* **188**, 142–149.
- Tsuchiya, T., R. Caracas, and J. Tsuchiya (2004). First principles determination of the phase boundaries of high-pressure polymorphs of silica. *Geophys. Res. Lett.* **31**, L11610.
- Utada, H., T. Koyama, H. Shimizu, and A. D. Chave (2003). A semi-global reference model for electrical conductivity in the mid-mantle beneath the north Pacific region. *Geophys. Res. Lett.* **30**, 1194.
- van Hunen, Jeroen and Jean-François Moyen (2012). Archean subduction: Fact or fiction? *Annu. Rev. Earth Planet. Sci.* **40**, 195–219.
- van Keken, P. E., E. H. Hauri, and C. J. Ballentine (2002). Mantle mixing: the generation, preservation, and destruction of chemical heterogeneity. *Annu. Rev. Earth Planet. Sci.* **30**, 493–525.
- Vinnik, L., M. Kato, and H. Kawakatsu (2001). Search for seismic discontinuities in the lower mantle. *Geophys. J. Int.* **147**, 41–56.

- Visser, K., J. Trampert, S. Lebedev, and B. L. N. Kennett (2008). Probability of radial anisotropy in the deep mantle. *Earth Planet. Sci. Lett.* **270**, 241–250.
- Voigt, W. (1928). *Lehrbuch der Kristallphysik*. Teubner, Leipzig, 979 pp. (in German).
- Wang, J., J. D. Bass, and T. Kastura (2014). Elastic properties of iron-bearing wadsleyite to 17.7 GPa: Implications for mantle mineral models. *Phys. Earth Planet. Inter.* **228**, 92–96.
- Waszek, L., N. C. Schmerr, and M. D. Ballmer (2018). Global observations of reflectors in the mid-mantle with implications for mantle structure and dynamics. *Nat. Commun.* **9**, 385.
- Watt, J. P., G. F. Davies, and R. J. O’Connell (1976). The elastic properties of composite materials. *Rev. Geophys.* **14**, 541–563.
- Wei, Q., N. Dubrovinskaia, and L. Dubrovinsky (2011). Ruby and Sm: YAG fluorescence pressure gauges up to 120 GPa and 700 K. *J. Appl. Phys.* **110**, 043513.
- Weidner, D. J., J. D. Bass, A. E. Ringwood, and W. Sinclair (1982). The single-crystal elastic moduli of stishovite. *J. Geophys. Res.: Solid Earth* **87**, 4740–4746.
- Whitfield, C. H., E. M. Brody, and W. A. Bassett (1976). Elastic moduli of NaCl by Brillouin scattering at high pressure in a diamond anvil cell. *Rev. Sci. Instrum.* **47**, 942–947.
- Wood, B. J. (1995). The effect of H₂O on the 410-kilometer seismic discontinuity. *Science* **268**, 74–76.
- Woodland, A. B. and R. J. Angel (1998). Crystal structure of a new spinelloid with the wadsleyite structure in the system Fe₂SiO₄-Fe₃O₄ and implications for the Earth’s Mantle. *Am. Mineral.* **83**, 404–408.
- (2000). Phase relations in the system fayalite–magnetite at high pressures and temperatures. *Contrib. Mineral. Petrol.* **139**, 734–747.
- Woodland, A. B., R. J. Angel, and M. Koch (2012). Structural systematics of spinel and spinelloid phases in the system MFe₂O₄-M₂SiO₄ with M = Fe²⁺ and Mg. *Eur. J. Mineral.* **24**, 657–668.
- Wu, Z., J. F. Justo, and R. M. Wentzcovitch (2013). Elastic anomalies in a spin-crossover system: Ferropericlase at lower mantle conditions. *Phys. Rev. Lett.* **110**, 228501.
- Xie, S. and P. J. Tackley (2004). Evolution of U-Pb and Sm-Nd systems in numerical models of mantle convection and plate tectonics. *J. Geophys. Res.: Solid Earth* **109**, B11204.
- Xu, W., C. Lithgow-Bertelloni, L. Stixrude, and J. Ritsema (2008). The effect of bulk composition and temperature on mantle seismic structure. *Earth Planet. Sci. Lett.* **275**, 70–79.
- Yamazaki, D., E. Ito, T. Yoshino, N. Tsujino, A. Yoneda, X. Guo, F. Xu, Y. Higo, and K. Funakoshi (2014). Over 1 Mbar generation in the Kawai-type multianvil apparatus and its application to compression of (Mg_{0.92}Fe_{0.08})SiO₃ perovskite and stishovite. *Phys. Earth Planet. Inter.* **228**, 262–267.
- Yang, R. and Z. Wu (2014). Elastic properties of stishovite and the CaCl₂-type silica at the mantle temperature and pressure: An ab initio investigation. *Earth Planet. Sci. Lett.* **404**, 14–21.
- Yang, X., H. Keppler, L. Dubrovinsky, and A. Kurnosov (2014). In-situ infrared spectra of hydroxyl in wadsleyite and ringwoodite at high pressure and high temperature. *Am. Mineral.* **99**, 724–729.
- Yoshino, T., G. Manthilake, T. Matsuzaki, and T. Katsura (2008). Dry mantle transition zone inferred from the conductivity of wadsleyite and ringwoodite. *Nature* **451**, 326–329.
- Young, T. E., H. W. Green II, A. M. Hofmeister, and D. Walker (1993). Infrared spectroscopic investigation of hydroxyl in β-(Mg,Fe)₂SiO₄ and coexisting olivine: Implications for mantle evolution and dynamics. *Phys. Chem. Miner.* **19**, 409–422.

- Zaug, J. M., E. H. Abramson, J. M. Brown, and L. J. Slutsky (1993). Sound velocities in olivine at Earth mantle pressures. *Science* **260**, 1487–1489.
- Zha, C.-S., T. S. Duffy, R. T. Downs, H.-K. Mao, and R. J. Hemley (1996). Sound velocity and elasticity of single-crystal forsterite to 16 GPa. *J. Geophys. Res.: Solid Earth* **101**, 17535–17545.
- Zha, C.-S., T. S. Duffy, H.-K. Mao, R. T. Downs, R. J. Hemley, and D. J. Weidner (1997). Single-crystal elasticity of β -Mg₂SiO₄ to the pressure of the 410 km seismic discontinuity in the Earth's mantle. *Earth Planet. Sci. Lett.* **147**, E9–E15.
- Zhang, J., B. Li, W. Utsumi, and R. C. Liebermann (1996). In situ X-ray observations of the coesite-stishovite transition: reversed phase boundary and kinetics. *Phys. Chem. Miner.* **23**, 1–10.
- Zhang, J. S. and J. D. Bass (2016). Sound velocities of olivine at high pressures and temperatures and the composition of Earth's upper mantle. *Geophys. Res. Lett.* **43**, 9611–9618.
- Zhao, D. (2004). Global tomographic images of mantle plumes and subducting slabs: insight into deep Earth dynamics. *Phys. Earth Planet. Inter.* **146**, 3–34.

List of Manuscripts and Statements of Author Contributions

- **Buchen, J.**, H. Marquardt, T. Boffa Ballaran, T. Kawazoe, and C. McCammon (2017). The equation of state of wadsleyite solid solutions: Constraining the effects of anisotropy and crystal chemistry. *Am. Mineral.* **102**, 2494–2504.

J. Buchen selected and characterized wadsleyite single crystals, performed the experiments, analyzed the data, proposed to construct and constructed the multi-end-member equation of state model, and wrote the manuscript. H. Marquardt proposed to study wadsleyite single crystals and to load two crystals inside the same diamond anvil cell and commented on the manuscript. T. Boffa Ballaran proposed to determine the equation of state, supervised X-ray diffraction experiments and data analysis, and commented on the manuscript. T. Kawazoe synthesized wadsleyite single crystals and commented on the manuscript. C. McCammon recorded and analyzed the Mössbauer spectrum and commented on the manuscript.

- **Buchen, J.**, A. Kurnosov, H. Marquardt, and T. Boffa Ballaran (2018). High-pressure elastic properties of single crystals from sound wave velocities: Comparing self-consistent inversion schemes. *J. Appl. Crystallogr.*, prepared for submission.

J. Buchen developed global inversion strategies, tested and compared different inversion strategies, and wrote the manuscript. A. Kurnosov proposed to develop and contributed in developing global inversion strategies. H. Marquardt provided ideas for testing and comparing different inversion strategies and commented on the manuscript. T. Boffa Ballaran proposed to develop global inversion strategies.

- **Buchen, J.**, H. Marquardt, S. Speziale, T. Kawazoe, T. Boffa Ballaran, and A. Kurnosov (2018). High-pressure single-crystal elasticity of wadsleyite and the seismic signature of water in the shallow transition zone. *Earth Planet. Sci. Lett.* **498**, 77–87.

J. Buchen selected and characterized wadsleyite single crystals, performed the experiments, analyzed the data, proposed to model and modeled seismic properties and contrasts, and wrote the manuscript. H. Marquardt proposed to study the elastic properties of wadsleyite, to load two crystals inside the same diamond anvil cell, and to evaluate the effect of water on sound wave velocities and wrote and commented on the manuscript. S. Speziale assisted with Brillouin spectroscopy experiments in Hamburg and with related data analysis and commented on the manuscript. T. Kawazoe synthesized wadsleyite single crystals and commented on the manuscript. T. Boffa Ballaran assisted with X-ray diffraction experiments and with related data analysis and commented on the manuscript. A. Kurnosov assisted with the preparation of experiments and data analysis and commented on the manuscript.

- **Buchen, J.**, H. Marquardt, K. Schulze, S. Speziale, T. Boffa Ballaran, N. Nishiyama, and M. Hanfland (2018). Equation of state of polycrystalline stishovite across the tetragonal–orthorhombic phase transition. *J. Geophys. Res. Solid Earth* **123**, 7347–7360.

J. Buchen analyzed the experimental data, modeled sound wave velocities, and wrote the manuscript. H. Marquardt proposed to study sintered polycrystalline stishovite, applied for beam time at the European Synchrotron Radiation Facility (ESRF), and commented on the manuscript. K. Schulze performed the experiments and commented on the manuscript. S. Speziale performed the experiments and commented on the manuscript. T. Boffa Ballaran assisted with data analysis and commented on the manuscript. N. Nishiyama synthesized and characterized sintered polycrystalline stishovite and commented on the manuscript. M. Hanfland assisted with the experiments at ESRF.

Chapter 4

The Equation of State of Wadsleyite Solid Solutions: Constraining the Effects of Anisotropy and Crystal Chemistry

Johannes BUCHEN^{a,✉}, Hauke MARQUARDT^a, Tiziana BOFFA BALLARAN^a, Takaaki KAWAZOE^a, and Catherine MCCAMMON^a

^aBayerisches Geoinstitut, Universität Bayreuth, 95440 Bayreuth, Germany
✉ johannes.buchen@uni-bayreuth.de

This chapter has been published as:
Buchen et al. (2017) *Am. Mineral.* **102**, 2494–2504.

Abstract

A quantitative knowledge of the equation of state of wadsleyite solid solutions is needed to refine thermodynamic and thermoelastic models for the transition zone in Earth's upper mantle. Here we present the results of high-pressure single-crystal X-ray diffraction experiments on two crystals of slightly hydrous iron-bearing wadsleyite with $\text{Fe}/(\text{Mg}+\text{Fe}) = 0.112(2)$, $\text{Fe}^{3+}/\Sigma\text{Fe} = 0.15(3)$, and 0.24(2) wt-% H_2O up to 20 GPa. By compressing two wadsleyite crystal sections inside the same diamond anvil cell, we find a negligible influence of crystal orientation on the derived equation of state parameters. Volume and linear compression curves were analyzed with finite-strain theory to demonstrate their mutual consistency for the Reuss bound indicating quasi-hydrostatic stress conditions. The results on the here-studied wadsleyite crystals are incorporated into a multi-end-member model to describe the equation of state for wadsleyite solid solutions in the system $\text{Mg}_2\text{SiO}_4\text{-Fe}_2\text{SiO}_4\text{-MgH}_2\text{SiO}_4\text{-Fe}_3\text{O}_4$. For the hypothetical ferrous wadsleyite end member, Fe_2SiO_4 , we find a substantially larger bulk modulus than expected by extrapolating currently accepted trends. The multi-end-member equation of state model may serve as a basis for the calculation of phase equilibria and the interpretation of seismic observations regarding the transition zone.

4.1 Introduction

In most models for Earth's upper mantle, wadsleyite, β -(Mg,Fe) $_2$ SiO $_4$, is assumed to be a major phase in the transition zone (Ringwood, 1991; Frost, 2008; Stixrude and Lithgow-Bertelloni, 2011). The steep increase in seismic velocities around 410 km depth has been attributed to the phase transition of olivine, α -(Mg,Fe) $_2$ SiO $_4$, to wadsleyite (Bina and Wood, 1987; Ringwood, 1991; Agee, 1998). Seismological observables related to the 410-km discontinuity such as the magnitude, depth, and depth interval of the velocity and density increase (Shearer, 2000; Houser, 2016) serve as anchor points to constrain the mineralogical, chemical, and thermal state of the upper mantle (Katsura et al., 2010; Wang et al., 2014; Chang et al., 2015; Zhang and Bass, 2016).

In addition to iron-magnesium substitution (Ringwood and Major, 1970; Frost, 2003), nominally anhydrous wadsleyite can incorporate substantial amounts of hydrogen (Smyth, 1994; Inoue et al., 1995) in the form of hydroxyl groups (McMillan et al., 1991; Young et al., 1993). Moreover, wadsleyites with Fe $^{3+}$ / Σ Fe up to 96 % have been synthesized under oxidizing conditions (Smyth et al., 1997; McCammon et al., 2004). Both hydrogen and ferric iron expand the stability field of wadsleyite to lower pressures and affect the pressure interval of the phase transition (Wood, 1995; Smyth and Frost, 2002; Frost and Dolejš, 2007; Frost and McCammon, 2009). To describe phase equilibria and to model seismic properties of wadsleyite, we need to know the equation of state (EOS) for wadsleyite solid solutions spanning the range of relevant compositions as captured by the system Mg $_2$ SiO $_4$ -Fe $_2$ SiO $_4$ -MgH $_2$ SiO $_4$ -Fe $_3$ O $_4$.

The variation of individual EOS parameters as a function of wadsleyite crystal chemistry has been addressed in previous studies, and certain trends have been established. Both iron and hydrogen incorporation expand the unit cell at ambient conditions but have opposing effects on the density (Finger et al., 1993; Holl et al., 2008; Mao et al., 2008). While the incorporation of hydrogen clearly enhances the compressibility of wadsleyite (Holl et al., 2008; Mao et al., 2008; Ye et al., 2010; Chang et al., 2015), the bulk modulus appears to be insensitive to iron-magnesium exchange when directly comparing experimental values determined with different techniques and based on different EOS assumptions (Wang et al., 2014; Chang et al., 2015). Only few studies addressed the combined effect of iron and hydrogen on the EOS of wadsleyite indicating that iron slightly counteracts the reduction of the bulk modulus due to hydrogen incorporation (Mao et al., 2011; Chang et al., 2015; Mao and Li, 2016).

Although ferric iron was shown to stabilize wadsleyite at lower pressures and to broaden the 410-km discontinuity (Frost and McCammon, 2009), little is known about the effect of the Fe $^{3+}$ cation on the elastic properties of wadsleyite. Hazen et al. (2000b) deduced a negligible effect of ferric iron on the compression behavior from their high-pressure single-crystal X-ray diffraction study on Fe $_{2.33}$ Si $_{0.67}$ O $_4$, a member of the low-pressure spinelloid III solid solution series (Woodland and Angel, 1998; Woodland and Angel, 2000; Koch et al., 2004). This solid solution series is isostructural with wadsleyite and spanned by the coupled substitution of octahedral Mg $^{2+}$ and Fe $^{2+}$ cations and tetrahedral Si $^{4+}$ by ferric iron (Woodland and Angel, 1998; Hazen et al., 2000b; Woodland et al., 2012). The fact that in many studies on the EOS of iron-bearing wadsleyites the amount of ferric iron has not been assessed could mask a potential impact of ferric iron on the elastic properties of wadsleyite solid solutions.

In the case of orthorhombic minerals like wadsleyite, single crystals respond to compression with anisotropic strain. This compressional anisotropy bears the potential to bias

extracted equation of state parameters in the presence of deviatoric stresses (Meng et al., 1993; Zhao et al., 2010). By comparing the compression behavior for crystals with different orientations relative to the stress field, potential bias due to deviatoric stresses should become apparent. Moreover, linear and bulk compressibilities derived from quasi-hydrostatic compression experiments should be mutually consistent for the Reuss bound (Angel, 2000; Angel et al., 2014).

Here we present the results of high-pressure single-crystal X-ray diffraction experiments on slightly hydrous iron-bearing wadsleyite with $\text{Fe}/(\text{Mg}+\text{Fe}) = 0.112(2)$, $\text{Fe}^{3+}/\Sigma\text{Fe} = 0.15(3)$, and 0.24 wt-% H_2O up to 20 GPa. Two crystals of the same composition were loaded together into the same pressure chamber of a diamond anvil cell (DAC) but with different crystallographic orientations relative to the compression axis. This setup aimed to detect any influence of crystal orientation on the derived EOS that may result from deviatoric stresses inside the DAC at high pressures. We analyzed volume and axial compression curves of both crystals with finite-strain equations of state to find mutually consistent descriptions of bulk and anisotropic compression. To describe anisotropic compression, we derived a linear EOS for each crystallographic axis.

We further reanalyzed available compression data employing a consistent analysis scheme and constructed a model for the EOS of wadsleyite solid solutions in the system $\text{Mg}_2\text{SiO}_4\text{-Fe}_2\text{SiO}_4\text{-MgH}_2\text{SiO}_4\text{-Fe}_3\text{O}_4$. The model captures the variation of unit cell volume and bulk modulus as a function of iron and hydrogen content. We extended this model to describe the anisotropic compression behavior of wadsleyite solid solutions by including single-crystal elasticity and anisotropic compression data.

4.2 Experimental

4.2.1 Single-Crystal Synthesis and Chemical Composition

Wadsleyite single crystals with sizes up to 500 μm were synthesized from San Carlos olivine powder in a 1000-ton multi-anvil press (run H4015). Details of the crystal synthesis have been reported elsewhere (Kawazoe et al., 2015). Four grains were mounted in resin and polished for subsequent electron microprobe analysis (EMPA) (15 kV, 15 nA, 1–2 μm beam diameter). Line scans indicated chemical homogeneity both for single grains and among different grains with $\text{Fe}/(\text{Mg}+\text{Fe}) = 0.112(2)$ and $M/\text{Si} = 1.92(1)$ where M stands for all analyzed metals (Mg, Fe, Ni, Ca, Al, Mn) other than silicon. Complete results of the EMPA are summarized in Appendix Table A.1¹.

4.2.2 Mössbauer Spectroscopy

A mixture of fine-grained material and several coarser grains was ground to a homogeneous powder and loaded into a hole in a 1 mm thick lead sheet with a diameter of 500 μm . Based on the physical thickness and chemical composition, we estimate the Mössbauer thickness to be 15 mg Fe/cm^2 . The lead sheet containing the powder was subsequently mounted in front of the ^{57}Co point source (nominal activity 370 MBq over $500 \times 500 \mu\text{m}^2$) of a constant acceleration Mössbauer spectrometer. A Mössbauer spectrum was recorded at room

¹Deposit item AM-17-126162, Supplemental Materials. Deposit items are free to all readers and found on the MSA web site, via the specific issue's Table of Contents.

temperature in transmission mode for 2 days. The velocity scale was calibrated using certified line positions of α -Fe (former National Bureau of Standards material no. 1541) and a Mössbauer spectrum collected on a 25 μm thick α -Fe foil.

The spectrum recorded on the wadsleyite powder was analyzed by fitting a series of Lorentzian functions to the transmission minima using the program MossA (Prescher et al., 2012). We applied five different fitting models based on Mössbauer spectral analyses of wadsleyite reported by Mrosko et al. (2015) and Kawazoe et al. (2016) to explore the sensitivity of the parameters to the model used. Details about the individual models can be found in the supplemental online material¹. The amount of Fe^{3+} as represented by the relative area of its absorption is independent of the applied fitting model within the experimental uncertainty. Our preferred fit is shown in Appendix Figure A.1¹ with the parameters listed in Appendix Table A.2¹ and yields $\text{Fe}^{3+}/\Sigma\text{Fe} = 0.15(3)$.

4.2.3 Single-Crystal X-Ray Diffraction at Ambient Conditions

Single crystals of at least 300 μm in size that showed uniform extinction when viewed between crossed polarizers were selected and glued onto a glass fiber for single-crystal X-ray diffraction. Crystal quality was assessed by scanning reflections on a Huber 4-circle Eulerian cradle diffractometer operating with $\text{Mo-}K\alpha$ radiation generated at 40 kV and 20–30 mA and a point detector. A total of 26 reflections were collected for two wadsleyite crystals with full widths at half peak heights of ω scans between 0.06° and 0.15° using the 8-position centering protocol (King and Finger, 1979) implemented in the SINGLE program (Angel and Finger, 2011). Unit cell parameters were refined assuming orthorhombic and monoclinic symmetry with space groups *Imma* (Horiuchi and Sawamoto, 1981) and *I2/m* (Smyth et al., 1997), respectively. Since unit cell edge lengths and volumes were identical within errors for both symmetries, only the orthorhombic values are summarized in Table 4.1 together with further X-ray diffraction results. The crystals, however, showed monoclinic distortions, $\beta > 90^\circ$, (Table 4.1) that fall in the range observed for wadsleyites of different hydration states (Smyth et al., 1997; Kudoh and Inoue, 1999; Jacobsen et al., 2005; Holl et al., 2008; Mao et al., 2008). After being oriented on the diffractometer as described by Jacobsen et al. (2005), the crystals were double-sided polished to plane-parallel thin sections parallel to either the (120) or (243) crystallographic planes, hereafter referred to as X120 and X243, respectively, with a final thickness of 10(1) μm .

4.2.4 Fourier-Transform Infrared Absorption Spectroscopy

Polarized and unpolarized infrared absorption spectra were recorded on X120 and X243 with a Bruker IFS 120 HR Fourier-transform infrared (FTIR) spectrometer in a spectral range from 2500 cm^{-1} to 4000 cm^{-1} (see supplemental online material¹ for details). By comparing spectra collected on at least 5 different spots on each crystal with spot diameters between 100 μm and 200 μm , we found the infrared absorption to be homogeneous across each crystal section. For polarized spectra, the electric field vector \mathbf{E} was oriented parallel to each of the two vibration directions, n' and n'' , as determined from the extinction positions of the single-crystal thin sections between crossed polarizers in visible light. Representative infrared absorption spectra for both crystal orientations, (120) and (243), are shown in Appendix Figures A.2a¹ and A.2b¹.

All spectra were dominated by two absorption bands centered around 3340 cm^{-1} and 3600 cm^{-1} (Appendix Figs. A.2¹ and A.3¹). These bands correspond to the most promi-

Table 4.1: Unit cell parameters and omega scan widths

Crystal cut (<i>hkl</i>)	X120 (120)	X243 (243)
Unit cell parameters		
<i>a</i> (Å)	5.7062(8)	5.7076(5)
<i>b</i> (Å)	11.4735(10)	11.4736(6)
<i>c</i> (Å)	8.2729(9)	8.2751(6)
<i>V</i> (Å ³)	541.62(11)	541.91(7)
β^a (°)	90.044(9)	90.052(3)
<i>b/a</i>	2.0107(3)	2.0102(2)
<i>N</i> ^b	26	26
FWHM^c		
$\Delta\omega_{\text{MIN}}$ (°)	0.060	0.059
$\Delta\omega_{\text{MAX}}$ (°)	0.085	0.151
$\langle\Delta\omega\rangle$ (°)	0.068(6)	0.091(23)

Note: Throughout this paper, standard deviations on the last digit are given in parentheses.

^aFor monoclinic unit cell.

^bNumber of centered reflections.

^cFull width at half maximum.

nent absorption features attributed to structurally bonded hydroxyl groups in wadsleyite (e. g. McMillan et al., 1991; Young et al., 1993; Jacobsen et al., 2005). To calculate total absorbances A_{TOT} and hydrogen contents from the polarized spectra, we made use of the principles explained by Libowitzky and Rossman (1996) and the crystal symmetry of wadsleyite (crystal class *mmm*) (Appendix Fig. A.4¹). To facilitate comparison between different calibrations and hydrogen contents reported in earlier work, we evaluated hydrogen concentrations with calibrations by Libowitzky and Rossman (1997), Paterson (1982), and Deon et al. (2010). Band specific absorbances, mean wave numbers, and hydrogen concentrations are summarized in Appendix Table A.4¹. More details can be found in the supplemental online material¹. Although we obtained identical total hydrogen concentrations when applying the calibrations by Deon et al. (2010) and Libowitzky and Rossman (1997), we emphasize that band specific hydrogen concentrations differ significantly between these calibrations (Appendix Table A.4¹). These differences demonstrate that the redistribution of absorption strength among bands at different frequencies as previously observed for iron-bearing wadsleyites (Bolfan-Casanova et al., 2012; Smyth et al., 2014) requires a wave number-dependent molar absorption coefficient as included in the calibrations by Libowitzky and Rossman (1997) and Paterson (1982). According to the calibration of Libowitzky and Rossman (1997), we found total hydrogen contents of 0.26(2) wt-% H₂O for X120 and 0.22(2) wt-% H₂O for X243. In view of the analytical uncertainties, both hydrogen contents are identical, and we use their mean value 0.24(2) wt-% H₂O for both crystals.

4.2.5 Sample Preparation and High-Pressure Experiments

After characterization by FTIR spectroscopy, the thin sections were glued onto metallic carriers and inserted into a FEI Scios dual beam device. A Ga^+ ion beam operated at an acceleration voltage of 30 kV was used to cut circular disks with diameters of 110 μm out of the single-crystal thin sections (Marquardt and Marquardt, 2012). In a second step, the circles were cut in half to semicircles. The ion beam current was adjusted between 7 nA and 30 nA depending on crystal thickness and available machine time.

Two semicircles of complementary orientations, i. e. one oriented parallel to (120), X120, and one parallel to (243), X243, were loaded together into a BX90 diamond anvil cell (DAC) (Kantor et al., 2012; Kurnosov et al., 2017; Schulze et al., 2017) equipped with diamond anvils of 500 μm culet size and tungsten carbide seats. The compression axis of the DAC was oriented along the plane normals, i. e. along the reciprocal lattice vectors (120) and (243). The symmetry equivalents of these vectors form pairs of almost perpendicular directions (Appendix Fig. A.4¹). The pressure chamber was formed by a circular hole with a diameter of 275 μm cut with an infrared laser in the center of the culet indentation of a rhenium gasket preindented to a thickness of about 60 μm . Neon gas precompressed to about 1.3 kbar was loaded as a pressure transmitting medium using the gas loading system at the Bayerisches Geoinstitut (Kurnosov et al., 2008). Solid neon was shown to create a quasi-hydrostatic stress environment up to 15 GPa (Meng et al., 1993; Klotz et al., 2009). For pressure determination, a ruby sphere was loaded into the DAC together with the crystal segments.

4.2.6 High-Pressure Single-Crystal X-Ray Diffraction

At high pressures, the lattice constants of the crystals inside the DAC were determined by single-crystal X-ray diffraction on the same diffractometer system as described above, now operated at 50 kV and 40 mA. Before gas loading, the lattice constants were obtained at ambient conditions with the specimens residing inside the DAC. Final ω scans were inspected and refit with the program WinIntegrStp (Angel, 2003). Profiles of low quality resulting in unreliable fits were rejected. At each pressure, the lattice constants were refined assuming first an orthorhombic and then a monoclinic unit cell. The number of reflections included in the refinements varied as a result of rejecting poor-quality profiles. For X120, unit cell parameters were computed using 16 to 20 reflections of the families 013, 211, 103, 141, 033, 231, 004, 240, 204, 105, 341, 244, and 271 with $15^\circ < 2\theta < 30^\circ$ and, for X243, using 11 to 20 reflections of the families 013, 211, 103, 141, 033, 231, 240, 053, 204, 105, 303, 341, 244, 073, 271, 413, 305, 084, and 404 with $15^\circ < 2\theta < 36^\circ$.

4.3 Results and Discussion

4.3.1 Equation of State

Since both volume and linear incompressibilities for orthorhombic and monoclinic unit cells, including the symmetry-adapted dimensions $a \sin \beta$ and $c \sin \beta$, turned out to be indistinguishable within their uncertainties, we restrict the following discussion to orthorhombic symmetry. This approximation is further justified by the fact that we could not resolve a systematic change of the monoclinic angle β with pressure. For both crystals, orthorhombic unit cell volumes V and edge lengths a , b , and c are compiled in Appendix Table A.5¹ and

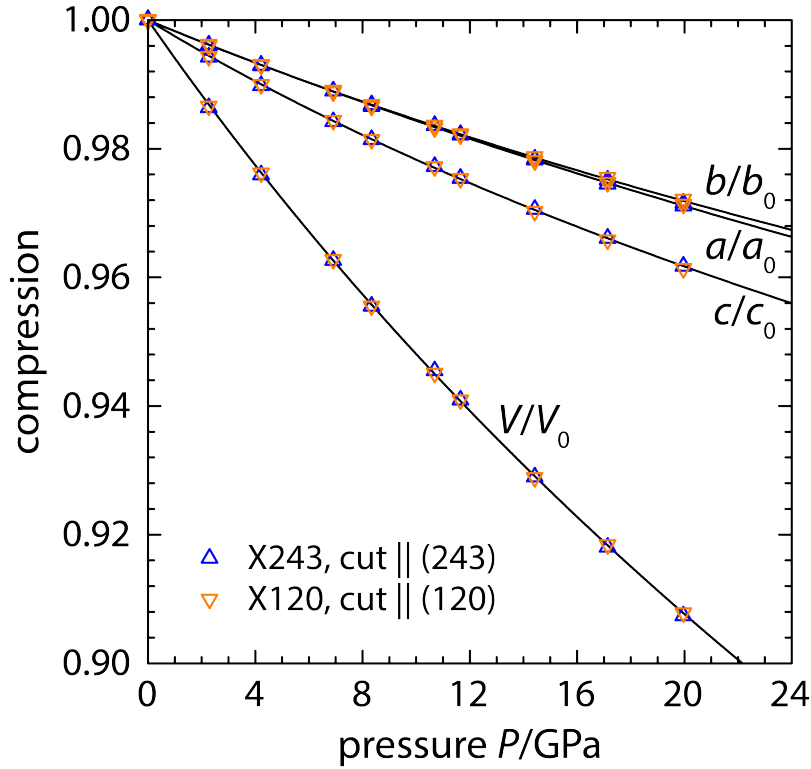


Figure 4.1: Volume and linear compression curves for both crystal sections. Errors are within the size of the symbols. Lines show third-order Birch-Murnaghan EOS curves.

plotted in Figure 4.1 as a function of pressure P . Differences in the unit cell dimensions between the two crystals amount to less than 0.1 % at the highest pressure (Appendix Fig. A.5¹) and remain on the same order of magnitude as the experimental uncertainties.

Following previous high-pressure single-crystal X-ray diffraction studies on wadsleyite (Yusa and Inoue, 1997; Hazen et al., 2000a; Hazen et al., 2000b; Holl et al., 2008; Ye et al., 2010; Chang et al., 2015), the volume compression was described by a third-order Birch-Murnaghan (BM-3) EOS (Birch, 1947)

$$P = (1 + 2f_E)^{5/2} \left(3K_0 f_E + \frac{9}{2} K_0 (K'_0 - 4) f_E^2 \right) \quad (4.1)$$

with the isotropic Eulerian finite strain $f_E = [(V_0/V)^{2/3} - 1]/2$, the unit cell volume V_0 , the bulk modulus K_0 , and its first pressure derivative K'_0 at ambient conditions. The variation of normalized pressure F_E with Eulerian finite strain f_E indicated a third-order contribution of the finite strain (Angel, 2000) (Appendix Fig. A.6¹).

To reveal any difference in compressional behavior between the two crystal sections oriented differently relative to the compression axis of the DAC, each crystal was first treated separately. The resulting unit cell volumes at ambient conditions overlap within their uncertainties. Furthermore, we found identical bulk moduli and related pressure derivatives for the two crystals (Table 4.2). These results demonstrate that both crystal sections follow a common compression behavior irrespective of their orientation relative to the compression axis of the DAC. We therefore combined both P - V datasets in a single EOS and obtained $V_0 = 542.09(7) \text{ \AA}^3$ and $K_0 = 167(1) \text{ GPa}$ with $K'_0 = 4.4(2)$.

Table 4.2: Refined equation of state parameters

Crystal	X120	X243	Combined
Third-order Birch-Murnaghan (BM-3) EOS			
V_0 (Å ³)	542.20(8)	542.05(10)	542.09(7)
K_0 (GPa)	166.7(14)	166.7(20)	166.9(13)
K'_0	4.4(2)	4.4(3)	4.4(2)
a_0 (Å)	5.7086(5)	5.7071(4)	5.7075(3)
b_0 (Å)	11.4765(10)	11.4765(8)	11.4765(7)
c_0 (Å)	8.2762(11)	8.2759(8)	8.2760(7)
k_{10} (GPa)	578(10)	583(8)	583(7)
k_{20} (GPa)	567(10)	580(8)	575(7)
k_{30} (GPa)	398(7)	389(6)	393(5)
k'_{10}	11.4(13)	10.7(12)	10.8(10)
k'_{20}	15.8(15)	12.5(13)	13.9(11)
k'_{30}	12.4(10)	14.5(10)	13.5(8)
Second-order Birch-Murnaghan (BM-2) EOS^a			
V_0 (Å ³)	542.11(8)	542.00(10)	542.03(7)
K_0 (GPa)	169.5(6)	169.1(8)	169.3(5)
a_0 (Å)	5.7087(5)	5.7072(4)	5.7077(3)
b_0 (Å)	11.4750(9)	11.4764(8)	11.4759(6)
c_0 (Å)	8.2759(10)	8.2751(8)	8.2754(7)
k_{10} (GPa)	574(4)	575(3)	576(3)
k_{20} (GPa)	592(4)	583(4)	586(3)
k_{30} (GPa)	401(3)	403(3)	402(2)
^a $K'_0 = 4$; $k'_{10} = k'_{20} = k'_{30} = 12$.			

4.3.2 Anisotropic Compression Behavior and the Stress State Inside the Diamond Anvil Cell

To describe the anisotropic compression behavior, we followed the approach outlined by Angel (2000) and Angel et al. (2014) who proposed to substitute the volume in an EOS with the cube of a unit cell edge length. This results in the linear BM-3 EOS

$$P = (1 - 2E_i)^{5/2} \left(-k_{i0}E_i + \frac{1}{2}k_{i0}(k'_{i0} - 12)E_i^2 \right) \quad (4.2)$$

with the linear moduli k_{i0} , their pressure derivatives k'_{i0} , and the components of the Eulerian finite-strain tensor $E_i = [1 - (a_{i0}/a_i)^2]/2$ ($i = 1, 2, \text{ or } 3$ for $a, b, \text{ or } c$, respectively). Again, each crystal was treated separately first, and the linear moduli for the two crystals overlap within their uncertainties (Table 4.2). The linear moduli pressure derivatives differ slightly for the two crystals but still overlap within their 2σ uncertainty intervals. In analogy to the volume EOS, we combined both datasets in a single linear EOS for compression along each crystallographic axis. As for volume compression, the anisotropic compression behavior appears to be independent of how the crystal section is oriented relative to the compression axis of the DAC.

Using the two crystal orientations as determined by X-ray diffraction and the derived linear moduli (Table 4.2), we calculated the effect of potential deviatoric stresses on vol-

ume strain using equation (12) of Zhao et al. (2010). Crystal X243 is oriented parallel (243) so that the compression axis of the DAC intersects all three crystallographic axes at nearly equal angles (Appendix Fig. A.4¹). In this orientation, the volume strain should be almost insensitive to deviatoric stresses (Zhao et al., 2010). For crystal X120, in contrast, the effect of deviatoric stresses on volume strain is predicted to be an order of magnitude larger than for crystal X243. Since we observed only negligible differences between the unit cell volumes of both crystals (Appendix Table A.5¹, Appendix Fig. A.5¹), we conclude that deviatoric stresses were not large enough to significantly affect the volume strain.

For hydrostatic stress conditions (Reuss bound; Reuss, 1929; Watt et al., 1976), the linear moduli can be expressed in terms of single-crystal compliances s_{ij} as $k_i^R = 1/(s_{i1} + s_{i2} + s_{i3})$ (Angel et al., 2014). For isotropic strain conditions (Voigt bound; Voigt, 1928; Watt et al., 1976), the linear moduli can be calculated from single-crystal stiffnesses c_{ij} as $k_i^V = c_{i1} + c_{i2} + c_{i3}$. According to these relations, the linear moduli can be combined to the respective bulk moduli (Watt et al., 1976; Nye, 1985; Haussühl, 2007):

$$\text{Reuss bound (hydrostatic stress): } K_0^R = 1 / \sum_i (s_{i10} + s_{i20} + s_{i30}) = 1 / \sum_i k_{i0}^{R-1} \quad (4.3a)$$

$$\text{Voigt bound (isotropic strain): } K_0^V = \sum_i (c_{i10} + c_{i20} + c_{i30}) / 9 = \sum_i k_{i0}^V / 9 \quad (4.3b)$$

To evaluate which stress state, hydrostatic stress or isotropic strain, better reflects the conditions inside the DAC for the setup used in our experiments, we calculated the Reuss and Voigt bound from the linear moduli k_{i0} obtained from our analysis of anisotropic compression and compared them with the bulk modulus K_0 obtained from our volume compression data. Using the linear BM-3 EOS parameters given in Table 4.2, we obtain $K_0^R = 1 / \sum_i k_{i0}^{-1} = 166.7(12)$ GPa (eqn. (4.3a)) and $K_0^V = \sum_i k_{i0} / 9 = 172.3(12)$ GPa (eqn. (4.3b)). The fact that the bulk modulus obtained by fitting the P - V data with a BM-3 EOS is virtually identical to the Reuss bound (Table 4.2) and coincides with the individual bulk moduli for the two crystals attests to the quasi-hydrostatic stress field inside the pressure chamber of the DAC. For the explored pressure range, deviatoric stresses remained too weak to affect the compression behavior.

4.3.3 Equation of State of Wadsleyite Solid Solutions

Available compression and elasticity data on wadsleyite solid solutions cover compositions spanned by four end members: Mg_2SiO_4 (mgwa), Fe_2SiO_4 (fewa), MgH_2SiO_4 (hywa), and $\text{Fe}^{2+}\text{Fe}_2^{3+}\text{O}_4$ (fe3wa). In defining these end members, we assumed that hydrogen incorporation is charge balanced by vacancies on the octahedral sites (Inoue, 1994; Smyth, 1994; Inoue et al., 1995; Kawamoto et al., 1996; Kudoh et al., 1996; Smyth et al., 1997; Litasov et al., 2011), i. e. by the mechanism $M_M^\times + O_O^\times + \text{H}_2\text{O} = V_M'' + 2(\text{OH})_O^\bullet + \text{MO}$, and that ferric iron enters both the octahedral and tetrahedral sites by the charge coupled substitution $M_M^\times + \text{Si}_{\text{Si}}^\times + \text{Fe}_2\text{O}_3 = \text{Fe}_M^\bullet + \text{Fe}'_{\text{Si}} + \text{MO} + \text{SiO}_2$ (Woodland and Angel, 1998; Richmond and Brodholt, 2000; Frost and McCammon, 2009), where M stands for Mg^{2+} or Fe^{2+} in octahedral coordination. Although alternative mechanisms to incorporate hydrogen, ferric iron, or coupled substitutions involving both of them have been proposed (Nishihara et al., 2008; Frost and McCammon, 2009; Bolfan-Casanova et al., 2012; Smyth et al., 2014; Kawazoe et al., 2016), the chosen end members comprise the relevant chemical variability.

We can write a general wadsleyite formula as $(\text{Mg}, \text{Fe}^{2+}, \text{Fe}^{3+})_{2-y}\text{H}_{2y}(\text{Si}, \text{Fe}^{3+})\text{O}_4$ where y stands for the number of H_2O molecular equivalents per formula unit. The iron content

is conventionally stated as the ratio $x = \text{Fe}/(\text{Mg}+\text{Fe})$ without differentiating between iron oxidation states ($\text{Fe} = \text{Fe}^{2+} + \text{Fe}^{3+}$) and the ferric iron content as $z = \text{Fe}^{3+}/\Sigma\text{Fe}$. The following relations decompose a given wadsleyite formula into molar fractions x_m of the end members m :

$$\text{Mg}_2\text{SiO}_4 \text{ (mgwa):} \quad x_{\text{mgwa}} = (1 - y/2)[1 - x(2 - z)/(2 - xz)] - y/2 \quad (4.4a)$$

$$\text{Fe}_2\text{SiO}_4 \text{ (fewa):} \quad x_{\text{fewa}} = (1 - y/2)x(2 - 3z)/(2 - xz) \quad (4.4b)$$

$$\text{MgH}_2\text{SiO}_4 \text{ (hywa):} \quad x_{\text{hywa}} = y \quad (4.4c)$$

$$\text{Fe}_3\text{O}_4 \text{ (fe3wa):} \quad x_{\text{fe3wa}} = (1 - y/2)2xz/(2 - xz) \quad (4.4d)$$

For each end member species m , the EOS parameters may have different values referred to as V_{0m} , K_{0m} , and K'_{0m} . Assuming ideal mixing behavior, the unit cell volume of wadsleyite solid solution members can be expressed as a function of the respective molar fractions

$$V = \sum_m x_m V_m = x_{\text{mgwa}} V_{\text{mgwa}} + x_{\text{fewa}} V_{\text{fewa}} + x_{\text{hywa}} V_{\text{hywa}} + x_{\text{fe3wa}} V_{\text{fe3wa}} \quad (4.5)$$

For wadsleyite solid solutions, ideal volumes of mixing have been observed for the dry system ($y = 0$) (Finger et al., 1993; Woodland et al., 2012), and the unit cell volume was found to be a linear function of the hydrogen concentration (Holl et al., 2008; Chang et al., 2015).

In Appendix Table A.6¹, we compile published unit cell parameters for wadsleyites with different compositions. This dataset can be complemented by unit cell parameters for magnesium-free (Woodland and Angel, 2000) and magnesium-bearing (Woodland et al., 2012) members of the spinelloid III solid solution series to cover the relevant composition space in the Mg_2SiO_4 - Fe_2SiO_4 - MgH_2SiO_4 - Fe_3O_4 system (Fig. 4.2). A least squares fit of equation (4.5) to 72 unit cell volumes yields $V_{\text{mgwa}0} = 538.5(2) \text{ \AA}^3$, $V_{\text{fewa}0} = 569.6(3) \text{ \AA}^3$, $V_{\text{hywa}0} = 547.5(19) \text{ \AA}^3$, and $V_{\text{fe3wa}0} = 598.5(5) \text{ \AA}^3$ (Table 4.3). These unit cell volumes agree very well with previous estimates from solid solution analyses (Holl et al., 2008; Stixrude and Lithgow-Bertelloni, 2011; Woodland et al., 2012; Chang et al., 2015). For example, the unit cell volume obtained for the fictive hydrous end member MgH_2SiO_4 (15.2 wt-% H_2O) falls in between the values estimated using the formulas given by Holl et al. (2008) and Chang et al. (2015), i. e. $553.1(8) \text{ \AA}^3$ and $547.4(31) \text{ \AA}^3$, respectively.

To calculate the elastic moduli of wadsleyite solid solutions, we follow previous approaches to analyze the elastic properties of solid solutions (Takahashi and Liu, 1970; Jackson et al., 1978; Stixrude and Lithgow-Bertelloni, 2005) that are based on the Reuss average for the elastic properties of multi-phase aggregates. The elastic modulus M of a solid solution can then be calculated from the elastic moduli M_m , the molar fractions x_m , and the unit cell volumes V_m of the relevant end members (Hill, 1963; Watt et al., 1976):

$$M^{\text{R}} = \frac{\sum_m x_m V_m}{\sum_m x_m V_m / M_m} \quad (4.6)$$

Alternatively, the elastic modulus of a solid solution can be calculated from the end member moduli as a Voigt average (Hill, 1963; Watt et al., 1976):

$$M^{\text{V}} = \frac{\sum_m x_m V_m M_m}{\sum_m x_m V_m} \quad (4.7)$$

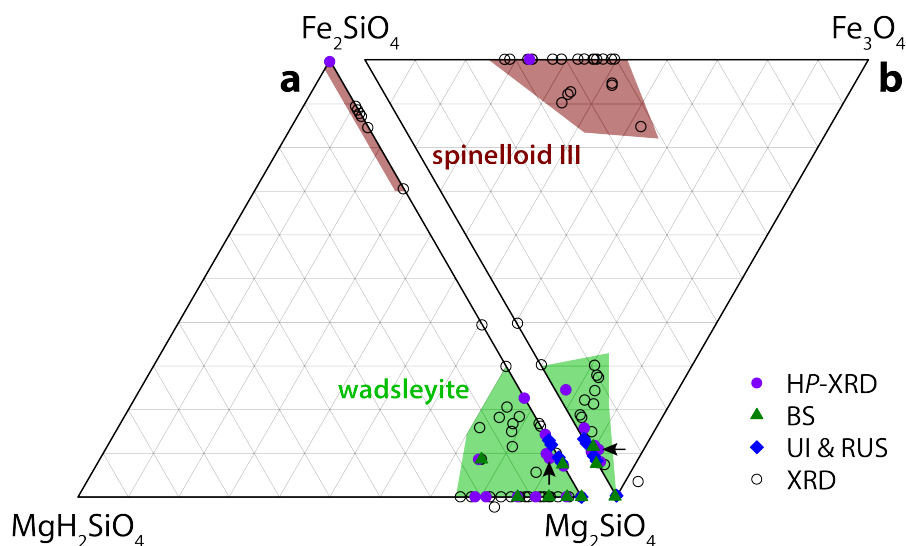


Figure 4.2: Wadsleyite compositions (end member molar fractions) of the EOS data set (Appendix Tables A.6¹ and A.7¹) projected into the ternary diagrams **a**) Mg_2SiO_4 - Fe_2SiO_4 - MgH_2SiO_4 and **b**) Mg_2SiO_4 - Fe_2SiO_4 - Fe_3O_4 . Published EOS and elasticity data cluster around compositions relevant for Earth's mantle with the exception of an isolated data point for $\text{Fe}_{2.33}\text{Si}_{0.67}\text{O}_4$ (Hazen et al., 2000b). The arrows indicate the composition of the present study. HP-XRD high-pressure X-ray diffraction, BS Brillouin spectroscopy, UI ultrasonic interferometry, RUS resonant ultrasound spectroscopy, XRD X-ray diffraction (ambient conditions unit cells).

The choice between the two models depends on whether a single crystal of the solid solution is characterized by a homogeneous internal stress field (Reuss model) or is internally homogeneously strained (Voigt model). Note that equations (4.6) and (4.7) average over end members or phases with different elastic properties while equation (4.3) gives directional averages of elastic anisotropy for a single crystal.

To generate a set of comparable EOS for wadsleyites with different chemical compositions, we reanalyzed available room temperature compression data (Appendix Fig. A.7¹). Since much of this data is limited to pressures below 10 GPa, we restricted our analysis of volume and axial compression curves to second-order Birch-Murnaghan (BM-2) EOS (eqns. (4.1) and (4.2)). The set of isothermal bulk and linear moduli can be complemented by adiabatic moduli determined with dynamic methods such as Brillouin spectroscopy, ultrasonic interferometry, and resonant ultrasound spectroscopy by converting adiabatic moduli to isothermal moduli. The resulting dataset is compiled in Appendix Table A.7¹ together with the respective references. Details about the procedures to reanalyze and convert previously published EOS and elasticity data can be found in the supplemental online material¹.

Figure 4.2 projects the wadsleyite compositions listed in Appendix Table A.7¹ into ternary diagrams. Each ternary represents a projection from either the Fe_3O_4 end member (Fig. 4.2a) or the MgH_2SiO_4 end member (Fig. 4.2b) onto the opposite face of a fictitious tetrahedron spanned by the four end members at the corners. The compositions reported in previous EOS and elasticity studies cluster around the Mg_2SiO_4 end member and along the binary branches Mg_2SiO_4 - Fe_2SiO_4 and Mg_2SiO_4 - MgH_2SiO_4 . Including that of the present study, only few compositions represent complex solid solutions that plot within the wadsleyite fields shown in Figure 4.2 rather than on the binary axes of the diagram. The wadsleyite fields cover the relevant compositional space as inferred from the reported maximum

Table 4.3: Calculated second-order Birch-Murnaghan equation of state parameters for wadsleyite end members (Reuss model)

End member	Volume V_0 (Å ³)	Isothermal bulk and linear moduli				
		K_0 (GPa)	k_{10} (GPa)	k_{20} (GPa)	k_{30} (GPa)	$K_0^{\text{R}^a}$ (GPa)
Three-end-member model						
Mg ₂ SiO ₄	538.5(2)	169(2)	578(10)	598(9)	404(7)	170(2)
Fe ₂ SiO ₄	569.6(3)	195(22)	718(112)	689(80)	478(79)	203(18)
MgH ₂ SiO ₄	547.5(19)	92(6)	327(35)	242(15)	210(21)	84(4)
Four-end-member model						
Mg ₂ SiO ₄	538.5(2)	170(2)	580(10)	598(8)	405(7)	170(2)
Fe ₂ SiO ₄	569.6(3)	201(38)	861(246)	780(151)	460(113)	217(32)
MgH ₂ SiO ₄	547.5(19)	92(6)	326(35)	243(15)	209(21)	84(4)
Fe ₃ O ₄	598.5(5)	145(49)	279(65)	405(98)	613(464)	130(27)

$$^a K_0^{\text{R}} = 1/(1/k_{10} + 1/k_{20} + 1/k_{30}).$$

values $x_{\text{hywa}} = 0.25$ (Smyth, 1994; Inoue et al., 1995) and $x_{\text{fewa}} = 0.3$ (Akaogi et al., 1989; Frost, 2003; Stixrude and Lithgow-Bertelloni, 2011) for wadsleyite solid solutions.

We derived end member bulk moduli K_m by fitting equations (4.6) and (4.7) to the bulk moduli reported for different compositions (Appendix Table A.7¹) and using the end member unit cell volumes V_m given in Table 4.3. We used the Reuss bounds for bulk and linear moduli as calculated from single-crystal elastic constants that were determined by Brillouin spectroscopy and employed the BM-2 bulk and linear moduli from compression curves for which the bulk modulus K_0 obtained from volume compression is close to the Reuss bound K_0^{R} calculated from the linear moduli (eqn. (4.3), Appendix Table A.7¹). Results reused in successive studies (Sinogeikin et al., 1998; Wang et al., 2014) were included only once. We found that both Reuss and Voigt models describe the wadsleyite bulk and linear moduli equally well and, within errors, give identical results for intermediate compositions as well as for end members. The moduli for the hydrous end member MgH₂SiO₄ are the only exceptions with the Voigt model moduli being significantly smaller than the Reuss model moduli (Table 4.3 and Appendix Table A.3¹). Since both models predict virtually identical moduli for intermediate compositions, we focus the following discussion on the Reuss model for clarity.

Table 4.3 lists the results of least squares fits of equation (4.6) (Reuss model) to 21 compositions and the corresponding bulk and linear moduli for the ternary system Mg₂SiO₄-Fe₂SiO₄-MgH₂SiO₄. The resulting bulk modulus for the Mg₂SiO₄ end member agrees with those reported in previous solid solution analyses (Jeanloz and Hazen, 1991; Holl et al., 2008; Mao et al., 2008; Stixrude and Lithgow-Bertelloni, 2011; Chang et al., 2015; Mao and Li, 2016). The incorporation of hydrogen into wadsleyite reduces the bulk modulus as reported in earlier studies (Holl et al., 2008; Mao et al., 2008; Tsuchiya and Tsuchiya, 2009; Ye et al., 2010; Mao et al., 2011; Chang et al., 2015; Mao and Li, 2016). Moreover, hydrogen weakens the structure along all three crystallographic axes with the strongest reduction of the linear modulus along **b** (Table 4.3).

The compression behavior of the Mg₂SiO₄-Fe₂SiO₄ solid solution is not tightly constrained by the available studies. As a result, the bulk modulus for the ferrous iron-bearing end member Fe₂SiO₄ has large uncertainties. In contrast to earlier studies concluding that iron has a small or negligible effect on the bulk modulus (Stixrude and Lithgow-Bertelloni,

2011; Wang et al., 2014; Chang et al., 2015; Mao and Li, 2016), however, the combination of our new data with a careful reanalysis of previous studies indicates that the substitution of Mg^{2+} by Fe^{2+} increases the incompressibility of wadsleyite by about 14%. Ferrous iron appears to stiffen the crystal structure along all three crystallographic axes with the strongest stiffening along **a** (Table 4.3).

A similar increase in bulk modulus with iron content has been observed for ringwoodite (Rigden and Jackson, 1991; Jackson et al., 2000; Higo et al., 2006) and olivine (Sumino, 1979; Zha et al., 1996; Speziale et al., 2004). These experimental observations are consistent with first-principle calculations based on density functional theory (DFT) suggesting that the bulk moduli increase with increasing iron content for all three $(\text{Mg,Fe})_2\text{SiO}_4$ polymorphs (Núñez-Valdez et al., 2011; Núñez-Valdez et al., 2013). In the case of wadsleyite, the DFT calculations predict the absolute difference in bulk modulus between the magnesium and iron end members to be 22 GPa (Núñez-Valdez et al., 2011) and 42 GPa (Núñez-Valdez et al., 2013). These values are similar in magnitude to the difference of 25 GPa observed in our analysis.

For the quaternary system $\text{Mg}_2\text{SiO}_4\text{-Fe}_2\text{SiO}_4\text{-MgH}_2\text{SiO}_4\text{-Fe}_3\text{O}_4$, we also included the moduli for the member of the spinelloid III solid solution (Hazen et al., 2000b). The effect of Fe^{3+} is weakly constrained leading to large uncertainties on the moduli for the iron-bearing end members (Table 4.3). However, the trends observed for the ternary system remained unchanged. In contrast to the stiffening of the crystal structure by ferrous iron, ferric iron appears to soften the crystal structure on compression, especially along the **a** axis (Table 4.3). This behavior differs from the situation in the spinel-structured solid solution, in which the bulk moduli for magnetite (186 GPa; Finger et al., 1986; Reichmann and Jacobsen, 2004) and for Mg_2SiO_4 ringwoodite (185 GPa; Jackson et al., 2000; Higo et al., 2006) are essentially identical.

Most iron-bearing wadsleyites can be expected to contain some ferric iron (O'Neill et al., 1993; McCammon et al., 2004; Frost and McCammon, 2009; Bolfan-Casanova et al., 2012) even though the amount of ferric iron has not always been stated for the samples described in the literature. The competing effects of ferrous and ferric iron on the volume and anisotropic compression of wadsleyite could have masked each other in previous attempts to resolve the effect of iron-magnesium substitution on the compression behavior compelling to conclude this effect to be negligible for wadsleyite (Wang et al., 2014; Chang et al., 2015; Mao and Li, 2016).

The bulk moduli compiled in Appendix Table A.7¹ are plotted as a function of $\text{Fe}/(\text{Mg}+\text{Fe})$ and the number of H_2O molecular equivalents in Figures 4.3a and 4.3b, respectively (for linear moduli see Appendix Fig. A.8¹). For each composition listed in Appendix Table A.7¹, the modulus as calculated from the end member models (Table 4.3) is shown for comparison. The models reasonably capture the competing effects arising from the different cation substitutions even though several experimental data clearly deviate from the calculated values. Deviations may arise from the presence of hydrogen and ferric iron, whose concentrations have not been accurately determined in several studies, or from systematic errors in the compression studies. For example, the bulk moduli in excess of 180 GPa at $\text{Fe}/(\text{Mg}+\text{Fe})$ ratios of 0 and 0.25 (Fig. 4.3a, Appendix Table A.7¹) were both obtained from refitting the compression data of Hazen et al. (2000a). Even though the bulk modulus values are much larger than any other values obtained from compression data, they still display the trend of increasing bulk moduli with increasing $\text{Fe}/(\text{Mg}+\text{Fe})$ ratio. Moreover, both data points have counterparts with fairly low bulk modulus values for identical compositions

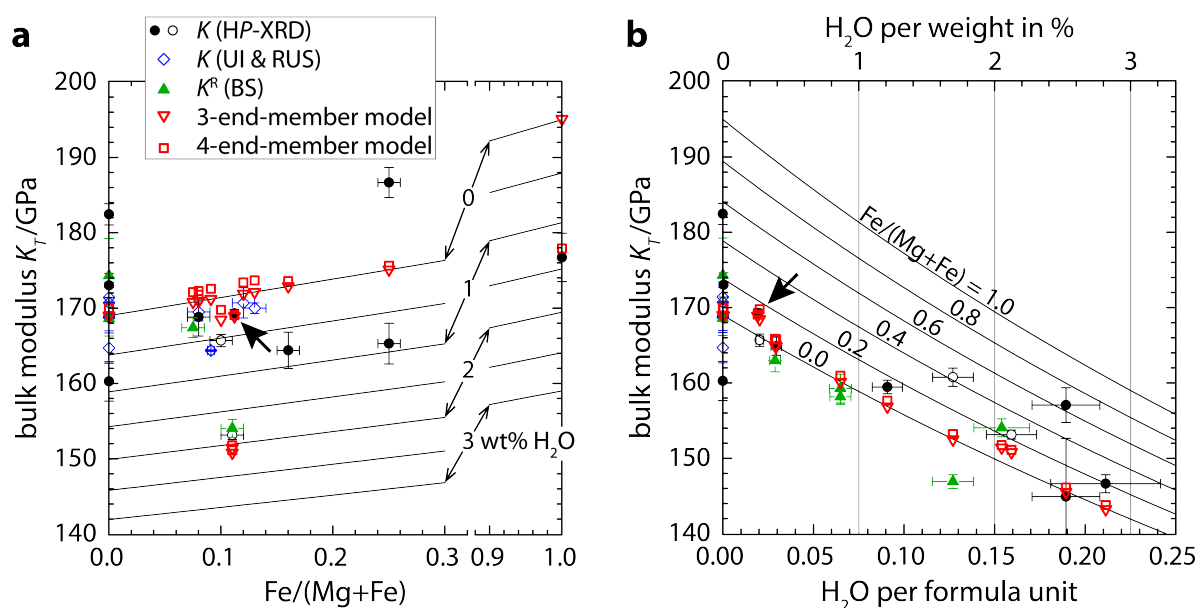


Figure 4.3: Isothermal bulk moduli for wadsleyite as a function of **a)** $\text{Fe}/(\text{Mg}+\text{Fe})$ and **b)** H_2O molecular equivalents per formula unit. See Appendix Table A.7¹ for references. Contours were calculated from the three-end-member model (Table 4.3). In **a)**, compositions spread vertically for different hydrogen and ferric iron contents. In **b)**, compositions spread vertically for different iron (ferrous and ferric) contents. Solid arrows indicate the composition of the present study. Data points with open symbols were not included in the multi-end-member analysis. HP-XRD high-pressure X-ray diffraction, BS Brillouin spectroscopy, UI ultrasonic interferometry, RUS resonant ultrasound spectroscopy.

(Fig. 4.3a, Appendix Table A.7¹; Hazen et al., 1990) that again follow the trend of our model.

4.3.4 Relationship of Compression Behavior to Crystal Chemistry

In the wadsleyite crystal structure, iron preferentially enters the $M3$ and $M1$ octahedral sites (Sawamoto and Horiuchi, 1990; Finger et al., 1993; Hazen et al., 2000a). While the $M3$ octahedra form edge-sharing double chains along the a axis, the $M1$ octahedra interconnect these chains along the c axis by sharing edges with octahedra belonging to two double chains. In contrast to bulk modulus-volume systematics for coordination polyhedra (Hazen and Finger, 1979), the $M1$ and $M3$ octahedra stiffen along with the expansion arising from the replacement of Mg^{2+} by the larger Fe^{2+} cation (Finger et al., 1993; Hazen et al., 2000a). As a consequence, we found that the wadsleyite crystal structure becomes less compressible when Mg^{2+} is replaced by Fe^{2+} . The stiffening of coordination polyhedra by incorporation of iron may be caused by geometrical constraints imposed by the rigid sorosilicate group (Hazen et al., 2000a) in addition to changes in the chemical bonding character.

For ringwoodite, the increase of the bulk modulus with iron content has been related to d electron interactions between iron cations occupying edge-sharing coordination octahedra (Hazen, 1993). Indeed, d electron interactions have been observed for both iron-bearing ringwoodite and wadsleyite in the form of $\text{Fe}^{2+} \rightarrow \text{Fe}^{3+}$ intervalence charge transfer between edge-sharing octahedra by Mössbauer spectroscopy (McCammon et al., 2004; Mrosko et al., 2015) and optical absorption spectroscopy (Ross, 1997; Keppler and Smyth, 2005). The

fact that Mg-Fe solid solutions of both ringwoodite and wadsleyite appear to contradict bulk modulus-volume systematics, which are essentially based on ionic bonding models (Anderson and Anderson, 1970; Chung, 1972), suggests a change in bonding character and crystal-chemical behavior of the Fe^{2+} cation at high pressure (Hazen, 1993).

Required to charge balance structurally bound hydroxyl groups in wadsleyite (Smyth, 1994; Inoue et al., 1995; Kudoh et al., 1996; Smyth et al., 1997; Demouchy et al., 2005; Jacobsen et al., 2005; Litasov et al., 2011), octahedral vacancies are probably responsible for the enhanced compressibility of the wadsleyite structure with increasing degree of hydration (Holl et al., 2008; Tsuchiya and Tsuchiya, 2009; Ye et al., 2010). On one hand, octahedral vacancies disrupt the polyhedral framework of the crystal structure and allow the structure to relax into the created voids. On the other hand, hydroxyl groups and accompanying hydrogen bonds counteract the repulsive forces between neighboring oxygen anions (Kleppe et al., 2001; Kleppe et al., 2006; Jacobsen et al., 2005). Both vacancies and hydrogen bonds can therefore be expected to reduce the bulk modulus of wadsleyite.

The incorporation of Fe^{3+} into the wadsleyite structure follows a coupled substitution with Si^{4+} and M^{2+} ($M^{2+} = \text{Mg}^{2+}$ or Fe^{2+}) being replaced by two Fe^{3+} , one at a tetrahedral and one at an octahedral site (Woodland and Angel, 1998; Richmond and Brodholt, 2000). The presence of ferric iron in the tetrahedron was confirmed by the single-crystal X-ray diffraction study of Smyth et al. (2014). However, using chemical compositional trends, Frost and McCammon (2009) showed that a substantial fraction of the ferric iron substitutes for octahedral cations only, following the reaction $3M_M^x + \text{Fe}_2\text{O}_3 = 2\text{Fe}_M^\bullet + V_M'' + 3\text{MO}$ with $M = \text{Mg}^{2+}$ or Fe^{2+} . The created vacancies V_M'' will enhance the compressibility with respect to the Mg_2SiO_4 end member as might be reflected in the low value estimated for the bulk modulus of the Fe_3O_4 end member (Table 4.3).

4.3.5 Bulk Modulus Systematics

We visualize the variation of volume and bulk modulus across the wadsleyite solid solutions using a diagram relating the product of the bulk modulus K and the mean atomic volume V_A , KV_A , to the mean atomic mass M_A (Chung, 1972), where $V_A = V/(ZN)$ and $M_A = M/N$ with the unit cell volume V , the formula mass M , the number of formula units per unit cell Z , and the number of atoms per formula N . Based on a theoretical model for ionic bonding and an empirical analysis of isostructural compounds, the product KV_A was shown to remain constant for isostructural and isovalent exchange, i. e. when cations of equal charges substitute in the same crystal structure (Anderson and Anderson, 1970; Chung, 1972).

In Figure 4.4, we plot the data of Appendix Table A.7¹ together with the trends calculated using the four-end-member EOS model (eqns. (4.4), (4.5), and (4.6), Table 4.3) into a KV_A - M_A diagram. In cases where unit cell volumes are not reported in the original publications, we calculated unit cell volumes according to our model. The M_A axis splits up the trends of iron-magnesium substitution and hydration since they increase or decrease the mean atomic mass, respectively. In general, the experimental data follow the trends predicted by the EOS model. In addition to measurement uncertainties, scatter results from solid solutions in the ternary or quaternary system that should fall between the lines calculated for the binary systems.

From a purely ionic perspective, replacing Mg^{2+} by Fe^{2+} should spread the data along a horizontal line of constant KV_A extending from the Mg_2SiO_4 end member towards higher mean atomic masses. Based on the EOS model, however, the product KV_A increases with in-

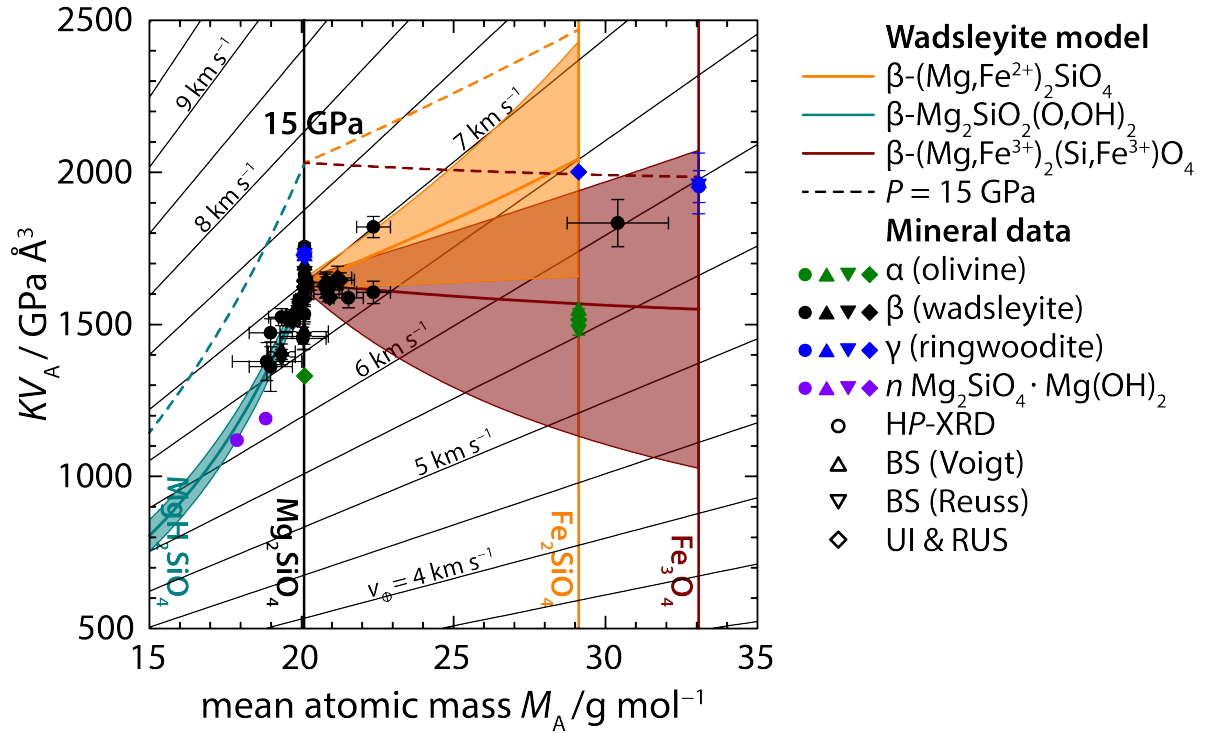


Figure 4.4: The product of bulk modulus K and mean atomic volume V_A as a function of mean atomic mass M_A for wadsleyites (see Appendix Table A.7¹ for references), forsterite (Isaak et al., 1989; Yoneda and Morioka, 1992; Zha et al., 1996), fayalite (Sumino, 1979; Speziale et al., 2004), Mg-ringwoodite (Weidner et al., 1984; Jackson et al., 2000; Higo et al., 2006), Fe-ringwoodite (Rigden and Jackson, 1991), magnetite (Finger et al., 1986; Reichmann and Jacobsen, 2004), hydroxylclinohumite, and hydroxylchondrodite (Ross and Crichton, 2001). Bold lines were calculated from the four-end-member model (Table 4.3). Shaded areas depict uncertainties. Contours in the background show the variation of the bulk sound velocity v_ϕ . HP-XRD high-pressure X-ray diffraction, BS Brillouin spectroscopy, UI ultrasonic interferometry, RUS resonant ultrasound spectroscopy.

creasing ferrous iron content, supporting the conclusion above that an assumption of purely ionic bonding is not valid for iron-bearing wadsleyites. A change in bonding character away from predominantly ionic Mg–O bonds in Mg_2SiO_4 towards an increasing contribution of more covalent Fe^{2+} –O bonds, on the other hand, may explain the deviation from constant KV_A . The incorporation of Fe^{3+} , in contrast, decreases the product KV_A . Most of the data plot between the two opposing trends further suggesting that ferric iron is present in many wadsleyite samples.

In the case of hydration, both experimental data and the EOS model define a clear trend towards lower products KV_A with decreasing mean atomic mass. The steep slope of this trend again contradicts the simple picture of ionic bonding and isostructural cation exchange. In wadsleyite, hydration goes along with creation of vacancies (Smyth, 1994; Inoue et al., 1995; Kudoh et al., 1996) and formation of hydrogen bonds (Kleppe et al., 2001; Kleppe et al., 2006). Exchanging a divalent octahedral cation for two protons results in local structural rearrangements (Jacobsen et al., 2005; Tsuchiya and Tsuchiya, 2009; Deon et al., 2010; Griffin et al., 2013). These fundamental rearrangements are not captured by a simple ionic model based on isostructural cation exchange.

In addition to the wadsleyite data, Figure 4.4 includes information about the $(\text{Mg,Fe})_2\text{SiO}_4$ polymorphs olivine and ringwoodite. For these structures, the magnesian and ferrous end members exist as stable compounds, and their properties can be measured directly. For both polymorphs, the product KV_A increases with increasing Fe^{2+} content, and the differences between the two end members are similar to the difference calculated using our EOS model for wadsleyite. This parallelism between the $(\text{Mg,Fe})_2\text{SiO}_4$ polymorphs not only points to the importance of covalent bonding in mineral structures but also supports the validity of our multi-end-member EOS model for wadsleyite solid solutions.

4.4 Implications

Contradicting previous inferences (Wang et al., 2014; Chang et al., 2015; Mao and Li, 2016), the combination of our new data with a careful reanalysis of previously published work suggests that the incorporation of ferrous iron into wadsleyite increases its bulk modulus. In many mantle minerals including the $(\text{Mg,Fe})_2\text{SiO}_4$ polymorphs and ferropericlase, $(\text{Mg,Fe})\text{O}$, as an adequate standard material for the behavior of $M\text{--O}$ bonds ($M = \text{Mg}^{2+}$, Fe^{2+}), substitution of Mg^{2+} by Fe^{2+} stiffens the crystal structure (Jackson et al., 1978; Hazen, 1993; Stixrude and Lithgow-Bertelloni, 2011) in response to the related gain in covalent bonding. These findings are important for the modelling of seismic wave velocities in potentially iron-enriched mantle regions in Earth’s transition zone. Since the Martian mantle likely contains at least twice the amount of iron as compared to Earth’s mantle (McGetchin and Smith, 1978), our model for wadsleyite $(\text{Mg,Fe})_2\text{SiO}_4$ solid solutions will also facilitate the interpretation of future seismic data of the deep Martian mantle provided by the InSight space mission.

For example, the bulk sound velocity $v_\phi = (KV_A/M_A)^{1/2}$ can be directly obtained from our model neglecting the small ($\sim 1\%$) isothermal to adiabatic conversion for the bulk modulus. The contours in Figure 4.4 show lines of constant bulk sound velocity. Changing the wadsleyite composition away from pure Mg_2SiO_4 and along the trends between the end members reduces the bulk sound velocity as contour lines are crossed. Increasing pressure to 15 GPa shifts the trends between the end members of our model (dotted lines in Fig. 4.4) to higher bulk sound velocities. However, the mutual differences in bulk sound velocity among the end members are retained with Mg_2SiO_4 being the fastest and Fe_3O_4 the slowest. This conclusion, however, only holds for $K'_0 = 4$ for every end member. Our P - V data clearly show that $K'_0 > 4$ for iron-bearing wadsleyite (Table 4.2) while the values for K'_0 reported in the literature not only cover a wide range but also contradict each other for specific compositions (Mao et al., 2011; Chang et al., 2015). Future studies are needed to accurately determine the pressure derivative of the bulk modulus and to clarify whether changes in composition may lead to velocity crossovers for specific wadsleyite compositions at high pressures as observed for forsterite (Mao et al., 2010).

Acknowledgments

We thank A. Potzel and D. Krause for electron microprobe analyses and R. Njul and H. Schulze for polishing the crystal sections. This research was supported through the project “GeoMaX”, funded under the Emmy-Noether Program of the German Science Foundation (MA4534/3-1). H. M. acknowledges support from the Bavarian Academy of Sciences. The

FEI Scios DualBeam machine at the Bayerisches Geoinstitut (University of Bayreuth) was supported by the German Science Foundation under Grant INST 91/315-1 FUGG. This study was further supported by the German Science Foundation through grant GRK 2156/1.

Author Contributions

J. Buchen selected and characterized wadsleyite single crystals, performed the experiments, analyzed the data, proposed to construct and constructed the multi-end-member equation of state model, and wrote the manuscript. H. Marquardt proposed to study wadsleyite single crystals and to load two crystals inside the same diamond anvil cell and commented on the manuscript. T. Boffa Ballaran proposed to determine the equation of state, supervised X-ray diffraction experiments and data analysis, and commented on the manuscript. T. Kawazoe synthesized wadsleyite single crystals and commented on the manuscript. C. McCammon recorded and analyzed the Mössbauer spectrum and commented on the manuscript.

Supplementary Materials

See appendix A.1 on page 175 for Supplementary Methods, Figures, and Tables.

References

- Agee, C. B. (1998). Phase transformations and seismic structure in the upper mantle and transition zone. *Rev. Mineral.* **37**, 165–203.
- Akaogi, M., E. Ito, and A. Navrotsky (1989). Olivine-modified spinel-spinel transitions in the system $\text{Mg}_2\text{SiO}_4 - \text{Fe}_2\text{SiO}_4$: Calorimetric measurements, thermochemical calculation, and geophysical application. *J. Geophys. Res.: Solid Earth* **94**, 15671–15685.
- Anderson, D. L. and O. L. Anderson (1970). The bulk modulus-volume relationship for oxides. *J. Geophys. Res.* **75**, 3494–3500.
- Angel, R. J. (2000). Equations of state. *Rev. Mineral. Geochem.* **41**, 35–59.
- (2003). Automated profile analysis for single-crystal diffraction data. *J. Appl. Crystallogr.* **36**, 295–300.
- Angel, R. J. and L. W. Finger (2011). *SINGLE*: a program to control single-crystal diffractometers. *J. Appl. Crystallogr.* **44**, 247–251.
- Angel, R. J., M. Alvaro, and J. Gonzalez-Platas (2014). EosFit7c and a Fortran module (library) for equation of state calculations. *Z. Kristallogr. - Cryst. Mater.* **229**, 405–419.
- Bina, C. R. and B. J. Wood (1987). Olivine-spinel transitions: Experimental and thermodynamic constraints and implications for the nature of the 400-km seismic discontinuity. *J. Geophys. Res.: Solid Earth* **92**, 4853–4866.
- Birch, F. (1947). Finite elastic strain of cubic crystals. *Phys. Rev.* **71**, 809–824.
- Bolfan-Casanova, N., M. Muñoz, C. McCammon, E. Deloule, A. Férot, S. Demouchy, L. France, D. Andrault, and S. Pascarelli (2012). Ferric iron and water incorporation in wadsleyite under hydrous and oxidizing conditions: A XANES, Mössbauer, and SIMS study. *Am. Mineral.* **97**, 1483–1493.

- Chang, Y.-Y., S. D. Jacobsen, C. R. Bina, S.-M. Thomas, J. R. Smyth, D. J. Frost, T. Boffa Ballaran, C. A. McCammon, E. H. Hauri, T. Inoue, et al. (2015). Comparative compressibility of hydrous wadsleyite and ringwoodite: Effect of H₂O and implications for detecting water in the transition zone. *J. Geophys. Res.: Solid Earth* **120**, 8259–8280.
- Chung, D. H. (1972). Birch's law: Why is it so good? *Science* **177**, 261–263.
- Demouchy, S., E. Deloule, D. J. Frost, and H. Keppler (2005). Pressure and temperature-dependence of water solubility in Fe-free wadsleyite. *Am. Mineral.* **90**, 1084–1091.
- Deon, F., M. Koch-Müller, D. Rhede, M. Gottschalk, R. Wirth, and S.-M. Thomas (2010). Location and quantification of hydroxyl in wadsleyite: New insights. *Am. Mineral.* **95**, 312–322.
- Finger, L. W., R. M. Hazen, and A. M. Hofmeister (1986). High-pressure crystal chemistry of spinel (MgAl₂O₄) and Magnetite (Fe₃O₄): Comparisons with silicate spinels. *Phys. Chem. Miner.* **13**, 215–220.
- Finger, L. W., R. M. Hazen, J. Zhang, J. Ko, and A. Navrotsky (1993). The effect of Fe on the crystal structure of wadsleyite β -(Mg_{1-x}Fe_x)₂SiO₄, 0.00 \leq x \leq 0.40. *Phys. Chem. Miner.* **19**, 361–368.
- Frost, D. J. (2003). The structure and sharpness of (Mg,Fe)₂SiO₄ phase transformations in the transition zone. *Earth Planet. Sci. Lett.* **216**, 313–328.
- (2008). The upper mantle and transition zone. *Elements* **4**, 171–176.
- Frost, D. J. and D. Dolejš (2007). Experimental determination of the effect of H₂O on the 410-km seismic discontinuity. *Earth Planet. Sci. Lett.* **256**, 182–195.
- Frost, D. J. and C. A. McCammon (2009). The effect of oxygen fugacity on the olivine to wadsleyite transformation: Implications for remote sensing of mantle redox state at the 410 km seismic discontinuity. *Am. Mineral.* **94**, 872–882.
- Griffin, J. M., A. J. Berry, D. J. Frost, S. Wimperis, and S. E. Ashbrook (2013). Water in the Earth's mantle: a solid-state NMR study of hydrous wadsleyite. *Chem. Sci.* **4**, 1523–1538.
- Haussühl, S. (2007). *Physical Properties of Crystals: An Introduction*. Wiley-VCH, Weinheim, 439 pp.
- Hazen, R. M. (1993). Comparative compressibilities of silicate spinels: Anomalous behavior of (Mg,Fe)₂SiO₄. *Science* **259**, 206–209.
- Hazen, R. M. and L. W. Finger (1979). Bulk modulus–volume relationship for cation-anion polyhedra. *J. Geophys. Res.* **84**, 6723–6728.
- Hazen, R. M., J. Zhang, and J. Ko (1990). Effects of Fe/Mg on the compressibility of synthetic wadsleyite: β -(Mg_{1-x}Fe_x)₂SiO₄ ($x \leq 0.25$). *Phys. Chem. Miner.* **17**, 416–419.
- Hazen, R. M., M. B. Weinberger, H. Yang, and C. T. Prewitt (2000a). Comparative high-pressure crystal chemistry of wadsleyite, β -(Mg_{1-x}Fe_x)₂SiO₄, with $x = 0$ and 0.25. *Am. Mineral.* **85**, 770–777.
- Hazen, R. M., H. Yang, and C. T. Prewitt (2000b). High-pressure crystal chemistry of Fe³⁺-wadsleyite, β -Fe_{2.33}Si_{0.67}O₄. *Am. Mineral.* **85**, 778–783.
- Higo, Y., T. Inoue, B. Li, T. Irifune, and R. C. Liebermann (2006). The effect of iron on the elastic properties of ringwoodite at high pressure. *Phys. Earth Planet. Inter.* **159**, 276–285.
- Hill, R. (1963). Elastic properties of reinforced solids: Some theoretical principles. *J. Mech. Phys. Solids* **11**, 357–372.
- Holl, C. M., J. R. Smyth, S. D. Jacobsen, and D. J. Frost (2008). Effects of hydration on the structure and compressibility of wadsleyite, β -(Mg₂SiO₄). *Am. Mineral.* **93**, 598–607.
- Horiuchi, H. and H. Sawamoto (1981). β -Mg₂SiO₄: Single-crystal X-ray diffraction study. *Am. Mineral.* **66**, 568–575.

- Houser, C. (2016). Global seismic data reveal little water in the mantle transition zone. *Earth Planet. Sci. Lett.* **448**, 94–101.
- Inoue, T (1994). Effect of water on melting phase relations and melt composition in the system $\text{Mg}_2\text{SiO}_4\text{--MgSiO}_3\text{--H}_2\text{O}$ up to 15 GPa. *Phys. Earth Planet. Inter.* **85**, 237–263.
- Inoue, T., H. Yurimoto, and Y. Kudoh (1995). Hydrous modified spinel, $\text{Mg}_{1.75}\text{SiH}_{0.5}\text{O}_4$: A new water reservoir in the mantle transition region. *Geophys. Res. Lett.* **22**, 117–120.
- Isaak, D. G., O. L. Anderson, T. Goto, and I. Suzuki (1989). Elasticity of single-crystal forsterite measured to 1700 K. *J. Geophys. Res.: Solid Earth* **94**, 5895–5906.
- Jackson, I., R. C. Liebermann, and A. E. Ringwood (1978). The elastic properties of $(\text{Mg}_x\text{Fe}_{1-x}\text{O})$ solid solutions. *Phys. Chem. Miner.* **3**, 11–31.
- Jackson, J. M., S. V. Sinogeikin, and J. D. Bass (2000). Sound velocities and elastic properties of $\gamma\text{-Mg}_2\text{SiO}_4$ to 873 K by Brillouin spectroscopy. *Am. Mineral.* **85**, 296–303.
- Jacobsen, S. D., S. Demouchy, D. J. Frost, T. Boffa Ballaran, and J. Kung (2005). A systematic study of OH in hydrous wadsleyite from polarized FTIR spectroscopy and single-crystal X-ray diffraction: Oxygen sites for hydrogen storage in Earth's interior. *Am. Mineral.* **90**, 61–70.
- Jeanloz, R. and R. M. Hazen (1991). Finite-strain analysis of relative compressibilities: Application to the high-pressure wadsleyite phase as an illustration. *Am. Mineral.* **76**, 1765–1768.
- Kantor, I., V. Prakapenka, A. Kantor, P. Dera, A. Kurnosov, S. Sinogeikin, N. Dubrovinskaia, and L. Dubrovinsky (2012). BX90: A new diamond anvil cell design for X-ray diffraction and optical measurements. *Rev. Sci. Instrum.* **83**, 125102.
- Katsura, T., A. Yoneda, D. Yamazaki, T. Yoshino, and E. Ito (2010). Adiabatic temperature profile in the mantle. *Phys. Earth Planet. Inter.* **183**, 212–218.
- Kawamoto, T., R. L. Hervig, and J. R. Holloway (1996). Experimental evidence for a hydrous transition zone in the early Earth's mantle. *Earth Planet. Sci. Lett.* **142**, 587–592.
- Kawazoe, T., J. Buchen, and H. Marquardt (2015). Synthesis of large wadsleyite single crystals by solid-state recrystallization. *Am. Mineral.* **100**, 2336–2339.
- Kawazoe, T., A. Chaudhari, J. R. Smyth, and C. McCammon (2016). Coupled substitution of Fe^{3+} and H^+ for Si in wadsleyite: A study by polarized infrared and Mössbauer spectroscopies and single-crystal X-ray diffraction. *Am. Mineral.* **101**, 1236–1239.
- Keppler, H. and J. R. Smyth (2005). Optical and near infrared spectra of ringwoodite to 21.5 GPa: Implications for radiative heat transport in the mantle. *Am. Mineral.* **90**, 1209–1212.
- King, H. E. and L. W. Finger (1979). Diffracted beam crystal centering and its application to high-pressure crystallography. *J. Appl. Crystallogr.* **12**, 374–378.
- Kleppe, A. K., A. P. Jephcoat, H. Olijnyk, A. E. Slesinger, S. C. Kohn, and B. J. Wood (2001). Raman spectroscopic study of hydrous wadsleyite ($\beta\text{-Mg}_2\text{SiO}_4$) to 50 GPa. *Phys. Chem. Miner.* **28**, 232–241.
- Kleppe, A. K., A. P. Jephcoat, and J. R. Smyth (2006). High-pressure Raman spectroscopic study of Fo_{90} hydrous wadsleyite. *Phys. Chem. Miner.* **32**, 700–709.
- Klotz, S., J.-C. Chervin, P. Munsch, and G. Le Marchand (2009). Hydrostatic limits of 11 pressure transmitting media. *J. Phys. D: Appl. Phys.* **42**, 075413.
- Koch, M., A. B. Woodland, and R. J. Angel (2004). Stability of spinelloid phases in the system $\text{Mg}_2\text{SiO}_4\text{--Fe}_2\text{SiO}_4\text{--Fe}_3\text{O}_4$ at 1100 °C and up to 10.5 GPa. *Phys. Earth Planet. Inter.* **143–144**, 171–183.

- Kudoh, Y. and T. Inoue (1999). Mg-vacant structural modules and dilution of the symmetry of hydrous wadsleyite, β - $\text{Mg}_{2-x}\text{SiH}_{2x}\text{O}_4$ with $0.00 \leq x \leq 0.25$. *Phys. Chem. Miner.* **26**, 382–388.
- Kudoh, Y., T. Inoue, and H. Arashi (1996). Structure and crystal chemistry of hydrous wadsleyite, $\text{Mg}_{1.75}\text{SiH}_{0.5}\text{O}_4$: possible hydrous magnesium silicate in the mantle transition zone. *Phys. Chem. Miner.* **23**, 461–469.
- Kurnosov, A., I. Kantor, T. Boffa-Ballaran, S. Lindhardt, L. Dubrovinsky, A. Kuznetsov, and B. H. Zehnder (2008). A novel gas-loading system for mechanically closing of various types of diamond anvil cells. *Rev. Sci. Instrum.* **79**, 045110.
- Kurnosov, A., H. Marquardt, D. J. Frost, T. Boffa Ballaran, and L. Ziberna (2017). Evidence for a Fe^{3+} -rich pyrolitic lower mantle from (Al,Fe)-bearing bridgmanite elasticity data. *Nature* **543**, 543–546.
- Libowitzky, E. and G. R. Rossman (1996). Principles of quantitative absorbance measurements in anisotropic crystals. *Phys. Chem. Miner.* **23**, 319–327.
- (1997). An IR absorption calibration for water in minerals. *Am. Mineral.* **82**, 1111–1115.
- Litasov, K. D., A. Shatskiy, E. Ohtani, and T. Katsura (2011). Systematic study of hydrogen incorporation into Fe-free wadsleyite. *Phys. Chem. Miner.* **38**, 75–84.
- Mao, Z. and X. Y. Li (2016). Effect of hydration on the elasticity of mantle minerals and its geophysical implications. *Sci. China: Earth Sci.* **59**, 873–888.
- Mao, Z., S. D. Jacobsen, F. M. Jiang, J. R. Smyth, C. M. Holl, D. J. Frost, and T. S. Duffy (2008). Single-crystal elasticity of wadsleyites, β - Mg_2SiO_4 , containing 0.37–1.66 wt.% H_2O . *Earth Planet. Sci. Lett.* **268**, 540–549.
- Mao, Z., S. D. Jacobsen, F. Jiang, J. R. Smyth, C. M. Holl, D. J. Frost, and T. S. Duffy (2010). Velocity crossover between hydrous and anhydrous forsterite at high pressures. *Earth Planet. Sci. Lett.* **293**, 250–258.
- Mao, Z., S. D. Jacobsen, D. J. Frost, C. A. McCammon, E. H. Hauri, and T. S. Duffy (2011). Effect of hydration on the single-crystal elasticity of Fe-bearing wadsleyite to 12 GPa. *Am. Mineral.* **96**, 1606–1612.
- Marquardt, H. and K. Marquardt (2012). Focused ion beam preparation and characterization of single-crystal samples for high-pressure experiments in the diamond-anvil cell. *Am. Mineral.* **97**, 299–304.
- McCammon, C. A., D. J. Frost, J. R. Smyth, H. M. S. Laustsen, T. Kawamoto, N. L. Ross, and P. A. van Aken (2004). Oxidation state of iron in hydrous mantle phases: implications for subduction and mantle oxygen fugacity. *Phys. Earth Planet. Inter.* **143–144**, 157–169.
- McGetchin, T. R. and J. R. Smith (1978). The mantle of Mars: Some possible geological implications of its high density. *Icarus* **34**, 512–536.
- McMillan, P. F., M. Akaogi, R. K. Sato, B. Poe, and J. Foley (1991). Hydroxyl groups in β - Mg_2SiO_4 . *Am. Mineral.* **76**, 354–360.
- Meng, Y., D. J. Weidner, and Y. Fei (1993). Deviatoric stress in a quasi-hydrostatic diamond anvil cell: Effect on the volume-based pressure calibration. *Geophys. Res. Lett.* **20**, 1147–1150.
- Mrosko, M., M. Koch-Müller, C. McCammon, D. Rhede, J. R. Smyth, and R. Wirth (2015). Water, iron, redox environment: effects on the wadsleyite–ringwoodite phase transition. *Contrib. Mineral. Petrol.* **170**, 9.
- Nishihara, Y., T. Shinmei, and S.-i. Karato (2008). Effect of chemical environment on the hydrogen-related defect chemistry in wadsleyite. *Am. Mineral.* **93**, 831–843.

- Núñez-Valdez, M., P. da Silveira, and R. M. Wentzcovitch (2011). Influence of iron on the elastic properties of wadsleyite and ringwoodite. *J. Geophys. Res.: Solid Earth* **116**, B12207.
- Núñez-Valdez, M., Z. Wu, Y. G. Yu, and R. M. Wentzcovitch (2013). Thermal Elasticity of $(\text{Fe}_x, \text{Mg}_{1-x})_2\text{SiO}_4$ olivine and wadsleyite. *Geophys. Res. Lett.* **40**, 290–294.
- Nye, J. F. (1985). *Physical Properties of Crystals: Their Representation by Tensors and Matrices*. Oxford University Press, Oxford, 329 pp.
- O'Neill, H. St.C., C. A. McCammon, D. Canil, D. C. Rubie, C. R. Ross II, and F. Seifert (1993). Mössbauer spectroscopy of mantle transition zone phases and determination of minimum Fe^{3+} content. *Am. Mineral.* **78**, 456–460.
- Paterson, M. S. (1982). The determination of hydroxyl by infrared absorption in quartz, silicate glasses and similar materials. *Bull. Mineral.* **105**, 20–29.
- Prescher, C., C. McCammon, and L. Dubrovinsky (2012). MossA: a program for analyzing energy-domain Mössbauer spectra from conventional and synchrotron sources. *J. Appl. Crystallogr.* **45**, 329–331.
- Reichmann, H. J. and S. D. Jacobsen (2004). High-pressure elasticity of a natural magnetite crystal. *Am. Mineral.* **89**, 1061–1066.
- Reuss, A. (1929). Berechnung der Fließgrenze von Mischkristallen auf Grund der Plastizitätsbedingung für Einkristalle. *Z. Angew. Math. Mech.* **9**, 49–58 (in German).
- Richmond, N. C. and J. P. Brodholt (2000). Incorporation of Fe^{3+} into forsterite and wadsleyite. *Am. Mineral.* **85**, 1155–1158.
- Rigden, S. M. and I. Jackson (1991). Elasticity of germanate and silicate spinels at high pressure. *J. Geophys. Res.: Solid Earth* **96**, 9999–10006.
- Ringwood, A. E. (1991). Phase transformations and their bearing on the constitution and dynamics of the mantle. *Geochim. Cosmochim. Acta* **55**, 2083–2110.
- Ringwood, A. E. and A. Major (1970). The system $\text{Mg}_2\text{SiO}_4\text{-Fe}_2\text{SiO}_4$ at high pressures and temperatures. *Phys. Earth Planet. Inter.* **3**, 89–108.
- Ross, N. L. (1997). Optical absorption spectra of transition zone minerals and implications for radiative heat transport. *Phys. Chem. Earth* **22**, 113–118.
- Ross, N. L. and W. A. Crichton (2001). Compression of synthetic hydroxylclinohumite $[\text{Mg}_9\text{Si}_4\text{O}_{16}(\text{OH})_2]$ and hydroxylchondrodite $[\text{Mg}_5\text{Si}_2\text{O}_8(\text{OH})_2]$. *Am. Mineral.* **86**, 990–996.
- Sawamoto, H. and H. Horiuchi (1990). β $(\text{Mg}_{0.9}, \text{Fe}_{0.1})_2\text{SiO}_4$: Single crystal structure, cation distribution, and properties of coordination polyhedra. *Phys. Chem. Miner.* **17**, 293–300.
- Schulze, K., J. Buchen, K. Marquardt, and H. Marquardt (2017). Multi-sample loading technique for comparative physical property measurements in the diamond-anvil cell. *High Pressure Res.* **37**, 159–169.
- Shearer, P. M. (2000). Upper mantle seismic discontinuities. In: *Earth's Deep Interior: Mineral Physics and Tomography From the Atomic to the Global Scale*. Ed. by S.-i. Karato, A. Forte, R. Liebermann, G. Masters, and L. Stixrude. American Geophysical Union, Washington, DC, 115–131.
- Sinogeikin, S. V., T. Katsura, and J. D. Bass (1998). Sound velocities and elastic properties of Fe-bearing wadsleyite and ringwoodite. *J. Geophys. Res.: Solid Earth* **103**, 20819–20825.
- Smyth, J. R. (1994). A crystallographic model for hydrous wadsleyite (β - Mg_2SiO_4): An ocean in the Earth's interior? *Am. Mineral.* **79**, 1021–1024.
- Smyth, J. R. and D. J. Frost (2002). The effect of water on the 410-km discontinuity: An experimental study. *Geophys. Res. Lett.* **29**, 123.

- Smyth, J. R., T. Kawamoto, S. D. Jacobsen, R. J. Swope, R. L. Hervig, and J. R. Holloway (1997). Crystal structure of monoclinic hydrous wadsleyite [β -(Mg,Fe) $_2$ SiO $_4$]. *Am. Mineral.* **82**, 270–275.
- Smyth, J. R., N. Bolfan-Casanova, D. Avignant, M. El-Ghozzi, and S. M. Hirner (2014). Tetrahedral ferric iron in oxidized hydrous wadsleyite. *Am. Mineral.* **99**, 458–466.
- Speziale, S., T. S. Duffy, and R. J. Angel (2004). Single-crystal elasticity of fayalite to 12 GPa. *J. Geophys. Res.: Solid Earth* **109**, B12202.
- Stixrude, L. and C. Lithgow-Bertelloni (2005). Thermodynamics of mantle minerals – I. Physical properties. *Geophys. J. Int.* **162**, 610–632.
- (2011). Thermodynamics of mantle minerals – II. Phase equilibria. *Geophys. J. Int.* **184**, 1180–1213.
- Sumino, Y. (1979). The elastic constants of Mn $_2$ SiO $_4$, Fe $_2$ SiO $_4$ and Co $_2$ SiO $_4$, and the elastic properties of olivine group minerals at high temperature. *J. Phys. Earth* **27**, 209–238.
- Takahashi, T. and L.-G. Liu (1970). Compression of ferromagnesian garnets and the effect of solid solutions on the bulk modulus. *J. Geophys. Res.* **75**, 5757–5766.
- Tsuchiya, J. and T. Tsuchiya (2009). First principles investigation of the structural and elastic properties of hydrous wadsleyite under pressure. *J. Geophys. Res.: Solid Earth* **114**, B02206.
- Voigt, W. (1928). *Lehrbuch der Kristallphysik*. Teubner, Leipzig, 979 pp. (in German).
- Wang, J., J. D. Bass, and T. Kastura (2014). Elastic properties of iron-bearing wadsleyite to 17.7 GPa: Implications for mantle mineral models. *Phys. Earth Planet. Inter.* **228**, 92–96.
- Watt, J. P., G. F. Davies, and R. J. O’Connell (1976). The elastic properties of composite materials. *Rev. Geophys.* **14**, 541–563.
- Weidner, D. J., H. Sawamoto, S. Sasaki, and M. Kumazawa (1984). Single-crystal elastic properties of the spinel phase of Mg $_2$ SiO $_4$. *J. Geophys. Res.: Solid Earth* **89**, 7852–7860.
- Wood, B. J. (1995). The effect of H $_2$ O on the 410-kilometer seismic discontinuity. *Science* **268**, 74–76.
- Woodland, A. B. and R. J. Angel (1998). Crystal structure of a new spinelloid with the wadsleyite structure in the system Fe $_2$ SiO $_4$ -Fe $_3$ O $_4$ and implications for the Earth’s Mantle. *Am. Mineral.* **83**, 404–408.
- (2000). Phase relations in the system fayalite–magnetite at high pressures and temperatures. *Contrib. Mineral. Petrol.* **139**, 734–747.
- Woodland, A. B., R. J. Angel, and M. Koch (2012). Structural systematics of spinel and spinelloid phases in the system MFe $_2$ O $_4$ -M $_2$ SiO $_4$ with M = Fe $^{2+}$ and Mg. *Eur. J. Mineral.* **24**, 657–668.
- Ye, Y., J. R. Smyth, A. Hushur, M. H. Manghnani, D. Lonappan, P. Dera, and D. J. Frost (2010). Crystal structure of hydrous wadsleyite with 2.8% H $_2$ O and compressibility to 60 GPa. *Am. Mineral.* **95**, 1765–1772.
- Yoneda, A. and M. Morioka (1992). Pressure derivatives of elastic constants of single crystal forsterite. In: *High-Pressure Research: Application to Earth and Planetary Sciences*. Ed. by Y. Syono and M. H. Manghnani. American Geophysical Union, Washington, DC, 207–214.
- Young, T. E., H. W. Green II, A. M. Hofmeister, and D. Walker (1993). Infrared spectroscopic investigation of hydroxyl in β -(Mg,Fe) $_2$ SiO $_4$ and coexisting olivine: Implications for mantle evolution and dynamics. *Phys. Chem. Miner.* **19**, 409–422.
- Yusa, H. and T. Inoue (1997). Compressibility of hydrous wadsleyite (β -phase) in Mg $_2$ SiO $_4$ by high pressure X-ray diffraction. *Geophys. Res. Lett.* **24**, 1831–1834.

- Zha, C.-S., T. S. Duffy, R. T. Downs, H.-K. Mao, and R. J. Hemley (1996). Sound velocity and elasticity of single-crystal forsterite to 16 GPa. *J. Geophys. Res.: Solid Earth* **101**, 17535–17545.
- Zhang, J. S. and J. D. Bass (2016). Sound velocities of olivine at high pressures and temperatures and the composition of Earth's upper mantle. *Geophys. Res. Lett.* **43**, 9611–9618.
- Zhao, J., R. J. Angel, and N. L. Ross (2010). Effects of deviatoric stresses in the diamond-anvil pressure cell on single-crystal samples. *J. Appl. Crystallogr.* **43**, 743–751.

Chapter 5

High-Pressure Elastic Properties of Single Crystals from Sound Wave Velocities: Comparing Self-Consistent Inversion Schemes

Johannes BUCHEN^{a,✉}, Alexander KURNOSOV^a, Hauke MARQUARDT^{a,b}, and Tiziana BOFFA BALLARAN^a

^aBayerisches Geoinstitut, Universität Bayreuth, 95440 Bayreuth, Germany

^bDepartment of Earth Sciences, University of Oxford, Oxford OX1 3AN, United Kingdom

✉ johannes.buchen@uni-bayreuth.de

This chapter has been prepared for submission to:

Journal of Applied Crystallography

Abstract

The elastic properties of crystalline materials at high pressures are needed to address a variety of technological and geophysical problems including acoustic and seismic anisotropy. Here we introduce self-consistent strategies for the inversion of single-crystal sound wave velocities determined at high pressures to finite-strain equations that capture the changes in the components of the elastic stiffness tensor as a function of volume and pressure. In comparison to conventional inversion strategies, we found improvements in both precision and accuracy of retrieved elastic stiffness tensors when simultaneously inverting sound wave velocities at all sampled pressures. We compare different inversion strategies and discuss correlations between extracted finite-strain parameters and their systematic errors. The introduced inversion scheme is modular and applicable to any crystal symmetry. The presented solutions for sound wave velocities in elastically anisotropic media can be readily adopted to analyze single-crystal sound wave velocities at a given pressure-temperature combination for any crystal symmetry. Similarly, the finite-strain part can be used to analyze the evolution of the elastic stiffness tensor with pressure without being linked to sound wave velocities. Depending on experimental strategy, sound wave velocities can be inverted in combination with determined unit cell volumes or pressures. The isotropic generalization

may be used to invert sound wave velocities of polycrystalline samples determined at high pressures and high temperatures.

5.1 Introduction

The elastic properties of materials reflect their interatomic forces. High pressures substantially change interatomic distances and therefore the shape of the interatomic potential that ultimately determines the elastic properties. For this reason, the high-pressure elastic behavior of technologically relevant materials receives increasing attention, for example in the field of relaxor ferroelectrics (Ahart et al., 2009; Marquardt et al., 2013) and semiconductors (Decremps et al., 2010). A more intuitive application of high-pressure elasticity arises in the field of geophysics, and in particular seismology, where the elastic properties of minerals and rocks in Earth's interior govern the propagation of seismic waves (Duffy and Anderson, 1989; Stixrude and Lithgow-Bertelloni, 2005; Almqvist and Mainprice, 2017) and influence other processes such as deformation (Karato, 2008) and trace element partitioning (Blundy and Wood, 2003).

At high pressures, elastic properties are commonly derived from the analysis of experimentally determined sound wave velocities (Angel et al., 2009). In particular, complete elastic stiffness tensors of single crystals can be obtained from sound wave velocity measurements on samples compressed in diamond anvil cells using light scattering techniques such as Brillouin spectroscopy (Marquardt et al., 2009; Speziale et al., 2014; Kurnosov et al., 2017) and Impulsively Stimulated Light Scattering (ISLS) (Zaug et al., 1993; Yang et al., 2015) or recently developed phonon imaging methods (Decremps et al., 2010). Conventionally, a set of sound wave velocities determined at a given pressure (or a pressure-temperature combination) is inverted to obtain the elastic stiffness tensor at the respective conditions, and in a second step, the pressure evolution of individual components c_{ijkl} of the elastic stiffness tensor is analyzed by combining results obtained at different pressures (Zha et al., 1998; Sinogeikin and Bass, 2000; Speziale and Duffy, 2002; Speziale et al., 2004; Mao et al., 2011).

As an alternative to the conventional inversion strategy, we introduce and test an inversion procedure that inverts sound wave velocities determined on single crystals along a compression path directly to a set of self-consistent finite-strain equations. Instead of inverting sound wave velocities to elastic stiffness tensors at each experimental pressure, the components c_{ijkl} are replaced by finite-strain expressions, and sound wave velocities at all pressures are jointly inverted to obtain the elastic stiffness tensor at ambient conditions together with the pressure derivatives of its components. This global inversion procedure reduces the number of refined parameters and improves both accuracy and precision in the retrieved elastic stiffness tensors.

5.2 Outline of the Inversion Procedure

The here-discussed inversion procedures can be divided into the description of sound wave velocities in anisotropic media and the finite-strain formalism. Each of these two parts can be used separately to analyze single-crystal sound wave velocities or the pressure evolution of the elastic stiffness tensor, respectively. However, we show in section 5.3 that the linkage

of both parts yields the best results in terms of reproducing the pressure evolution of the elastic stiffness tensor.

5.2.1 Coordinate Systems

All tensor properties and vectors are described in the crystal-physical coordinate system \mathbf{e}_i . This Cartesian reference system is related to the crystallographic system according to the convention (Haussühl, 2007):

$$\begin{aligned} \mathbf{e}_1 &= \mathbf{e}_2 \times \mathbf{e}_3 \\ \mathbf{e}_2 &= \frac{\mathbf{b}^*}{b^*} \\ \mathbf{e}_3 &= \frac{\mathbf{c}}{c} \end{aligned} \quad (5.1)$$

with the crystallographic \mathbf{c} axis and the reciprocal \mathbf{b}^* axis of lengths c and b^* , respectively.

In the case of high-pressure Brillouin spectroscopy experiments, the wave vectors \mathbf{k} of acoustic phonons or sound waves probed in a single crystal typically lie within the same crystallographic plane with unit normal vector \mathbf{n} :

$$\mathbf{n} = \begin{pmatrix} n_1 = \cos \varphi \sin \theta \\ n_2 = \sin \varphi \sin \theta \\ n_3 = \cos \theta \end{pmatrix} \quad (5.2)$$

where θ is the angle between \mathbf{e}_3 and \mathbf{n} , and φ is the angle between \mathbf{e}_1 and the projection of \mathbf{n} into the plane perpendicular to \mathbf{e}_3 . For the unit propagation vector $\mathbf{g} = \mathbf{k}/k$, we then have:

$$\mathbf{g} \cdot \mathbf{n} = 0 \quad (5.3)$$

To describe a rotation of \mathbf{g} around \mathbf{n} by an angle φ' , we fix the unit propagation vector \mathbf{g}_0 for $\varphi' = 0$ to:

$$\mathbf{g}_0 = \frac{\mathbf{e}_3 \times \mathbf{n}}{|\mathbf{e}_3 \times \mathbf{n}|} \quad (5.4)$$

From the components of the unit normal vector (eqn. (5.2)), we obtain from (5.4):

$$\mathbf{g}_0 = \begin{pmatrix} g_{01} = -n_2 / \sin(\cos^{-1} n_3) \\ g_{02} = n_1 / \sin(\cos^{-1} n_3) \\ g_{03} = 0 \end{pmatrix} \quad (5.5)$$

Now, we can define the following rotation system \mathbf{e}'_i :

$$\begin{aligned} \mathbf{e}'_1 &= \mathbf{g}_0 \\ \mathbf{e}'_2 &= \mathbf{e}'_3 \times \mathbf{e}'_1 = \mathbf{n} \times \mathbf{g}_0 \\ \mathbf{e}'_3 &= \mathbf{n} \end{aligned} \quad (5.6)$$

The rotation angle φ' can be linked to an experimental rotation of the crystal, for example with a goniometer, about an angle χ by setting $\varphi' = \chi - \chi_0$ when a rotation to χ_0 rotates the crystal to \mathbf{g}_0 . Any propagation vector in the plane perpendicular to \mathbf{n} can then be expressed in the rotation system as:

$$\mathbf{g}' = \begin{pmatrix} g'_1 = \cos \varphi' = \cos(\chi - \chi_0) \\ g'_2 = \sin \varphi' = \sin(\chi - \chi_0) \\ g'_3 = 0 \end{pmatrix} \quad (5.7)$$

For the transformation of the unit propagation vector from the rotation system \mathbf{e}'_i to the crystal-physical system \mathbf{e}_i , i. e. $\mathbf{g}' \rightarrow \mathbf{g}$, we find:

$$\mathbf{g} = \mathbf{A}\mathbf{g}' \quad (5.8)$$

with the transformation matrix:

$$\mathbf{A} = \begin{pmatrix} g_{01} & n_2 g_{03} - n_3 g_{02} & n_1 \\ g_{02} & n_3 g_{01} - n_1 g_{03} & n_2 \\ g_{03} & n_1 g_{02} - n_2 g_{01} & n_3 \end{pmatrix} \quad (5.9)$$

5.2.2 Sound Wave Velocities in Anisotropic Media

In this section, we focus on sound wave velocities. More complete treatments of sound wave propagation in anisotropic media can be found elsewhere (Auld, 1973; Every, 1980; Jaeken and Cottenier, 2016). The propagation velocities v of acoustic plane waves in an elastically anisotropic medium of density ρ can be obtained by solving the characteristic equation (Nye, 1985; Haussühl, 2007):

$$\left| c_{ijkl} g_j g_l - \rho v^2 \delta_{ik} \right| = \begin{vmatrix} c_{1j1l} g_j g_l - \rho v^2 & c_{1j2l} g_j g_l & c_{1j3l} g_j g_l \\ c_{2j1l} g_j g_l & c_{2j2l} g_j g_l - \rho v^2 & c_{2j3l} g_j g_l \\ c_{3j1l} g_j g_l & c_{3j2l} g_j g_l & c_{3j3l} g_j g_l - \rho v^2 \end{vmatrix} = |A_{ik}| = 0 \quad (5.10)$$

where $A_{ik} = B_{ik} + x \delta_{ik}$ with $B_{ik} = c_{ijkl} g_j g_l$ and $x = -\rho v^2$. The B_{ik} are sums over indices j and l of combinations of components of the adiabatic elastic stiffness tensor c_{ijkl} and components of the unit propagation vector \mathbf{g} (see section 5.2.1).

Writing out the determinant in equation (5.10), we obtain:

$$\begin{aligned} |A_{ik}| = 0 = & x^3 + x^2(B_{11} + B_{22} + B_{33}) \\ & + x(B_{11}B_{22} + B_{22}B_{33} + B_{11}B_{33} - B_{13}B_{31} - B_{12}B_{21} - B_{23}B_{32}) \\ & + B_{11}B_{22}B_{33} + B_{12}B_{23}B_{31} + B_{13}B_{32}B_{21} \\ & - B_{13}B_{31}B_{22} - B_{12}B_{21}B_{33} - B_{23}B_{32}B_{11} \end{aligned} \quad (5.11)$$

with $x = -\rho v^2$. Equation (5.11) resembles a general cubic equation of the form:

$$A_3 x^3 + A_2 x^2 + A_1 x + A_0 = 0 \quad (5.12)$$

From a comparison of (5.11) and (5.12), we find:

$$\begin{aligned} A_3 &= 1 \\ A_2 &= B_{11} + B_{22} + B_{33} \\ A_1 &= B_{11}B_{22} + B_{22}B_{33} + B_{11}B_{33} - B_{13}B_{31} - B_{12}B_{21} - B_{23}B_{32} \\ A_0 &= B_{11}B_{22}B_{33} + B_{12}B_{23}B_{31} + B_{13}B_{32}B_{21} - B_{13}B_{31}B_{22} - B_{12}B_{21}B_{33} - B_{23}B_{32}B_{11} \end{aligned} \quad (5.13)$$

To use Cardano's solution for cubic equations, we define the following auxiliary parameters:

$$\begin{aligned} p &= \frac{9A_3 A_1 - 3A_2^2}{9A_3^2} \\ q &= \frac{2A_2^3 - 9A_3 A_2 A_1 + 27A_3^2 A_0}{27A_3^3} \end{aligned} \quad (5.14)$$

The three solutions of equation (5.10) can then be written in terms of the velocities for two quasi-transversely polarized (shear) waves v_{S1} and v_{S2} and for one quasi-longitudinally polarized (compressional) wave v_P :

$$\rho v_{S1}^2 = -\sqrt{-\frac{4}{3}p} \cos\left(\frac{1}{3} \cos^{-1}\left(-\frac{q}{2} \sqrt{-\frac{27}{p^3}}\right)\right) + \frac{A_2}{3A_3} \quad (5.15)$$

$$\rho v_{S2}^2 = \sqrt{-\frac{4}{3}p} \cos\left(\frac{1}{3} \cos^{-1}\left(-\frac{q}{2} \sqrt{-\frac{27}{p^3}}\right) + \frac{\pi}{3}\right) + \frac{A_2}{3A_3} \quad (5.16)$$

$$\rho v_P^2 = \sqrt{-\frac{4}{3}p} \cos\left(\frac{1}{3} \cos^{-1}\left(-\frac{q}{2} \sqrt{-\frac{27}{p^3}}\right) - \frac{\pi}{3}\right) + \frac{A_2}{3A_3} \quad (5.17)$$

where $v_{S1} < v_{S2} < v_P$.

Together with section 5.2.1, the preceding relations offer a compact way to compute sound wave velocities for any symmetry of the medium, i. e. crystal symmetry, and for any propagation direction. To extract the elastic stiffness tensor from a set of sound wave velocities, the above relations can be used in a least-squares procedure that minimizes the differences between observed and calculated sound wave velocities and treats the components c_{ijkl} of the elastic stiffness tensor as adjustable parameters. Propagation directions can either be described by individual \mathbf{g} vectors or, if coplanar, by a combination of the angles θ , φ , χ_0 , and χ . Depending on the redundancy and spatial distribution of sound wave velocities and their propagation vectors, the orientation of the plane containing coplanar propagation vectors might also be obtained by refining the angles θ , φ , and χ_0 .

5.2.3 Finite-Strain Formulation of High-Pressure Elastic Properties

We follow the self-consistent finite-strain formalism as developed by Stixrude and Lithgow-Bertelloni (2005) but restrict the discussion to those relations relevant for the inversion procedure. Accordingly, we use the Eulerian definition of the finite-strain tensor E_{ij} and assume the finite strain that results from hydrostatic compression to be isotropic, i. e. $E_{ij} = -f_E \delta_{ij}$ with $f_E = [(V_0/V)^{2/3} - 1]/2$ and the unit cell volumes V in the strained state and V_0 at ambient conditions. For a truncation of the Helmholtz free energy expansion after the fourth-order term in finite strain (Stixrude and Lithgow-Bertelloni, 2005), the components of the adiabatic elastic stiffness tensor vary with finite strain and temperature as (Stixrude and Lithgow-Bertelloni, 2005):

$$c_{ijkl} = (1 + 2f_E)^{5/2} \left(c_{ijkl} + (3K_0 c'_{ijkl} - 5c_{ijkl}) f_E \right) \quad (5.18)$$

$$+ \left[6K_0 c'_{ijkl} - 14c_{ijkl} - \frac{3}{2} K_0 \delta_{kl}^{ij} (3K'_0 - 16) \right] f_E^2 \quad (5.19)$$

$$+ \frac{1}{2} \left[9K_0^2 c''_{ijkl} + 3K_0 (c'_{ijkl} + \delta_{kl}^{ij}) (3K'_0 - 16) + 63c_{ijkl} \right] (1 + 2f_E) f_E^2 \quad (5.20)$$

$$- \frac{9}{2} K_0 \delta_{kl}^{ij} \left[K_0 K''_0 + K'_0 (K'_0 - 7) + \frac{143}{9} \right] f_E^3$$

$$+ \left[\gamma_{ij}\gamma_{kl} + \frac{1}{2} (\gamma_{ij}\delta_{kl} + \gamma_{kl}\delta_{ij}) - \eta_{ijkl} \right] \frac{\Delta U_{QH}}{V} - \gamma_{ij}\gamma_{kl} \frac{\Delta(C_V T)}{V} \quad (5.21)$$

$$+ \gamma_{ij}\gamma_{kl} \frac{C_V T}{V} \quad (5.22)$$

with the components c_{ijkl0} of the isothermal elastic stiffness tensor and the isothermal bulk modulus K_0 at ambient conditions. Primed (double-primed) symbols refer to the first (second) pressure derivatives of the respective parameters and $\delta_{kl}^{ij} = -\delta_{ij}\delta_{kl} - \delta_{il}\delta_{jk} - \delta_{jl}\delta_{ik}$. The components of the Grüneisen tensor γ_{ij} and their strain derivatives η_{ijkl} are themselves functions of finite strain (Stixrude and Lithgow-Bertelloni, 2005). The thermal part of the internal energy U_{QH} and the isochoric heat capacity C_V are computed from a quasi-harmonic Debye model (Ita and Stixrude, 1992) with a finite-strain-dependent Debye temperature (Ita and Stixrude, 1992; Stixrude and Lithgow-Bertelloni, 2005). At a given finite strain, ΔU_{QH} and $\Delta(C_V T)$ are the changes in the thermal part of the internal energy U_{QH} and in the product of isochoric heat capacity C_V and temperature T , $C_V T$, respectively, with respect to the reference temperature.

Expressions (5.18) to (5.20) give the second-order (5.18), third-order (5.19), and fourth-order (5.20) contributions of finite strain to the cold part of the respective component of the elastic stiffness tensor. As we assumed the finite strain to be isotropic, the bulk modulus in expressions (5.18) to (5.20) is calculated from the components of the isothermal elastic stiffness tensor according to the Voigt bound (Watt et al., 1976; Stixrude and Lithgow-Bertelloni, 2005):

$$K_0 = c_{ijkl0} \delta_{ij} \delta_{kl} / 9 \quad (5.23)$$

Analogous expressions can be written down for the pressure derivatives K'_0 and K''_0 by replacing the components of the elastic stiffness tensor with their respective pressure derivatives c'_{ijkl0} and c''_{ijkl0} . Expression (5.21) gives the thermal contribution and expression (5.22) the isothermal-to-adiabatic conversion (Wehner and Klein, 1971; Davies, 1974). In the following, we will mainly focus on the cold part of the c_{ijkl} . More details on the thermal contributions can be found in Stixrude and Lithgow-Bertelloni (2005).

Based on expressions (5.18) to (5.22), the components of the adiabatic elastic stiffness tensor at any finite strain and temperature can be combined to the adiabatic bulk modulus K_S and the shear modulus G . For the Voigt bound, this yields the equations for the bulk and shear modulus as a function of finite strain and temperature given by Stixrude and Lithgow-Bertelloni (2005):

$$K_S = (1 + 2f_E)^{5/2} \left(K_0 + (3K_0 K'_0 - 5K_0) f_E \right) \quad (5.24)$$

$$+ \frac{27}{2} (K_0 K'_0 - 4K_0) f_E^2 \quad (5.25)$$

$$+ \frac{3}{2} K_0 \left[K_0 K''_0 + K'_0 (K'_0 - 7) + \frac{143}{9} \right] (3 + 11f_E) f_E^2 \quad (5.26)$$

$$+ (\gamma^2 + \gamma - \eta_B) \frac{\Delta U_{QH}}{V} - \gamma^2 \frac{\Delta(C_V T)}{V} \quad (5.27)$$

$$+ \gamma^2 \frac{C_V T}{V} \quad (5.28)$$

$$G = (1 + 2f_E)^{5/2} \left(G_0 + (3K_0G'_0 - 5G_0)f_E \right) \quad (5.29)$$

$$+ \left[6K_0G'_0 - 24K_0 - 14G_0 - \frac{9}{2}K_0K'_0 \right] f_E^2 \quad (5.30)$$

$$+ \frac{1}{2} \left[9K_0^2G''_0 + 3K_0(G'_0 - 1)(3K'_0 - 16) + 63G_0 \right] (1 + 2f_E) f_E^2 \quad (5.31)$$

$$+ \frac{9}{2}K_0 \left[K_0K''_0 + K'_0(K'_0 - 7) + \frac{143}{9} \right] f_E^3 \Big) - \eta_s \frac{\Delta U_{QH}}{V} \quad (5.32)$$

with the respective (isothermal) moduli K_0 and G_0 at ambient conditions and their first (primed) and second (double-primed) pressure derivatives. The isotropic Grüneisen parameter is related to the Grüneisen tensor by $\gamma = \gamma_{ij} \delta_{ij} / 3$. The derivatives of the Grüneisen parameter with respect to compressional and shear strain, η_B and η_s , are computed from the components η_{ijkl} in the same way as the bulk and shear moduli, respectively, from the components c_{ijkl} of the elastic stiffness tensor (Watt et al., 1976).

The pressure P can be linked to finite strain and temperature by the corresponding equation of state (EOS) (Stixrude and Lithgow-Bertelloni, 2005):

$$P = \frac{1}{3} (1 + 2f_E)^{5/2} \left(9K_0f_E + \frac{27}{2}K_0(K'_0 - 4)f_E^2 \right) \quad (5.33)$$

$$+ \frac{27}{2}K_0 \left(K_0K''_0 + K'_0(K'_0 - 7) + \frac{143}{9} \right) f_E^3 \Big) \quad (5.34)$$

$$+ \gamma \frac{\Delta U_{QH}}{V} \quad (5.35)$$

with up to third-order finite-strain contributions in expression (5.33), fourth-order contributions in (5.34), and the thermal contribution in (5.35). Note that the EOS (5.33)–(5.34) uses the isothermal bulk modulus $K_0 = K_{T0}$ at ambient conditions. At given temperature and finite strain, adiabatic and isothermal bulk moduli are related by (Wehner and Klein, 1971; Davies, 1974):

$$K_S - K_T = \gamma^2 \frac{C_V T}{V} \quad (5.36)$$

i. e. by subtracting the term (5.28) from the adiabatic bulk modulus. Since the differences between the pressure derivatives of the components of the isothermal and adiabatic elastic stiffness tensors and between the pressure derivatives of the isothermal and adiabatic bulk moduli are typically smaller than experimental uncertainties, we will neglect these differences. As a consequence, adiabatic elastic properties can be analyzed along an isotherm using only the (isothermal) cold parts of the c_{ijkl} and the bulk modulus K_S , i. e. with relations (5.18)–(5.20) and (5.24)–(5.26). For pressure calculations, however, the obtained adiabatic bulk modulus at ambient conditions (K_0 in expressions (5.24)–(5.26)) has to be converted to the isothermal modulus before being used in the EOS (5.33)–(5.34).

Expressions (5.18) to (5.22) describe the variation of the components of the elastic stiffness tensor c_{ijkl} with finite strain and temperature and can be inserted into equation (5.10) to compute anisotropic sound wave velocities at a given combination of finite strain and

temperature. In reverse, sets of sound wave velocities determined at different compression states, i. e. at different finite strains or pressures, and temperatures can be used to constrain the parameters in expressions (5.18) to (5.22) by refining them in a least-squares procedure that simultaneously involves all sets of sound wave velocities. The differences between observed and calculated sound wave velocities will then be minimized by adjusting the finite-strain parameters in expressions (5.18) to (5.22) (c_{ijkl0} , c'_{ijkl0} , c''_{ijkl0} , etc.) rather than adjusting the c_{ijkl} at each pressure-temperature combination. In such a global inversion of sound wave velocities, the total number of adjusted parameters will be reduced with respect to the conventional approach where all c_{ijkl} are refined at each pressure-temperature combination.

Finite strains (and densities in eqn. (5.10)) can be directly determined from measurements of the unit cell volume at the same set of conditions where sound wave velocities are determined. Alternatively, unit cell volumes (or densities) can be indirectly constrained by pressure measurements via the EOS (5.33)–(5.35). In this case, the unit cell volumes (or densities) at all pressure-temperature combinations are treated as adjustable parameters that simultaneously have to satisfy equations (5.10) and (5.33)–(5.35).

The evolution of the elastic stiffness tensor with finite strain and temperature can also be analyzed with expressions (5.18) to (5.22) without linking them to sound wave velocities. Note that individual components of the elastic stiffness tensor are linked to each other through the bulk modulus at ambient conditions (eqn. (5.23)). To maintain self-consistency, the variation of individual c_{ijkl} with pressure and temperature should always be analyzed taking into account expressions (5.18)–(5.22) for all other c_{ijkl} at the same time. For example, individually adjusting c_{ijkl0} and c'_{ijkl0} for each c_{ijkl} and calculating the bulk modulus and its pressure derivative at ambient conditions with equation (5.23) using the results for all c_{ijkl} may result in values for the bulk modulus and its pressure derivative that differ from those initially inserted into expressions (5.18)–(5.22) during the refinement.

Although we focus here on the analysis of single-crystal sound wave velocities, relations (5.24)–(5.28) and (5.29)–(5.32) can be coupled to aggregate sound wave velocities in an analogous way with:

$$v_p = \sqrt{\frac{K_S + \frac{4}{3}G}{\rho}} \quad (5.37)$$

$$v_s = \sqrt{\frac{G}{\rho}} \quad (5.38)$$

Instead of inverting single-crystal sound wave velocities to single-crystal finite-strain parameters (c_{ijkl0} , c'_{ijkl0} , c''_{ijkl0} , etc.), aggregate sound wave velocities can be self-consistently inverted to aggregate finite-strain parameters, i. e. K_0 , K'_0 , G_0 , G'_0 , etc..

5.3 Testing Inversion Strategies

To test and compare different inversion strategies, we first generated synthetic sets of single-crystal sound wave velocities at different pressures using known finite-strain parameters. These sets of sound wave velocities were then analyzed using the conventional and global inversion procedures. In contrast to experimental data, analyzing synthetic data allows to assess both accuracy and precision of the results since the initial (or true) finite-strain parameters (marked with an asterisk*) are known. Although we focus here on the analysis of

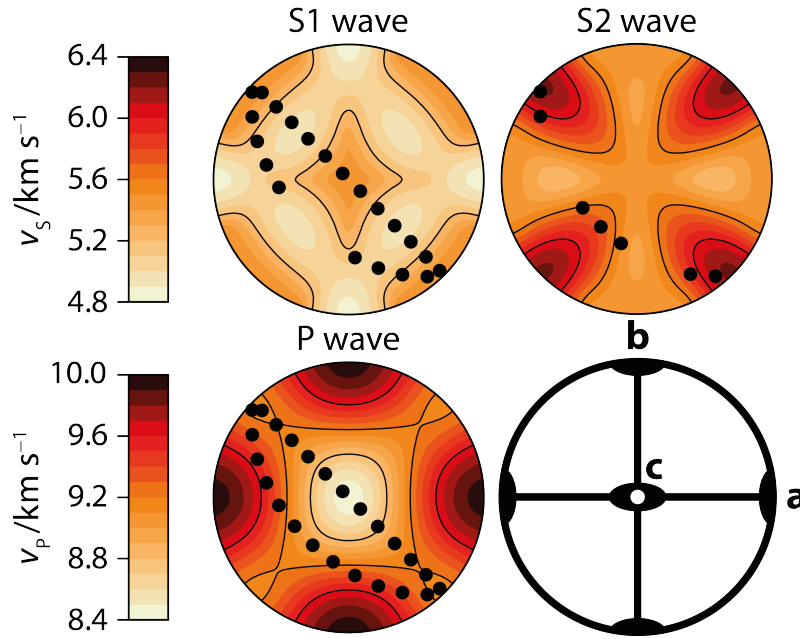


Figure 5.1: Equal-area projections showing sound wave velocities of a wadsleyite single crystal at ambient conditions. Solid black circles indicate propagation directions along which the respective velocities were sampled to generate the synthetic data set.

(synthetic) high-pressure data at ambient temperature, the procedure can be readily modified to include thermal parameters as introduced in section 5.2.3 by taking into account their finite-strain dependencies given by Stixrude and Lithgow-Bertelloni (2005).

5.3.1 Synthetic Data Set

To generate a synthetic data set of single-crystal sound wave velocities, we used a recent experimental data set of sound wave velocities determined on wadsleyite single crystals by Brillouin spectroscopy (Buchen et al., 2018) as template in terms of number and propagation directions of sampled sound wave velocities. As an orthorhombic high-pressure mineral, wadsleyite is well suited to test anisotropic inversion procedures as it involves both relatively low symmetry and the concomitant limitations in determining sound wave velocities, for example due to orientation-dependent photon-phonon scattering efficiency.

Accordingly, we used the third-order finite-strain parameters given by Buchen et al. (2018) to compute sound wave velocities at 11 pressures equally spaced between 0 and 20 GPa, i. e. at pressure steps of 2 GPa. At each pressure, 26 propagation directions were sampled as a function of the rotation angle χ (see section 5.2.1): 13 in the crystallographic (120) plane and 13 in the (243) plane. Individual propagation vectors were separated by a 15° rotation around the plane normal to span an arc of 180° within the respective plane. For the (120) plane, we only retained S1 and P wave velocities, i. e. v_{S1} and v_P . For the (243) plane, the sampling of velocities varied as a function of rotation angle. Figure 5.1 displays the spatial sampling pattern.

In the case of Brillouin spectroscopy on samples inside a diamond anvil cell, sound wave velocities can be typically determined with an accuracy of about 1 % and a precision around 0.5 % (Speziale et al., 2014). Each sampled sound wave velocity v was assigned an absolute synthetic error Δv that was estimated based on a relative error $\Delta v/v$ of random magnitude

between 0.25 % and 0.75 % representing a mean relative precision $\overline{\sigma_p}$ of 0.5 %. Assuming a mean relative accuracy $\overline{\sigma_A}$ of 1 %, we perturbed each individual sampled sound wave velocity to a random value between

$$v - \Delta v \times \overline{\sigma_A} / \overline{\sigma_p} < v < v + \Delta v \times \overline{\sigma_A} / \overline{\sigma_p} \quad (5.39)$$

The statistical contribution to the deviation of each perturbed sound wave velocity from its unperturbed value therefore depends on the assigned error Δv and the ratio between accuracy and precision.

In addition to statistical deviations, misalignments of diamond anvils or sample surfaces as well as uncertainties in calibrations of the scattering angle and frequency shifts might contribute to systematic errors (Zha et al., 1996; Sinogeikin and Bass, 2000). We modeled such systematic errors by shifting the entire set of randomly perturbed S1, S2, and P wave velocities at a given pressure. This systematic perturbation δ varied in magnitude randomly from pressure to pressure between $-1 \% < \delta < 1 \%$. δ was scaled with the respective mean velocity \bar{v} for each type of wave and added as $\delta \times \bar{v}$ to all velocities sampled at a given pressure.

In addition to sound wave velocities, unit cell volumes or pressures are needed to extract finite-strain parameters. We computed unit cell volumes V at each sampled pressure and randomly perturbed their values to

$$V - \Delta V \times \overline{\sigma_A} / \overline{\sigma_p} < V < V + \Delta V \times \overline{\sigma_A} / \overline{\sigma_p} \quad (5.40)$$

with a mean relative precision of $\overline{\sigma_p} = 0.03 \%$ and a mean relative accuracy of $\overline{\sigma_A} = 0.1 \%$. Individual unit cell volumes were assigned random relative errors $\Delta V/V$ between 0.01 % and 0.05 % in magnitude. In analogy, random errors on pressures P were estimated assuming relative errors $\Delta P/P$ between 0.5 % and 1 % with $\overline{\sigma_p} = 0.75 \%$. Pressures were then randomly perturbed to

$$P - \Delta P \times \overline{\sigma_A} / \overline{\sigma_p} < P < P + \Delta P \times \overline{\sigma_A} / \overline{\sigma_p} \quad (5.41)$$

with $\overline{\sigma_A} = 3 \%$ (Mao et al., 1986). While the perturbation of absolute values intended to resemble scatter in experimentally determined quantities, assigned errors served as weights during least-squares minimization procedures (Angel, 2000).

5.3.2 Inversion Strategies

We analyzed the synthetic data set with three different inversion strategies. In accordance with the initial model, we restricted the analysis to third order in finite strain. For all three inversion strategies, initial guesses of adjustable parameters were refined using a least-squares procedure. The unit cell volume at ambient conditions was fixed to the mean value of both sampled (and perturbed) volumes at 0 GPa, $V_0 = 542.53 \text{ \AA}^3$. Sound wave velocities and pressures were assigned weights w based on their estimated errors Δ following the scheme $w = \Delta^{-2}$ (Angel, 2000). Further details about least-squares refinement procedures can be found elsewhere (Press et al., 2007). The angles θ , φ , and χ_0 were fixed in all three inversions strategies considered here. When varied within reasonable uncertainties of few degrees, θ , φ , and χ_0 are not expected to change the results significantly.

The first (1st) or conventional strategy involved the inversion of single-crystal sound wave velocities at a given pressure to elastic stiffness tensors at each pressure. During the

inversion procedure, densities (or unit cell volumes) and orientation parameters were fixed to the synthetic values in the data set. Experimentally, this situation corresponds to either directly determining these quantities by X-ray diffraction, for instance, or estimating the densities from a previously known EOS and the angles θ , φ , and χ_0 from X-ray diffraction at ambient conditions or other observations. The pressure evolution of individual components of the elastic stiffness tensor was subsequently analyzed using the self-consistent formalism described in section 5.2.3 to extract finite-strain parameters.

For the second (2nd) or global inversion strategy, the components c_{ijkl} of the elastic stiffness tensor in equation (5.10) were replaced by expressions (5.18)–(5.19) to link the finite-strain parameters directly to sampled sound wave velocities without explicitly computing elasticity tensors at each pressure. Again, unit cell volumes and orientation parameters were fixed to the synthetic values. Similarly to the 1st inversion strategy, the 2nd strategy does not require to experimentally determine pressures as long as unit cell volumes are directly determined by X-ray diffraction. After the inversion, the components of the elastic stiffness tensor at each sampled pressure can be computed from the retrieved finite-strain parameters using expressions (5.18)–(5.19) for comparison with the results of the first inversion strategy.

As a third (3rd) inversion strategy, we applied the global inversion procedure in combination with sampled pressures instead of unit cell volumes. While finite strains can be directly calculated from sampled unit cell volumes, they have to be indirectly inferred from sampled pressures by including the EOS (5.33) in the inversion procedure. In addition to sound wave velocities, pressures were treated as observations while the unit cell volumes at each pressure were treated as adjustable parameters. Experimentally, this situation corresponds to the determination of sound wave velocities together with pressure as for instance by Brillouin spectroscopy combined with pressure measurements using the ruby fluorescence method.

5.3.3 Inversion Results: Elastic Stiffness Tensors

The adiabatic elastic stiffness tensors at ambient conditions and their pressure derivatives are listed in Table 5.1 as obtained from each inversion strategy. For the components of the elastic stiffness tensor c_{ijkl0} , mean estimated standard deviations (MESD) $\overline{\sigma}$ and mean absolute deviations (MAD) from the initial values $\overline{|c_{ijkl0} - c_{ijkl0}^*|}$ are smallest for the 2nd inversion strategy. For the pressure derivatives c'_{ijkl0} , however, MESDs are still smallest for the 2nd inversion strategy but MADs are slightly smaller for the 1st inversion strategy.

Estimated standard deviations (ESD) σ and absolute deviations (AD) $|c_{ijkl0} - c_{ijkl0}^*|$ for individual components and their pressure derivatives are compared in Figures 5.2a and 5.2b, respectively. The results for all inversion strategies fall beneath the $|c_{ijkl0} - c_{ijkl0}^*| = 2\sigma$ line indicating that doubled ESDs are always larger than ADs from the initial values, i. e. $2\sigma > |c_{ijkl0} - c_{ijkl0}^*|$. Moreover, the 2nd inversion strategy tends to have lower ESDs while ADs are similar between all inversion strategies with few exceptions for pressure derivatives c'_{ijkl0} . We therefore conclude that the global inversion strategies correctly reproduce initial finite-strain parameters within 2σ uncertainty limits. Note that this also holds for the 3rd inversion strategy even though unit cell volumes were not constrained to sampled values but self-consistently refined.

Figure 5.3 shows the components of the elastic stiffness tensors at each sampled pressure for all three inversion strategies. In more than 80 % of direct comparisons, individual c_{ijkl}

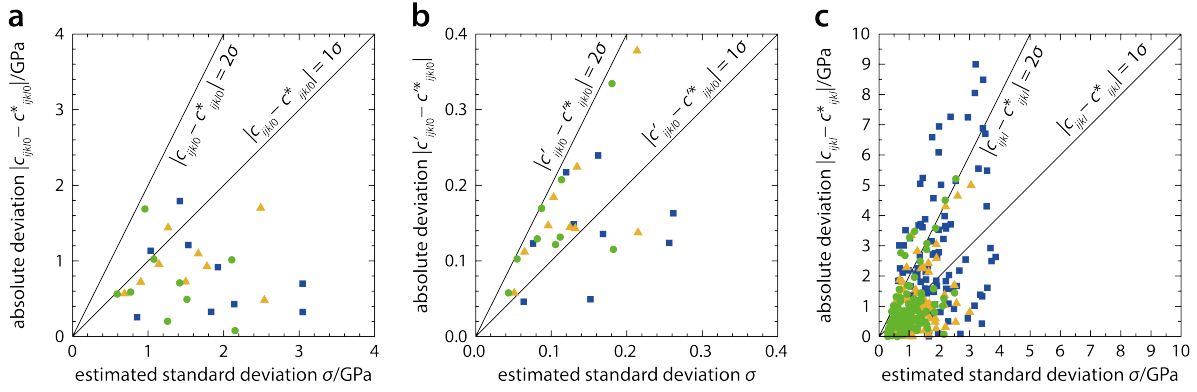


Figure 5.2: Comparison of absolute deviations and estimated standard deviations for the components of the elastic stiffness tensor at ambient conditions (a), for their pressure derivatives (b), and for the components of the elastic stiffness tensor at high pressures (c). Blue squares: 1st inversion strategy; green circles: 2nd inversion strategy; yellow triangles: 3rd inversion strategy.

as obtained with the global inversion strategies are closer to the values of individual c_{ijkl} computed using the initial finite-strain parameters than those obtained from inversions at each pressure, i. e. by the 1st inversion procedure. In more than 90 %, doubled ESDs on individual c_{ijkl} as obtained with the global inversion strategies are smaller than ADs from values computed using the initial finite-strain parameters as opposed to less than 73 % for the 1st or conventional inversion strategy. This improvement in accuracy becomes apparent in Figure 5.2c where the spread in ESDs and ADs of components c_{ijkl} obtained with the 1st inversion strategy by far exceeds the spread produced by global inversion strategies and extends substantially beyond the $|c_{ijkl} - c_{ijkl}^*| = 2\sigma$ line.

With the 1st inversion strategy, we obtained 0.44 as the root of the mean squared correlation coefficient (RMSC) of all 11 individually inverted elastic stiffness tensors. In comparison, the RMSC of the elastic stiffness tensor at ambient conditions as obtained by the 2nd and 3rd inversion strategy amounts to 0.45. For the overall RMSC including all 117 parameters ($9 c_{ijkl}$ at 11 pressures + $9 c_{ijkl0} + 9 c'_{ijkl0}$ for finite-strain equations) refined with the 1st inversion strategy, we obtain 0.41 as compared to 0.40 and 0.36 using the 2nd and 3rd inversion strategy, respectively, and refining 18 (2nd strategy: $9 c_{ijkl0} + 9 c'_{ijkl0}$ for finite-strain equations) and 38 parameters (3rd strategy: 10 unit cell volumes for $P > 0$ GPa + $9 c_{ijkl0} + 9 c'_{ijkl0}$ for finite-strain equations). Even though the total number of refined parameters is substantially reduced using the global inversion procedures, overall correlations between refined parameters are not increased.

In the case of global inversion strategies, reduced ESDs and ADs of individual c_{ijkl} reflect the fact that c_{ijkl} are computed from the refined finite-strain parameters rather than from a direct fit to sound wave velocities. In this way, the impact of systematic errors that bias sampled sound wave velocities at each pressure differently is substantially suppressed. When sound wave velocities are directly inverted to elastic stiffness tensors at each pressure as in the 1st inversion strategy, the self-consistent formalism described in section 5.2.3 provides an alternative way to compensate for systematic errors in tensor components that were inherited from systematic errors in sound wave velocities. Since all inversion strategies yield very similar finite-strain parameters, the simultaneous refinement of all components c_{ijkl0} and their pressure derivatives c'_{ijkl0} , linked to each other through K_0 and K'_0 (eqns. (5.18)–

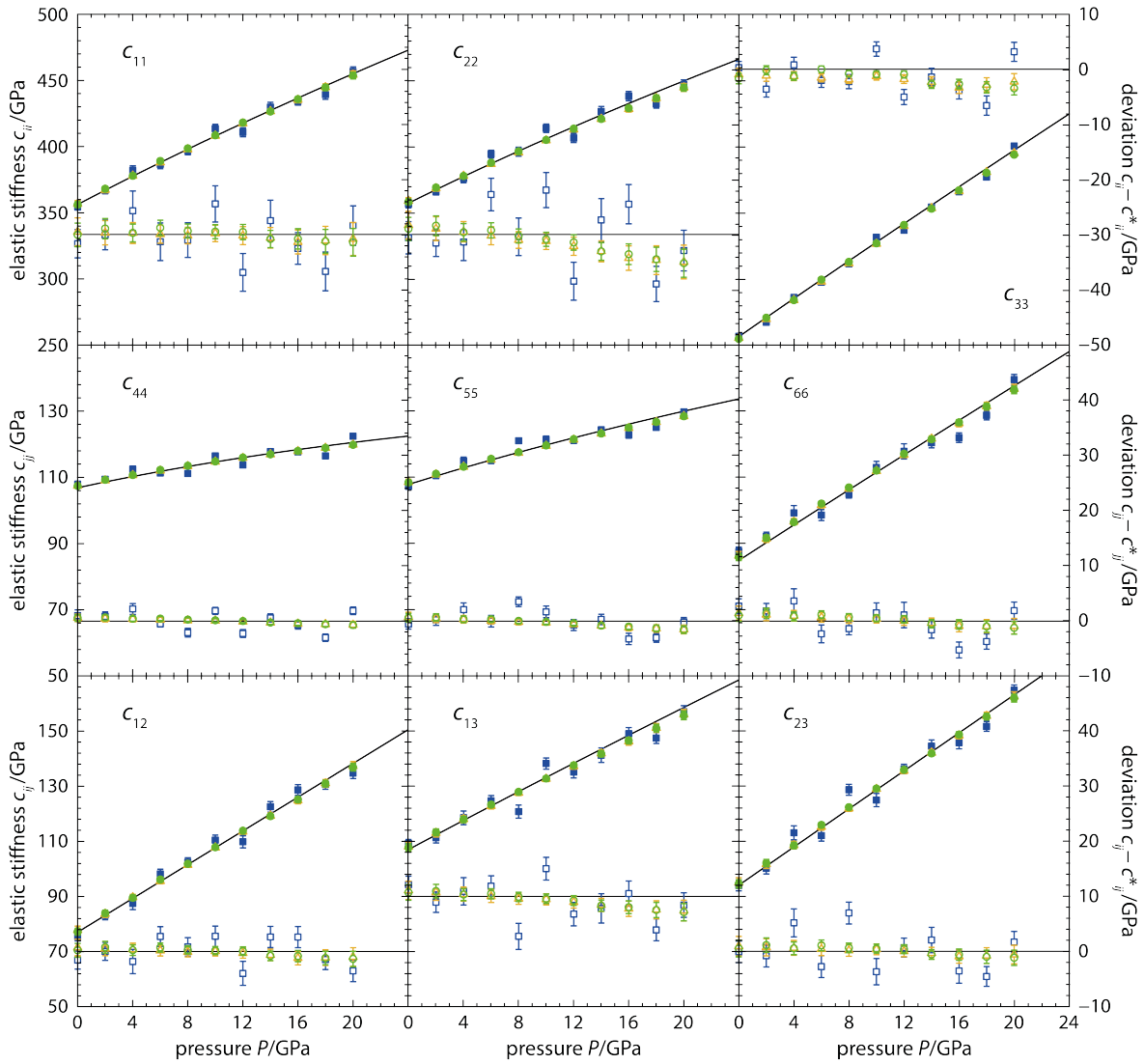


Figure 5.3: Components of the elastic stiffness tensor (contracted index notation; see Table 5.1) at high pressures. Solid symbols: absolute values; open symbols: deviations from initial finite-strain curves (thick black curves); blue squares: 1st inversion strategy; green circles: 2nd inversion strategy; yellow triangles: 3rd inversion strategy.

(5.20) and (5.23)), allows to extract correct finite-strain parameters even from stiffness tensors that are biased by systematic errors.

5.3.4 Inversion Results: Aggregate Elastic Moduli

From the elastic stiffness tensor and the complementary elastic compliance tensor, bounds on the elastic bulk and shear moduli of an isotropic aggregate composed of anisotropic single crystals can be computed (Watt et al., 1976). Here, we focus on the Voigt (V) and Reuss (R) bounds for homogeneous strain and stress throughout the aggregate, respectively, and their arithmetic mean known as the Voigt-Reuss-Hill (VRH) average (Hill, 1952; Watt et al.,

Table 5.1 : Single-crystal finite-strain parameters from different inversion strategies

Elastic stiffness tensor				Pressure derivatives											
<i>ijkl</i>	Initial	1st strategy	2nd strategy	3rd strategy	Initial	1st strategy	2nd strategy	3rd strategy	3rd strategy						
<i>(ij)^a</i>	C_{ijkl}^* (GPa)	C_{ijkl} (GPa)	σ (GPa)	C_{ijkl} (GPa)	σ (GPa)	C_{ijkl}^* (GPa)	C'_{ijkl} (GPa)	σ	C'_{ijkl} (GPa)	σ					
1111	(11)	356	355.30	3.05	355.92	2.15	356.48	2.54	5.5	5.38	0.26	5.38	0.18	5.36	0.21
2222	(22)	357	357.32	3.05	358.01	2.11	358.70	2.49	5.2	5.04	0.26	4.87	0.18	4.82	0.21
3333	(33)	256	254.21	1.42	254.31	0.96	255.04	1.14	7.3	7.15	0.13	7.13	0.09	7.12	0.10
2323	(44)	107	107.26	0.86	107.56	0.59	107.57	0.69	0.9	0.85	0.06	0.84	0.04	0.84	0.05
1313	(55)	108	109.13	1.03	108.59	0.77	108.72	0.90	1.3	1.18	0.08	1.20	0.06	1.19	0.06
1212	(66)	85	86.21	1.53	86.02	1.08	86.44	1.27	2.7	2.48	0.12	2.57	0.08	2.55	0.10
1122	(12)	77	76.67	1.84	77.20	1.26	77.72	1.50	3.1	3.05	0.15	2.98	0.11	2.96	0.12
1133	(13)	107	107.92	1.93	107.71	1.42	108.09	1.67	2.7	2.46	0.16	2.49	0.11	2.48	0.13
2233	(23)	94	94.43	2.14	94.49	1.51	94.93	1.78	3.5	3.36	0.17	3.37	0.11	3.36	0.13
MESD ^b				1.87		1.32		1.55			0.15		0.15		0.13
MAD ^c				0.79		0.71		0.96			0.14		0.15		0.17

^aContracted index notation.

^bMean estimated standard deviation.

^cMean absolute deviation.

Table 5.2: Aggregate finite-strain parameters from different inversion strategies

Aggregate elastic moduli						Pressure derivatives								
	Initial	1st strategy	2nd strategy	3rd strategy	Initial	1st strategy	2nd strategy	3rd strategy	3rd strategy	3rd strategy	3rd strategy			
	M_0^* (GPa)	M_0 (GPa)	σ (GPa)	M_0 (GPa)	σ (GPa)	M_0^* (GPa)	M_0' (GPa)	σ	M_0' (GPa)	σ	M_0' (GPa)	σ		
K_0^V	169.44	169.43	0.91	169.67	0.64	170.19	0.76	4.07	3.92	0.08	3.90	0.05	3.88	0.06
K_0^R	166.73	166.89	1.06	167.07	0.82	167.59	0.94	4.22	4.06	0.15	4.07	0.05	4.04	0.06
K_{0}^{VRH}	167.98	168.16	1.01	168.37	0.78	168.89	0.88	4.13	3.99	0.12	3.98	0.05	3.96	0.06
G_0^V	106.07	106.37	0.56	106.36	0.39	106.51	0.46	1.56	1.48	0.04	1.49	0.03	1.48	0.04
G_0^R	102.60	102.85	0.50	102.83	0.35	103.02	0.41	1.72	1.62	0.05	1.64	0.03	1.63	0.04
G_0^{VRH}	104.34	104.61	0.53	104.59	0.37	104.77	0.44	1.64	1.55	0.05	1.57	0.03	1.56	0.04

Standard deviations in *italics* cannot be obtained from refinements and were adopted from the Voigt bound.

1976). As mentioned in section 5.2.3, the Voigt bounds can be directly computed from the components of the elastic stiffness tensor (Hill, 1952; Watt et al., 1976):

$$K^V = [c_{1111} + c_{2222} + c_{3333} + 2(c_{1122} + c_{1133} + c_{2233})] / 9 \quad (5.42)$$

$$G^V = [c_{1111} + c_{2222} + c_{3333} + 3(c_{2323} + c_{1313} + c_{1212}) - (c_{1122} + c_{1133} + c_{2233})] / 15 \quad (5.43)$$

Hence for the Voigt bounds, the finite-strain parameters K_0 and G_0 of expressions (5.24)–(5.26) and (5.29)–(5.31) can be directly calculated from the components of the elastic stiffness tensor at ambient conditions c_{ijkl0} and the corresponding pressure derivatives K'_0 and G'_0 (K''_0 and G''_0) by replacing the c_{ijkl0} in equations (5.42) and (5.43) by the respective pressure derivatives c'_{ijkl0} (and c''_{ijkl0} for fourth-order terms).

While the Voigt bounds are provided by the inversion procedure as a byproduct, the Reuss bounds in general require the calculation of the elastic compliance tensor by matrix inversion from the elastic stiffness tensor. The Reuss bounds are calculated from the components of the elastic compliance tensor s_{ijkl} as (Hill, 1952; Watt et al., 1976):

$$K^R = 1 / [s_{1111} + s_{2222} + s_{3333} + 2(s_{1122} + s_{1133} + s_{2233})] \quad (5.44)$$

$$G^R = 15 / [4(s_{1111} + s_{2222} + s_{3333}) + 3(s_{2323} + s_{1313} + s_{1212}) - 4(s_{1122} + s_{1133} + s_{2233})] \quad (5.45)$$

To describe the pressure evolution of the Reuss bounds on the bulk and shear moduli with expressions (5.24)–(5.26) and (5.29)–(5.31), we need the bounds at ambient conditions, i. e. K_0^R and G_0^R , and their pressure derivatives.

At ambient conditions and at each sampled pressure, K^R and G^R can be computed from the c_{ijkl} as explained above. Their pressure derivatives, however, are not readily calculated from available results of the inversion procedures. Therefore, we computed the Reuss bounds at each sampled pressure (or unit cell volume) and fit expressions (5.24)–(5.25) and (5.29)–(5.30) to the finite-strain dependencies of K^R and G^R . To maintain self-consistency, K_0^R and G_0^R were fixed to their values calculated from the components of the elastic compliance tensor s_{ijkl0} at ambient conditions, and only their pressure derivatives were treated as adjustable parameters. Since both expressions (5.24)–(5.26) and (5.29)–(5.31) contain the pressure derivatives of the bulk modulus K'_0 (and K''_0), K'_0 and G'_0 (and K''_0 and G''_0 for fourth-order terms) are correlated and have to be refined simultaneously.

For the Voigt-Reuss-Hill averages, elastic moduli were computed at ambient conditions and at each sampled pressure as:

$$K^{VRH} = (K^V + K^R) / 2 \quad (5.46)$$

$$G^{VRH} = (G^V + G^R) / 2 \quad (5.47)$$

and analyzed in an analogous way to the Reuss bounds to obtain corresponding pressure derivatives K'_0 and G'_0 . The results for all inversion strategies are collected in Table 5.2, and ADs are plotted versus ESDs in Figure 5.4.

ESDs of aggregate moduli at ambient conditions were calculated by propagating the ESDs of individual components of the elastic stiffness tensor at ambient conditions through equations (5.42)–(5.43), (5.44)–(5.45), and (5.46)–(5.47) for each inversion strategy. ESDs of the pressure derivatives K'_0 and G'_0 (and K''_0 and G''_0) can be obtained by fitting expressions (5.24)–(5.26) and (5.29)–(5.31) to the finite-strain dependencies of K and G and refining the moduli at ambient conditions together with their pressure derivatives to capture mutual correlations between parameters. This approach, however, is appropriate

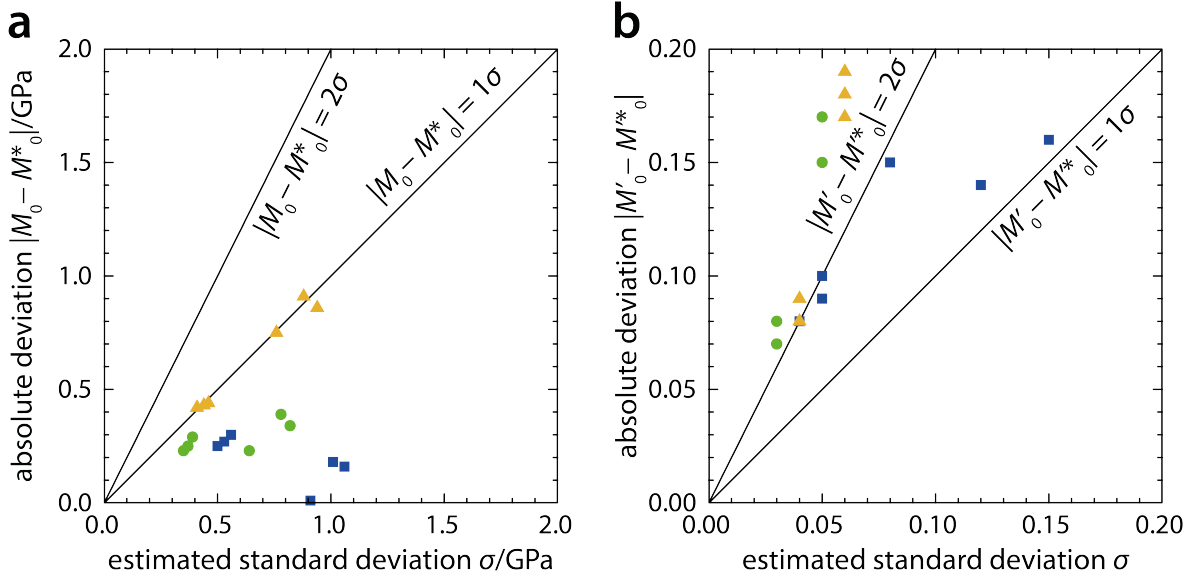


Figure 5.4: Comparison of absolute deviations and estimated standard deviations for elastic moduli at ambient conditions (a) and their pressure derivatives (b). For each modulus, the results for Voigt and Reuss bounds as well as for the Voigt-Reuss-Hill average are shown. Blue squares: 1st inversion strategy; green circles: 2nd inversion strategy; yellow triangles: 3rd inversion strategy.

only for the results of the 1st inversion strategy because in this case the original scatter in sound wave velocities translates into scatter in aggregate moduli via individual elasticity tensors. For the 2nd and 3rd inversion strategies, ESDs of pressure derivatives of the moduli would be underestimated by combined refinements of aggregate moduli and their pressure derivatives at ambient conditions since the aggregate moduli at high pressures were computed using the derived single-crystal finite-strain equations and therefore do not anymore represent the scatter of the original data. Instead, we computed the ESDs for the pressure derivatives of aggregate moduli of the 2nd and 3rd inversion strategy by propagating the ESDs of pressure derivatives of components of the elastic stiffness tensor through equations (5.42) and (5.43).

While the results for K_0 and G_0 and for all bounds and inversion strategies comply with the condition $2\sigma > |M_0 - M_0^*|$ (Fig. 5.4a), only the 1st inversion strategy yields ESDs for pressure derivatives K'_0 and G'_0 that fulfill the analogous condition $2\sigma > |M'_0 - M_0^*|$ (Fig. 5.4b). ADs from the initial values, however, have similar magnitudes for all three inversion strategies implying similar accuracy. Since the ESDs represent statistical uncertainties only, their underestimation with respect to ADs points to systematical bias.

5.4 Discussion of Correlations and Systematic Errors

In sections 5.3.3 and 5.3.4, we found all inversion strategies to correctly reproduce the initial components c_{ijkl0} of the elastic stiffness tensor and their pressure derivatives c'_{ijkl0} within 2σ uncertainties. For elastic moduli, however, the global inversion procedures appear to be affected by systematic errors. In Figure 5.5, the differences between retrieved and initial finite-strain parameters are plotted together for components of the elastic stiffness tensor (Fig. 5.5a), for bulk moduli (Fig. 5.5b), and for shear moduli (Fig. 5.5c). For both, com-

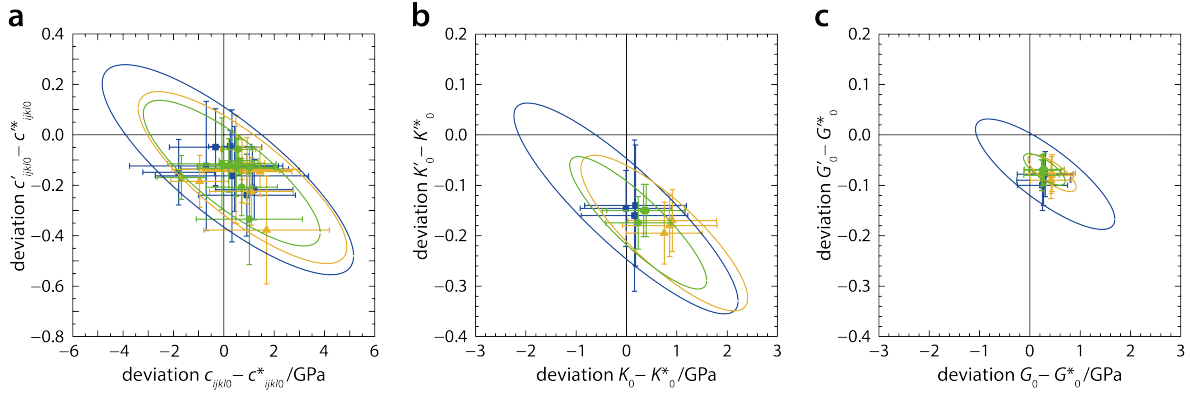


Figure 5.5: Correlation between deviations of finite-strain parameters and their pressure derivatives from the initial values for the components of the elastic stiffness tensor **(a)**, bulk moduli **(b)**, and shear moduli **(c)**. Mean confidence ellipses (95.4 % confidence level) were drawn from averaged variances and covariances for each inversion strategy. Blue ellipses and squares: 1st inversion strategy; green ellipses and circles: 2nd inversion strategy; yellow ellipses and triangles: 3rd inversion strategy.

ponents of the elastic stiffness tensor and elastic moduli, pressure derivatives are always underestimated while the components c_{ijkl0} and the moduli K_0 and G_0 themselves tend to be slightly overestimated. This correlation clearly reveals a systematic bias present in all three tested inversion strategies.

Figure 5.5 also shows confidence ellipses (95.4 % (2σ) confidence level) for correlations between c_{ijkl0} and c'_{ijkl0} (Fig. 5.5a), K_0 and K'_0 (Fig. 5.5b), and G_0 and G'_0 (Fig. 5.5c). To display correlations between c_{ijkl0} and c'_{ijkl0} , we plotted the mean confidence ellipse while the ellipses for pairwise correlations between K_0 and K'_0 and G_0 and G'_0 were computed from the covariance matrices between c_{ijkl0} and c'_{ijkl0} based on equations (5.42) and (5.43) (Angel, 2000). As indicated by the systematic differences between retrieved and initial finite-strain parameters, negative correlations between each parameter and its pressure derivative become apparent from the negative slopes of the ellipses. In the case of single-crystal finite-strain parameters (Fig. 5.5a), the confidence ellipses for all three inversion strategies include the origin of the diagrams, i. e. the initial values of finite-strain parameters fall within the uncertainties of the solutions found. For aggregate elastic moduli, however, only the ellipse for correlations between G_0 and G'_0 of the 1st inversion strategy barely reaches the origin.

Taking into account correlations between finite-strain parameters substantially expands their uncertainty limits and explains the directions of systematic errors. Correlations alone, however, cannot explain the full extent of systematic errors and why components of the elastic stiffness tensor and elastic moduli at ambient conditions tend to be overestimated while their pressure derivatives are underestimated. This systematic bias might be imposed by the employed finite-strain formalism itself or simply reflect a peculiarity of the simulated synthetic data set.

Relations (5.18)–(5.20) are derived based on the assumption of isotropic finite strain (Stixrude and Lithgow-Bertelloni, 2005), i. e. conditions that correspond to the Voigt bound. For this reason and to maintain self-consistency, the bulk modulus K_0 and its pressure derivative K'_0 in expressions (5.18)–(5.19) were computed from the components of the elastic stiffness tensor c_{ijkl0} and their pressure derivatives c'_{ijkl0} according to the Voigt bound (eqns.

(5.23) and (5.42)). The Voigt bound, however, gives the uppermost bound on the bulk modulus (Watt et al., 1976) that might not be appropriate for quasi-hydrostatic compression experiments. The synthetic data set analyzed here, however, was generated using exactly the same formalism that was used for the analysis. In the case of the synthetic data set, the Voigt bound should therefore not overestimate the bulk modulus.

In expressions (5.18)–(5.20), the bulk modulus K_0 is multiplied with the pressure derivatives c'_{ijkl0} (and c''_{ijkl0} for fourth-order terms). Overestimation of the bulk modulus, due to an inappropriate bounding scheme or due to the nature of the analyzed data set, will decrease the values of the pressure derivatives c'_{ijkl0} via multiplication. Following the chain of correlations, the components c_{ijkl0} of the elastic stiffness tensor at ambient conditions will be overestimated. Indeed, Figure 5.3 reveals subtle trends in individual components c_{ijkl} to slightly decrease along the compression path as a result of overestimating c_{ijkl0} and underestimating c'_{ijkl0} . These systematic deviations will then propagate to affect elastic moduli and their pressure derivatives.

5.5 Conclusions

We introduced and compared self-consistent strategies to analyze the high-pressure elastic properties of single crystals in the realm of finite-strain theory. Reflecting common experimental practice, the presented inversion strategies are based on observations of single-crystal sound wave velocities and unit cell volumes at high pressures. By testing three inversion strategies, we showed that inversion strategies involving the simultaneous or global inversion of observations at all sampled pressures reduce the estimated standard deviations, i. e. increase the precision, of retrieved single-crystal finite-strain parameters (c_{ijkl0} and c'_{ijkl0}) and better reproduce the elastic stiffness tensors at high pressures when compared to inversions of sound wave velocities at individual pressures. All tested inversion procedures, however, yield correct single-crystal finite-strain parameters within their 2σ uncertainties.

For aggregate elastic moduli, we found that correlations between finite-strain parameters and their pressure derivatives in combination with systematic errors might result in an underestimation of pressure derivatives beyond their estimated standard deviations. In the case of real experimental data, systematic errors might arise from the assumption of isotropic finite strain and the concomitant usage of the Voigt bound in the employed finite-strain formalism. We note that finite-strain expressions for components of the elastic stiffness tensor of the form of expressions (5.18)–(5.20) are widely used to analyze changes in the elastic properties along compression paths. When used in a self-consistent way, however, the finite-strain formalism based on isotropic finite strain may induce systematic errors in finite-strain parameters retrieved from single-crystal sound wave velocities at high pressures. Future developments might involve the derivation of a complementary formalism based on the assumption of isotropic stress instead of isotropic finite strain.

Acknowledgments

This work was supported by the German Research Foundation [grant numbers MA4534/3-1, GRK 2156/1]. H. M. acknowledges support from the Bavarian Academy of Sciences and Humanities.

Author Contributions

J. Buchen developed global inversion strategies, tested and compared different inversion strategies, and wrote the manuscript. A. Kurnosov proposed to develop and contributed in developing global inversion strategies. H. Marquardt provided ideas for testing and comparing different inversion strategies and commented on the manuscript. T. Boffa Ballaran proposed to develop global inversion strategies.

References

- Ahart, M., M. Somayazulu, Z.-G. Ye, R. E. Cohen, H.-k. Mao, and R. J. Hemley (2009). High-pressure Brillouin scattering of $\text{Pb}(\text{Mg}_{1/3}\text{Nb}_{2/3})\text{O}_3$. *Phys. Rev. B* **79**, 132103.
- Almqvist, B. S. G. and D. Mainprice (2017). Seismic properties and anisotropy of the continental crust: Predictions based on mineral texture and rock microstructure. *Rev. Geophys.* **55**, 367–433.
- Angel, R. J. (2000). Equations of state. *Rev. Mineral. Geochem.* **41**, 35–59.
- Angel, R. J., J. M. Jackson, H. J. Reichmann, and S. Speziale (2009). Elasticity measurements on minerals: a review. *Eur. J. Mineral.* **21**, 525–550.
- Auld, B. A. (1973). *Acoustic Fields and Waves in Solids I & II*. John Wiley & Sons, New York, 423 pp. & 414 pp.
- Blundy, J. and B. Wood (2003). Partitioning of trace elements between crystals and melts. *Earth Planet. Sci. Lett.* **210**, 383–397.
- Buchen, J., H. Marquardt, S. Speziale, T. Kawazoe, T. Boffa Ballaran, and A. Kurnosov (2018). High-pressure single-crystal elasticity of wadsleyite and the seismic signature of water in the shallow transition zone. *Earth Planet. Sci. Lett.* **498**, 77–87.
- Davies, G. F. (1974). Effective elastic moduli under hydrostatic stress—I. Quasi-harmonic theory. *J. Phys. Chem. Solids* **35**, 1513–1520.
- Decremps, F., L. Belliard, M. Gauthier, and B. Perrin (2010). Equation of state, stability, anisotropy and nonlinear elasticity of diamond-cubic (ZB) silicon by phonon imaging at high pressure. *Phys. Rev. B* **82**, 104119.
- Duffy, T. S. and D. L. Anderson (1989). Seismic velocities in mantle minerals and the mineralogy of the upper mantle. *J. Geophys. Res.: Solid Earth* **94**, 1895–1912.
- Every, A. G. (1980). General closed-form expressions for acoustic waves in elastically anisotropic solids. *Phys. Rev. B* **22**, 1746–1760.
- Haussühl, S. (2007). *Physical Properties of Crystals: An Introduction*. Wiley-VCH, Weinheim, 439 pp.
- Hill, R. (1952). The elastic behaviour of a crystalline aggregate. *Proc. Phys. Soc., London, Sect. A* **65**, 349–354.
- Ita, J. and L. Stixrude (1992). Petrology, elasticity, and composition of the mantle transition zone. *J. Geophys. Res.: Solid Earth* **97**, 6849–6866.
- Jaeken, J. W. and S. Cottenier (2016). Solving the Christoffel equation: Phase and group velocities. *Comput. Phys. Commun.* **207**, 445–451.
- Karato, S.-i. (2008). *Deformation of Earth Materials: An Introduction to the Rheology of Solid Earth*. Cambridge University Press, Cambridge, 463 pp.
- Kurnosov, A., H. Marquardt, D. J. Frost, T. Boffa Ballaran, and L. Ziberna (2017). Evidence for a Fe^{3+} -rich pyrolitic lower mantle from (Al,Fe)-bearing bridgmanite elasticity data. *Nature* **543**, 543–546.

- Mao, H. K., J. Xu, and P. M. Bell (1986). Calibration of the ruby pressure gauge to 800 kbar under quasi-hydrostatic conditions. *J. Geophys. Res.: Solid Earth* **91**, 4673–4676.
- Mao, Z., S. D. Jacobsen, D. J. Frost, C. A. McCammon, E. H. Hauri, and T. S. Duffy (2011). Effect of hydration on the single-crystal elasticity of Fe-bearing wadsleyite to 12 GPa. *Am. Mineral.* **96**, 1606–1612.
- Marquardt, H., S. Speziale, H. J. Reichmann, D. J. Frost, F. R. Schilling, and E. J. Garnero (2009). Elastic shear anisotropy of ferropericlase in Earth's lower mantle. *Science* **324**, 224–226.
- Marquardt, H., N. Waesermann, M. Wehber, R. J. Angel, M. Gospodinov, and B. Mihailova (2013). High-Pressure Brillouin scattering of the single-crystal $\text{PbSc}_{1/2}\text{Ta}_{1/2}\text{O}_3$ relaxor ferroelectric. *Phys. Rev. B* **87**.
- Nye, J. F. (1985). *Physical Properties of Crystals: Their Representation by Tensors and Matrices*. Oxford University Press, Oxford, 329 pp.
- Press, W. H., S. A. Teukolsky, W. T. Vetterling, and B. P. Flannery (2007). *Numerical Recipes: The Art of Scientific Computing*. 3rd edition. Cambridge University Press, Cambridge, 1256 pp.
- Sinogeikin, S. V. and J. D. Bass (2000). Single-crystal elasticity of pyrope and MgO to 20 GPa by Brillouin scattering in the diamond cell. *Phys. Earth Planet. Inter.* **120**, 43–62.
- Speziale, S. and T. S. Duffy (2002). Single-crystal elastic constants of fluorite (CaF_2) to 9.3 GPa. *Phys. Chem. Miner.* **29**, 465–472.
- Speziale, S., T. S. Duffy, and R. J. Angel (2004). Single-crystal elasticity of fayalite to 12 GPa. *J. Geophys. Res.: Solid Earth* **109**, B12202.
- Speziale, S., H. Marquardt, and T. S. Duffy (2014). Brillouin scattering and its application in geosciences. *Rev. Mineral. Geochem.* **78**, 543–603.
- Stixrude, L. and C. Lithgow-Bertelloni (2005). Thermodynamics of mantle minerals – I. Physical properties. *Geophys. J. Int.* **162**, 610–632.
- Watt, J. P., G. F. Davies, and R. J. O'Connell (1976). The elastic properties of composite materials. *Rev. Geophys.* **14**, 541–563.
- Wehner, R. K. and R. Klein (1971). Adiabatic and isothermal elastic constants from space- and time-dependent response theory. *Physica* **52**, 92–108.
- Yang, J., X. Tong, J.-F. Lin, T. Okuchi, and N. Tomioka (2015). Elasticity of ferropericlase across the spin crossover in the Earth's lower mantle. *Sci. Rep.* **5**, 17188.
- Zaug, J. M., E. H. Abramson, J. M. Brown, and L. J. Slutsky (1993). Sound velocities in olivine at Earth mantle pressures. *Science* **260**, 1487–1489.
- Zha, C.-S., T. S. Duffy, R. T. Downs, H.-K. Mao, and R. J. Hemley (1996). Sound velocity and elasticity of single-crystal forsterite to 16 GPa. *J. Geophys. Res.: Solid Earth* **101**, 17535–17545.
- Zha, C.-s., T. S. Duffy, R. T. Downs, H.-k. Mao, and R. J. Hemley (1998). Brillouin scattering and X-ray diffraction of San Carlos olivine: direct pressure determination to 32 GPa. *Earth Planet. Sci. Lett.* **159**, 25–33.

Chapter 6

High-Pressure Single-Crystal Elasticity of Wadsleyite and the Seismic Signature of Water in the Shallow Transition Zone

Johannes BUCHEN^{a,✉}, Hauke MARQUARDT^{a,b}, Sergio SPEZIALE^c,
Takaaki KAWAZOE^{a,1}, Tiziana BOFFA BALLARAN^a, and Alexander KURNOSOV^a

^aBayerisches Geoinstitut, Universität Bayreuth, 95440 Bayreuth, Germany

^bDepartment of Earth Sciences, University of Oxford, Oxford OX1 3AN, United Kingdom

^cDeutsches GeoForschungsZentrum, 14473 Potsdam, Germany

✉ johannes.buchen@uni-bayreuth.de

This chapter has been published as:

Buchen et al. (2018) *Earth Planet. Sci. Lett.* **498**, 77–87.

Abstract

Earth's transition zone at depths between 410 km and 660 km plays a key role in Earth's deep water cycle since large amounts of hydrogen can be stored in the nominally anhydrous minerals wadsleyite and ringwoodite, $(\text{Mg,Fe})_2\text{SiO}_4$. Previous mineral physics experiments on iron-free wadsleyite proposed low seismic velocities as an indicative feature for hydration in the transition zone. Here we report simultaneous sound wave velocity and density measurements on iron-bearing wadsleyite single crystals with 0.24 wt-% H_2O . By comparison with earlier studies, we show that pressure suppresses the velocity reduction caused by higher degrees of hydration in iron-bearing wadsleyite, ultimately leading to a velocity cross-over for both P waves and S waves. Modeling based on our experimental results shows that wave speed variations within the transition zone as well as velocity jumps at the 410-km seismic discontinuity, both of which have been used in previous work to detect mantle hydration, are poor water sensors. Instead, the impedance contrast across the 410-km seismic discontinuity that is reduced in the presence of water can serve as a more robust indicator for hydrated parts of the transition zone.

¹Now at: Department of Earth and Planetary Systems Science, Hiroshima University, Hiroshima 739-8526, Japan

6.1 Introduction

Water strongly affects physical and chemical properties of rocks in Earth's mantle including viscosity (Hirth and Kohlstedt, 1996; Fei et al., 2017) and melting temperatures (Hirschmann, 2006). Tracing the deep hydrogen or H₂O ("water") cycle through Earth's interior thus remains a key challenge in understanding global geodynamic processes and their surface expressions. Several studies have argued that Earth's transition zone, at depths between 410 km and 660 km, might act as a deep water reservoir that remains stable for geological timescales (Bercovici and Karato, 2003; Kuritani et al., 2011) and plays a key role in the dynamic and geochemical evolution of the entire mantle (Bercovici and Karato, 2003). Aqueous fluids released by dehydration reactions may cause melting atop (Song et al., 2004) and below the transition zone (Schmandt et al., 2014) as well as trigger deep earthquakes (Richard et al., 2007). Furthermore, it has been proposed that a hydrous transition zone might be the source of continental flood basalts (Wang et al., 2015).

The hypothesis of the transition zone being a deep water reservoir is motivated by high-pressure high-temperature experiments showing that the nominally anhydrous minerals wadsleyite and ringwoodite, (Mg,Fe)₂SiO₄, that constitute up to 60 vol-% of transition zone rocks (Frost, 2008), can incorporate significant amounts of H₂O equivalents as point defects into their crystal structures (Inoue et al., 1995; Kohlstedt et al., 1996). The recent discovery of a hydrous ringwoodite inclusion in a natural diamond (Pearson et al., 2014) confirms the experimental predictions and strengthens the hypothesis of a (at least partly) hydrated transition zone. Further direct evidence for water in Earth's transition zone comes from ice-VII inclusions in diamonds that were interpreted to represent former aqueous fluids entrapped at pressures of the transition zone (Tschauner et al., 2018). However, the actual amount of water stored in the transition zone on a global scale cannot be constrained by these isolated observations.

Instead, global-scale three-dimensional mapping of the water content in the transition zone requires geophysical remote sensing. Electrical conductivity and seismic wave propagation are both sensitive to water incorporation and have thus been proposed as promising geophysical observables to quantify hydration (Huang et al., 2005; Smyth and Jacobsen, 2006; Yoshino et al., 2008; Mao et al., 2008a; Kelbert et al., 2009; Meier et al., 2009; Houser, 2016). Unfortunately, attempts to map hydration within the transition zone using electrical conductivity variations are hampered by contradicting experimental determinations on the quantitative effects of hydration on mineral electrical conductivity (Huang et al., 2005; Yoshino et al., 2008) as well as the limited spatial resolution in electrical induction measurements (Kelbert et al., 2009).

In contrast, seismological methods provide higher three-dimensional resolution and offer a variety of observables that have been proposed to be sensitive to hydration, including lateral wave speed variations as depicted by seismic tomography and the characteristics of seismic discontinuities (Chambers et al., 2005; Meier et al., 2009; Thio et al., 2016; Houser, 2016). Previous attempts to map the water distribution using seismic data found the transition zone to be strongly hydrated (Mao et al., 2008a), essentially dry (Houser, 2016), or partly hydrated away from subducting slabs (Meier et al., 2009), a conclusion that opposes the common assumption of water being carried into the mantle through subduction processes (Thompson, 1992; Ohtani et al., 2004). In addition to discrepancies arising from the use of different seismic data and their uncertainties, it remains difficult to unravel the competing effects of hydration, temperature, and possible changes in iron content on the seismic signature. Here we show that the disagreement among previous conclusions is in

part caused by incomplete information on the expected effects of hydration on the seismic signal at conditions of the Earth's transition zone.

Earlier studies have shown that, at pressures close to the top of the transition zone (~ 14 GPa), hydration of Mg_2SiO_4 wadsleyite with 0.84 wt-% H_2O lowers P wave and S wave velocities by 2.7 % and 3.6 %, respectively (Zha et al., 1997; Mao et al., 2008a). Changing the Fe/(Mg+Fe) ratio from 0 to 0.08 has a similar effect (Zha et al., 1997; Wang et al., 2014). The combined effect of iron and hydrogen on seismic velocities, however, remains unclear at high pressure due to the lack of elasticity data for iron-bearing compositions with different hydrogen contents but equal Fe/(Mg+Fe) ratios (Mao et al., 2011). In particular, to separate the effects of iron and hydrogen, elasticity data on iron-bearing wadsleyite with an as small as possible but well characterized hydrogen content (< 0.5 wt-% H_2O) is required. Since water fugacity strongly affects wadsleyite grain growth (Nishihara et al., 2006), a small hydrogen content in wadsleyite is unavoidable in order to synthesize single crystals of suitable size and quality (Kawazoe et al., 2015).

We performed simultaneous high-pressure Brillouin spectroscopy and X-ray diffraction experiments on wadsleyite single crystals with Fe/(Mg+Fe) = 0.112(2), an iron-content expected for mantle wadsleyite (Irfune and Isshiki, 1998; Frost, 2003a), and 0.24(2) wt-% H_2O up to a pressure of 19.7 GPa. From our data, the effect of water on the high-pressure sound wave velocities can be directly inferred by comparison to previous experimental results on wadsleyite with the same iron content, but 1.93 wt-% H_2O (Mao et al., 2011).

In contrast to previous studies on the high-pressure elasticity of supposedly anhydrous iron-bearing wadsleyite (Li and Liebermann, 2000; Liu et al., 2009; Wang et al., 2014), we determined the hydrogen concentrations of the wadsleyite crystals used in our high-pressure experiments. Any quantitative assessment of the effect of hydration on the elastic properties of wadsleyite requires a reliable determination of hydrogen concentrations. Since water enhances the crystal growth of wadsleyite (Nishihara et al., 2006), the determination of hydrogen concentration is especially important in single-crystal studies. The here-studied wadsleyite crystals complement existing elasticity data by providing the first iron-bearing composition with low but known hydrogen concentration. A comprehensive review of available equation of state parameters for different wadsleyite compositions has been reported in Buchen et al. (2017).

6.2 Experimental

6.2.1 Sample Synthesis and Characterization

Large single crystals of iron-bearing wadsleyite were synthesized from San Carlos olivine powder in a multi-anvil press as previously reported (Kawazoe et al., 2015). Electron microprobe analyses on four grains showed homogeneous compositions with Fe/(Mg+Fe) = 0.112(2). Hydrogen concentrations were determined by Fourier transform infrared (FTIR) spectroscopy on the same oriented single-crystal sections used for subsequent high-pressure experiments. Polarized infrared absorption spectra were recorded at 10 different spots distributed over 4 crystals. Absorption bands attributed to structurally bonded hydroxyl groups in wadsleyite (Jacobsen et al., 2005) were decomposed into individual peaks and the total integrated absorbances (Libowitzky and Rossman, 1996) converted to H_2O concentrations (Libowitzky and Rossman, 1997). The average of all four crystal sections yields 0.24(2) wt-% H_2O . Mössbauer spectroscopy on a powder sample prepared from the same experimental

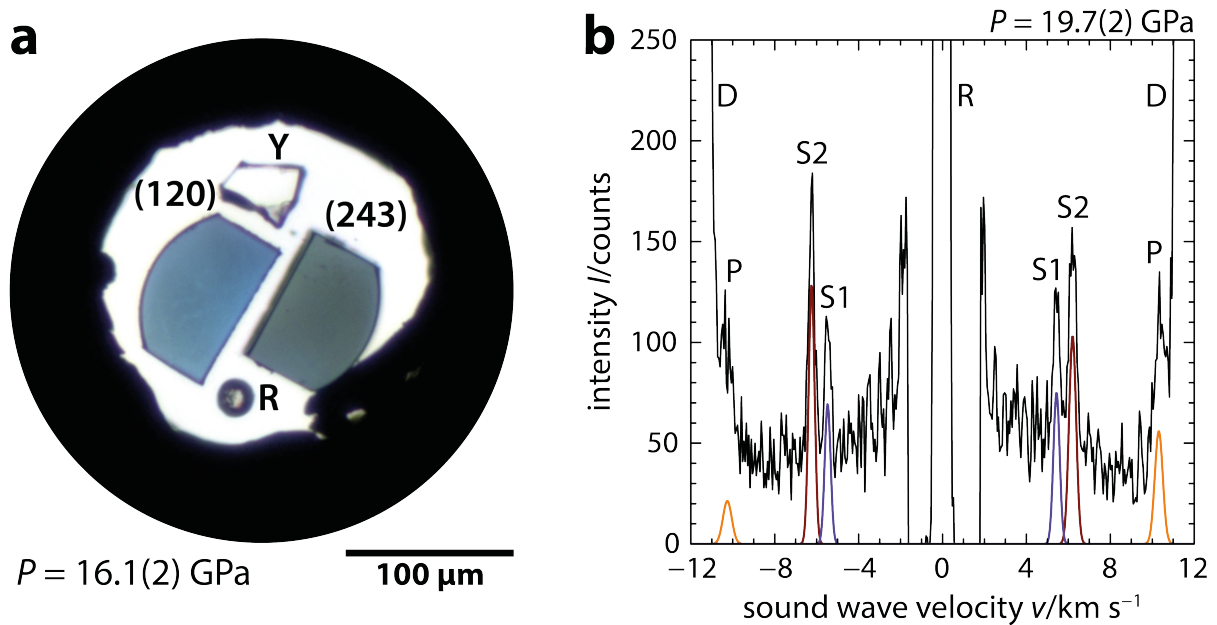


Figure 6.1: High-pressure elasticity measurements. **a)** View into the diamond anvil cell at 16.1 GPa showing two wadsleyite crystals with indicated orientations, a ruby sphere (R), and a Sm:YAG crystal (Y). **b)** Brillouin spectrum recorded at 19.7 GPa (black line) showing signals of quasi-transverse (S1 and S2) and longitudinal (P) acoustic waves in the sample as well as scattering by diamond anvils (D) and elastic (Rayleigh) scattering (R). Orange, red, and violet lines show peak-fitting results.

run (H4015) as the crystals gave $\text{Fe}^{3+}/\Sigma\text{Fe} = 0.15(3)$. The fraction of hydroxyl groups that combine with Fe^{3+} to substitute for tetrahedral Si^{4+} can be estimated from the deconvolution of FTIR spectra (Kawazoe et al., 2016) and is minor in our samples. More details on sample characterization can be found in Buchen et al. (2017). All chemical information was combined to calculate the molar mass and densities of the wadsleyite crystals.

6.2.2 High-Pressure Experiments

Oriented, double-sided polished single-crystal thin sections were prepared parallel to either the (120) or the (243) crystallographic planes with final thicknesses of 19 μm for experiments below 17 GPa and 10 μm for higher pressures. Semicircular disks were cut out of these thin sections using a focused ion beam (Marquardt and Marquardt, 2012). Two disks of complementary orientations were loaded together into a BX90 (Kantor et al., 2012) diamond anvil cell (DAC) along with a ruby sphere for provisional pressure determination (Mao et al., 1986; Dewaele et al., 2008). Precompressed neon was loaded as pressure-transmitting medium (Kurnosov et al., 2008). The two-crystal approach (Fig. 6.1a) facilitates sound wave velocity measurements in sufficient crystallographic directions to obtain all nine orthorhombic single-crystal elastic constants at consistent stress conditions while, at the same time, reducing the correlations between individual constants (Mao et al., 2015; Schulze et al., 2017; Kurnosov et al., 2017).

6.2.3 Brillouin Spectroscopy and X-Ray Diffraction

At 8 pressures up to 19.7 GPa, sound wave velocities were determined by Brillouin spectroscopy (Speziale et al., 2014) for at least 13 different wave vectors within the plane of each platelet. Individual wave vectors were typically spaced by a 15° rotation around the DAC compression axis. Brillouin spectra were recorded at DESY Hamburg in forward symmetric scattering geometry with a scattering angle close to 50° . The actual scattering angle was calibrated with an oriented MgO single crystal using known elastic constants (Spetzler, 1970). The scattered light was analyzed for frequency shifts with a six-pass tandem Fabry-Perot interferometer. A Brillouin spectrum recorded at 19.7 GPa is shown in Figure 6.1b. At each pressure, single-crystal X-ray diffraction experiments were performed on an Eulerian 4-circle diffractometer at BGI Bayreuth to obtain the unit cell volume and crystal orientation for each crystal section. The diffractometer operated with Mo- $K\alpha$ radiation generated by an X-ray tube at 50 kV and 40 mA and detected by a point detector. We followed the 8-position centering protocol (King and Finger, 1979) as implemented in the SINGLE program (Angel and Finger, 2011) and manually rejected poor-quality reflection profiles from the refinement of unit cell parameters. For every crystal, unit cell parameters were also determined at ambient pressure inside the DAC before gas loading.

6.3 Results and Discussion

6.3.1 High-Pressure Elasticity

To find an internally consistent description for the high-pressure elasticity, we jointly inverted single-crystal sound wave velocities v and unit cell volumes V (or densities ρ) at all pressures by tying the Christoffel equation $|c_{ijkl}g_jg_l - \rho v^2\delta_{ik}| = 0$ to third-order finite-strain equations for individual elastic constants c_{ij} (contracted index notation) of the form $c_{ij} = c_{ij}(V)$ (Stixrude and Lithgow-Bertelloni, 2005; Kurnosov et al., 2017) (Fig. 6.2, Table 6.1). In addition to this global inversion strategy, we inverted sound wave velocities to elastic constants at each pressure and, in a second step, analyzed the evolution of elastic constants along the compression path with third-order finite-strain equations (Fig. 6.2, Table A.8). During the inversions, densities and crystal orientations were fixed to those derived from single-crystal X-ray diffraction for each crystal section and at each pressure. Within mutual uncertainties, both inversion strategies gave identical results in terms of retrieved single-crystal finite-strain parameters with comparable overall correlations between refined parameters (Tables A.8 and A.9). Based on the smaller number N of refined parameters, we chose the results of the global inversion with $N = 18$ as compared to $N = 90$ for the conventional inversion strategy. The pressure evolution of individual elastic constants is compared to results of previous studies on wadsleyite single crystals in Figure 6.2.

From the single-crystal elastic constants and unit cell volumes at high pressures, we derived bounds on the bulk K and shear G moduli (Watt et al., 1976) as well as their respective pressure derivatives K' and G' (Tables 6.1 and A.8). Using available thermodynamic parameters (Stixrude and Lithgow-Bertelloni, 2011), the adiabatic bulk moduli as obtained from the global inversion procedure were converted to isothermal bulk moduli as required for the isothermal equation of state (EOS). Assuming a quasi-hydrostatic stress environment inside the DAC (Buchen et al., 2017), we calculated experimental pressures with the Reuss isothermal EOS (Table 6.1) by inserting the average unit cell volumes of both crystals at every pressure (Table A.8).

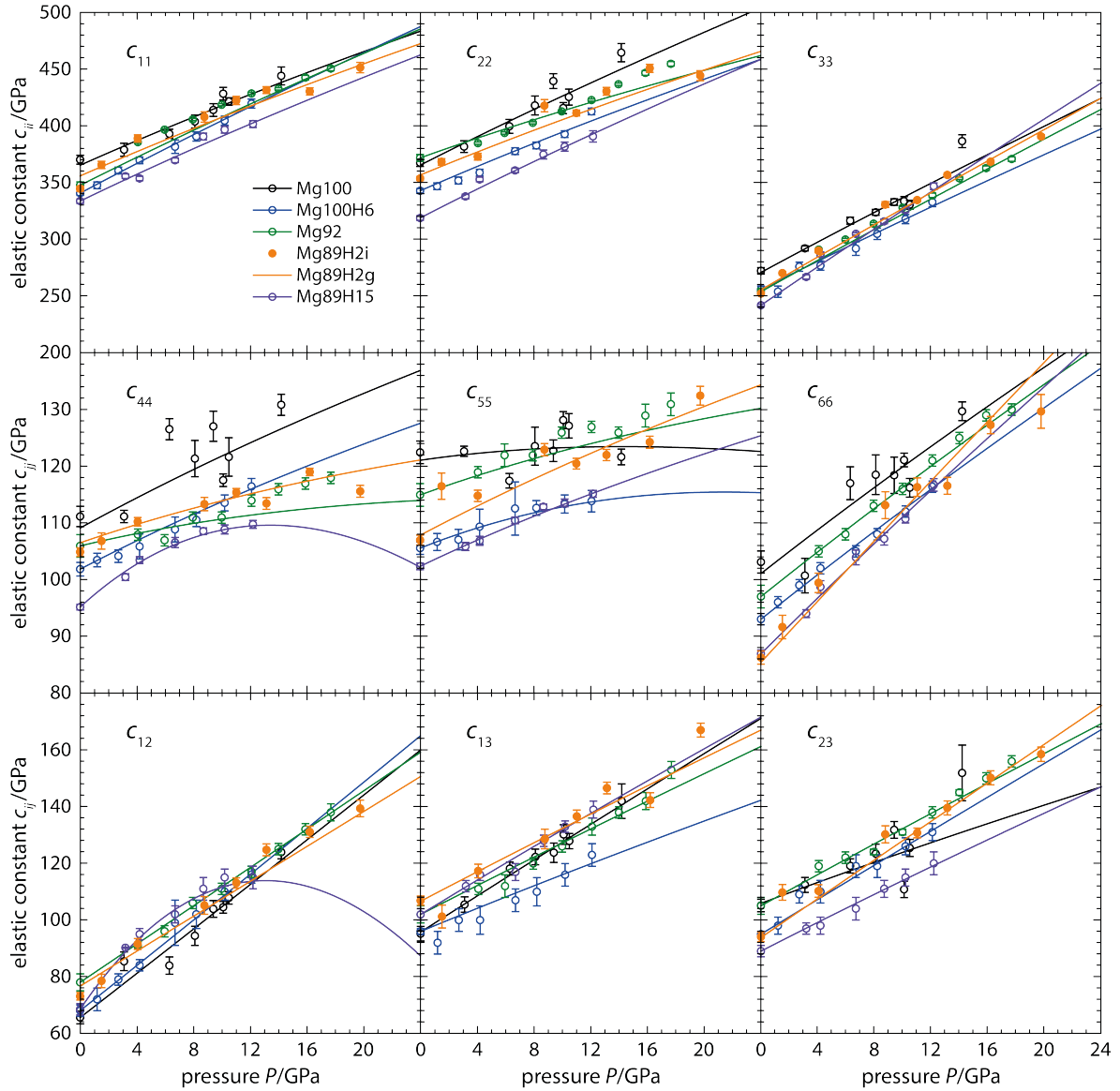


Figure 6.2: High-pressure single-crystal elastic constants of different wadsleyite compositions. Mg100: Mg_2SiO_4 (Zha et al., 1997), Mg100H6: $\text{Mg}_{1.94}\text{H}_{0.12}\text{SiO}_4$ (0.84 wt-% H_2O) (Mao et al., 2008a), Mg92: $(\text{Mg}_{0.92}\text{Fe}_{0.08})_2\text{SiO}_4$ (Wang et al., 2014), Mg89H2i: $(\text{Mg}_{0.89}\text{Fe}_{0.11})_{1.98}\text{H}_{0.04}\text{SiO}_4$ (0.24 wt-% H_2O) this study (individual inversions), Mg89H2g: $(\text{Mg}_{0.89}\text{Fe}_{0.11})_{1.98}\text{H}_{0.04}\text{SiO}_4$ (0.24 wt-% H_2O) this study (global inversion), Mg89H15: $(\text{Mg}_{0.89}\text{Fe}_{0.11})_{1.85}\text{H}_{0.30}\text{SiO}_4$ (1.92 wt-% H_2O) (Mao et al., 2011).

From the Voigt-Reuss-Hill averages (Watt et al., 1976), we obtained the adiabatic bulk modulus $K_{S0} = 168.0(9)$ GPa and the shear modulus $G_0 = 104.3(5)$ GPa at ambient conditions with the pressure derivatives $K'_{S0} = 4.13(8)$ and $G'_0 = 1.64(4)$. Compared to our results, the bulk and shear moduli of hydrous iron-bearing wadsleyite with the same Fe/(Mg+Fe) ratio of 0.11 (Mao et al., 2011) (Table 6.2) are lower at ambient conditions while their pressure derivatives, $K'_0 = 4.8(1)$ and $G'_0 = 1.9(1)$, are significantly higher, paralleling observations for iron-bearing ringwoodite (Schulze et al., 2018). The ferric iron contents of both samples, i.e. $\text{Fe}^{3+}/\Sigma\text{Fe} = 0.15(3)$ in this study and $\text{Fe}^{3+}/\Sigma\text{Fe} = 0.11(6)$ for the sample of Mao et al. (2011), are indistinguishable within their uncertainties. Differ-

Table 6.1: Third-order finite-strain parameters for iron-bearing wadsleyite

ij	c_{ij0}/GPa	c'_{ij0}		M_0/GPa	M'_0
11	356(2)	5.5(2)		Voigt bound	
22	357(2)	5.2(2)	K_{S0}^V	169.2(8)	4.05(7)
33	256(1)	7.3(1)	K_{T0}^V	167.9(8)	4.05(7)
44	107(1)	0.9(1)	G_0^V	106.1(5)	1.56(4)
55	108(1)	1.3(1)		Reuss bound	
66	85(1)	2.7(1)	K_{S0}^R	166.7(11)	4.22(9)
12	77(2)	3.1(1)	K_{T0}^R	165.4(11)	4.22(9)
13	107(2)	2.7(2)	G_0^R	102.6(4)	1.72(4)
23	94(2)	3.5(1)		Voigt-Reuss-Hill average	
$V_0/\text{\AA}^3$	542.12(3)	—	K_{S0}^{VRH}	168.0(9)	4.13(8)
$\rho_0/\text{g cm}^{-3}$	3.598(11)	—	K_{T0}^{VRH}	166.7(10)	4.13(8)
$M/\text{g mol}^{-1}$	146.81(43)	—	G_0^{VRH}	104.3(5)	1.64(4)

Italic numbers assume that $K'_{T0} \approx K'_{S0}$.

ences in elastic properties between both studies are therefore best explained in terms of the substantially different hydrogen contents. Accordingly, we attribute the observed reduction of the moduli at ambient conditions to the effect of hydration (Mao et al., 2008b; Buchen et al., 2017).

6.3.2 Aggregate Sound Wave Velocities

From the elastic properties, we calculated P wave and S wave velocities of an isotropic aggregate and compare them with sound wave velocities of hydrous iron-bearing wadsleyite ($\text{Fe}/(\text{Mg}+\text{Fe}) = 0.11$, 1.93 wt-% H_2O ; Mao et al., 2011) (Figs. 6.3a and 6.3b). In agreement with previous findings, hydration of iron-bearing wadsleyite reduces the sound wave velocities at ambient conditions (Mao et al., 2011). The sound wave velocities of hydrous iron-bearing wadsleyite, however, rise faster with increasing pressure and approach those of our less hydrous composition. When extrapolating the experimental results of Mao et al. (2011) by about 3 GPa along their finite-strain curves, we found that both P wave and S wave velocities of hydrous and less hydrous iron-bearing wadsleyite cross over at pressures close to or within the transition zone. Combining the results on hydrous iron-bearing wadsleyite (Mao et al., 2011) with those of the present study on slightly hydrous iron-bearing wadsleyite allows for the first time to directly quantify the effect of hydrogen on the single-crystal sound wave velocities of iron-bearing wadsleyite at high pressures. For all hydrogen concentrations between 0 and 3 wt-% H_2O , a velocity cross-over with anhydrous wadsleyite takes place at pressures relevant to the transition zone.

Previous attempts to compare sound wave velocities of anhydrous and hydrous wadsleyite compositions did not reveal velocity cross-overs up to about 14 GPa (Mao et al., 2008a; Mao et al., 2011). In addition to the limited pressure range covered by previous experiments, these comparisons were either based on iron-free wadsleyite (Mao et al., 2008a) or on wadsleyite compositions with slightly different iron contents (Mao et al., 2011) and unknown concentrations of hydrogen and ferric iron (Liu et al., 2009). For iron-bearing wadsleyite, sound wave velocities have been determined on single crystals using Brillouin spectroscopy (Mao et al., 2011; Wang et al., 2014) and on polycrystalline samples using

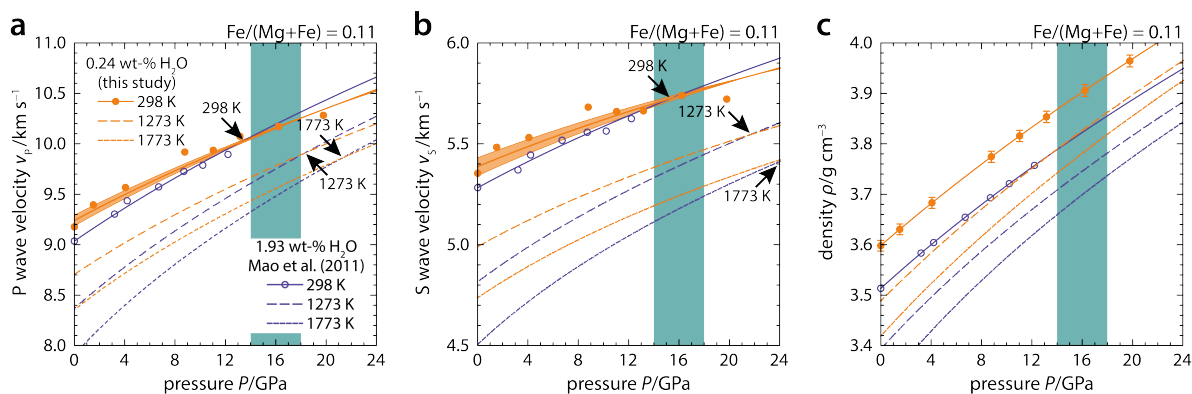


Figure 6.3: Sound wave velocities for isotropic aggregates and densities of iron-bearing wadsleyite with $\text{Fe}/(\text{Mg}+\text{Fe}) = 0.11$. **a)** P wave velocities, **b)** S wave velocities, and **c)** densities of iron-bearing wadsleyite as a function of pressure at different temperatures. Black arrows mark the velocity cross-over points between less hydrous (0.24 wt-% H_2O ; this study) and strongly hydrous (1.93 wt-% H_2O ; Mao et al., 2011) iron-bearing wadsleyite at the indicated temperatures. Note the shift of velocity cross-over points to higher pressures with increasing temperature. Orange shading in **a)** and **b)** indicates the Voigt and Reuss bounds on the results of the present study. Green shaded regions mark the pressure range of wadsleyite stability in the transition zone.

ultrasonic interferometry (Li and Liebermann, 2000; Liu et al., 2009). Sound wave velocities determined on polycrystalline wadsleyite samples by ultrasonic techniques (Li and Liebermann, 2000; Liu et al., 2009) are systematically higher than those determined here but similar to those determined by Wang et al. (2014) on single crystals by Brillouin spectroscopy even though iron contents were higher in the polycrystalline samples (Fig. A.9). To avoid potential inconsistencies, we based our comparison in Figure 6.3 on sound wave velocities that were determined by Brillouin spectroscopy and on wadsleyite single crystals with known contents of hydrogen and ferric iron.

By comparing elastic moduli and densities for different wadsleyite compositions at high pressures (Fig. 6.4), the elevated pressure derivatives of hydrous iron-bearing wadsleyite (Mao et al., 2011) with $K'_0 = 4.8$ and $G'_0 = 1.9$ can be identified as the main cause for the enhanced pressure dependence of its sound wave velocities. The densities of anhydrous and hydrous iron-bearing wadsleyite differ clearly throughout the relevant pressure range (Fig. 6.3c). Our results are supported by first-principles calculations that indicate an increase in the pressure derivatives of elastic moduli on hydration of Mg_2SiO_4 wadsleyite (Tsuchiya and Tsuchiya, 2009; Liu et al., 2012). In contrast, a systematic change in the pressure derivatives could not be confirmed by an experimental study on hydrous (0.84 wt-% H_2O) Mg_2SiO_4 wadsleyite (Mao et al., 2008a) (Fig. 6.4b). Possible explanations for these contradicting results include a threshold hydrogen concentration necessary to measurably alter the high-pressure elastic properties and a minimum experimental pressure range to resolve the changes in pressure derivatives caused by hydration.

In the case of olivine, a velocity cross-over was observed between anhydrous and hydrous forsterite, Mg_2SiO_4 , even though at considerably lower pressures (Zha et al., 1996; Mao et al., 2010). Given the similar incorporation mechanisms for hydrogen in both phases (Inoue et al., 1995; Smyth et al., 2006; Jacobsen et al., 2005), *M*-site vacancies possibly give rise to the elevated pressure derivatives of elastic moduli observed for hydrous olivine and hydrous wadsleyite. On compression, vacancies relax more than intact crystal structural

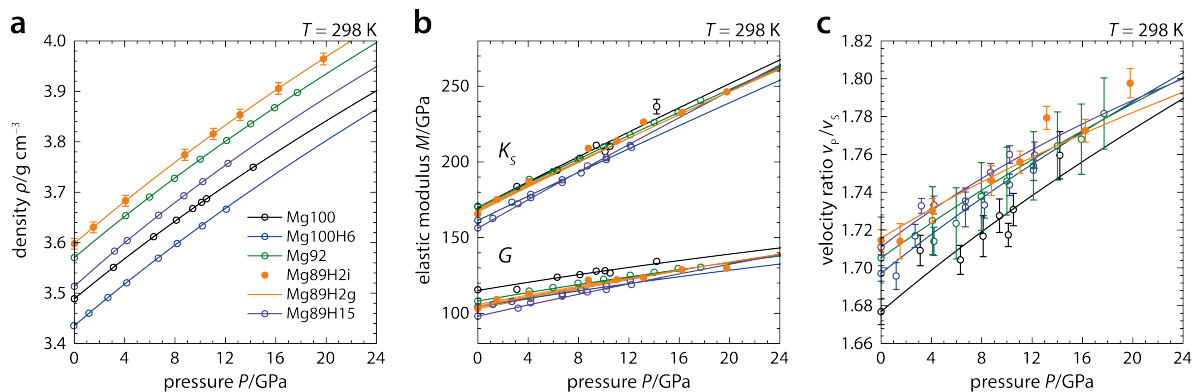


Figure 6.4: Comparison of high-pressure single-crystal elasticity studies on different wadsleyite compositions. **a)** Densities, **b)** adiabatic bulk moduli K_S and shear moduli G , and **c)** P wave to S wave velocity ratios v_P/v_S as a function of pressure at ambient temperature. Orange shading in **b)** indicates the Voigt and Reuss bounds on the results of the present study. Mg100: Mg_2SiO_4 (Zha et al., 1997), Mg100H6: $\text{Mg}_{1.94}\text{H}_{0.12}\text{SiO}_4$ (0.84 wt-% H_2O) (Mao et al., 2008a), Mg92: $(\text{Mg}_{0.92}\text{Fe}_{0.08})_2\text{SiO}_4$ (Wang et al., 2014), Mg89H2i: $(\text{Mg}_{0.89}\text{Fe}_{0.11})_{1.98}\text{H}_{0.04}\text{SiO}_4$ (0.24 wt-% H_2O) this study (individual inversions), Mg89H2g: $(\text{Mg}_{0.89}\text{Fe}_{0.11})_{1.98}\text{H}_{0.04}\text{SiO}_4$ (0.24 wt-% H_2O) this study (global inversion), Mg89H15: $(\text{Mg}_{0.89}\text{Fe}_{0.11})_{1.85}\text{H}_{0.30}\text{SiO}_4$ (1.92 wt-% H_2O) (Mao et al., 2011).

units and partly collapse as reflected in reduced O—H···O distances (Kleppe et al., 2006). With increasing pressure, repulsive O—O interactions take over, and the weakening effect of vacancies declines leading to high pressure derivatives of bulk (Holl et al., 2008) and shear moduli. As a result, the elastic moduli of anhydrous and hydrous iron-bearing wadsleyite converge at high pressures (Fig. 6.4b). For sound wave velocities to cross over, however, the related difference in density is essential (Figs. 6.3c and 6.4a). The reduction in density caused by the incorporation of a given amount of hydrogen increases with the Fe/(Mg+Fe) ratio as more heavier Fe atoms are replaced by protons.

We modeled the high-pressure high-temperature sound wave velocities of nearly anhydrous and hydrous iron-bearing wadsleyite (see section 6.3.3) and predict the velocity cross-over points to shift to higher pressures with increasing temperature (Fig. 6.3). In relatively cold regions (1273 K) of the transition zone, where hydration is most likely (Thompson, 1992; Ohtani et al., 2004), the relative differences in P wave and S wave velocities between anhydrous (0 wt-% H_2O) and hydrous (1 wt-% H_2O) wadsleyite range from $\Delta v_P/v_P = 0.6\%$ and $\Delta v_S/v_S = 0.8\%$ to $\Delta v_P/v_P = 0.1\%$ and $\Delta v_S/v_S = 0.3\%$ for pressures of 12 GPa and 18 GPa, respectively, bracketing the expected pressure range of the wadsleyite stability field (Ohtani et al., 2004; Stixrude and Lithgow-Bertelloni, 2011). Even in high-temperature regions (1773 K) and the uppermost transition zone (14 GPa), i.e. furthest away from the cross-over points, the estimated relative differences in P wave and S wave velocities remain below 0.8% and 1.1%, respectively, for hydration with 0 to 1 wt-% H_2O .

The calculations above were performed for single-phase wadsleyite, which is expected to contribute with less than 60 vol-% to a polyminerale transition zone rock. Therefore, we expect the effects of hydration on average wave velocities to be further reduced by almost 50% possibly pushing them below the detection limit of seismic tomography ($\Delta v/v \sim 1\%$; de Wit et al., 2012). We emphasize that the here-found differences between anhydrous and hydrous iron-bearing wadsleyites are significantly smaller than those inferred at the same conditions from previous results on iron-free wadsleyites ($\Delta v_P/v_P \approx 3.0\%$, $\Delta v_S/v_S \approx 4.6\%$;

Zha et al., 1997; Mao et al., 2008a). For very hydrous compositions and at temperatures below 1273 K, wadsleyite may coexist with hydrous phases such as phase E and superhydrous phase B (Ohtani et al., 2004). The modal proportions of these phases, however, are predicted to remain low when compared to the abundance of wadsleyite in a hydrous peridotitic rock (Ohtani et al., 2004).

6.3.3 Modeling of Sound Wave Velocities

We combined the results of the present study on slightly hydrous iron-bearing wadsleyite with high-pressure single-crystal data on iron-free wadsleyite (Zha et al., 1997), hydrous iron-bearing wadsleyite (Mao et al., 2011), forsterite (Zha et al., 1996), hydrous forsterite (Mao et al., 2010), and San Carlos olivine (Mao et al., 2015; Zhang and Bass, 2016) (Table 6.2). To accurately capture the effect of hydration on the properties of wadsleyite, we only included results on samples with known H₂O contents. Since there are no high-temperature elasticity data available for either hydrous wadsleyite or hydrous olivine, we used the same high-temperature formalism and thermoelastic parameters (Stixrude and Lithgow-Bertelloni, 2005; Stixrude and Lithgow-Bertelloni, 2011) for both anhydrous and hydrous wadsleyite and anhydrous and hydrous forsterite, respectively. We relied on elastic moduli and their pressure derivatives as reported in the respective publication while using compiled thermoelastic parameters (Stixrude and Lithgow-Bertelloni, 2011) for extrapolation to high temperatures (Table 6.2). For San Carlos olivine, however, we obtained elastic moduli, pressure derivatives, and thermoelastic parameters by combining recent high-pressure high-temperature single-crystal elasticity datasets (Mao et al., 2015; Zhang and Bass, 2016) and analyzing the merged dataset with the zero-pressure Debye temperature $\theta_0 = 790$ K and the zero-pressure (isotropic) Grüneisen parameter $\gamma_{ij0} = \delta_{ij}\gamma_0 = 1$ fixed to reported values (Stixrude and Lithgow-Bertelloni, 2011). To calculate the sound wave velocities for a given phase and chemical composition, bulk and shear moduli as well as the density of the mentioned species were calculated at the desired pressure and temperature and their compositions mixed to yield the required composition. Sound wave velocities were then calculated from the moduli and densities according to a Voigt-Reuss-Hill scheme (Watt et al., 1976).

6.3.4 Sound Wave Velocities of Wadsleyite

To resolve the competing effects of hydrogen, iron, and temperature on the sound wave velocities of wadsleyite, we mapped P wave and S wave velocities at 16 GPa and varying temperatures over the relevant compositional space in terms of iron (Frost, 2003b) and hydrogen (Inoue et al., 1995) by complementing our data with previous results on wadsleyite (Zha et al., 1997; Mao et al., 2011) as described in section 6.3.3 (Fig. 6.5). At 16 GPa and room temperature, hydrogen does not change the sound wave velocities significantly. At temperatures relevant to subduction environments (e.g. ~ 1273 K; Thompson, 1992), where highest water contents are expected in the transition zone, P wave and S wave velocities of wadsleyite remain virtually insensitive to hydration. A low sensitivity of seismic wave velocities to hydration has previously been proposed for hydrogen contents below 0.1 wt-% H₂O (Karato, 2011). In contrast, our conclusions apply to a significantly wider range of hydrogen contents in wadsleyite (Fig. 6.5). We note that a similar insensitivity to hydration has recently been reported for ringwoodite at mantle transition zone pressures (Schulze et al., 2018).

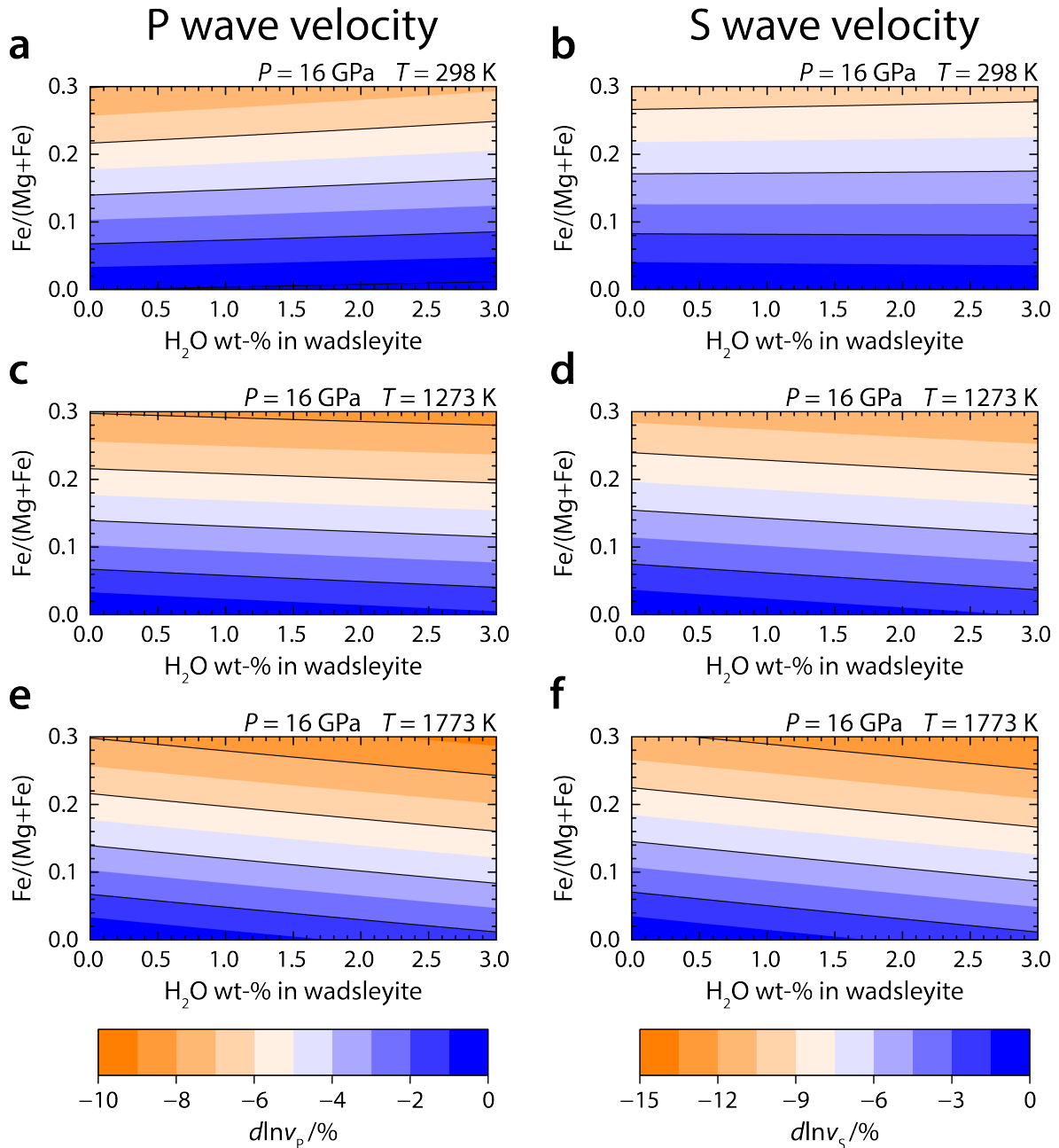


Figure 6.5: Maps of P wave and S wave velocity variations spanning relevant wadsleyite compositions. **a,b)** 16 GPa, 298 K, **c,d)** 16 GPa, 1273 K, **e,f)** 16 GPa, 1773 K. Note the low sensitivity of sound wave velocities to H₂O content as opposed to the Fe/(Mg+Fe) ratio.

As an alternative to absolute velocities, elevated P wave to S wave velocity ratios v_p/v_s have been invoked as a characteristic feature for hydrated regions within the transition zone (Smyth and Jacobsen, 2006; Thio et al., 2016). Our data, however, show v_p/v_s ratios indistinguishable from those of hydrous iron-bearing wadsleyite (Mao et al., 2011) (Fig. 6.4c). Li et al. (2011) suggested the seismic ratio $R = d \ln v_s / d \ln v_p$ derived from lateral variations in seismic velocities to be sensitive to hydration. We mapped the ratio R of wadsleyite for variations in sound wave velocities induced by hydration (0–1 wt-% H₂O, $R_{\text{H}_2\text{O}}$), by changing the iron content (Fe/(Mg+Fe) of 0–0.2, R_{Fe}), and by temperature variations (1273–1773 K, R_T) as a function of pressure and temperature ($R_{\text{H}_2\text{O}}$ and R_{Fe}) and of hydrogen and iron

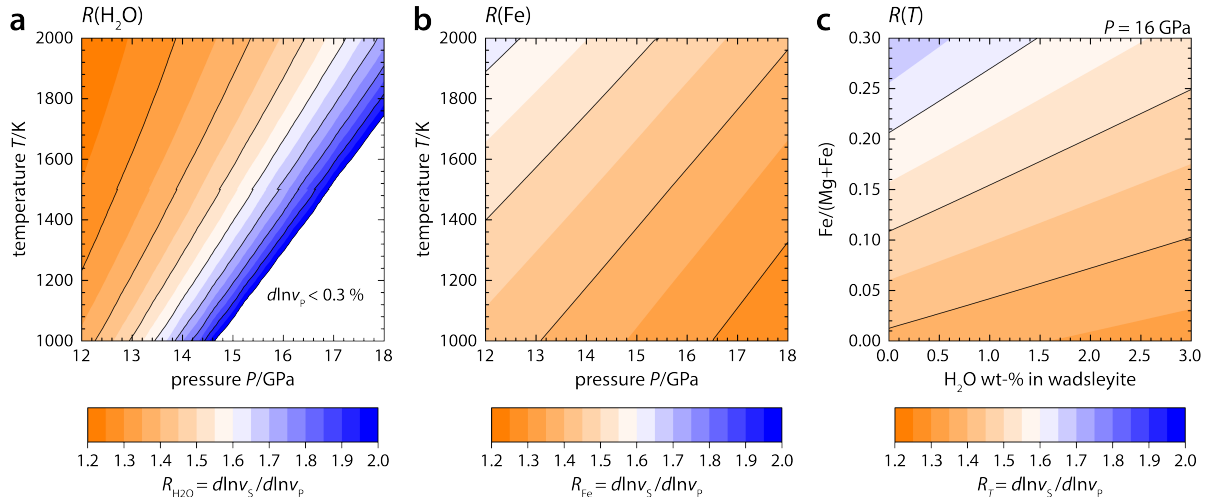


Figure 6.6: The seismic ratio $R = d \ln v_s / d \ln v_p$ of wadsleyite for sound wave velocity variations induced by **a)** hydration (0–1 wt-% H_2O), **b)** changes in iron content ($\text{Fe}/(\text{Mg}+\text{Fe})$ of 0–0.2), and **c)** temperature variations (1273–1773 K). In the lower right corner of **a)**, relative differences in P wave velocities $d \ln v_p$ become too small to compute meaningful values of $R_{\text{H}_2\text{O}}$.

content (R_T), respectively (Fig. 6.6). While R_T and R_{Fe} vary in rather narrow ranges of 1.4 to 1.5 and 1.3 to 1.6, respectively, $R_{\text{H}_2\text{O}}$ might exceed 2 at pressures above 16 GPa and temperatures around 1273 K indicating an increasing sensitivity to hydration with depth (Fig. 6.6a). At lower temperatures or higher pressures, relative differences in P wave velocities $d \ln v_p$ between hydrous and anhydrous wadsleyite drop below 0.3 % due to the proximity to the velocity cross-over. In view of the uncertainties on sound wave velocities extrapolated in pressure and temperature, the calculation of $R_{\text{H}_2\text{O}}$ becomes inappropriate for such small differences in sound wave velocities.

Albeit in qualitative agreement with the findings of Li et al. (2011), our results indicate that at typical temperatures and pressures the seismic ratios R would be very similar regardless whether lateral variations in seismic velocities are caused by temperature gradients or by variations in hydrogen or iron content, in particular in the shallowest part of the transition zone. As a consequence, we conclude that lateral variations in seismic wave speeds within the upper part of the transition zone cannot directly be used to map hydration. By raising the pressure dependence of sound wave velocities, however, hydration may contribute to steep seismic gradients as observed in the transition zone (Dziewonski and Anderson, 1981; Kennett et al., 1995). In the absence of quantitative data on anelastic effects related to wadsleyite, we note that anelastic behavior may enhance the hydration sensitivity of seismic wave velocities and impose a frequency dependence (Karato, 2011). Recent results, however, suggest that structurally bonded hydroxyl groups do not enhance seismic wave attenuation in olivine (Cline II et al., 2018).

6.3.5 Seismic Contrasts across the 410-km Discontinuity

The 410-km seismic discontinuity is thought to arise from the olivine-wadsleyite phase transition (Frost, 2008). Attempts to constrain mantle mineralogy by comparing sound wave velocity contrasts calculated from mineral physics information to seismically observed velocity contrasts at the 410-km discontinuity concluded that a pyrolitic mantle composition with 55–60 vol-% of $(\text{Mg},\text{Fe})_2\text{SiO}_4$ polymorphs cannot explain the detected velocity jumps

Table 6.2: Olivine and wadsleyite species used to model densities and sound wave velocities

Species	Olivine			Wadsleyite		
	Mg100	Mg90	Mg100H7	Mg100	Mg89H2	Mg89H15
Chemical composition						
Fe/(Mg+Fe)	0	0.1	0	0	0.112(2)	0.11(1)
[H ₂ O]/wt-%	0	0	0.9(1)	0	0.24(2)	1.93(22)
Physical properties^a						
$V_0/\text{\AA}^3$	289.6(4)	291.63(19)	290.50(3)	535.8(2)	542.12(3)	542.23(12)
$\rho_0/\text{g cm}^{-3}$	3.227(4)	3.341(3)	3.180(3)	3.488(1)	3.598(11)	3.513(7)
K_{T0}/GPa	128.0(5)	130.5(5)	124.6(2)	169(2)	166.7(10)	154.9(6)
K_{S0}/GPa	128.8(5)	131.3(5)	125.4(2)	170(2)	168.0(9)	156.2(5)
K'_0	4.2(2)	4.24(4)	4.50(5)	4.3(2)	4.13(8)	4.8(1)
K''_0/GPa^{-1}	-0.032	-0.032	-0.037	-0.025	-0.024	-0.034
G_0/GPa	81.6(2)	78.2(2)	79.6(1)	115(2)	104.3(5)	98.0(3)
G'_0	1.42(3)	1.71(6)	1.75(5)	1.4(2)	1.64(4)	1.9(1)
G''_0/GPa^{-1}	-0.031	-0.085(10)	-0.030	-0.025	-0.021	-0.025
θ_0/K^b	809(1)	790(1)	809(7)	844(7)	825(8)	827(22)
γ_0^b	0.99(3)	1.00(3)	0.99(3)	1.21(9)	1.21(8)	1.21(8)
q_0^b	2.1(2)	3.2(3)	2.1(2)	2.0(10)	2.0(9)	2.0(8)
η_{S0}^b	2.30(10)	1.39(13)	2.30(10)	2.60(40)	2.43(36)	2.45(32)

Italic numbers are values implied by third-order finite-strain equations.

We assume that $K'_{T0} \approx K'_{S0}$ and $K''_{T0} \approx K''_{S0}$.

^aSee Stixrude and Lithgow-Bertelloni (2005) for definitions and formalism.

^bThermoelastic parameters from Stixrude and Lithgow-Bertelloni (2011).

References for olivine: Mg100: Zha et al. (1996), Mg90: Mao et al. (2015), Zhang and Bass (2016), Mg100H7: Mao et al. (2010)

References for wadsleyite: Mg100: Zha et al. (1997), Mg89H2: this study, Mg89H15: Mao et al. (2011)

(Cammarano and Romanowicz, 2007; Wang et al., 2014; Thio et al., 2016). Based on the previously assumed water-induced reduction of wadsleyite sound wave velocities (Mao et al., 2008a; Mao et al., 2008b; Mao et al., 2011), a hydrated transition zone has been invoked to reconcile the pyrolite model with seismological observations (Mao et al., 2008a; Mao et al., 2010).

To explore the seismic sensitivity of the 410-km discontinuity to hydration, we calculated the relative changes (in %) $d \ln X = 200 \times (X_{\text{WA}} - X_{\text{OL}})/(X_{\text{OL}} + X_{\text{WA}})$, where X_{OL} and X_{WA} are the velocity v , density ρ , or acoustic impedance $Z = v\rho$ of olivine and wadsleyite, respectively. We accounted for iron partitioning between olivine, wadsleyite, and mainly garnet assuming $\text{Fe}/(\text{Mg}+\text{Fe}) = 0.08$ for olivine and $\text{Fe}/(\text{Mg}+\text{Fe}) = 0.11$ for wadsleyite (Irifune and Isshiki, 1998; Frost, 2003a). At high temperatures, we also included the effect of latent heat associated with the phase transition by raising the temperature of wadsleyite by 60 K with respect to olivine (Katsura et al., 2010). We mapped the velocity, density, and impedance contrasts across the olivine-wadsleyite phase transition as functions of water content in both minerals (Fig. 6.7). Our calculations show that the velocity contrasts depend only slightly on the water content of wadsleyite (Figs. 6.7a and 6.7b) suggesting that the velocity cross-over in wadsleyite not only masks water within the transition zone from being

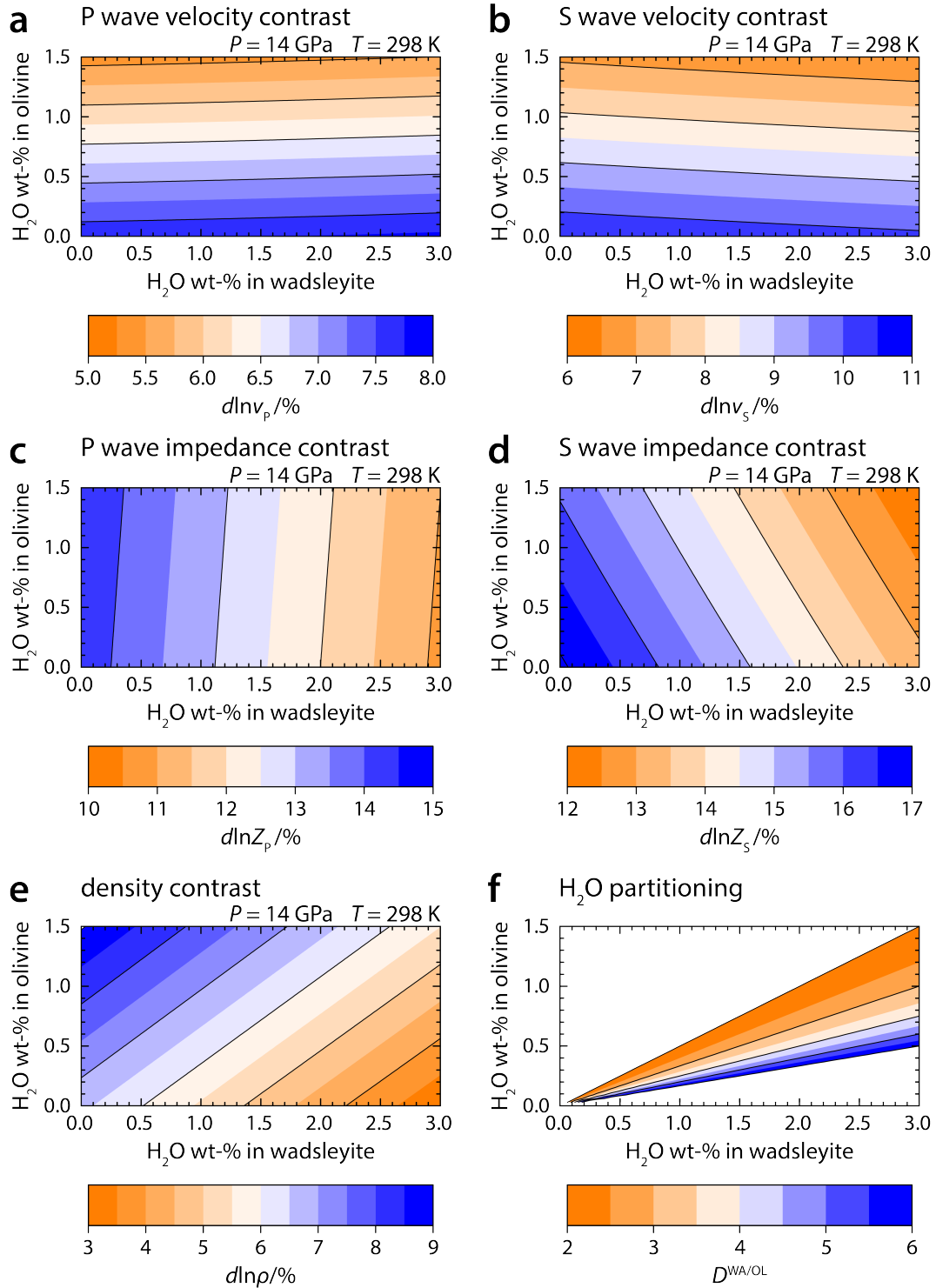


Figure 6.7: Velocity, impedance, and density contrasts across the olivine-wadsleyite phase transition. **a)** P wave velocity, **b)** S wave velocity, **c)** P wave impedance, **d)** S wave impedance, and **e)** density contrast as a function of olivine and wadsleyite H₂O contents at 14 GPa and 298 K. Note the low sensitivity of velocity contrasts and the high sensitivity of impedance contrasts to the H₂O content of wadsleyite. **f)** Range of observed H₂O partition coefficients between olivine and wadsleyite (Thio et al., 2016). Note that water preferentially partitions into wadsleyite relative to olivine.

detected by seismic tomography but also significantly reduces the sensitivity of the velocity contrasts at the 410-km discontinuity to hydration.

In contrast to the behavior of seismic wave velocities, impedance contrasts across the 410-km seismic discontinuity depend strongly on the water content of wadsleyite (Figs. 6.7c and 6.7d). We predict the impedance contrasts of P waves and S waves to become even more sensitive to hydration at high temperatures (Fig. A.10). This enhanced sensitivity at high temperatures results from the shift of the cross-over points to higher pressures (Fig. 6.3). While an increase in temperature by 100 K decreases the P wave and S wave impedance contrasts by only 0.04 % and 0.22 %, respectively, hydration of wadsleyite with 1 wt-% H₂O at 1273 K and 12 GPa leads to a reduction by 2.0 % and 2.2 %, respectively.

The actual sensitivity of the impedance contrasts depends on the H₂O partitioning between olivine and wadsleyite (Fig. 6.7f). The range of reported partition coefficients (Thio et al., 2016) suggests that water preferentially accumulates in wadsleyite and that the impedance contrasts are sensitive to hydration regardless of the assumed partitioning behavior. Even for a fairly low water partition coefficient between wadsleyite and olivine of $D^{\text{WA/OL}} = 2$ and assuming 1 wt-% H₂O in wadsleyite, the impedance contrasts for P waves and S waves at 1273 K and 12 GPa are reduced by 1.6 % and 2.0 % compared to the anhydrous system. Lateral variations in the impedance contrasts of the 410-km discontinuity might therefore serve to map hydrous regions in the deep upper mantle.

Experiments have shown that the pressure interval of the olivine-wadsleyite phase transition widens in the presence of water (Frost and Dolejš, 2007). Such broadening of the phase transition will decrease seismic gradients across the 410-km discontinuity, especially at lower temperatures (Frost and Dolejš, 2007). Decreased seismic gradients, in turn, reduce the effective reflectivity of the discontinuity in addition to the hydration-induced reduction of the impedance contrast. Broadening of the 410-km discontinuity in the presence of water will therefore amplify the impedance-based seismic sensitivity to hydration by further reducing the amplitudes of reflected seismic waves.

Only few observations of local variations in impedance contrasts of the 410-km discontinuity are available to date (Chambers et al., 2005; Bagley and Revenaugh, 2008; Thio et al., 2016). Assuming a pyrolitic mantle rock with 55 vol-% olivine and wadsleyite above and below the 410-km discontinuity, respectively (Frost, 2008), we can scale the impedance contrasts reported by Chambers et al. (2005) and compare them with impedance contrasts predicted by our comparison of olivine and wadsleyite properties at 14 GPa and 1773 K (Fig. A.10). While the scaled P wave impedance contrasts spread over a range of $8\% < d \ln Z_p < 16\%$, S wave impedance contrasts cluster between $13\% < d \ln Z_s < 18\%$ and fall in the upper quarter or outside of the range predicted by our model. Such high S wave impedance contrasts would be compatible with water contents below 0.5 wt-% H₂O in wadsleyite (Fig. A.10). Taking into account uncertainties on seismically observed impedance contrasts, however, would raise this upper limit in water content substantially. While the observations of Chambers et al. (2005) appear to be representative for impedance contrasts at the 410-km discontinuity (Thio et al., 2016), P wave and S wave impedance contrasts show poor consistency in terms of inferred water contents. This inconsistency might arise from averaging over geodynamically heterogeneous regions or be related to a complex interplay of other parameters that affect the observed impedance contrasts.

For example, dehydration melting in a layer atop the transition zone (Bercovici and Karato, 2003; Song et al., 2004; Schmerr and Garnero, 2007; Freitas et al., 2017) would not only disturb the detected impedance contrasts at the 410-km discontinuity but also result in chemical exchange and redistribution of chemical elements across the olivine-wadsleyite

phase transition (Bercovici and Karato, 2003; Schmerr and Garnero, 2007; Freitas et al., 2017). In the above calculations, we did not consider the effects of anelasticity or anisotropy, which may be expected to have stronger impact on S waves (Karato, 1993; Chambers et al., 2005). While for olivine anelastic relaxation appears to be independent of hydrogen content (Cline II et al., 2018), the anelastic behavior of wadsleyite remains poorly constrained. Seismically observed impedance contrasts most probably reflect a superposition of contrasts in mineral physical properties and dynamic processes across the 410-km discontinuity.

6.4 Conclusion

Our modeling, which is based on our experimental results and previous studies, clearly shows that wave speed variations for P waves and S waves within the transition zone as reported by seismic tomography and velocity contrasts at the 410-km seismic discontinuity show a very small sensitivity to the hydration state of the transition zone. At mantle temperatures (~ 1773 K), the reduction in sound wave velocities of pyrolite brought about by hydration of wadsleyite with 1 wt-% H_2O is equivalent to a temperature increase of less than 100 K. Temperatures are expected to vary by more than 500 K across different geodynamic settings (Thompson, 1992; Ohtani et al., 2004). We therefore predict that thermal effects will dominate variations in wave speeds masking the comparatively small contribution of hydration. Instead, we argue that the impedance contrast across the 410-km discontinuity, which can be inferred from seismic reflectivity studies (Chambers et al., 2005; Bagley and Revenaugh, 2008), is a more robust indicator for the hydration state of the mantle. Direct determinations of sound wave velocities of hydrous olivine and hydrous wadsleyite at combined high pressures and high temperatures as well as a quantification of anelastic contributions are needed to refine the extrapolation of our findings to realistic mantle temperatures. Combining our results with future seismic studies dedicated to map the reflectivity of the 410-km discontinuity may contribute to detect reservoirs and pathways of deep water cycling in Earth's mantle.

Acknowledgements

We thank R. Njul and H. Schulze for polishing the crystal sections. This work was supported by the German Research Foundation [grant numbers MA4534/3-1, INST 91/315-1 FUGG, GRK 2156/1]. H. M. acknowledges support from the Bavarian Academy of Sciences and Humanities.

Author Contributions

J. Buchen selected and characterized wadsleyite single crystals, performed the experiments, analyzed the data, proposed to model and modeled seismic properties and contrasts, and wrote the manuscript. H. Marquardt proposed to study the elastic properties of wadsleyite, to load two crystals inside the same diamond anvil cell, and to evaluate the effect of water on sound wave velocities and wrote and commented on the manuscript. S. Speziale assisted with Brillouin spectroscopy experiments in Hamburg and with related data analysis and commented on the manuscript. T. Kawazoe synthesized wadsleyite single crystals and commented on the manuscript. T. Boffa Ballaran assisted with X-ray diffraction experiments

and with related data analysis and commented on the manuscript. A. Kurnosov assisted with the preparation of experiments and data analysis and commented on the manuscript.

Supplementary Materials

See appendix A.2 on page 192 for Supplementary Figures and Tables.

References

- Angel, R. J. and L. W. Finger (2011). *SINGLE*: a program to control single-crystal diffractometers. *J. Appl. Crystallogr.* **44**, 247–251.
- Bagley, B. and J. Revenaugh (2008). Upper mantle seismic shear discontinuities of the Pacific. *J. Geophys. Res.: Solid Earth* **113**, B12301.
- Bercovici, D. and S.-i. Karato (2003). Whole-mantle convection and the transition-zone water filter. *Nature* **425**, 39–44.
- Buchen, J., H. Marquardt, T. Boffa Ballaran, T. Kawazoe, and C. McCammon (2017). The equation of state of wadsleyite solid solutions: Constraining the effects of anisotropy and crystal chemistry. *Am. Mineral.* **102**, 2494–2504.
- Cammarano, F. and B. Romanowicz (2007). Insights into the nature of the transition zone from physically constrained inversion of long-period seismic data. *Proc. Natl. Acad. Sci. U. S. A.* **104**, 9139–9144.
- Chambers, K., A. Deuss, and J. H. Woodhouse (2005). Reflectivity of the 410-km discontinuity from PP and SS precursors. *J. Geophys. Res.: Solid Earth* **110**, B02301.
- Cline II, C. J., U. H. Faul, E. C. David, A. J. Berry, and I. Jackson (2018). Redox-influenced seismic properties of upper-mantle olivine. *Nature* **555**, 355–358.
- de Wit, R. W. L., J. Trampert, and R. D. van der Hilst (2012). Toward quantifying uncertainty in travel time tomography using the null-space shuttle. *J. Geophys. Res.: Solid Earth* **117**, B03301.
- Dewaele, A., M. Torrent, P. Loubeyre, and M. Mezouar (2008). Compression curves of transition metals in the Mbar range: Experiments and projector augmented-wave calculations. *Phys. Rev. B* **78**, 104102.
- Dziewonski, A. M. and D. L. Anderson (1981). Preliminary reference Earth model. *Phys. Earth Planet. Inter.* **25**, 297–356.
- Fei, H., D. Yamazaki, M. Sakurai, N. Miyajima, H. Ohfuji, T. Katsura, and T. Yamamoto (2017). A nearly water-saturated mantle transition zone inferred from mineral viscosity. *Sci. Adv.* **3**, e1603024.
- Freitas, D., G. Manthilake, F. Schiavi, J. Chantel, N. Bolfan-Casanova, M. A. Bouhifd, and D. Andrault (2017). Experimental evidence supporting a global melt layer at the base of the Earth's upper mantle. *Nat. Commun.* **8**, 2186.
- Frost, D. J. (2003a). Fe²⁺-Mg partitioning between garnet, magnesiowüstite, and (Mg,Fe)₂SiO₄ phases of the transition zone. *Am. Mineral.* **88**, 387–397.
- (2003b). The structure and sharpness of (Mg,Fe)₂SiO₄ phase transformations in the transition zone. *Earth Planet. Sci. Lett.* **216**, 313–328.
- (2008). The upper mantle and transition zone. *Elements* **4**, 171–176.
- Frost, D. J. and D. Dolejš (2007). Experimental determination of the effect of H₂O on the 410-km seismic discontinuity. *Earth Planet. Sci. Lett.* **256**, 182–195.

- Hirschmann, M. M. (2006). Water, melting, and the deep Earth H₂O cycle. *Annu. Rev. Earth Planet. Sci.* **34**, 629–653.
- Hirth, G. and D. L. Kohlstedt (1996). Water in the oceanic upper mantle: implications for rheology, melt extraction and the evolution of the lithosphere. *Earth Planet. Sci. Lett.* **144**, 93–108.
- Holl, C. M., J. R. Smyth, S. D. Jacobsen, and D. J. Frost (2008). Effects of hydration on the structure and compressibility of wadsleyite, β -(Mg₂SiO₄). *Am. Mineral.* **93**, 598–607.
- Houser, C. (2016). Global seismic data reveal little water in the mantle transition zone. *Earth Planet. Sci. Lett.* **448**, 94–101.
- Huang, X., Y. Xu, and S.-i. Karato (2005). Water content in the transition zone from electrical conductivity of wadsleyite and ringwoodite. *Nature* **434**, 746–749.
- Inoue, T., H. Yurimoto, and Y. Kudoh (1995). Hydrous modified spinel, Mg_{1.75}SiH_{0.5}O₄: A new water reservoir in the mantle transition region. *Geophys. Res. Lett.* **22**, 117–120.
- Irifune, T. and M. Isshiki (1998). Iron partitioning in a pyrolite mantle and the nature of the 410-km seismic discontinuity. *Nature* **392**, 702–705.
- Jacobsen, S. D., S. Demouchy, D. J. Frost, T. Boffa Ballaran, and J. Kung (2005). A systematic study of OH in hydrous wadsleyite from polarized FTIR spectroscopy and single-crystal X-ray diffraction: Oxygen sites for hydrogen storage in Earth's interior. *Am. Mineral.* **90**, 61–70.
- Kantor, I., V. Prakapenka, A. Kantor, P. Dera, A. Kurnosov, S. Sinogeikin, N. Dubrovinskaia, and L. Dubrovinsky (2012). BX90: A new diamond anvil cell design for X-ray diffraction and optical measurements. *Rev. Sci. Instrum.* **83**, 125102.
- Karato, S.-i. (1993). Importance of anelasticity in the interpretation of seismic tomography. *Geophys. Res. Lett.* **20**, 1623–1626.
- (2011). Water distribution across the mantle transition zone and its implications for global material circulation. *Earth Planet. Sci. Lett.* **301**, 413–423.
- Katsura, T., A. Yoneda, D. Yamazaki, T. Yoshino, and E. Ito (2010). Adiabatic temperature profile in the mantle. *Phys. Earth Planet. Inter.* **183**, 212–218.
- Kawazoe, T., J. Buchen, and H. Marquardt (2015). Synthesis of large wadsleyite single crystals by solid-state recrystallization. *Am. Mineral.* **100**, 2336–2339.
- Kawazoe, T., A. Chaudhari, J. R. Smyth, and C. McCammon (2016). Coupled substitution of Fe³⁺ and H⁺ for Si in wadsleyite: A study by polarized infrared and Mössbauer spectroscopies and single-crystal X-ray diffraction. *Am. Mineral.* **101**, 1236–1239.
- Kelbert, A., A. Schultz, and G. Egbert (2009). Global electromagnetic induction constraints on transition-zone water content variations. *Nature* **460**, 1003–1006.
- Kennett, B. L. N., E. R. Engdahl, and R. Buland (1995). Constraints on seismic velocities in the Earth from traveltimes. *Geophys. J. Int.* **122**, 108–124.
- King, H. E. and L. W. Finger (1979). Diffracted beam crystal centering and its application to high-pressure crystallography. *J. Appl. Crystallogr.* **12**, 374–378.
- Kleppe, A. K., A. P. Jephcoat, and J. R. Smyth (2006). High-pressure Raman spectroscopic study of Fo₉₀ hydrous wadsleyite. *Phys. Chem. Miner.* **32**, 700–709.
- Kohlstedt, D. L., H. Keppler, and D. C. Rubie (1996). Solubility of water in the α , β and γ phases of (Mg,Fe)₂SiO₄. *Contrib. Mineral. Petrol.* **123**, 345–357.
- Kuritani, T., E. Ohtani, and J.-I. Kimura (2011). Intensive hydration of the mantle transition zone beneath China caused by ancient slab stagnation. *Nat. Geosci.* **4**, 713–716.
- Kurnosov, A., I. Kantor, T. Boffa-Ballaran, S. Lindhardt, L. Dubrovinsky, A. Kuznetsov, and B. H. Zehnder (2008). A novel gas-loading system for mechanically closing of various types of diamond anvil cells. *Rev. Sci. Instrum.* **79**, 045110.

- Kurnosov, A., H. Marquardt, D. J. Frost, T. Boffa Ballaran, and L. Ziberna (2017). Evidence for a Fe³⁺-rich pyrolitic lower mantle from (Al,Fe)-bearing bridgmanite elasticity data. *Nature* **543**, 543–546.
- Li, B. and R. C. Liebermann (2000). Sound velocities of wadsleyite β -(Mg_{0.88}Fe_{0.12})₂SiO₄ to 10 GPa. *Am. Mineral.* **85**, 292–295.
- Li, L., D. J. Weidner, J. P. Brodholt, and D. Alfè (2011). Prospecting for water in the transition zone: $d \ln(V_s)/d \ln(V_p)$. *Phys. Earth Planet. Inter.* **189**, 117–120.
- Libowitzky, E. and G. R. Rossman (1996). Principles of quantitative absorbance measurements in anisotropic crystals. *Phys. Chem. Miner.* **23**, 319–327.
- (1997). An IR absorption calibration for water in minerals. *Am. Mineral.* **82**, 1111–1115.
- Liu, W., J. Kung, B. Li, N. Nishiyama, and Y. Wang (2009). Elasticity of (Mg_{0.87}Fe_{0.13})₂SiO₄ wadsleyite to 12 GPa and 1073 K. *Phys. Earth Planet. Inter.* **174**, 98–104.
- Liu, W., L.-Y. Tian, J.-J. Zhao, H. Liu, L. Liu, and J.-G. Du (2012). Water effect on high-pressure elasticity of olivine, wadsleyite and ringwoodite in Mg₂SiO₄ by first-principles. *Int. J. Mod. Phys. B* **26**, 1250106.
- Mao, H. K., J. Xu, and P. M. Bell (1986). Calibration of the ruby pressure gauge to 800 kbar under quasi-hydrostatic conditions. *J. Geophys. Res.: Solid Earth* **91**, 4673–4676.
- Mao, Z., S. D. Jacobsen, F. Jiang, J. R. Smyth, C. M. Holl, and T. S. Duffy (2008a). Elasticity of hydrous wadsleyite to 12 GPa: Implications for Earth's transition zone. *Geophys. Res. Lett.* **35**, L21305.
- Mao, Z., S. D. Jacobsen, F. M. Jiang, J. R. Smyth, C. M. Holl, D. J. Frost, and T. S. Duffy (2008b). Single-crystal elasticity of wadsleyites, β -Mg₂SiO₄, containing 0.37–1.66 wt.% H₂O. *Earth Planet. Sci. Lett.* **268**, 540–549.
- Mao, Z., S. D. Jacobsen, F. Jiang, J. R. Smyth, C. M. Holl, D. J. Frost, and T. S. Duffy (2010). Velocity crossover between hydrous and anhydrous forsterite at high pressures. *Earth Planet. Sci. Lett.* **293**, 250–258.
- Mao, Z., S. D. Jacobsen, D. J. Frost, C. A. McCammon, E. H. Hauri, and T. S. Duffy (2011). Effect of hydration on the single-crystal elasticity of Fe-bearing wadsleyite to 12 GPa. *Am. Mineral.* **96**, 1606–1612.
- Mao, Z., D. Fan, J.-F. Lin, J. Yang, S. N. Tkachev, K. Zhuravlev, and V. B. Prakapenka (2015). Elasticity of single-crystal olivine at high pressures and temperatures. *Earth Planet. Sci. Lett.* **426**, 204–215.
- Marquardt, H. and K. Marquardt (2012). Focused ion beam preparation and characterization of single-crystal samples for high-pressure experiments in the diamond-anvil cell. *Am. Mineral.* **97**, 299–304.
- Meier, U., J. Trampert, and A. Curtis (2009). Global variations of temperature and water content in the mantle transition zone from higher mode surface waves. *Earth Planet. Sci. Lett.* **282**, 91–101.
- Nishihara, Y., T. Shinmei, and S.-i. Karato (2006). Grain-growth kinetics in wadsleyite: Effects of chemical environment. *Phys. Earth Planet. Inter.* **154**, 30–43.
- Ohtani, E., K. Litasov, T. Hosoya, T. Kubo, and T. Kondo (2004). Water transport into the deep mantle and formation of a hydrous transition zone. *Phys. Earth Planet. Inter. New Developments in High-Pressure Mineral Physics and Applications to the Earth's Interior* **143–144**, 255–269.
- Pearson, D. G., F. E. Brenker, F. Nestola, J. McNeill, L. Nasdala, M. T. Hutchison, S. Matveev, K. Mather, G. Silversmit, S. Schmitz, et al. (2014). Hydrous mantle transition zone indicated by ringwoodite included within diamond. *Nature* **507**, 221–224.

- Richard, G., M. Monnereau, and M. Rabinowicz (2007). Slab dehydration and fluid migration at the base of the upper mantle: implications for deep earthquake mechanisms. *Geophys. J. Int.* **168**, 1291–1304.
- Schmandt, B., S. D. Jacobsen, T. W. Becker, Z. Liu, and K. G. Dueker (2014). Dehydration melting at the top of the lower mantle. *Science* **344**, 1265–1268.
- Schmerr, N. and E. J. Garnero (2007). Upper mantle discontinuity topography from thermal and chemical heterogeneity. *Science* **318**, 623–626.
- Schulze, K., J. Buchen, K. Marquardt, and H. Marquardt (2017). Multi-sample loading technique for comparative physical property measurements in the diamond-anvil cell. *High Pressure Res.* **37**, 159–169.
- Schulze, K., H. Marquardt, T. Kawazoe, T. Boffa Ballaran, C. McCammon, M. Koch-Müller, A. Kurnosov, and K. Marquardt (2018). Seismically invisible water in Earth's transition zone? *Earth Planet. Sci. Lett.* **498**, 9–16.
- Smyth, J. R. and S. D. Jacobsen (2006). Nominally anhydrous minerals and Earth's deep water cycle. In: *Earth's Deep Water Cycle*. Ed. by S. D. Jacobsen and S. van der Lee. American Geophysical Union, Washington, DC, 1–11.
- Smyth, J. R., D. J. Frost, F. Nestola, C. M. Holl, and G. Bromiley (2006). Olivine hydration in the deep upper mantle: Effects of temperature and silica activity. *Geophys. Res. Lett.* **33**, L15301.
- Song, T.-R. A., D. V. Helmberger, and S. P. Grand (2004). Low-velocity zone atop the 410-km seismic discontinuity in the northwestern United States. *Nature* **427**, 530–533.
- Spetzler, H. (1970). Equation of state of polycrystalline and single-crystal MgO to 8 kilobars and 800°K. *J. Geophys. Res.* **75**, 2073–2087.
- Speziale, S., H. Marquardt, and T. S. Duffy (2014). Brillouin scattering and its application in geosciences. *Rev. Mineral. Geochem.* **78**, 543–603.
- Stixrude, L. and C. Lithgow-Bertelloni (2005). Thermodynamics of mantle minerals – I. Physical properties. *Geophys. J. Int.* **162**, 610–632.
- (2011). Thermodynamics of mantle minerals – II. Phase equilibria. *Geophys. J. Int.* **184**, 1180–1213.
- Thio, V., L. Cobden, and J. Trampert (2016). Seismic signature of a hydrous mantle transition zone. *Phys. Earth Planet. Inter.* **250**, 46–63.
- Thompson, A. B. (1992). Water in the Earth's upper mantle. *Nature* **358**, 295–302.
- Tschauner, O., S. Huang, E. Greenberg, V. B. Prakapenka, C. Ma, G. R. Rossman, A. H. Shen, D. Zhang, M. Newville, A. Lanzirrotti, et al. (2018). Ice-VII inclusions in diamonds: Evidence for aqueous fluid in Earth's deep mantle. *Science* **359**, 1136–1139.
- Tsuchiya, J. and T. Tsuchiya (2009). First principles investigation of the structural and elastic properties of hydrous wadsleyite under pressure. *J. Geophys. Res.: Solid Earth* **114**, B02206.
- Wang, J., J. D. Bass, and T. Kastura (2014). Elastic properties of iron-bearing wadsleyite to 17.7 GPa: Implications for mantle mineral models. *Phys. Earth Planet. Inter.* **228**, 92–96.
- Wang, X.-C., S. A. Wilde, Q.-L. Li, and Y.-N. Yang (2015). Continental flood basalts derived from the hydrous mantle transition zone. *Nat. Commun.* **6**, 7700.
- Watt, J. P., G. F. Davies, and R. J. O'Connell (1976). The elastic properties of composite materials. *Rev. Geophys.* **14**, 541–563.
- Yoshino, T., G. Manthilake, T. Matsuzaki, and T. Katsura (2008). Dry mantle transition zone inferred from the conductivity of wadsleyite and ringwoodite. *Nature* **451**, 326–329.

References

- Zha, C.-S., T. S. Duffy, R. T. Downs, H.-K. Mao, and R. J. Hemley (1996). Sound velocity and elasticity of single-crystal forsterite to 16 GPa. *J. Geophys. Res.: Solid Earth* **101**, 17535–17545.
- Zha, C.-S., T. S. Duffy, H.-K. Mao, R. T. Downs, R. J. Hemley, and D. J. Weidner (1997). Single-crystal elasticity of β -Mg₂SiO₄ to the pressure of the 410 km seismic discontinuity in the Earth's mantle. *Earth Planet. Sci. Lett.* **147**, E9–E15.
- Zhang, J. S. and J. D. Bass (2016). Sound velocities of olivine at high pressures and temperatures and the composition of Earth's upper mantle. *Geophys. Res. Lett.* **43**, 9611–9618.

Chapter 7

Equation of State of Polycrystalline Stishovite across the Tetragonal–Orthorhombic Phase Transition

Johannes BUCHEN^{a,✉}, Hauke MARQUARDT^{a,b}, Kirsten SCHULZE^a, Sergio SPEZIALE^c, Tiziana BOFFA BALLARAN^a, Norimasa NISHIYAMA^{d,1}, and Michael HANFLAND^e

^aBayerisches Geoinstitut, Universität Bayreuth, 95440 Bayreuth, Germany

^bDepartment of Earth Sciences, University of Oxford, Oxford OX1 3AN, United Kingdom

^cDeutsches GeoForschungsZentrum, 14473 Potsdam, Germany

^dDeutsches Elektronen-Synchrotron DESY, 22603 Hamburg, Germany

^eEuropean Synchrotron Radiation Facility ESRF, 38043 Grenoble, France

✉ johannes.buchen@uni-bayreuth.de

This chapter has been published as:

Buchen et al. (2018) *J. Geophys. Res. Solid Earth* **123**, 7347–7360.

Abstract

High-pressure silica polymorphs may contribute to lithologies in Earth's lower mantle. Stishovite, the tetragonal rutile-type polymorph of SiO₂, distorts to an orthorhombic CaCl₂-type structure at pressures and temperatures of the lower mantle. We compressed sintered polycrystalline stishovite and determined the unit cell parameters as a function of pressure using synchrotron X-ray diffraction. The compression behavior of sintered polycrystalline stishovite deviates systematically from previous results on stishovite powder and single crystals. Following an initial stiffening, the bulk modulus of sintered polycrystalline stishovite drops at the ferroelastic phase transition. We analyzed the observed spontaneous strains using Landau theory to predict the complete elastic behavior of sintered polycrystalline silica across the phase transition. The reduction in bulk modulus at the phase transition as derived

¹Now at: Laboratory for Materials and Structures, Tokyo Institute of Technology, Yokohama 226-8503, Japan

here from the compression curve of sintered polycrystalline silica may have implications for the seismic detection of silica-rich materials in Earth's lower mantle.

7.1 Introduction

The physical properties of crystalline high-pressure phases of silica, SiO_2 , are of importance for geophysics and material sciences (e.g. Hemley et al., 1994). Along a typical geotherm, stishovite would be the stable SiO_2 polymorph at pressures above 10 GPa (Zhang et al., 1996). At pressures above 120 GPa and temperatures around 2500 K, SiO_2 crystallizes in the $\alpha\text{-PbO}_2$ crystal structure as seifertite (Murakami et al., 2003; Tsuchiya et al., 2004; El Goresy et al., 2008; Grocholski et al., 2013). Both diamond inclusions and high-pressure high-temperature experiments indicate that stishovite contributes to basaltic lithologies at conditions of Earth's lower mantle (Joswig et al., 1999; Hirose et al., 1999). The results of recent experiments and calculations suggest that silica might exsolve from Earth's outer core (Hirose et al., 2017) and be dispersed throughout the lower mantle (Helffrich et al., 2018). Besides its relevance to geophysics, polycrystalline stishovite is considered the hardest known oxide that remains metastable at ambient conditions (Léger et al., 1996; Nishiyama et al., 2014).

At ambient temperature and around 50 GPa, stishovite (space group $P4_2/mnm$; Stishov and Belov, 1962) undergoes a ferroelastic phase transition from the tetragonal rutile crystal structure to an orthorhombic phase with CaCl_2 -type structure (space group $Pnmm$; Kingma et al., 1995; Karki et al., 1997b; Andrault et al., 1998), hereafter referred to as CaCl_2 -type SiO_2 . This phase transition has received considerable attention as it possibly entails a strong reduction of the shear modulus at or close to the transition pressure (Karki et al., 1997a; Karki et al., 1997b; Carpenter et al., 2000; Shieh et al., 2002; Asahara et al., 2013). Consequently, the presence of stishovite-bearing rocks such as subducted oceanic crust in Earth's lower mantle has been inferred from seismic observations of low shear wave velocities (Niu et al., 2003; Kaneshima and Helffrich, 2010; Helffrich et al., 2018). Previous experimental work on the elastic properties of stishovite and CaCl_2 -type SiO_2 was either limited to low pressures (Jiang et al., 2009) or focused on the equation of state (EOS) of single crystals (Hemley et al., 2000) and powders (Andrault et al., 1998; Andrault et al., 2003; Grocholski et al., 2013; Nisr et al., 2017). The effect of nonhydrostatic compression on the phase transition from stishovite to CaCl_2 -type SiO_2 has been investigated on powders (Shieh et al., 2002; Singh et al., 2012) and on sintered polycrystalline material (Asahara et al., 2013). In the absence of direct measurements of elastic constants of stishovite to relevant pressures, the elastic properties can be estimated by analyzing the evolution of unit cell parameters across the ferroelastic phase transition using Landau theory (Carpenter et al., 2000).

In contrast to single crystals or unconsolidated powders, compression of a sintered polycrystalline material composed of elastically anisotropic crystals may give rise to considerable internal stresses between grains. The complex stress field may alter the elastic response of the polycrystal and, in the case of stishovite, interact with the ferroelastic phase transition. For example, deviatoric stresses were shown to shift the transition from stishovite to CaCl_2 -type SiO_2 to lower pressures (Shieh et al., 2002; Singh et al., 2012; Asahara et al., 2013). We compressed sintered polycrystalline stishovite using neon as quasi-hydrostatic pressure-transmitting medium to investigate the effect of internal stresses arising from grain-grain interactions on the elastic response and the ferroelastic phase transition of stishovite. Based

on the results of our X-ray diffraction experiments, we derive EOS for stishovite and CaCl_2 -type SiO_2 as well as a Landau theory description for the arising spontaneous strains. We further use Landau theory to evaluate the changes in elastic properties of polycrystalline silica across the ferroelastic phase transition and discuss potential consequences for the seismic detection of stishovite-bearing materials in Earth's lower mantle.

7.2 Experimental

Sintered polycrystalline stishovite was synthesized from a pure silica glass rod at 15 GPa and 1573 K using a Kawai-type multi-anvil apparatus. After annealing the silica rod for 30 min, the temperature was decreased to around 723 K and the sample decompressed at this temperature to prevent cracking of the sintered polycrystalline product. Purity and crystallinity of the synthesized stishovite were verified using synchrotron X-ray diffraction at beamline P02.1 at PETRA III/DESY in Hamburg and electron microscopy. Details of sample synthesis and characterization have been reported elsewhere (Nishiyama et al., 2014). A plane-parallel double-sided polished thin section with a final thickness of 13(1) μm was prepared from the synthesis product by mechanical polishing. Circles with diameters of 40 μm were cut from the thin section using a focused beam of Ga^+ ions (Marquardt and Marquardt, 2012; Schulze et al., 2017). A sintered polycrystalline stishovite platelet was loaded in a BX90 diamond anvil cell (Kantor et al., 2012) along with a ruby sphere for pressure determination (Dewaele et al., 2008). We used diamond anvils with 200 μm culets that were glued to tungsten carbide seats and a rhenium foil as gasket after preindenting it to a thickness of about 40 μm and cutting a hole with 120 μm diameter in the center of the indentation using an infrared laser. Precompressed neon was loaded as pressure-transmitting medium (Kurnosov et al., 2008) to create a quasi-hydrostatic stress environment upon compression.

X-ray diffraction patterns were recorded at beamline ID15B of the European Synchrotron Radiation Facility (ESRF) at 30 pressures between 9 and 73 GPa and at ambient temperature. Monochromatic X-rays with a wavelength of 0.410768 \AA were focused on the sample and the diffracted radiation detected by an Mar555 image plate in transmission geometry. The exact diffraction geometry was calibrated using a powdered Si standard. Exposure times were 2 to 3 s. Two-dimensional diffraction patterns were integrated to intensity- 2θ profiles using the FIT2D software (Hammersley, 2016). Lattice parameters of stishovite and CaCl_2 -type SiO_2 were extracted from Le Bail refinements performed with the program MAUD (Lutterotti et al., 2007). We used the structural model for stishovite reported by Ross et al. (1990) and refined lattice parameters and microstrains at every pressure after adjusting a polynomial baseline to account for background intensity. Uncertainties on lattice parameters were rescaled as proposed by Bézar and Lelann (1991). At the lowest pressure, we also refined the average crystallite size of the sintered polycrystalline stishovite. The result of 165 nm agrees with estimates based on electron microscopy (Nishiyama et al., 2014). At pressures clearly above the phase transition, the crystal symmetry was reduced accordingly and the appropriate parameters added to the refinement procedure. For pressures close to the phase transition, we performed two separate refinements assuming first tetragonal and then orthorhombic symmetry.

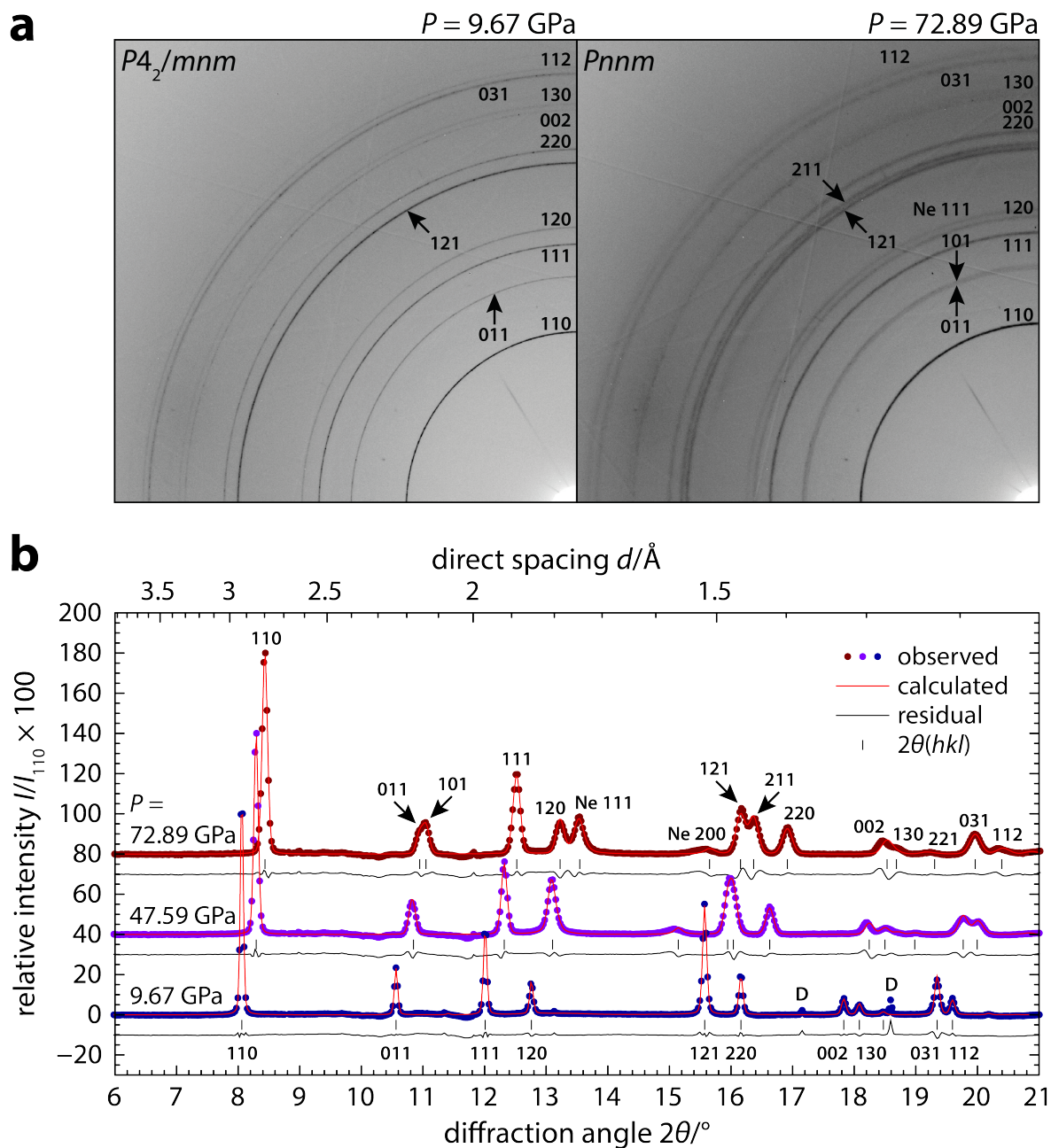


Figure 7.1: Segments of two-dimensional diffraction patterns (**a**) and integrated diffraction patterns (**b**) of sintered polycrystalline stishovite ($P4_2/mnm$) and CaCl_2 -type SiO_2 ($Pnmm$). In **b**, solid circles show background-corrected observed diffracted intensities; red lines show refined intensities; black lines show residuals; black bars indicate refined diffraction angles. Black arrows indicate splitting of the tetragonal 011 and 121 reflections into the pairs of orthorhombic 011 and 101 and 121 and 211 reflections. Note the initial broadening of these reflections close to the phase transition around 45 GPa. D marks reflections from diamond anvils.

Table 7.1: Refined unit cell parameters of sintered polycrystalline stishovite and CaCl₂-type SiO₂ at high pressures

Pressure <i>P</i> (GPa)	Unit cell parameters				
	<i>a</i> (Å)	<i>b</i> (Å)	<i>c</i> (Å)	<i>V</i> (Å ³)	<i>wR</i> (%) ^a
Stishovite – <i>P4</i>₂/<i>mm</i>					
9.67(48)	4.1319(4)	4.1319(4)	2.6501(7)	45.24(1)	1.08
11.38(10)	4.1251(7)	4.1251(7)	2.6468(11)	45.04(2)	1.27
13.99(70)	4.1156(9)	4.1156(9)	2.6422(15)	44.75(3)	1.50
15.77(79)	4.1093(8)	4.1093(8)	2.6395(13)	44.57(3)	1.63
17.74(4)	4.1030(7)	4.1030(7)	2.6365(11)	44.38(2)	1.47
19.59(98)	4.0961(4)	4.0961(4)	2.6340(6)	44.19(1)	1.14
21.40(10)	4.0910(4)	4.0910(4)	2.6307(6)	44.03(1)	1.06
23.15(3)	4.0848(4)	4.0848(4)	2.6288(7)	43.86(1)	1.07
24.99(9)	4.0794(4)	4.0794(4)	2.6257(6)	43.70(1)	1.10
27.16(41)	4.0738(4)	4.0738(4)	2.6229(7)	43.53(1)	1.11
30.45(152)	4.0685(3)	4.0685(3)	2.6203(5)	43.37(1)	1.11
31.02(3)	4.0615(4)	4.0615(4)	2.6168(7)	43.17(1)	1.10
33.27(9)	4.0559(5)	4.0559(5)	2.6135(9)	42.99(2)	1.17
35.70(3)	4.0494(5)	4.0494(5)	2.6101(10)	42.80(2)	1.15
38.05(8)	4.0433(6)	4.0433(6)	2.6071(11)	42.62(2)	1.17
40.39(5)	4.0365(6)	4.0365(6)	2.6031(12)	42.41(2)	1.15
42.89(8)	4.0303(7)	4.0303(7)	2.5982(14)	42.20(3)	1.27
45.27(1)	4.0241(8)	4.0241(8)	2.5943(15)	42.01(3)	1.26
47.59(6)	4.0169(7)	4.0169(7)	2.5903(14)	41.79(3)	1.23
49.87(13)	4.0117(6)	4.0117(6)	2.5872(11)	41.64(2)	1.31
CaCl₂-type SiO₂ – <i>Pnm</i>					
45.27(1)	3.9973(19)	4.0510(19)	2.5946(9)	42.01(3)	0.96
47.59(6)	3.9884(23)	4.0458(23)	2.5905(11)	41.80(4)	0.94
49.87(13)	3.9824(24)	4.0417(25)	2.5874(12)	41.65(4)	1.05
52.16(12)	3.9712(22)	4.0406(22)	2.5834(12)	41.45(4)	1.03
54.38(10)	3.9629(24)	4.0362(25)	2.5801(12)	41.27(4)	1.00
56.40(6)	3.9530(28)	4.0345(29)	2.5763(14)	41.09(5)	0.97
58.51(301)	3.9444(27)	4.0331(28)	2.5727(15)	40.93(5)	0.97
62.63(12)	3.9267(24)	4.0282(25)	2.5654(13)	40.58(4)	0.95
64.64(1)	3.9181(25)	4.0262(26)	2.5620(14)	40.41(4)	0.97
66.59(341)	3.9082(28)	4.0240(30)	2.5597(15)	40.26(5)	0.95
66.96(343)	3.9056(27)	4.0233(29)	2.5584(15)	40.20(5)	0.95
70.99(23)	3.8937(31)	4.0186(31)	2.5520(17)	39.93(5)	0.97
72.89(375)	3.8880(31)	4.0131(31)	2.5505(17)	39.80(5)	1.00

Numbers in parentheses are standard errors on the last digit.

^aWeighted *R* factor.

7.3 EOS of Sintered Polycrystalline Stishovite

Typical diffraction patterns of stishovite and CaCl_2 -type SiO_2 are shown in Figure 7.1. Following previous studies on the tetragonal-to-orthorhombic phase transition (Ono et al., 2002; Nomura et al., 2010), we used the splitting of the 121 reflection to identify CaCl_2 -type SiO_2 . Due to the continuous nature of the phase transition, the orthorhombic 121 and 211 reflections clearly separate only after an initial broadening of the joint peak corresponding to the tetragonal 121 reflection (Fig. 7.1b). From the inspection of diffraction patterns alone, we locate the phase transition between 40 and 50 GPa. As we would expect different grains of the sintered material to be subjected to different stress conditions, we cannot exclude that both tetragonal and orthorhombic structures coexist for a range of pressures as observed by Nisir et al. (2017).

Unit cell edge lengths a , b , and c and unit cell volumes V are listed in Table 7.1 for both stishovite and CaCl_2 -type SiO_2 . Their evolution with pressure is shown in Figure 7.2 together with results of compression experiments on single-crystal stishovite and silica powder (Andrault et al., 2003). In their high-pressure powder diffraction experiments, Andrault et al. (2003) used NaCl as pressure-transmitting medium and heated the silica powder with an infrared laser to reduce nonhydrostatic stresses. We recalculated the experimental pressures of Andrault et al. (2003) based on revised EOS for B2-structured NaCl and platinum (Fei et al., 2007) as these standard materials were used for pressure determination in the experiments of Andrault et al. (2003). The revised EOS from Fei et al. (2007) gave slightly higher pressures for B2-structured NaCl than those reported by Andrault et al. (2003) with a maximum difference of 1.4 GPa and lower pressures for platinum with a maximum difference of 9.3 GPa at the highest pressure. To better assess the effect of the stress environment imposed by the pressure-transmitting medium, we also compare our results to compression of stishovite powder in helium (Nisir et al., 2017).

While all three data sets are consistent around 10 GPa, sintered polycrystalline stishovite is less compressible along the \mathbf{a} axis leading to an increasing deviation of the \mathbf{a} axis length and the unit cell volume from those of stishovite powder up to the transition pressure. Above the transition pressure, however, the orthorhombic \mathbf{a} and \mathbf{b} axes as well as the volume compression curve of the sintered polycrystalline material evolve in parallel to the powder compression curves of Andrault et al. (2003) with increasing pressure. The \mathbf{c} axes of powdered and sintered polycrystalline stishovite and CaCl_2 -type SiO_2 essentially follow the same compression curve.

To extract quantitative information on the axial and volume compression behavior, we analyzed axial and volume compression curves of sintered polycrystalline stishovite and CaCl_2 -type SiO_2 with third-order finite-strain EOS (Birch, 1947; Angel, 2000). For volume compression, we have

$$P = (1 + 2f_E)^{5/2} \left(3K_0 f_E + \frac{9}{2} K_0 (K'_0 - 4) f_E^2 \right) \quad (7.1)$$

with the Eulerian finite volume strain $f_E = [(V_0/V)^{2/3} - 1]/2$, the unit cell volume V_0 , the bulk modulus K_0 , and its pressure derivative K'_0 at the chosen reference pressure, and for linear compression

$$P = (1 - 2E_i)^{5/2} \left(-k_{i0} E_i + \frac{1}{2} k_{i0} (k'_{i0} - 12) E_i^2 \right) \quad (7.2)$$

with the linear moduli k_{i0} , their pressure derivatives k'_{i0} , and the diagonal components of the Eulerian finite-strain tensor $E_i = [1 - (a_{i0}/a_i)^2]/2$ ($i = 1, 2, 3$ for a , b , or c , respectively).

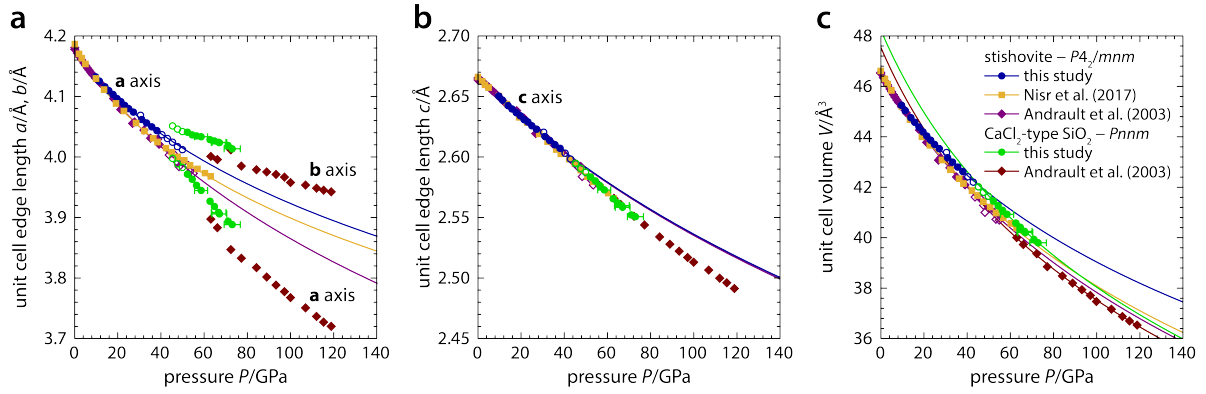


Figure 7.2: Unit cell edge lengths (a,b) and unit cell volumes (c) of stishovite and CaCl_2 -type SiO_2 as a function of pressure. Curves show finite-strain equations of state. Open symbols show data excluded from analysis. Close to the tetragonal-orthorhombic phase transition, unit cell parameters were refined for both symmetries. This study: sintered polycrystalline silica in neon; Nisir et al. (2017): powder in helium; Andrault et al. (2003): powder in NaCl or without medium (single-crystal data for $P < 10$ GPa).

Equation (7.1) was fit to the volume compression curves of stishovite and CaCl_2 -type SiO_2 and equation (7.2) to the axial compression curves of stishovite. To avoid any bias caused by a mixture of both phases, we excluded data between 40 and 50 GPa from the analysis. Based on the variation of normalized stress with finite strains (Angel, 2000), we set $k'_{30} = 12$ for stishovite and $K'_0 = 4$ for CaCl_2 -type SiO_2 implying a second-order finite-strain EOS. For each phase, we chose the lowest pressure included in the analysis as the reference pressure and, for comparison, extrapolated the results back to ambient pressure using the obtained EOS parameters. The results are listed in Table 7.2.

To see the effect of the revised EOS for B2-structured NaCl and platinum (Fei et al., 2007) on the EOS parameters, we reanalyzed the combined data set of single-crystal stishovite and silica powder (Andrault et al., 2003). In contrast to the original EOS with $K'_0 = 4.59(23)$ for stishovite as reported by Andrault et al. (2003), we set $K'_0 = 4$ for both stishovite and CaCl_2 -type SiO_2 based on virtually constant normalized stresses for increasing finite strains (Angel, 2000). Similarly, $k'_{10} = k'_{30} = 12$ were fixed in the analysis of axial compression curves. For stishovite, we excluded data above 40 GPa to avoid any influence of the phase transition on the derived EOS. The results are included in Table 7.2 together with the EOS parameters for compression of stishovite in helium (Nisir et al., 2017).

A comparison of EOS parameters for stishovite in Table 7.2 shows that sintered polycrystalline stishovite has the highest bulk modulus at ambient conditions and also the highest pressure derivative of the bulk modulus. Hence, sintered polycrystalline stishovite is less compressible and stiffens faster with pressure than stishovite powder. The differences between the EOS for laser-annealed stishovite powder compressed in NaCl or without pressure-transmitting medium (Andrault et al., 2003) and the EOS for stishovite powder compressed in helium (Nisir et al., 2017) may arise from different stress environments such as deviations from hydrostaticity imposed by the different pressure-transmitting media. Taking into account their uncertainties, both EOS for stishovite powder in Table 7.2 are consistent with the range of bulk moduli and their pressure derivatives of earlier studies as compiled by Fischer et al. (2018).

Table 7.2: Refined equation of state parameters for stishovite and CaCl₂-type SiO₂

	Sintered poly-crystalline silica	Neon	Powder ^a (& single crystal)	Powder ^b
Medium			NaCl/none with laser annealing	Helium
Stishovite – $P4_2/mnm$				
P_0 (GPa) ^c	9.67	0	0	0
V_0 (Å ³)	45.23(3)	46.43(10)	46.51(2)	46.569
K_0 (GPa)	401(15)	344(25)	320(2)	312(2)
K'_0	5.8(11)	6.0(11)	4	4.59
a_0 (Å)	4.1319(8)	4.1737(27)	4.1767(8)	
c_0 (Å)	2.6498(2)	2.6667(4)	2.6666(3)	
k_{10} (GPa)	1060(41)	867(44)	808(10)	
k_{30} (GPa)	1584(15)	1467(15)	1459(17)	
k'_{10}	19.3(31)	20.5(31)	12	
k'_{30}	12	12.0(3)	12	
CaCl₂-type SiO₂ – $Pnmm$				
P_0 (GPa) ^c	52.16	0	62.99	0
V_0 (Å ³)	41.46(3)	48.22(44)	39.98(2)	47.54(18)
K_0 (GPa)	467(17)	241(18)	514(6)	238(6)
K'_0	4	4.72(4)	4	4.82(2)

Values in *italics* were fixed during refinement.

Numbers in parentheses are standard errors on the last digit.

^aCompression data from Andrault et al. (2003);

single-crystal data in water-ethanol-methanol for $P < 10$ GPa.

^bEquation of state from Nisir et al. (2017).

^cReference pressure.

The finite-strain curves in Figure 7.2c reveal a kink in the volume compression curve for sintered polycrystalline silica associated with a drop in the bulk modulus at the phase transition. This behavior differs from the smooth volume variation observed for stishovite powder. After initial stiffening, sintered polycrystalline silica becomes more compressible at pressures above the phase transition to CaCl₂-type SiO₂. Our reanalysis of the EOS of silica powder (Andrault et al., 2003) across the phase transition from stishovite to CaCl₂-type SiO₂ reveals a small drop in bulk modulus at the phase transition as well. Except for the unit cell volumes at ambient conditions, the EOS for CaCl₂-type SiO₂ powder and sintered polycrystalline CaCl₂-type SiO₂ are identical within uncertainties.

In a powder, individual grains are free to distort and to adapt to the prevailing stress environment. Laser annealing further stimulates the relaxation of nonhydrostatic stresses (Andrault et al., 2003; Singh et al., 2012). The compression experiments on stishovite powder by Andrault et al. (2003) and in helium by Nisir et al. (2017) therefore capture the compression behavior of a mechanically relaxed material. In contrast, grain boundaries are locked to each other in sintered polycrystalline stishovite. As a result, compression of elastically anisotropic crystals with different orientations will inevitably lead to internal

stresses as grains get clamped by their neighboring grains. The effect of clamping depends on the number of grain-grain interactions. In comparison to previous studies (Shieh et al., 2002; Andrault et al., 2003; Singh et al., 2012), the small grain size of the here-used sample might therefore enhance stresses between grains. When grain sizes get substantially smaller than in our polycrystalline stishovite sample, however, the elastic properties of grain boundaries themselves significantly contribute to the overall elastic response (Marquardt et al., 2011a; Marquardt et al., 2011b).

Mechanical clamping and the related internal stresses can change the elastic response of sintered polycrystalline stishovite and give rise to elastic stiffening as observed here (Fig. 7.2). At the tetragonal-orthorhombic phase transition, the silica crystals gain an additional degree of freedom due to the symmetry reduction and the related possibility to distort accordingly. By distorting, they adapt to their individual stress environments and partially release the stresses accumulated during compression. As internal stresses relax, the extent of mechanical clamping decreases, and the material becomes more compressible until internal stresses build up again due to further compression. We therefore attribute the stiffening of sintered polycrystalline stishovite followed by the compressional softening at the phase transition to CaCl_2 -type SiO_2 to the build-up of internal stresses in sintered polycrystalline stishovite and their partial relaxation at the phase transition.

7.4 Landau Theory Analysis

Further insight into the elastic behavior of sintered polycrystalline stishovite can be obtained by an analysis of the spontaneous strains e_i arising from the ferroelastic phase transition (Carpenter and Salje, 1998; Carpenter, 2006). Here we follow the Landau theory approach of Carpenter et al. (2000) with some small modifications. The Landau free energy expansion for the pseudo-proper ferroelastic phase transition (Wadhawan, 1982) from tetragonal stishovite to orthorhombic CaCl_2 -type SiO_2 ($P4_2/mnm \rightleftharpoons Pnmm$) was given by Carpenter et al. (2000) as

$$\begin{aligned}
 G = & \frac{1}{2}a(P - P_c)Q^2 + \frac{1}{4}bQ^4 + \lambda_1(e_1 + e_2)Q^2 + \lambda_2(e_1 - e_2)Q \\
 & + \lambda_3e_3Q^2 + \lambda_4(e_4^2 - e_5^2)Q + \lambda_6e_6^2Q^2 \\
 & + \frac{1}{4}(c_{11}^0 + c_{12}^0)(e_1 + e_2)^2 + \frac{1}{4}(c_{11}^0 - c_{12}^0)(e_1 - e_2)^2 \\
 & + c_{13}^0(e_1 + e_2)e_3 + \frac{1}{2}c_{33}^0e_3^2 + \frac{1}{2}c_{44}^0(e_4^2 + e_5^2) + \frac{1}{2}c_{66}^0e_6^2
 \end{aligned} \tag{7.3}$$

with the driving order parameter Q , the critical pressure P_c , the Landau coefficients a and b , the coupling coefficients λ_1 – λ_6 , and the bare elastic constants c_{ij}^0 . Due to coupling between spontaneous strains and the driving order parameter, the structure distorts at a transition pressure P_c^* that is different from the critical pressure (Carpenter et al., 2000):

$$P_c^* = P_c + \frac{2\lambda_2^2}{a(c_{11}^0 - c_{12}^0)} \tag{7.4}$$

The order parameter evolves with pressure as (Carpenter et al., 2000)

$$Q^2 = \frac{a}{b^*}(P_c^* - P) \tag{7.5}$$

with the renormalized 4th-order coefficient

$$b^* = b - 2 \left(\frac{\lambda_3^2(c_{11}^0 + c_{12}^0) + 2\lambda_1^2 c_{33}^0 - 4\lambda_1 \lambda_3 c_{13}^0}{c_{33}^0(c_{11}^0 + c_{12}^0) - 2c_{13}^0{}^2} \right) \quad (7.6)$$

Following the steps laid out by Carpenter and Salje (1998), we find for the symmetry-adapted spontaneous strains that arise from the tetragonal-orthorhombic phase transition:

$$(e_1 + e_2) = \left(\frac{2\lambda_3 c_{13}^0 - 2\lambda_1 c_{33}^0}{c_{33}^0(c_{11}^0 + c_{12}^0) - 2c_{13}^0{}^2} \right) Q^2 \quad (7.7)$$

$$(e_1 - e_2) = \left(\frac{-2\lambda_2}{c_{11}^0 - c_{12}^0} \right) Q \quad (7.8)$$

$$e_3 = \left(\frac{2\lambda_1 c_{13}^0 - \lambda_3(c_{11}^0 + c_{12}^0)}{c_{33}^0(c_{11}^0 + c_{12}^0) - 2c_{13}^0{}^2} \right) Q^2 \quad (7.9)$$

These expressions are identical to those given by Carpenter (2006) except for a typo correction of c_{33}^0 to c_{13}^0 in the numerator of the formula for e_3 . By symmetry, $e_4 = e_5 = e_6 = 0$ in mechanical equilibrium. It can be seen from equation (7.3), however, that any imposed strain along the crystal axes or shear strain within the \mathbf{a} - \mathbf{b} plane may displace the transition pressure from its value under mechanical equilibrium. Non-equilibrium strains may arise from nonhydrostatic compression or from stresses due to grain-grain interactions. Further definitions and equations can be found in Carpenter et al. (2000), including the expressions for the variation of individual elastic constants across the phase transition.

Previous analyses of the elastic behavior across the ferroelastic phase transition of stishovite to CaCl_2 -type SiO_2 assumed a linear pressure dependence of bare elastic constants (Carpenter et al., 2000; Carpenter, 2006). In contrast, we express the variation of bare elastic constants in terms of finite strain for a self-consistent treatment of thermodynamic quantities at high pressures (Stixrude and Lithgow-Bertelloni, 2005):

$$c_{ijkl}^0 = (1 + 2f_E)^{5/2} \left(c_{ijkl}^0 + (3K_0 c_{ijkl}^{0'} - 5c_{ijkl}^0) f_E + \left[6K_0 c_{ijkl}^{0'} - 14c_{ijkl}^0 - \frac{3}{2} K_0 \delta_{kl}^{ij} (3K_0' - 16) \right] f_E^2 \right) \quad (7.10)$$

where c_{ijkl}^0 and $c_{ijkl}^{0'}$ are the bare elastic constants and their pressure derivatives at ambient conditions in full index notation, respectively, and $\delta_{kl}^{ij} = -\delta_{ij} \delta_{kl} - \delta_{il} \delta_{jk} - \delta_{jl} \delta_{ik}$. To keep equation (7.10) internally consistent, the bulk modulus is calculated from the elastic constants as the Voigt bound $K_0 = c_{iikk}^0/9$ and accordingly $K_0' = c_{iikk}^{0'}/9$ (Stixrude and Lithgow-Bertelloni, 2005). The actual elastic response of a polycrystalline material depends on the extent to which individual grains can adapt to the external stress field (Hill, 1952; Watt et al., 1976). The Reuss bound would be appropriate if every grain experiences the same stress field and can freely deform according to its orientation relative to the stress tensor. In contrast, the Voigt bound applies when grains are mechanically clamped and forced into an overall strain state. For quasi-hydrostatic compression of sintered polycrystalline stishovite, the Voigt bound might appear to be more appropriate. We note, however, that we used equation (7.10) merely to describe the dependence of elastic constants on finite volume strain.

The elastic constants of stishovite and their pressure derivatives have previously been determined by Brillouin spectroscopy (Weidner et al., 1982; Brazhkin et al., 2005; Jiang et al., 2009) and computed from first principles (Karki et al., 1997a; Yang and Wu, 2014). Since the experimentally determined elastic constants c_{11} and c_{12} (in contracted index notation) are affected by elastic softening even at pressures below the phase transition (Carpenter et al., 2000; Jiang et al., 2009), the corresponding bare elastic constants at ambient conditions ($P = 0$) were calculated by combining the two relations (Carpenter et al., 2000)

$$c_{110}^0 + c_{120}^0 = c_{110} + c_{120} \quad (7.11)$$

$$c_{110}^0 - c_{120}^0 = (c_{110} - c_{120}) \frac{P_c}{P_c^*} \quad (7.12)$$

Linking equations (7.4)–(7.12) to the EOS (7.1) of stishovite (Table 7.2), the spontaneous strains can be calculated as a function of finite strain, i.e. volume. Our approach is similar to previous formulations based on the Lagrangian definition of strain (Tröster et al., 2002; Tröster et al., 2014). The Landau and coupling coefficients can be obtained by a least-squares fit of calculated to experimentally observed spontaneous strains. We used the unit cell edge lengths for CaCl_2 -type SiO_2 at pressures above 50 GPa (Table 7.1) to derive spontaneous strains as (Carpenter et al., 2000)

$$e_1 = \frac{a - a^0}{a^0} \quad (7.13)$$

$$e_2 = \frac{b - a^0}{a^0} \quad (7.14)$$

$$e_3 = \frac{c - c^0}{c^0} \quad (7.15)$$

where the unit cell edge lengths of stishovite, a^0 and c^0 , were extrapolated to the experimental pressures using the respective axial EOS (7.2) (Table 7.2). Including the EOS analysis described in section 7.3, we treated the combined data set of single-crystal stishovite and silica powder (Andraut et al., 2003) in the same way. The spontaneous strains calculated from both data sets are shown in Figure 7.3.

As mentioned in section 7.3, the splitting of diffraction lines gives only a rough estimate for the transition pressure (Fig. 7.1). The transition pressure can be precisely located by observing structural properties that are directly linked to the transition mechanism such as the frequency of the soft optic mode (Kingma et al., 1995; Carpenter et al., 2000). The symmetry-breaking spontaneous strain ($e_1 - e_2$) reflects the main structural distortion of the phase transition. $(e_1 - e_2)^2$ should increase linearly with pressure, and the intersection of the linear trend with the pressure axis at zero spontaneous strain gives a reliable estimate of the transition pressure (Carpenter et al., 2000).

The symmetry-breaking spontaneous strains observed on sintered polycrystalline CaCl_2 -type SiO_2 follow the behavior predicted by Landau theory (Fig. 7.3a). Figure 7.3a shows that the transition pressures of sintered polycrystalline stishovite (44.7 ± 2.9 GPa) and stishovite powder (48.3 ± 1.7 GPa) are almost identical when considering their uncertainties as derived from the linear fits. Moreover, spontaneous strains observed on sintered polycrystalline CaCl_2 -type SiO_2 are consistent with the spontaneous strains of CaCl_2 -type SiO_2 powder at pressures close to the phase transition. Both Singh et al. (2012) and Asahara et al. (2013) observed the phase transition at substantially lower pressures upon nonhydrostatic compression (Fig. 7.3a). We therefore conclude that our experiments were not strongly affected by nonhydrostatic compression.

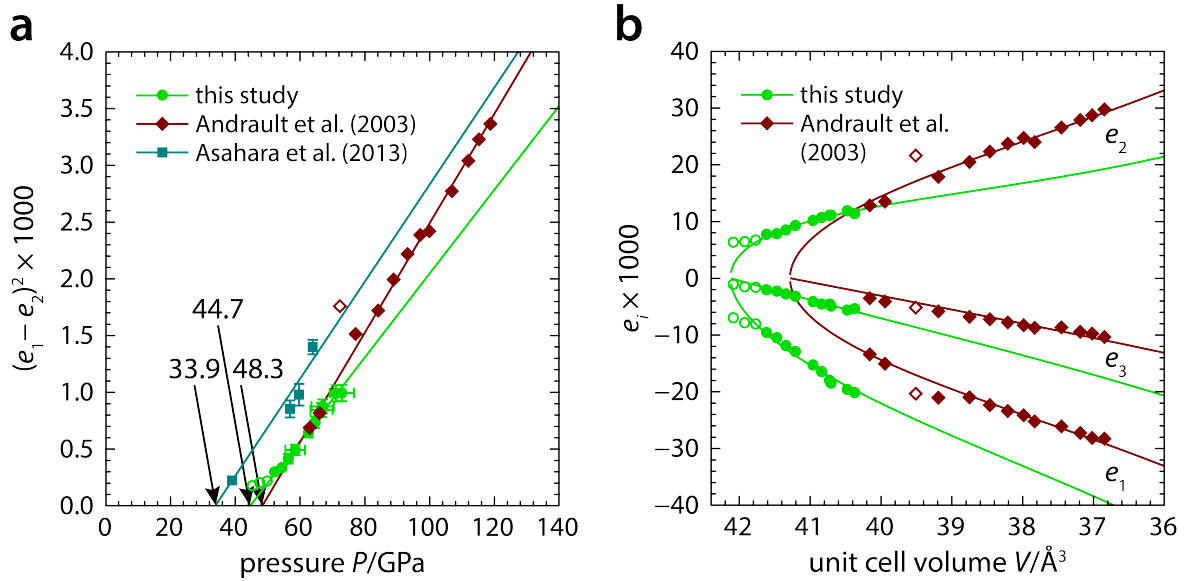


Figure 7.3: Spontaneous strains in orthorhombic CaCl_2 -type SiO_2 as a function of pressure (a) and unit cell volume (b). In (a), the intersection of the extrapolated squared symmetry-breaking strains $(e_1 - e_2)^2$ with the pressure axis gives the indicated transition pressures. In (b), curves show spontaneous strains predicted by Landau theory. Open symbols show data excluded from analysis. This study: sintered polycrystalline silica; Andrault et al. (2003): powder; Asahara et al. (2013): sintered polycrystalline silica (nonhydrostatic).

To determine all relevant coefficients of equation (7.3) by least-squares fits of calculated to experimentally observed spontaneous strains, we fixed the transition pressures to the values derived from Figure 7.3a. To reduce correlations between parameters, we further fixed the difference between the critical pressure and the transition pressure to the value given by Carpenter et al. (2000), i.e. $P_c - P_c^* = 50.7 \text{ GPa}$, and set $b = 11$ (Carpenter et al., 2000; Carpenter, 2006). Since the pressure derivatives of the bare elastic constants c_{110}^0 and c_{120}^0 should be affected by elastic softening (Jiang et al., 2009) but cannot be simply obtained by combining the experimentally observed pressure derivatives, we fixed $c_{110}^{0'} = 4.9$ to the value given by Jiang et al. (2009) and treated $c_{120}^{0'}$ as free parameter during the fitting procedure. Due to the limited pressure range of spontaneous strains observed on sintered polycrystalline CaCl_2 -type SiO_2 , however, $c_{120}^{0'}$ was fixed to the value obtained by fitting the spontaneous strains of CaCl_2 -type SiO_2 powder. All other relevant elastic constants and pressure derivatives were also fixed to their experimentally determined values (Jiang et al., 2009). Table 7.3 lists the final combinations of coefficients, and the predicted evolution of spontaneous strains is shown in Figure 7.3b. We note that our approach to derive Landau and coupling coefficients relies on a minimum of assumptions and is internally consistent.

7.5 Elasticity of Stishovite across the Ferroelastic Phase Transition

The variation of individual elastic constants with pressure as calculated using the expressions given by Carpenter et al. (2000) and the parameters of Table 7.3 is shown in Figure 7.4a. Besides the small difference in transition pressures, the elastic constants predicted for

Table 7.3: Refined Landau coefficients, coupling coefficients, and bare elastic constants for the stishovite–CaCl₂-type SiO₂ phase transition

	Sintered poly-crystalline silica	Powder ^a
Landau and coupling coefficients		
$P_c - P_c^*$ (GPa) ^b	50.7(50)	50.7(50)
P_c^* (GPa) ^c	44.7(29)	48.3(17)
a	-0.0342(40)	-0.0510(67)
b (GPa)	11	11
λ_1 (GPa)	31.39(89)	8.52(100)
λ_2 (GPa)	22.86(32)	27.59(104)
λ_3 (GPa)	44.74(99)	33.45(139)
Bare elastic constants^d		
c_{110}^0 (GPa)	600(24)	589(17)
c_{120}^0 (GPa)	54(24)	65(17)
$c_{120}^{0'}$	2.8(3)	2.8(3)

Values in *italics* were fixed during refinement. Numbers in parentheses are standard errors on the last digit.

^aCompression data from Andrault et al. (2003).

^bFrom Carpenter et al. (2000).

^cFrom linear fits in Figure 7.3a.

^dAll remaining elastic constants and pressure derivatives as given in Jiang et al. (2009).

sintered polycrystalline stishovite and CaCl₂-type SiO₂ are more perturbed at the phase transition when compared to the predictions for silica powder. Another fundamental difference becomes apparent when combining individual elastic constants to bulk and shear moduli (Figs. 7.4b and 7.4c). Similar to previous results (Carpenter et al., 2000), Landau theory predicts substantial softening of the shear modulus in the vicinity of the phase transition for both sintered polycrystalline stishovite and stishovite powder (Fig. 7.4b). While the powder data suggest only a small drop of the bulk modulus at the phase transition, however, the bulk modulus is predicted to drop significantly in the case of sintered polycrystalline silica (Fig. 7.4c). We note that this prediction is based on the analysis of spontaneous strains only and does not involve volume compression data. The analysis of volume compression data, however, indicated a kink in the compression curves and hence a drop in the bulk modulus as well (Fig. 7.2c).

The bulk moduli of stishovite and CaCl₂-type SiO₂ as calculated from the respective EOS are also shown in Figure 7.4c. For stishovite powder, the Landau theory prediction remains closer to the EOS bulk modulus when compared to sintered polycrystalline stishovite. The bulk moduli derived from the compression curves of sintered polycrystalline stishovite and CaCl₂-type SiO₂ are substantially higher than the Landau theory prediction. These differences arise from the low pressure derivative of the bulk modulus when computed from the pressure derivatives of individual elastic constants, $K_0' = c_{iikk0}^{0'}/9 = 3.0(1)$, in comparison

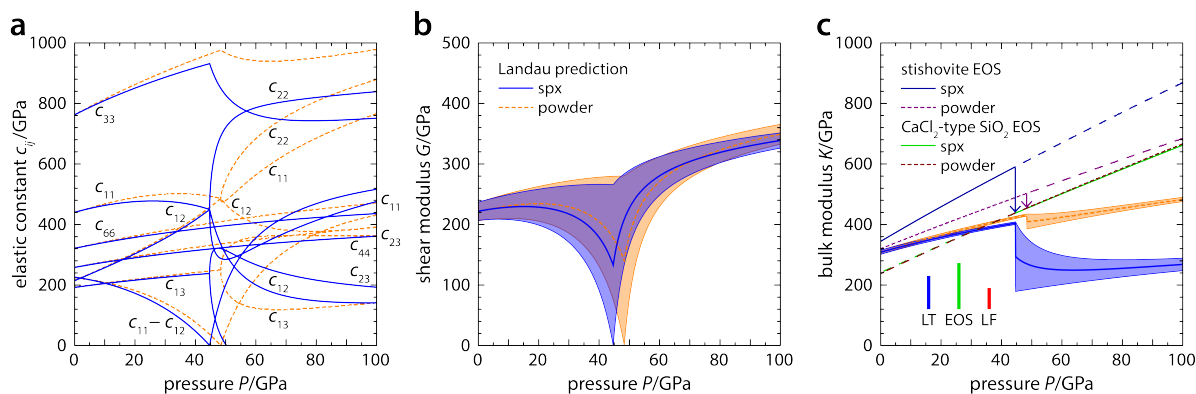


Figure 7.4: Pressure evolution of elastic constants (a), shear modulus (b), and bulk modulus (c) of stishovite and CaCl_2 -type SiO_2 across the ferroelastic phase transition as predicted by Landau theory (a,b,c) and calculated from the equations of state (EOS) (c). In (b) and (c), the shading indicates Voigt (upper) and Reuss (lower) bounds on the respective modulus while bold curves show the Voigt-Reuss-Hill average. In (c), vertical bars show the magnitudes of the drop in bulk modulus of sintered polycrystalline silica at the phase transition as estimated by Landau theory (LT), from the EOS, and by linear fits (LF) to pressure-volume pairs. Note the differences in pressure derivatives of the bulk moduli as derived from compression experiments and predicted by Landau theory. spx: sintered polycrystalline silica (this study); powder: compression data from Andrault et al. (2003).

to $K'_0 = 4$ to 6 as derived from compression experiments (Table 7.2). Landau theory predicts the evolution of individual elastic constants of a (isolated) single crystal but does not capture the interactions between grains that cause the initial stiffening observed in the compression curves. The magnitudes of the drops in bulk moduli, however, are very similar to the magnitudes predicted based on single-crystal elastic constants and spontaneous strains. To estimate the drop in bulk modulus independent of any assumption, we derived the bulk moduli of sintered polycrystalline stishovite and CaCl_2 -type SiO_2 close to the phase transition by fitting a linear trend to the three pressure-volume pairs of each phase closest to the transition pressure but outside of the potential two-phase region. The resulting drop in bulk modulus is approximately half of the drop inferred from the EOS but still amounts to about 70 GPa (Fig. 7.4c). We attribute the high absolute values and the acute drop of the bulk modulus at the phase transition to grain-grain interactions in sintered polycrystalline silica, potentially arising from locked grain boundaries, and to the partial relaxation of internal stresses at the phase transition, respectively.

7.6 Sound Wave Velocities of Stishovite and Geophysical Implications

To calculate aggregate sound wave velocities, we combined bulk moduli and densities from the experimental EOS of sintered polycrystalline silica and silica powder with shear moduli predicted by Landau theory. The calculated aggregate sound wave velocities are shown as a function of pressure in Figure 7.5. Apart from slightly different transition pressures, shear wave (S wave) velocities predicted based on our results on sintered polycrystalline silica and on previous studies on silica powder are consistent, including the magnitude and

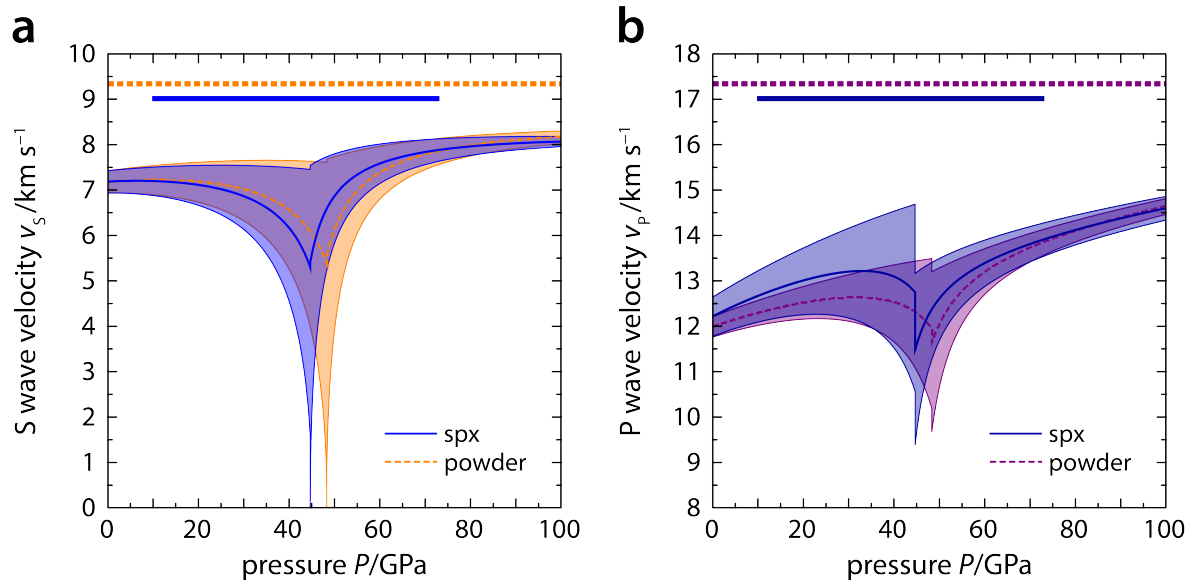


Figure 7.5: Pressure evolution of S wave (a) and P wave velocity (b) of stishovite and CaCl_2 -type SiO_2 across the ferroelastic phase transition. The shading indicates upper and lower bounds on the respective velocity calculated from the Voigt and Reuss bounds on the shear modulus, respectively, and the uncertainties of the EOS parameters. Bold curves show the aggregate velocity calculated from the Voigt-Reuss-Hill average of the shear modulus and the EOS bulk modulus. Horizontal bars indicate the pressure ranges covered by the respective compression experiments. spx: sintered polycrystalline silica (this study); powder: compression data from Andrault et al. (2003).

pressure range of shear wave softening (Fig. 7.5a). Our predictions based on compression experiments and Landau theory are also consistent with recent *ab initio* computations (Yang and Wu, 2014).

Predicted compressional wave (P wave) velocities, however, evolve differently with increasing pressure when using the results on sintered polycrystalline silica instead of those on silica powder (Fig. 7.5b). At pressures below the phase transition, P wave velocities are predicted to be faster and to rise steeper with increasing pressure reflecting the initial stiffening of sintered polycrystalline stishovite on compression (Fig. 7.2c). In addition to the softening of the shear modulus close to the phase transition, the compression curves in Figure 7.2c indicate a sharp drop of the bulk modulus at the phase transition (Fig. 7.4c). This sharp drop of the bulk modulus translates into an abrupt drop in P wave velocities, which is enhanced by the use of the EOS for sintered polycrystalline silica. At pressures above the phase transition, P wave velocities rise again as the softening declines and evolve similarly at higher pressures regardless of whether the compression behavior of sintered polycrystalline CaCl_2 -type SiO_2 or CaCl_2 -type SiO_2 powder is considered. At pressures above the phase transition, P wave velocities as predicted here by combining experimental EOS with Landau theory are in very good agreement with P wave velocities computed from first principles (Yang and Wu, 2014).

We can think of a powder as representing a completely relaxed rock without interactions between grains and internal stresses. Such a situation would be favored by high temperatures and on long time scales. A sintered polycrystalline material, in contrast, represents a situation without relaxation and hence involves the build-up of internal stresses between

elastically anisotropic grains in response to a changing external stress field. At temperatures of Earth's lower mantle, such a relaxation-free situation can only be maintained on very short time scales and after fast perturbations of the stress environment. Relaxation processes such as grain boundary movements, dislocation movements, and atomic diffusion operate on different time scales that depend on temperature (Jackson, 2007). Typical seismic frequencies (1 mHz to 1 Hz) might be high enough to probe a situation in between the totally relaxed and totally unrelaxed situations (Jackson, 2007). Grain sizes are expected to be larger in the lower mantle than in experimental samples (Solomatov et al., 2002). Differences in grain size might require additional corrections on sound wave velocities derived from experiments (Jackson, 2007). In terms of elastic interactions between grains, however, the elastic properties of a sintered polycrystalline material and an unconsolidated powder may serve as bounds for the propagation of seismic waves.

Taking the sound wave velocities as predicted based on the compression behavior of sintered polycrystalline silica and silica powder as bounds for seismic velocities, we speculate that P wave velocities of stishovite-bearing rocks might drop substantially at the ferroelastic phase transition of stishovite. In addition to elastic softening in the vicinity of the ferroelastic phase transition, P wave velocities might be further decreased by the relaxation of internal stresses at the phase transition as indicated by the compression curve of sintered polycrystalline stishovite (Fig. 7.2c). Above the phase transition, the similar EOS of sintered polycrystalline CaCl_2 -type SiO_2 and CaCl_2 -type SiO_2 powder suggest a decreasing difference in the elastic response of both materials with increasing pressure as reflected in similar sound wave velocities (Fig. 7.5). However, partial build-up and relaxation of internal stresses during the passage of a seismic wave might perturb the elastic response of stishovite-bearing rocks close to the ferroelastic phase transition beyond what would be expected based on a completely relaxed situation.

The results of our compression experiment on sintered polycrystalline stishovite and the analysis using Landau theory may have implications for detecting stishovite-bearing materials in Earth's lower mantle. At depths greater than 700 km, stishovite would contribute with 10 to 20 vol-% to the mineral assemblage of subducted oceanic crust with a MORB-like composition (Hirose et al., 1999; Perrillat et al., 2006; Ricolleau et al., 2010). Rocks with much higher volume fractions of silica phases would be expected to be dispersed in the lower mantle if silica exsolved from the outer core (Hirose et al., 2017; Helffrich et al., 2018). The high viscosity of stishovite prevents stishovite-bearing rocks from mixing with the surrounding mantle (Xu et al., 2017). Scattering of S waves in the lower mantle has been related to the presence of stishovite based on low S wave velocities predicted for stishovite at conditions close to the ferroelastic phase transition (Kaneshima and Helffrich, 2010; Helffrich et al., 2018). Our findings, however, emphasize the importance of P waves since they might be affected by the phase transition in stishovite more than previously thought. P waves are indeed reflected and scattered in the lower mantle (LeStunff et al., 1995; Hedlin et al., 1997). To relate seismic scattering in the lower mantle to the presence of stishovite, a more complete understanding of how the ferroelastic phase transition interacts with seismic waves is needed. Recently, the bulk modulus of ferropericlase has been determined at seismic frequencies and pressures of the lower mantle (Marquardt et al., 2018). Similar experiments on sintered polycrystalline silica could demonstrate to which extent the bulk modulus is affected by the ferroelastic phase transition at seismic frequencies. In particular, anelastic relaxation processes and acoustic attenuation (Carpenter et al., 2000; Jackson, 2007) as well as effects arising from internal stresses in sintered polycrystalline materials as

pointed out in the present study require measurements at seismic frequencies and at high pressures and high temperatures.

Acknowledgments

This work was supported by the Deutsche Forschungsgemeinschaft (DFG) [grant numbers MA4534/3-1, INST 91/315-1 FUGG, GRK 2156/1]. H. M. acknowledges support from the Bayerische Akademie der Wissenschaften (BAW). All relevant data are compiled in Table 7.1 or have been published previously as cited in the text.

Author Contributions

J. Buchen analyzed the experimental data, modeled sound wave velocities, and wrote the manuscript. H. Marquardt proposed to study sintered polycrystalline stishovite, applied for beam time at the European Synchrotron Radiation Facility (ESRF), and commented on the manuscript. K. Schulze performed the experiments and commented on the manuscript. S. Speziale performed the experiments and commented on the manuscript. T. Boffa Ballaran assisted with data analysis and commented on the manuscript. N. Nishiyama synthesized and characterized sintered polycrystalline stishovite and commented on the manuscript. M. Hanfland assisted with the experiments at ESRF.

References

- Andrault, D., G. Fiquet, F. Guyot, and M. Hanfland (1998). Pressure-induced Landau-type transition in stishovite. *Science* **282**, 720–724.
- Andrault, D., R. J. Angel, J. L. Mosenfelder, and T. Le Bihan (2003). Equation of state of stishovite to lower mantle pressures. *Am. Mineral.* **88**, 301–307.
- Angel, R. J. (2000). Equations of state. *Rev. Mineral. Geochem.* **41**, 35–59.
- Asahara, Y., K. Hirose, Y. Ohishi, N. Hirao, H. Ozawa, and M. Murakami (2013). Acoustic velocity measurements for stishovite across the post-stishovite phase transition under deviatoric stress: Implications for the seismic features of subducting slabs in the mid-mantle. *Am. Mineral.* **98**, 2053–2062.
- Bézar, J.-F. and P. Lelann (1991). E.s.d.'s and estimated probable error obtained in Rietveld refinements with local correlations. *J. Appl. Crystallogr.* **24**, 1–5.
- Birch, F. (1947). Finite elastic strain of cubic crystals. *Phys. Rev.* **71**, 809–824.
- Brazhkin, V. V., L. E. McNeil, M. Grimsditch, N. A. Bendeliani, T. I. Dyuzheva, and L. M. Lityagina (2005). Elastic constants of stishovite up to its amorphization temperature. *J. Phys.: Condens. Matter* **17**, 1869.
- Carpenter, M. A. (2006). Elastic properties of minerals and the influence of phase transitions. *Am. Mineral.* **91**, 229–246.
- Carpenter, M. A. and E. K. H. Salje (1998). Elastic anomalies in minerals due to structural phase transitions. *Eur. J. Mineral.* **10**, 693–812.
- Carpenter, M. A., R. J. Hemley, and H.-k. Mao (2000). High-pressure elasticity of stishovite and the $P4_2/mnm \rightleftharpoons Pnmm$ phase transition. *J. Geophys. Res.: Solid Earth* **105**, 10807–10816.

- Dewaele, A., M. Torrent, P. Loubeyre, and M. Mezouar (2008). Compression curves of transition metals in the Mbar range: Experiments and projector augmented-wave calculations. *Phys. Rev. B* **78**, 104102.
- El Goresy, A., P. Dera, T. G. Sharp, C. T. Prewitt, M. Chen, L. Dubrovinsky, B. Wopenka, N. Z. Boctor, and R. J. Hemley (2008). Seifertite, a dense orthorhombic polymorph of silica from the Martian meteorites Shergotty and Zagami. *Eur. J. Mineral.* **20**, 523–528.
- Fei, Y., A. Ricolleau, M. Frank, K. Mibe, G. Shen, and V. Prakapenka (2007). Toward an internally consistent pressure scale. *Proc. Natl. Acad. Sci. U. S. A.* **104**, 9182–9186.
- Fischer, R. A., A. J. Campbell, B. A. Chidester, D. M. Reaman, E. C. Thompson, J. S. Pigott, V. B. Prakapenka, and J. S. Smith (2018). Equations of state and phase boundary for stishovite and CaCl₂-type SiO₂. *Am. Mineral.* **103**, 792–802.
- Grocholski, B., S.-H. Shim, and V. B. Prakapenka (2013). Stability, metastability, and elastic properties of a dense silica polymorph, seifertite. *J. Geophys. Res.: Solid Earth* **118**, 4745–4757.
- Hammersley, A. P. (2016). *FIT2D*: a multi-purpose data reduction, analysis and visualization program. *J. Appl. Crystallogr.* **49**, 646–652.
- Hedlin, M. A. H., P. M. Shearer, and P. S. Earle (1997). Seismic evidence for small-scale heterogeneity throughout the Earth's mantle. *Nature* **387**, 145.
- Helfrich, G., M. D. Ballmer, and K. Hirose (2018). Core-exsolved SiO₂ dispersal in the Earth's mantle. *J. Geophys. Res.: Solid Earth* **123**, 176–188.
- Hemley, R. J., C. T. Prewitt, and K. J. Kingma (1994). High-pressure behavior of silica. *Rev. Mineral.* **29**, 41–81.
- Hemley, R. J., J. Shu, M. A. Carpenter, J. Hu, H. K. Mao, and K. J. Kingma (2000). Strain/order parameter coupling in the ferroelastic transition in dense SiO₂. *Solid State Commun.* **114**, 527–532.
- Hill, R. (1952). The elastic behaviour of a crystalline aggregate. *Proc. Phys. Soc., London, Sect. A* **65**, 349–354.
- Hirose, K., Y. Fei, Y. Ma, and H.-K. Mao (1999). The fate of subducted basaltic crust in the Earth's lower mantle. *Nature* **397**, 53.
- Hirose, K., G. Morard, R. Sinmyo, K. Umemoto, J. Hernlund, G. Helfrich, and S. Labrosse (2017). Crystallization of silicon dioxide and compositional evolution of the Earth's core. *Nature* **543**, 99–102.
- Jackson, I. (2007). Properties of rocks and minerals – Physical origins of anelasticity and attenuation in rock. In: *Treatise on Geophysics*. Ed. by G. Schubert. Elsevier, Amsterdam, 493–525.
- Jiang, F., G. D. Gwanmesia, T. I. Dyuzheva, and T. S. Duffy (2009). Elasticity of stishovite and acoustic mode softening under high pressure by Brillouin scattering. *Phys. Earth Planet. Inter.* **172**, 235–240.
- Joswig, W., T. Stachel, J. W. Harris, W. H. Baur, and G. P. Brey (1999). New Ca-silicate inclusions in diamonds — tracers from the lower mantle. *Earth Planet. Sci. Lett.* **173**, 1–6.
- Kaneshima, S. and G. Helfrich (2010). Small scale heterogeneity in the mid-lower mantle beneath the circum-Pacific area. *Phys. Earth Planet. Inter.* **183**, 91–103.
- Kantor, I., V. Prakapenka, A. Kantor, P. Dera, A. Kurnosov, S. Sinogeikin, N. Dubrovinskaia, and L. Dubrovinsky (2012). BX90: A new diamond anvil cell design for X-ray diffraction and optical measurements. *Rev. Sci. Instrum.* **83**, 125102.
- Karki, B. B., L. Stixrude, and J. Crain (1997a). Ab initio elasticity of three high-pressure polymorphs of silica. *Geophys. Res. Lett.* **24**, 3269–3272.

- Karki, B. B., M. C. Warren, L. Stixrude, G. J. Ackland, and J. Crain (1997b). Ab initio studies of high-pressure structural transformations in silica. *Phys. Rev. B* **55**, 3465–3471.
- Kingma, K. J., R. E. Cohen, R. J. Hemley, and H.-k. Mao (1995). Transformation of stishovite to a denser phase at lower-mantle pressures. *Nature* **374**, 243.
- Kurnosov, A., I. Kantor, T. Boffa-Ballaran, S. Lindhardt, L. Dubrovinsky, A. Kuznetsov, and B. H. Zehnder (2008). A novel gas-loading system for mechanically closing of various types of diamond anvil cells. *Rev. Sci. Instrum.* **79**, 045110.
- Léger, J. M., J. Haines, M. Schmidt, J. P. Petit, A. S. Pereira, and J. A. H. da Jornada (1996). Discovery of hardest known oxide. *Nature* **383**, 401.
- LeStunff, Y., C. W. Wicks, and B. Romanowicz (1995). P'P' precursors under Africa: Evidence for mid-mantle reflectors. *Science* **270**, 74–77.
- Lutterotti, L., M. Bortolotti, G. Ischia, I. Lonardelli, and H. R. Wenk (2007). Rietveld texture analysis from diffraction images. *Z. Kristallogr. Suppl.* **26**, 125–130.
- Marquardt, H. and K. Marquardt (2012). Focused ion beam preparation and characterization of single-crystal samples for high-pressure experiments in the diamond-anvil cell. *Am. Mineral.* **97**, 299–304.
- Marquardt, H., A. Gleason, K. Marquardt, S. Speziale, L. Miyagi, G. Neusser, H.-R. Wenk, and R. Jeanloz (2011a). Elastic properties of MgO nanocrystals and grain boundaries at high pressures by Brillouin scattering. *Phys. Rev. B* **84**, 064131.
- Marquardt, H., S. Speziale, K. Marquardt, H. J. Reichmann, Z. Konôpková, W. Morgenroth, and H.-P. Liermann (2011b). The effect of crystallite size and stress condition on the equation of state of nanocrystalline MgO. *J. Appl. Phys.* **110**, 113512.
- Marquardt, H., J. Buchen, A. S. J. Mendez, A. Kurnosov, M. Wendt, A. Rothkirch, D. Pennicard, and H.-P. Liermann (2018). Elastic softening of $(\text{Mg}_{0.8}\text{Fe}_{0.2})\text{O}$ ferropericlase across the iron spin crossover measured at seismic frequencies. *Geophys. Res. Lett.* **45**, 6862–6868.
- Murakami, M., K. Hirose, S. Ono, and Y. Ohishi (2003). Stability of CaCl_2 -type and α - PbO_2 -type SiO_2 at high pressure and temperature determined by in-situ X-ray measurements. *Geophys. Res. Lett.* **30**, 1207.
- Nishiyama, N., F. Wakai, H. Ohfuji, Y. Tamenori, H. Murata, T. Taniguchi, M. Matsushita, M. Takahashi, E. Kulik, K. Yoshida, et al. (2014). Fracture-induced amorphization of polycrystalline SiO_2 stishovite: a potential platform for toughening in ceramics. *Sci. Rep.* **4**, 6558.
- Nisr, C., K. Leinenweber, V. Prakapenka, C. Prescher, S. Tkachev, and S.-H. D. Shim (2017). Phase transition and equation of state of dense hydrous silica up to 63 GPa. *J. Geophys. Res.: Solid Earth* **122**, 6972–6983.
- Niu, F., H. Kawakatsu, and Y. Fukao (2003). Seismic evidence for a chemical heterogeneity in the midmantle: A strong and slightly dipping seismic reflector beneath the Mariana subduction zone. *J. Geophys. Res.: Solid Earth* **108**, 2419.
- Nomura, R., K. Hirose, N. Sata, and Y. Ohishi (2010). Precise determination of post-stishovite phase transition boundary and implications for seismic heterogeneities in the mid-lower mantle. *Phys. Earth Planet. Inter.* **183**, 104–109.
- Ono, S., K. Hirose, M. Murakami, and M. Isshiki (2002). Post-stishovite phase boundary in SiO_2 determined by in situ X-ray observations. *Earth Planet. Sci. Lett.* **197**, 187–192.
- Perrillat, J.-P., A. Ricolleau, I. Daniel, G. Fiquet, M. Mezouar, N. Guignot, and H. Cardon (2006). Phase transformations of subducted basaltic crust in the uppermost lower mantle. *Phys. Earth Planet. Inter.* **157**, 139–149.

- Ricolleau, A., J.-P. Perrillat, G. Fiquet, I. Daniel, J. Matas, A. Addad, N. Menguy, H. Cardon, M. Mezouar, and N. Guignot (2010). Phase relations and equation of state of a natural MORB: Implications for the density profile of subducted oceanic crust in the Earth's lower mantle. *J. Geophys. Res.: Solid Earth* **115**, B08202.
- Ross, N. L., J. Shu, and R. M. Hazen (1990). High-pressure crystal chemistry of stishovite. *Am. Mineral.* **75**, 739–747.
- Schulze, K., J. Buchen, K. Marquardt, and H. Marquardt (2017). Multi-sample loading technique for comparative physical property measurements in the diamond-anvil cell. *High Pressure Res.* **37**, 159–169.
- Shieh, S. R., T. S. Duffy, and B. Li (2002). Strength and elasticity of SiO₂ across the stishovite–CaCl₂-type structural phase boundary. *Phys. Rev. Lett.* **89**, 255507.
- Singh, A. K., D. Andrault, and P. Bouvier (2012). X-ray diffraction from stishovite under nonhydrostatic compression to 70 GPa: Strength and elasticity across the tetragonal → orthorhombic transition. *Phys. Earth Planet. Inter.* **208**, 1–10.
- Solomatov, V. S., R. El-Khozondar, and V. Tikare (2002). Grain size in the lower mantle: constraints from numerical modeling of grain growth in two-phase systems. *Phys. Earth Planet. Inter.* **129**, 265–282.
- Stishov, S. M. and N. V. Belov (1962). Crystalline structure of the new close-grained modification of silica, SiO₂. *Dokl. Akad. Nauk SSSR* **143**, 951–954 (in Russian).
- Stixrude, L. and C. Lithgow-Bertelloni (2005). Thermodynamics of mantle minerals – I. Physical properties. *Geophys. J. Int.* **162**, 610–632.
- Tröster, A., W. Schranz, and R. Miletich (2002). How to couple Landau theory to an equation of state. *Phys. Rev. Lett.* **88**, 055503.
- Tröster, A., W. Schranz, F. Karsai, and P. Blaha (2014). Fully consistent finite-strain Landau theory for high-pressure phase transitions. *Phys. Rev. X* **4**, 031010.
- Tsuchiya, T., R. Caracas, and J. Tsuchiya (2004). First principles determination of the phase boundaries of high-pressure polymorphs of silica. *Geophys. Res. Lett.* **31**, L11610.
- Wadhawan, V. K. (1982). Ferroelasticity and related properties of crystals. *Phase Transitions* **3**, 3–103.
- Watt, J. P., G. F. Davies, and R. J. O'Connell (1976). The elastic properties of composite materials. *Rev. Geophys.* **14**, 541–563.
- Weidner, D. J., J. D. Bass, A. E. Ringwood, and W. Sinclair (1982). The single-crystal elastic moduli of stishovite. *J. Geophys. Res.: Solid Earth* **87**, 4740–4746.
- Xu, F., D. Yamazaki, N. Sakamoto, W. Sun, H. Fei, and H. Yurimoto (2017). Silicon and oxygen self-diffusion in stishovite: Implications for stability of SiO₂-rich seismic reflectors in the mid-mantle. *Earth Planet. Sci. Lett.* **459**, 332–339.
- Yang, R. and Z. Wu (2014). Elastic properties of stishovite and the CaCl₂-type silica at the mantle temperature and pressure: An ab initio investigation. *Earth Planet. Sci. Lett.* **404**, 14–21.
- Zhang, J., B. Li, W. Utsumi, and R. C. Liebermann (1996). In situ X-ray observations of the coesite-stishovite transition: reversed phase boundary and kinetics. *Phys. Chem. Miner.* **23**, 1–10.

Appendix A

Appendix

A.1 The Equation of State of Wadsleyite Solid Solutions: Constraining the Effects of Anisotropy and Crystal Chemistry

A.1.1 Supplementary Methods

Analysis of Mössbauer Spectrum

To determine the ferric iron content of the wadsleyite sample, the recorded Mössbauer spectrum was fit to doublets of Lorentzian peaks using the program MossA (Prescher et al., 2012). We tested five different fitting models based on previous Mössbauer spectral analyses of wadsleyite (Mrosko et al., 2015; Kawazoe et al., 2016). For all models, conventional constraints for quadrupole doublets were applied (equal component widths and areas), with some additional constraints in some of the models: (1) two doublets in the thin approximation, one Fe^{2+} and one Fe^{3+} , constrained to have the same full width at half maximum (FWHM); (2) three doublets in the thin approximation, one Fe^{2+} and two Fe^{3+} , with Fe^{3+} doublets constrained to have the same FWHM; (3) three doublets in the thin approximation, two Fe^{2+} and one Fe^{3+} ; (4) three doublets in the thin approximation, two Fe^{2+} and one Fe^{3+} , with Fe^{2+} doublets constrained to have the same FWHM; and (5) model 3, but fit with the full transmission integral. We prefer model 4 (Appendix Fig. A.1, Appendix Table A.2) with $\text{Fe}^{3+}/\Sigma\text{Fe} = 0.15(3)$. However, in terms of the ferric iron content, all models are indistinguishable within experimental uncertainty.

Fourier-Transform Infrared Absorption Spectroscopy

Polarized and unpolarized infrared absorption spectra were recorded with a Bruker IFS 120 HR Fourier-transform infrared (FTIR) spectrometer in a spectral range from 2500 cm^{-1} to 4000 cm^{-1} and with a resolution of 4 cm^{-1} . The light from a tungsten lamp passed through a Michelson interferometer with a Si-coated CaF_2 beam splitter and was directed onto the single-crystal thin sections with an infrared microscope working with reflecting (Cassegrainian) optics. A liquid nitrogen cooled MCT detector recorded the light transmitted through the specimen. For polarized spectra, an infrared polarizer consisting of an aluminum grating coated on KRS-5 substrate was inserted into the light path just before the sample. The spectrometer optics were constantly purged with purified H_2O and CO_2 free air. 200 scans

were accumulated for each spectrum. The thin sections were laid onto a CaF₂ plate and immersed in polychlorotrifluoroethylene oil to reduce the amplitude of interference fringes resulting from internal reflections on the polished sample surfaces.

Analysis of Infrared Absorption Spectra and Calculation of Hydrogen Concentrations

For each crystal, we selected the spectrum less affected by interference fringes. Arising from different aperture sizes and other effects (interference, scattering, etc.), apparent background absorption was corrected for by subtracting a manually adjusted spline function. Close to absorption bands, however, we kept the background shape as simple as possible not to distort peak shapes by an uncertain extrapolation of interference fringes. A series of Gaussian functions was used to model the absorption bands. The low frequency band around 3330 cm⁻¹ was fit to two peaks located at 3333±3 cm⁻¹ and 3343±6 cm⁻¹ and the high frequency band around 3600 cm⁻¹ to two peaks at 3597±2 cm⁻¹ and 3614±1 cm⁻¹. These frequencies are similar to those observed by previous FTIR studies on wadsleyite (Jacobsen et al., 2005; Deon et al., 2010; Bolfan-Casanova et al., 2012). For most spectra, an additional peak between 3449 cm⁻¹ and 3484 cm⁻¹ was introduced to model a weak rise in absorption at intermediate frequencies, sometimes only present as a shoulder on the strong low frequency band. In our spectra, this weak feature could equally be a remnant of interference fringes. An absorption band around 3500 cm⁻¹ has been attributed to the coupled substitution of Fe³⁺ and H⁺ for Si⁴⁺ in wadsleyite (Bolfan-Casanova et al., 2012; Smyth et al., 2014; Kawazoe et al., 2016). Appendix Figure A.3 illustrates the band analysis procedure.

From the areas beneath individual Gaussian curves, area-weighted mean wave numbers $\langle \nu \rangle$ were calculated as described by Libowitzky and Rossman (1997) and the areas merged for each absorption band. The integrated absorbance A_{INT} of each band was converted to a volume concentration of H₂O equivalents using the wave number-dependent molar absorption coefficient for hydroxyl groups in minerals given by Libowitzky and Rossman (1997). We also applied the wadsleyite-specific molar absorption coefficient determined by Deon et al. (2010) and found agreement between both calibrations in terms of total hydrogen concentrations. For comparison with earlier work (Kohlstedt et al., 1996; Jacobsen et al., 2005), the background corrected spectrum was scaled with the wave number-dependent molar absorption coefficient for hydroxyl groups as calibrated by Paterson (1982) and the resulting curve integrated in intervals spanning the range of wave numbers where infrared absorption by hydroxyl groups has been reported for wadsleyite. This procedure again results in a volume concentration of H₂O equivalents for each spectral interval. The analysis was carried out for unpolarized spectra as well as for polarized spectra recorded at the same spot on the crystal. The results are summarized in Appendix Table A.4.

Following the ideas of Libowitzky and Rossman (1996), the total absorbance A_{TOT} for an absorption band can be obtained from polarized measurements on three mutually perpendicular crystal sections. In the following, we show how the polarized spectra acquired on the two sections cut parallel to the (120) and (243) planes can be combined to a total absorbance for each section. The relations between relevant crystallographic planes and directions are illustrated in the stereographic projection of Appendix Figure A.4. For the section parallel to (120), $n'_{(120)} \parallel \mathbf{c}$ and $n''_{(120)} \parallel [-210]$. $[-210]$ makes an angle close to 45° to both the \mathbf{a} and \mathbf{b} axis. Hence, any pair of equivalent directions $\langle 210 \rangle$ will enclose an angle close to 90°. Therefore, the spectra collected with the electric field vector $\mathbf{E} \parallel n'_{(120)} \parallel \mathbf{c}$ and $\mathbf{E} \parallel n''_{(120)} \parallel [-120]$ suffice to model the absorbance in three nearly per-

pendicular planes, e.g. (120), (−120), and (001), and to calculate the total absorbance (Appendix Table A.4). For the (243) section, we located the vibration directions $n'_{(243)}$ and $n''_{(243)}$ with the refractive indices at 589 nm reported by Sinogeikin et al. (1998) neglecting optical dispersion (Appendix Fig. A.4). In a next step, we calculated the absorbances for two perpendicular directions lying within (243), one of them points along [−210], the other one lies in the (−120) plane. With the arguments made above for the (120) plane and the [−210] direction (and their symmetry equivalents {120} and <120>), the absorbance for $\mathbf{E} \parallel \mathbf{c}$ can be estimated. Again, the calculated absorbances along [−210] and along the \mathbf{c} axis can be combined to the total absorbance (Appendix Table A.4).

Data Set for the Equation of State of Wadsleyite Solid Solutions

Chemical Compositions. In some studies, the ferric iron content of the iron-bearing wadsleyite sample was not determined or reported precluding calculation of the Fe_3O_4 component. The iron-bearing wadsleyites of Hazen et al. (1990), Finger et al. (1993), and Hazen et al. (2000a), however, were all synthesized in rhenium capsules at similar temperatures (Finger et al., 1993) suggesting similar oxygen fugacities. Therefore, we adopt the ratio $\text{Fe}^{3+}/\Sigma\text{Fe} = z = 0.08$ determined on the sample with $x = 0.16$ by Fei et al. (1992) for the whole suite of samples studied by Hazen et al. (1990), Finger et al. (1993), and Hazen et al. (2000a) except for the sample with $x = 0.395$ (Finger et al., 1993). For the wadsleyite sample of Smyth et al. (1997), the ferric iron content, $\text{Fe}^{3+}/\Sigma\text{Fe} = 0.96(5)$, was determined later by McCammon et al. (2004) and shifts the composition slightly out of the quaternary system with a maximum ratio of 2/3, i. e. as in Fe_3O_4 .

Hydrogen contents were adopted as stated in the original publications even if hydrogen contents on the same or a similar wadsleyite sample were later redetermined with a different technique (Jacobsen et al., 2005; Mao et al., 2008b; Mao et al., 2011; Chang et al., 2015). This conservative approach retains the spread in estimated hydrogen contents resulting from the use of different methods and calibrations such as the unit cell axis ratio b/a as obtained by single-crystal X-ray diffraction (Jacobsen et al., 2005), or direct measurements by secondary ion mass spectrometry (SIMS), Fourier-transform infrared absorption spectroscopy (FTIR) (Paterson, 1982; Libowitzky and Rossman, 1997; Deon et al., 2010), nuclear magnetic resonance (Kleppe et al., 2001), and neutron diffraction (Purevjav et al., 2016). When stated as H_2O wt-%, we converted hydrogen contents to H_2O molecular equivalents per formula unit taking into account the iron content and molar mass of the respective wadsleyite sample. Hydrogen contents stated as H_2O wt-% are strictly comparable only among samples with similar iron contents. For example, the hydrogen content for the hydrous wadsleyite sample ($\text{Mg}_{1.75}\text{SiH}_{0.5}\text{O}_4$) studied by Kudoh et al. (1996), Yusa and Inoue (1997), Kudoh and Inoue (1998), and Kudoh and Inoue (1999) of 2.5(3) wt-% H_2O (Inoue et al., 1995; Yusa and Inoue, 1997) translates to $y = 0.1894(187)$.

Unit Cell Volumes. End member unit cell volumes were obtained by fitting equation (4.5) to the unit cell volumes listed in Appendix Table A.6 and unit cell volumes for different spinelloid III compositions (Table 4 in Woodland and Angel, 2000; Table 2 in Woodland et al., 2012). Unit cell volumes that deviate significantly from any compositional trend were excluded from the fit. Excluding, in addition, unit cell volumes for which the hydrogen concentration was estimated using the b/a axis ratio (Jacobsen et al., 2005), and hence not determined directly, changed only slightly the estimate of the unit cell volume for the MgH_2SiO_4 end member to $V_{\text{hywa}0} = 546.3(24) \text{ \AA}^3$ while leaving the other end member unit cell volumes unchanged. Excluding from the fit the unit cell volume of the oxidized sample

of Smyth et al. (1997) that falls slightly outside the quaternary system had no effect on the end member unit cell volumes.

Bulk and Linear Moduli. When reanalyzing volume and linear compression curves with second-order Birch-Murnaghan (BM-2) equations of state (EOS) (eqns. (4.1) and (4.2)), we treated unit cell volumes and unit cell edge lengths at ambient conditions as free parameters. We calculated Voigt and Reuss bounds on the bulk modulus using the linear moduli obtained from the reanalysis of experimental axial compression curves (eqn. (4.3)). All results are compiled in Appendix Table A.7 together with references to the compression curves shown in Appendix Figure A.7. This uniform analysis procedure removes differences in EOS parameters arising from different parametrization schemes.

In the case of studies using dynamic methods, we selected adiabatic elastic constants and moduli determined at ambient conditions, when available, as they should not be affected by the choice of the EOS. When the ambient conditions moduli were not listed or determined, we relied on the moduli as extracted from the EOS analysis without correcting for the EOS order. For the conversion of adiabatic elastic constants and moduli to isothermal quantities, we assumed the Grüneisen tensor to be isotropic $\gamma_i = \gamma$ ($i = 1, 2, 3$) (Stixrude and Lithgow-Bertelloni, 2005; Stixrude and Lithgow-Bertelloni, 2011) and calculated the isochoric heat capacity C_V using a Debye model as described in Ita and Stixrude (1992) and Stixrude and Lithgow-Bertelloni (2005) with Grüneisen parameters γ and other thermodynamic quantities given in Stixrude and Lithgow-Bertelloni (2011).

For Brillouin spectroscopy studies, we converted individual adiabatic elastic constants c_{ijs} to isothermal constants c_{ijT} by applying the relation $c_{ijT} = c_{ijs} - \gamma_i \gamma_j T C_V / V$ (Wehner and Klein, 1971; Davies, 1974). From the isothermal single-crystal elastic constants, we calculated isothermal linear moduli $k_i^R = 1/(s_{i1} + s_{i2} + s_{i3})$ in the Reuss bound and isothermal bulk moduli in both the Reuss and Voigt bound (eqn. (4.3)). Ultrasonic interferometry and resonant ultrasound spectroscopy have been used to characterize the elasticity of wadsleyite polycrystals to directly determine aggregate bulk and shear moduli (e. g. Gwanmesia et al., 1990; Li et al., 1996; Katsura et al., 2001; Isaak et al., 2007). Since the stress states of individual grains during these measurements are unclear, polycrystal moduli cannot be easily related or converted to Voigt and Reuss bounds. Adiabatic bulk moduli were converted to isothermal bulk moduli using the relation $K_T = K_S - \gamma^2 T C_V / V$ with the same thermoelastic parameters and formulation as for single-crystal elastic constants (Stixrude and Lithgow-Bertelloni, 2005; Stixrude and Lithgow-Bertelloni, 2011). For the bulk modulus and typical wadsleyite compositions, this correction amounts to about 1.3 GPa.

A.1.2 Supplementary Figures

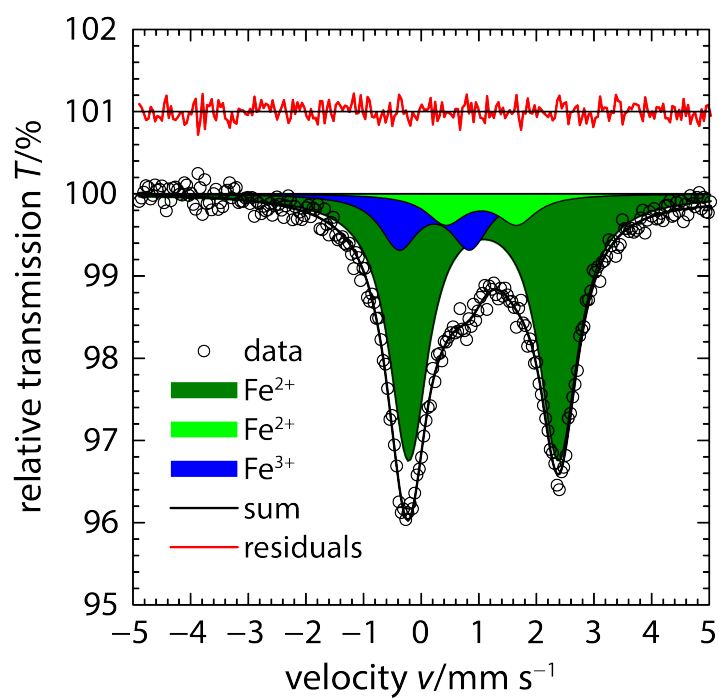


Figure A.1: Mössbauer spectrum of wadsleyite powder. The deconvolution according to model 4 (Appendix Table A.2) includes two doublets for Fe²⁺ and one doublet for Fe³⁺. The extra Fe²⁺ doublet may arise from variations in the next-nearest neighbor environment of Fe²⁺ due to solid solution effects.

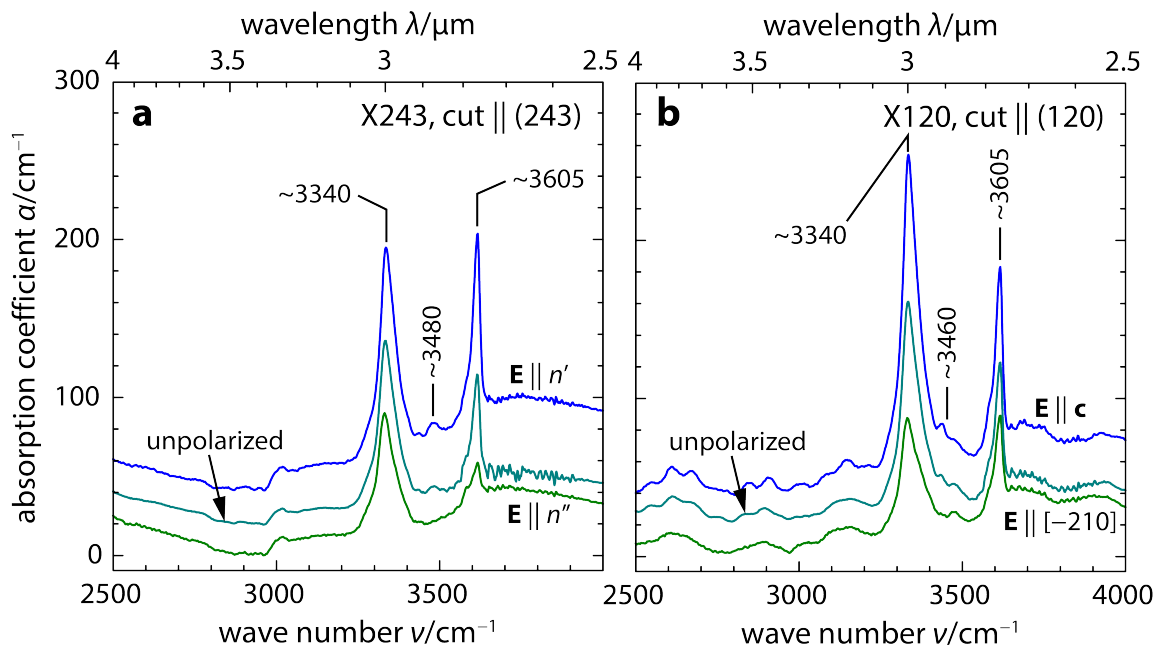


Figure A.2: Polarized and unpolarized FTIR absorption spectra for the crystal sections cut parallel to the **a)** (243) and **b)** (120) plane. The prominent absorption bands around 3340 cm^{-1} and 3600 cm^{-1} arise from structurally bonded hydroxyl groups in wadsleyite. Both bands show pleochroism. Note also the weak absorption feature around 3500 cm^{-1} . (Spectra vertically offset for clarity).

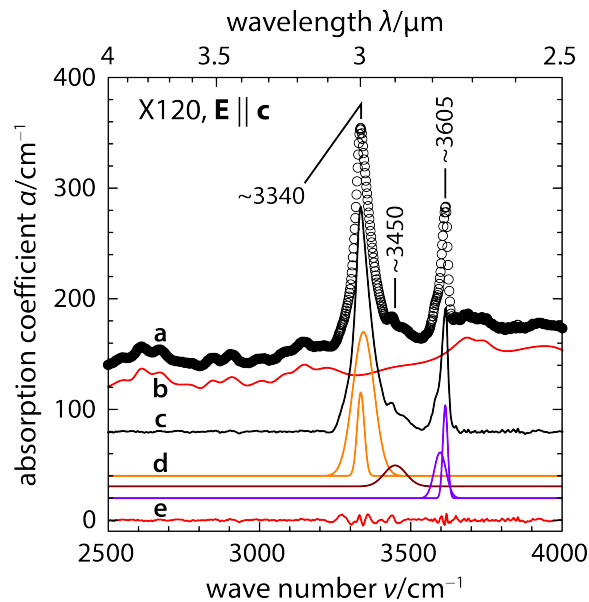


Figure A.3: Background correction and deconvolution for the spectrum with **E || c** recorded on the section cut parallel to (120). **a)** Raw spectrum, **b)** background, **c)** background-corrected spectrum, **d)** individual peaks grouped to bands at 3340 cm^{-1} , 3450 cm^{-1} , and 3605 cm^{-1} , **e)** residual absorption. (Components vertically offset for clarity).

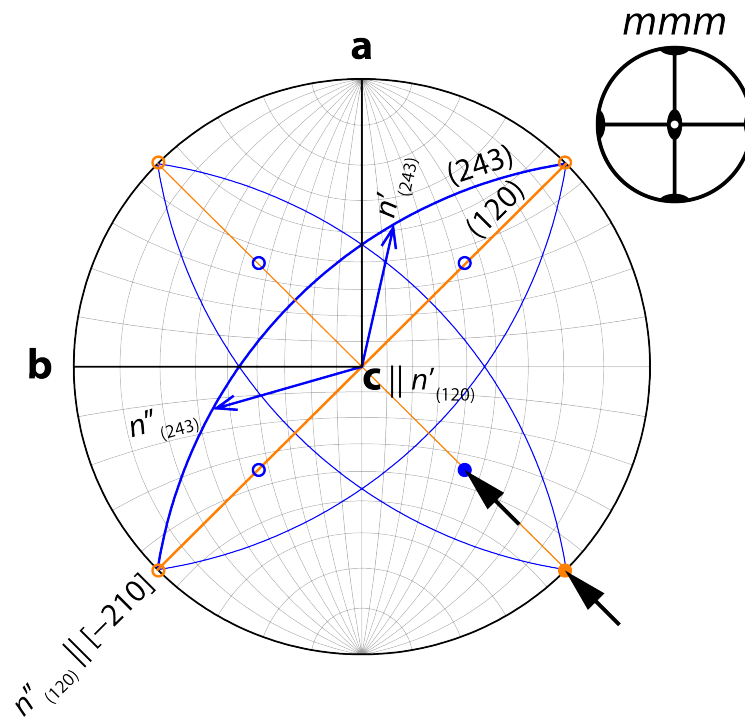


Figure A.4: Stereographic projection (lower hemisphere) illustrating the orientation relationships between the two crystal sections (thick lines; poles: solid circles), their optical vibration directions (n' and n''), and the compression direction of the diamond anvil cell (black arrows). For each section, the symmetry equivalents $\{243\}$ and $\{120\}$ are shown (thin lines; poles: open circles).

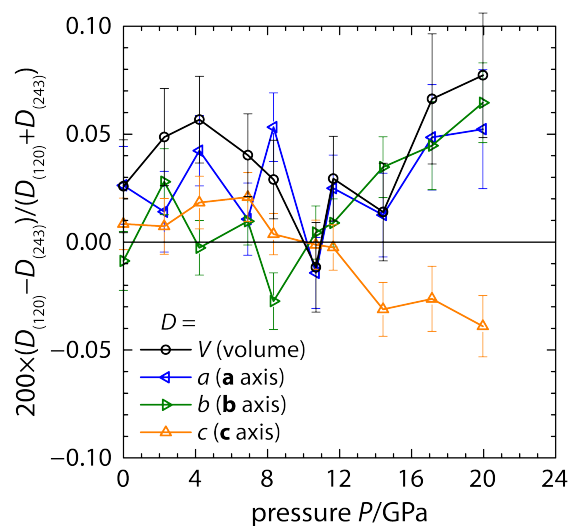


Figure A.5: Relative differences in volume and unit cell edge lengths between the two crystals as a function of pressure. Note the diverging trends for pressures above 12 GPa that might point to the presence of deviatoric stresses.

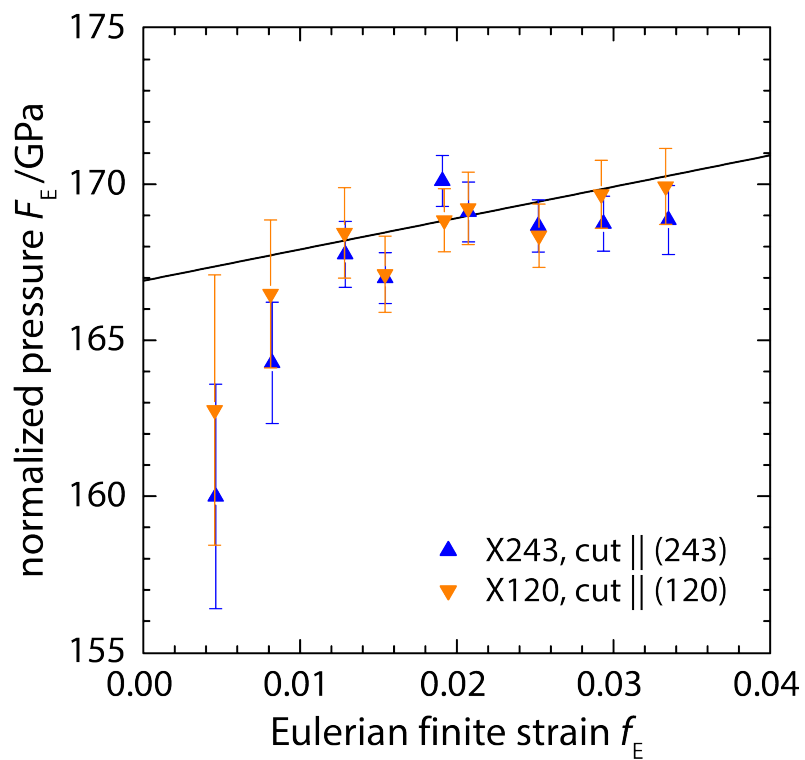


Figure A.6: Normalized pressure as a function of Eulerian finite strain (F - f plot). The black line was drawn according to the combined third-order Birch-Murnaghan EOS (Table 4.2).

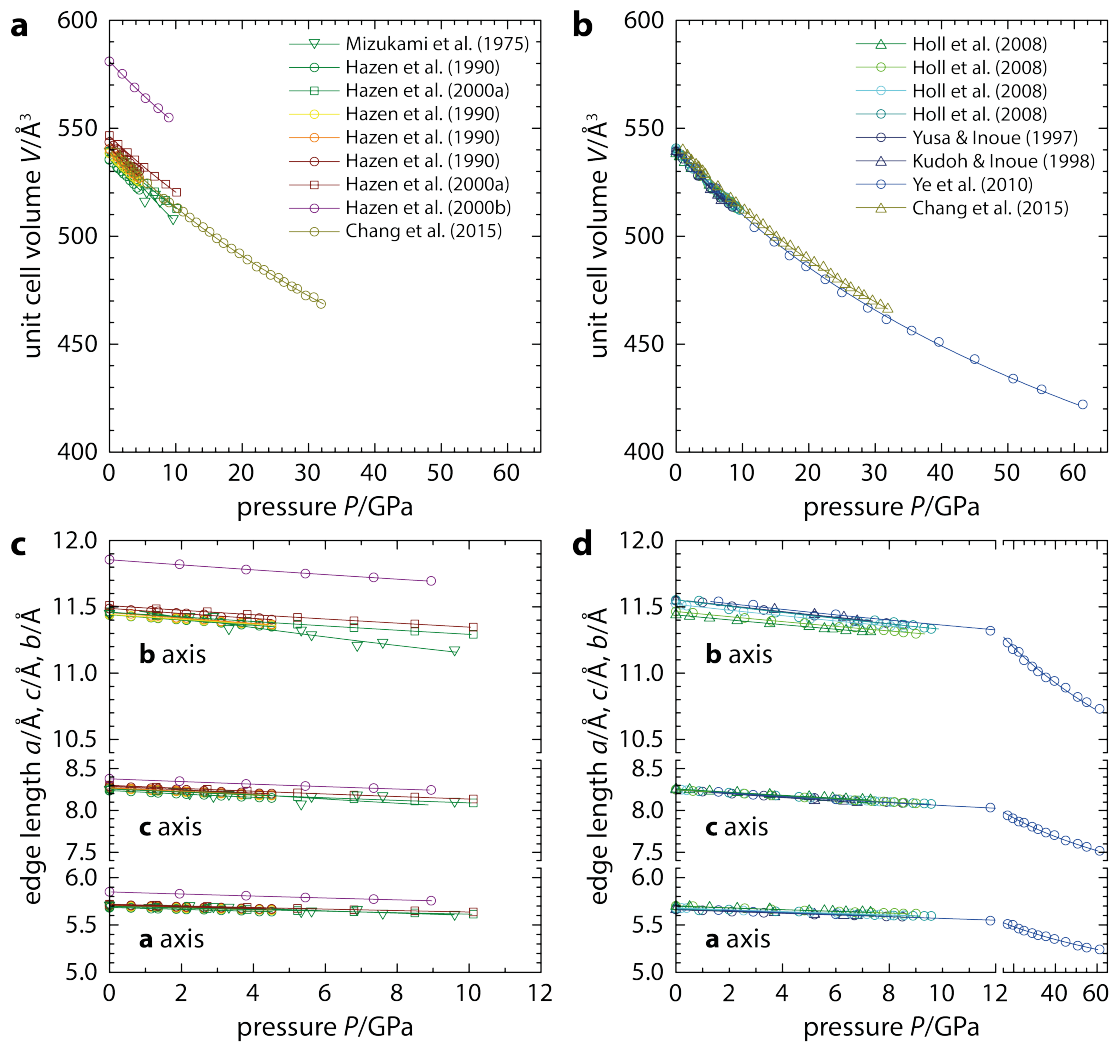


Figure A.7: a,b) Volume and c,d) linear compression curves for a,c) iron-bearing and b,d) hydrous wadsleyites. See Appendix Table A.7 for references and compositions. Lines show second-order Birch-Murnaghan EOS curves.

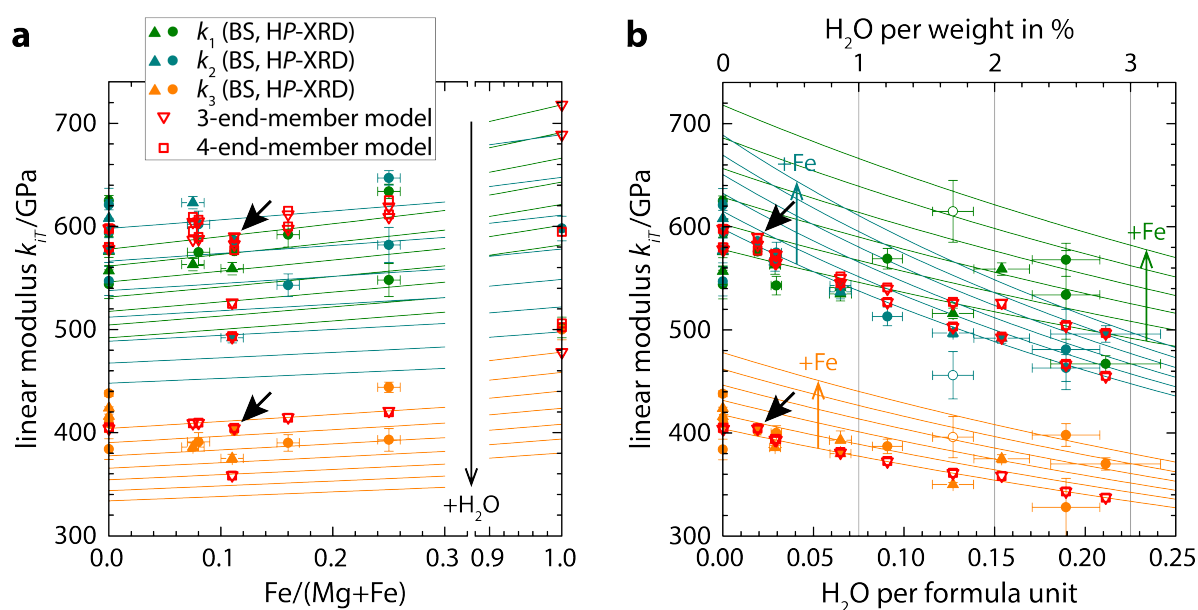


Figure A.8: Isothermal linear moduli for wadsleyite as a function of **a)** Fe/(Mg+Fe) and **b)** H₂O molecular equivalents per formula unit. See Appendix Table A.7 for references. Contours were calculated from the three-end-member model (Table 4.3) and range from 0 wt-% H₂O to 3 wt-% H₂O in steps of 0.5 wt-% H₂O in **a)** and from Fe/(Mg+Fe) = 0 to 1 in steps of 0.2 in **b)**. In **a)**, compositions spread vertically for different hydrogen and ferric iron contents. In **b)**, compositions spread vertically for different iron (ferrous and ferric) contents. Solid arrows indicate the composition of the present study. Data points with open symbols were not included in the multi-end-member analysis. HP-XRD high-pressure X-ray diffraction, BS Brillouin spectroscopy.

A.1.3 Supplementary Tables

Table A.1: Electron microprobe analysis

Oxide	wt-%	Atoms per 4 oxygens	
SiO ₂	41.3(2)	Si	1.020(6)
Al ₂ O ₃	0.03(1)	Al	0.0009(3)
FeO	10.6(2)	Fe	0.219(4)
MnO	0.13(3)	Mn	0.0027(6)
MgO	47.0(3)	Mg	1.73(1)
CaO	0.007(6)	Ca	0.0002(2)
NiO	0.37(4)	Ni	0.0073(8)
Total	99.4(4)	Total	2.98(2)
		Fe/(Mg+Fe)	0.112(2)
		M ^a /Si	1.92(1)

^aM = Al+Fe+Mn+Mg+Ca+Ni.

Table A.2: Hyperfine parameters from room temperature Mössbauer spectrum

$\chi^2 = 1.14$	CS ^a (mm s ⁻¹)	QS ^b (mm s ⁻¹)	FWHM ^c (mm s ⁻¹)	A ^d (%)
Doublet 1: Fe ²⁺	1.08(1)	2.60(3)	0.80(4)	77(3)
Doublet 2: Fe ²⁺	1.04(10)	1.2(2)	0.80(4)	8(2)
Doublet 3: Fe ³⁺	0.23(6)	1.23(13)	0.8(2)	15(3)

^aCenter shift relative to α -Fe.

^bQuadrupole splitting.

^cFull width at half maximum.

^dArea fraction.

Table A.3: Calculated second-order Birch-Murnaghan equation of state parameters for wadsleyite end members (Voigt model)

End member	Volume V_0 (Å ³)	Isothermal bulk and linear moduli				
		K_0 (GPa)	k_{10} (GPa)	k_{20} (GPa)	k_{30} (GPa)	K_0^{Ra} (GPa)
Three-end-member model						
Mg ₂ SiO ₄	538.5(2)	169(2)	577(10)	594(8)	403(7)	169(2)
Fe ₂ SiO ₄	569.6(3)	193(17)	700(74)	682(58)	474(57)	200(13)
MgH ₂ SiO ₄	547.5(19)	49(18)	183(91)	-92(67)	88(65)	-
Four-end-member model						
Mg ₂ SiO ₄	538.5(2)	169(2)	578(10)	593(8)	403(6)	170(2)
Fe ₂ SiO ₄	569.6(3)	200(27)	785(115)	752(88)	457(89)	209(21)
MgH ₂ SiO ₄	547.5(19)	48(18)	182(93)	-87(66)	86(65)	-
Fe ₃ O ₄	598.5(5)	135(72)	-47(263)	282(213)	592(237)	-

^a $K_0^{\text{R}} = 1/(1/k_{10} + 1/k_{20} + 1/k_{30})$; not calculated for $k_{10} < 0$.

Table A.4: Infrared absorption band parameters and hydrogen concentrations

Crystal Spectrum	X120, cut (120)			X243, cut (243)			
	unpolarized	E c	E [-210]	unpolarized	E n'	E n''	
< ν >	(cm ⁻¹)	3343.1(3)	3341.9(2)	3344.1(4)	3338.5(2)	3341.3(2)	3336.2(2)
A _{NT}	(cm ⁻²)	10162(70)	13694(89)	6199(53)	6938(86)	9155(109)	5504(52)
H ₂ O ^a	(mol L ⁻¹)	0.30(6)	0.14(3)	0.06(1)	0.20(4)	0.09(2)	0.05(1)
H ₂ O ^b	(mol L ⁻¹)	0.25(13)	0.11(4)	0.05(4)	0.16(24)	0.07(4)	0.04(4)
H ₂ O ^c	(mol L ⁻¹)	0.42(4)	0.19(2)	0.08(1)	0.29(3)	0.13(1)	0.08(1)
				3455-3515 cm⁻¹			
< ν >	(cm ⁻¹)	3458(1)	3449(1)	3470(1)	3484(2)	3481(1)	-
A _{NT}	(cm ⁻²)	1266(46)	1725(63)	714(28)	211(20)	731(27)	-
H ₂ O ^a	(mol L ⁻¹)	0.05(1)	0.023(5)	0.010(2)	0.010(2)	0.011(2)	-
H ₂ O ^b	(mol L ⁻¹)	0.02(4)	0.007(8)	0.01(1)	0.01(9)	0.01(1)	-
H ₂ O ^c	(mol L ⁻¹)	0.05(1)	0.024(2)	0.010(1)	0.009(1)	0.010(1)	-
				3515-3700 cm⁻¹			
< ν >	(cm ⁻¹)	3604.7(6)	3605.0(4)	3605.0(5)	3604.5(5)	3605.4(3)	3601(1)
A _{NT}	(cm ⁻²)	2569(83)	3722(78)	1968(53)	2425(60)	3873(62)	948(45)
H ₂ O ^a	(mol L ⁻¹)	0.21(4)	0.10(2)	0.05(1)	0.20(4)	0.11(2)	0.025(5)
H ₂ O ^b	(mol L ⁻¹)	0.15(22)	0.07(5)	0.04(8)	0.14(52)	0.08(6)	0.02(8)
H ₂ O ^c	(mol L ⁻¹)	0.11(1)	0.051(5)	0.027(3)	0.10(1)	0.053(5)	0.013(1)
				Total			
A [-210]	(cm ⁻²)		8882(80)			9848(70)	
A c	(cm ⁻²)		19141(134)			10364(76)	
A _{TOT}	(cm ⁻²)		36905(208)			30060(159)	
H ₂ O ^a	(wt-%)	0.28(4)	0.26(2)		0.21(3)	0.22(2)	
H ₂ O ^b	(wt-%)	0.21(13)	0.19(10)		0.15(29)	0.16(8)	
H ₂ O ^c	(wt-%)	0.29(3)	0.25(2)		0.20(2)	0.21(1)	

^aCalibration of Libowitzky and Rossmann (1997).

^bCalibration of Paterson (1982).

^cCalibration of Deon et al. (2010).

Table A.6: Unit cell parameters for wadsleyites of different compositions

Fe/(Mg+Fe)	H ₂ O (p.f.u.)	Fe ³⁺ /ΣFe	Unit cell edge lengths	Volume	Angle ^a	Sample ^e	Methods ^c	Reference
x	y	z	a(Å)	V(Å ³)	β(°)			
0		0	5.702(2)	538.2(4)		P	XRD	Suzuki et al. (1980)
0		0	5.6983(4)	538.14(7)		SX	XRD	Horuchi and Sawamoto (1981)
0		0	5.696(1)	538.59(12)		SX	XRD EMPA	Sawamoto (1986)
0		0	5.6921(2)	538.3(2)		SX	XRD EMPA	Finger et al. (1993)
0	0	0	5.703(5)	538.1(9)		P	XRD	Inoue et al. (2004)
0	0	0	5.7007(5)	538.81(7)		SX	XRD	Ye et al. (2009)
0	0	0	5.70158(8)	538.188(13)		P	XRD	Trois et al. (2012)
0.075(10)			5.705(2)	539.4(4)		SX	XRD EMPA	Sinogeikin et al. (1998)
0.08(1)		0.08(2) ^d	5.7037(9)	540.1(1)		SX	XRD EMPA MS ^d	Finger et al. (1993)
0.10(1)			5.7107(5)	542.09(9)		SX	XRD EMPA	Sawamoto (1986)
0.16(1)		0.08(2) ^d	5.7119(9)	542.4(1)		SX	XRD EMPA MS ^d	Finger et al. (1993)
0.25(1)		0.08(2) ^d	5.717(1)	545.9(2)		SX	XRD EMPA MS ^d	Finger et al. (1993)
0.30(1)			5.7216(2)	544.61(7)		SX	XRD EMPA	Sawamoto (1986)*
0.395(9)		0	5.739(2)	549.6(2)		SX	XRD EMPA MS	Finger et al. (1993)
1		0.37(1)	5.8559(2)	582.84(2)		P	XRD EMPA	Woodland and Angel (1998)
0	0.0004(1)	0	5.7002(2)	538.46(2)	90.004(2)	SX	XRD FTIR	Jacobsen et al. (2005)
0	0.0004(1)	0	5.7008(5)	538.61(7)	90.000(9)	SX	XRD	Holl et al. (2008)
0	0.0012(1)	0	5.6998(2)	538.34(3)	90.003(2)	SX	XRD FTIR	Jacobsen et al. (2005)
0	0.0249(24)	0	5.6941(2)	538.70(3)	90.002(3)	SX	XRD FTIR	Holl et al. (2005)
0	0.0295(29)	0	5.6951(3)	538.99(6)	90.001(9)	SX	XRD	Holl et al. (2008)
0	0.0465(44)	0	5.6881(3)	539.08(3)	90.055(3)	SX	XRD FTIR	Jacobsen et al. (2005)
0	0.0619(73)	0	5.693(6)	540.65(5)		SX	XRD SIMS	Deon et al. (2010)
0	0.0649(58)	0	5.6888(6)	539.08(8)		SX	XRD	Maio et al. (2008b)
0	0.0741(69)	0	5.6990(4)	539.13(4)	90.085(4)	SX	XRD FTIR	Jacobsen et al. (2005)
0	0.0817(75)	0	5.6900(2)	538.98(3)	90.125(3)	SX	XRD FTIR	Jacobsen et al. (2005)
0	0.0908(83)	0	5.6862(4)	539.75(6)	90.013(9)	SX	XRD	Holl et al. (2008)
0	0.1050(20)	0	5.6865(4)	540.52(5)	89.985(13)	P SX	XRD ND	Purevjav et al. (2016)
0	0.1113(123)	0	5.683(2)	539.7(2)		SX	XRD EMPA	Sano-Furukawa et al. (2011)
0	0.1225(68)	0	5.690(1)	541.80(8)		SX	XRD SIMS	Deon et al. (2010)
0	0.1263(111)	0	5.679(2)	541.1(4)		P	XRD EMPA NMR	Klepepe et al. (2001)
0	0.1270(112)	0	5.6807(3)	540.20(5)	90.090(7)	SX	XRD	Holl et al. (2008)
0	0.1400(100)	0	5.674(1)	536.2(1)	90.21(1)	SX	XRD EMPA SIMS	Kudoh and Inoue (1999)*
0	0.1598(136)	0	5.6803(7)	540.05(9)		SX	XRD	Ye et al. (2009)
0	0.1820(126)	0	5.679(1)	539.9(7)		P	XRD SIMS	Inoue et al. (2004)
0	0.1894(187) ^e	0	5.663(1)	539.2(5)		SX	XRD EMPA SIMS ^e	Kudoh et al. (1996)
0	0.1894(187)	0	5.675(3)	541.3(4)	90.09(4)	SX	XRD EMPA SIMS	Kudoh and Inoue (1999)
0	0.2113(303)	0	5.662(1)	540.3(2)		SX	XRD	Ye et al. (2010)
0	0.2186(174)	0	5.6646(4)	540.52(5)	90.051	P	XRD	Griffin et al. (2013)
0	0.2404(187)	0	5.6654(1)	541.79(11)	90.176	P	XRD	Griffin et al. (2013)

Table A.6: (continued)

Fe/(Mg+Fe) x	H ₂ O (pfu) y	Fe ^{3+/ΣFe} z	Unit cell edge lengths a (Å) b (Å) c (Å)			Volume V (Å ³)	Angle ^a β (°)	Sample ^b	Methods ^c	Reference
0.054(2)	0.1754(141)	0.96(5) ^f	5.6715(7)	11.5820(16)	8.2576(11)	542.43(12)	90.397(9)	SX	XRD SIMS MS ^g	Smyth et al. (1997)
0.074(1)	0.0610(72)	0.150(2)	5.6972(2)	11.4903(3)	8.2655(2)	541.1(3)		SX	XRD EMPA SIMS MS	Smyth et al. (2014)
0.10(1)	0.0203(20)		5.7045(4)	11.4765(4)	8.2707(4)	541.46(5)		SX	XRD FTIR	Chang et al. (2015)
0.11(1)	0.1539(153)	0.11(6)	5.6918(10)	11.5276(10)	8.2641(8)	542.23(12)		SX	XRD SIMS MS	Mao et al. (2011)
0.11(1)	0.1593(139)	0.11(6)	5.6929(2)	11.5275(2)	8.2648(1)	542.37(2)		SX	XRD SIMS MS	Chang et al. (2015)
0.112(2)	0.0192(18)	0.15(3)	5.7069(7)	11.4736(6)	8.2740(8)	541.77(9)	90.048(6)	SX	XRD EMPA FTIR MS	This study
0.150(2)	0.0778(33)	0.150(2)	5.7059(3)	11.5315(6)	8.2901(5)	545.47(5)		SX	XRD EMPA SIMS MS	Smyth et al. (2014)
0.222(4)	0.1176(149)	0.19(2)	5.711(2)	11.586(2)	8.293(2)	548.71(15)	90.138(9)	SX	XRD FTIR MS	Mrosko et al. (2015)
0.226(3)	0.0599(26)	0.247(2)	5.7194(3)	11.5434(6)	8.3030(5)	548.18(5)		SX	XRD EMPA SIMS MS	Smyth et al. (2014)
0.262(5)	0.0482(27)	0.275(5)	5.7237(1)	11.5302(4)	8.3034(2)	547.99(3)		SX	XRD EMPA SIMS MS	Smyth et al. (2014)
0.300(3)	0.0653(36)	0.303(3)	5.7243(2)	11.5804(4)	8.3108(3)	550.92(3)		SX	XRD EMPA SIMS MS	Smyth et al. (2014)
0.301(4)	0.0281(54)	0.310(3)	5.7238(3)	11.5844(7)	8.3124(5)	551.17(6)		SX	XRD EMPA SIMS MS	Smyth et al. (2014)
0.327(4)	0.0404(9)	0.300(3)	5.7276(2)	11.5680(5)	8.3072(3)	550.41(4)		SX	XRD EMPA SIMS MS	Smyth et al. (2014)

No entry implies that the respective information was not available.

^aFor monoclinic unit cell.

^bSX single crystal, P powder.

^cXRD X-ray diffraction, EMPA electron microprobe analysis, MS Mössbauer spectroscopy, FTIR Fourier-transform infrared absorption spectroscopy, SIMS secondary ion mass spectrometry, ND neutron diffraction, NMR nuclear magnetic resonance.

^dFe^{3+/ΣFe} adopted from Fei et al. (1992).

^eHydrogen concentration adopted from Inoue et al. (1995).

^fFe^{3+/ΣFe} adopted from McCammon et al. (2004).

*Not included in multi-end-member analysis.

Table A.7: Reanalyzed second-order Birch-Murnaghan equation of state parameters for wadsleyites of different compositions

Fe/(Mg+Fe)	H ₂ O (pfu)		Fe ³⁺ /ΣFe	Unit cell edge lengths			Volume V (Å ³)	Isothermal bulk modulus		
	x	y		z	a (Å)	b (Å)		c (Å)	K ₀ (GPa)	K ₀ ^R (GPa)
0			0	5.73(2)	11.50(5)	8.31(5)	541.5(23)	131.1(155)	95.4(177)	99.4(164)
0			0	5.696(1)	11.453(1)	8.256(1)	538.59(12)		174.3(49)	176.0(33)
0			0	5.6850(7)	11.4406(13)	8.2377(13)	535.75(13)	160.3(26)	159.5(24)	163.9(25)
0			0					168.7(20)		
0	0		0				535.8(2)		168.6(23)	170.1(22)
0			0					164.7(20)		
0			0					170.7(20)		
0			0	5.6972(4)	11.4605(7)	8.2558(7)	539.03(12)	182.4(14)	182.0(8)	187.1(9)
0			0				537.6(1)	171.4(20)		
0			0					168.9(19)		
0.075(10)				5.705(2)	11.450(4)	8.258(3)	539.4(4)		167.4(13)	170.2(13)
0.075(10)				5.705(2)	11.450(4)	8.258(3)	539.4(4)		167.4(13)	170.2(13)
0.08(1)			0.08(2) ^d	5.6984(5)	11.4431(10)	8.2611(11)	538.67(11)	168.8(25)	167.8(22)	174.2(23)
0.08(1)								169.5(12)		
0.091(3)								164.4(1)		
0.091(3)								164.4(1)		
0.12(1)								170.7(20)		
0.13(1)							542.0(3)	170.0(7)		
0.16(1)			0.08(2) ^d	5.7062(5)	11.4566(10)	8.2705(10)	540.65(12)	164.4(24)	164.1(20)	169.4(20)
0.25(1)			0.08(2) ^d	5.7122(7)	11.4887(14)	8.2870(15)	543.81(13)	165.3(27)	164.3(28)	169.2(29)
0.25(1)			0.08(2) ^d	5.7188(5)	11.5093(10)	8.3002(10)	546.30(16)	186.6(20)	186.0(12)	191.7(12)
1			0.28(2)	5.8496(11)	11.8554(19)	8.3774(16)	580.97(30)	176.7(32)	176.5(20)	177.8(21)
0	0.0004(1)		0	5.6982(8)	11.4394(16)	8.2573(16)	538.22(11)	173.0(16)	172.1(22)	177.6(23)
0	0.0288(30)		0	5.6941(2)	11.4597(3)	8.2556(2)	538.70(3)		163.0(15)	165.2(13)
0	0.0295(29)		0	5.7019(9)	11.4650(17)	8.2478(17)	539.15(12)	164.9(12)	164.5(17)	168.7(17)
0	0.0649(61)		0	5.6888(6)	11.4830(8)	8.2523(6)	539.08(8)		159.3(19)	160.7(7)
0	0.0649(58)		0	5.6888(6)	11.4830(8)	8.2523(6)	539.08(8)		158.2(10)	160.0(9)
0	0.0908(83)		0	5.6803(9)	11.5190(19)	8.2496(18)	539.77(9)	159.5(9)	159.0(17)	163.2(17)
0	0.1270(112)		0	5.6722(26)	11.5535(71)	8.2494(58)	540.33(15)	160.8(12)	157.6(46)	163.0(48)
0	0.1270(114)		0	5.6807(3)	11.5243(6)	8.2515(6)	540.20(5)		147.0(9)	148.8(9)
0	0.1894(187)		0	5.6614(13)	11.5526(33)	8.2437(27)	539.01(23)	157.1(23)	155.4(25)	158.8(26)
0	0.1894(187)		0	5.6653(38)	11.5557(86)	8.2473(90)	539.79(88)	145.0(77)	142.8(70)	149.2(72)
0	0.2113(303)		0	5.6766(27)	11.5699(52)	8.2503(49)	541.74(40)	146.7(12)	145.8(14)	148.1(14)
0.10(1)	0.0203(20)		0				541.97(22)	165.7(8)		
0.11(1)	0.1539(153)	0.11(6)		5.6918(10)	11.5276(10)	8.2641(8)	542.23(12)		154.1(12)	155.8(8)
0.11(1)	0.1593(139)	0.11(6)					543.46(19)	153.2(6)		
0.112(2)	0.0192(18)	0.15(3)		5.7077(3)	11.4759(6)	8.2754(7)	542.03(7)	169.3(5)	168.6(5)	173.8(5)

No entry implies that the respective information was not available. See supplemental online material¹ for further information on data treatment.

^aSX single crystal, PX polycrystal, P powder.

^bHP-XRD high-pressure X-ray diffraction, BS Brillouin spectroscopy, UI ultrasonic interferometry, RUS resonant ultrasound spectroscopy.

^cMA multi-anvil press, PC piston-cylinder press, DAC diamond anvil cell with pressure medium: ME methanol-ethanol,

MEW methanol-ethanol-water, Ar argon, He helium, Ne neon.

^dFe³⁺/ΣFe adopted from Fei et al. (1992).

*Included in multi-end-member analysis.

Table A.7: (continued)

Isothermal linear moduli			Sample ^a	Methods ^b	Environment ^c	Pressure P_{MAX} (GPa)	Reference
k_{10} (GPa)	k_{20} (GPa)	k_{30} (GPa)					
388(94)	264(66)	243(93)	P	HP-XRD	MA	9.6	Mizukami et al. (1975)
576(14)	608(29)	424(12)	SX	BS		0	Sawamoto et al. (1984)*
544(14)	547(14)	384(10)	SX	HP-XRD	DAC	4.5	Hazen et al. (1990)*
			PX	UI	MA	12.5	Li et al. (1996)
557(13)	577(12)	416(9)	SX	BS	DAC (Ar/ME/He)	14.2	Zha et al. (1997)*
			PX	UI	PC MA	14.5	Fujisawa (1998)
			PX	UI HP-XRD	MA	7.0	Li et al. (1998)
625(5)	621(5)	438(3)	SX	HP-XRD	DAC (ME)	10.1	Hazen et al. (2000a)*
			PX	UI HP-XRD	MA	7.1	Li et al. (2001)
			PX	RUS		0	Isaak et al. (2007)
563(6)	623(6)	386(4)	SX	BS		0	Sinogeikin et al. (1998)*
563(6)	623(6)	386(4)	SX	BS	DAC (MEW)	17.7	Wang et al. (2014)
575(13)	602(13)	391(9)	SX	HP-XRD	DAC	4.5	Hazen et al. (1990)*
			PX	RUS		0	Isaak et al. (2010)
			PX	RUS		0	Katsura et al. (2001)
			PX	RUS		0	Mayama et al. (2004)
			PX	UI	MA	9.6	Li and Liebermann (2000)
			PX	UI HP-XRD	MA	12.4	Liu et al. (2009)
592(12)	543(11)	390(8)	SX	HP-XRD	DAC	4.5	Hazen et al. (1990)*
548(16)	582(17)	393(11)	SX	HP-XRD	DAC	4.5	Hazen et al. (1990)*
634(7)	647(7)	444(5)	SX	HP-XRD	DAC (ME)	10.1	Hazen et al. (2000a)*
502(10)	598(12)	500(10)	SX	HP-XRD	DAC (ME)	9.0	Hazen et al. (2000b)*
594(13)	595(13)	409(9)	SX	HP-XRD	DAC (MEW)	7.3	Holl et al. (2008)*
563(9)	566(9)	386(2)	SX	BS		0	Mao et al. (2008b)*
543(9)	575(10)	400(7)	SX	HP-XRD	DAC (MEW)	9.0	Holl et al. (2008)*
535(7)	537(7)	393(9)	SX	BS	DAC (MEW)	12.0	Mao et al. (2008a)*
541(5)	543(5)	380(3)	SX	BS		0	Mao et al. (2008b)*
569(10)	513(9)	387(7)	SX	HP-XRD	DAC (MEW)	8.6	Holl et al. (2008)*
615(30)	456(23)	396(20)	SX	HP-XRD	DAC (MEW)	9.6	Holl et al. (2008)
516(5)	497(4)	350(2)	SX	BS		0	Mao et al. (2008b)*
568(16)	463(13)	398(11)	P	HP-XRD	DAC (MEW)	8.5	Yusa and Inoue (1997)*
534(43)	481(39)	328(28)	SX	HP-XRD	DAC (ME)	6.8	Kudoh and Inoue (1998)*
467(8)	496(8)	370(6)	SX	HP-XRD	DAC (Ne)	61.3	Ye et al. (2010)*
			SX	HP-XRD	DAC (Ne)	31.9	Chang et al. (2015)
559(6)	492(5)	375(4)	SX	BS	DAC (MEW)	12.2	Mao et al. (2011)*
			SX	HP-XRD	DAC (Ne)	31.9	Chang et al. (2015)
576(3)	586(3)	402(2)	SX	HP-XRD	DAC (Ne)	20.0	This study*

A.2 High-Pressure Single-Crystal Elasticity of Wadsleyite and the Seismic Signature of Water in the Shallow Transition Zone

A.2.1 Supplementary Figures and Tables

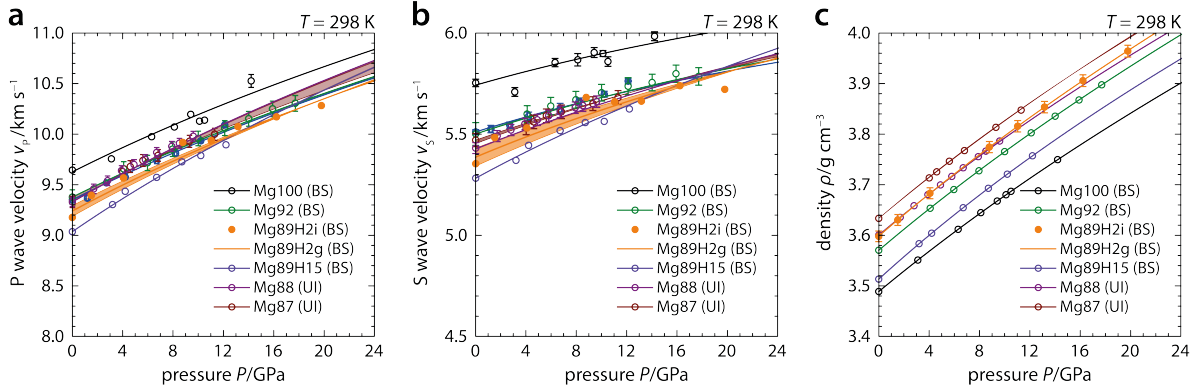


Figure A.9: Sound wave velocities and densities of wadsleyites with different iron contents. **a)** P wave velocities, **b)** S wave velocities, and **c)** densities of wadsleyite as a function of pressure. Orange shading in **a)** and **b)** indicates the Voigt and Reuss bounds on the results of the present study. Dark red shading in **a)** and **b)** indicates two alternative sets of finite-strain curves as given by Liu et al. (2009). Mg100: Mg_2SiO_4 (Zha et al., 1997), Mg92: $(\text{Mg}_{0.92}\text{Fe}_{0.08})_2\text{SiO}_4$ (Wang et al., 2014), Mg89H2i: $(\text{Mg}_{0.89}\text{Fe}_{0.11})_{1.98}\text{H}_{0.04}\text{SiO}_4$ (0.24 wt-% H_2O) this study (individual inversions), Mg89H2g: $(\text{Mg}_{0.89}\text{Fe}_{0.11})_{1.98}\text{H}_{0.04}\text{SiO}_4$ (0.24 wt-% H_2O) this study (global inversion), Mg89H15: $(\text{Mg}_{0.89}\text{Fe}_{0.11})_{1.85}\text{H}_{0.30}\text{SiO}_4$ (1.92 wt-% H_2O) (Mao et al., 2011), Mg88: $(\text{Mg}_{0.88}\text{Fe}_{0.12})_2\text{SiO}_4$ (Li and Liebermann, 2000), Mg87: $(\text{Mg}_{0.87}\text{Fe}_{0.13})_2\text{SiO}_4$ (Liu et al., 2009), BS: Brillouin spectroscopy, UI: ultrasonic interferometry.

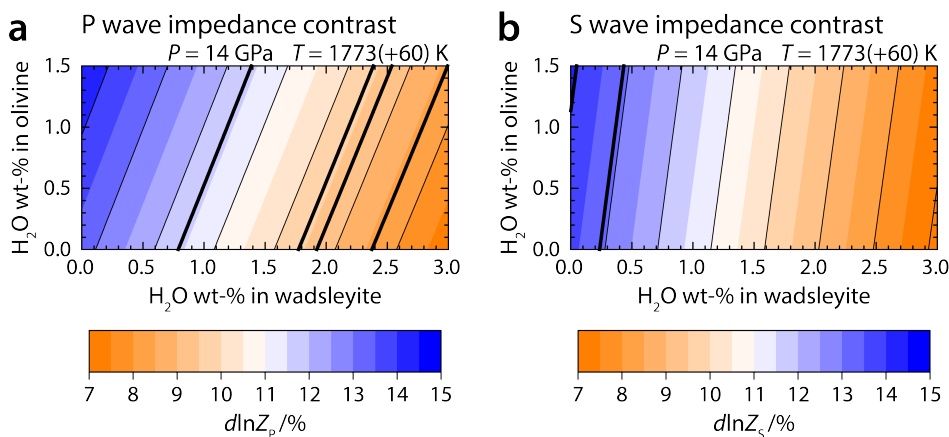


Figure A.10: Impedance contrasts across the olivine-wadsleyite phase transition. **a)** P wave impedance contrast and **b)** S wave impedance contrast as a function of olivine and wadsleyite H_2O contents at 14 GPa and 1773 K. Wadsleyite was assumed to be 60 K hotter than olivine due to the latent heat of transformation. Thick black lines show seismically observed impedance contrasts (Chambers et al., 2005) scaled for 55 vol-% of olivine/wadsleyite.

Table A.8: Unit cell volumes, densities, single-crystal elastic constants, and aggregate elastic properties of iron-bearing wadsleyite

Pressure ^a	Unit cell volume	Density	Adiabatic single-crystal elastic constants											RMSC ^b				Aggregate elastic properties (Voigt-Reuss-Hill averages)	
			V (Å ³)	ρ (g cm ⁻³)	c_{11} (GPa)	c_{22} (GPa)	c_{33} (GPa)	c_{44} (GPa)	c_{55} (GPa)	c_{66} (GPa)	c_{12} (GPa)	c_{13} (GPa)	c_{23} (GPa)	K_S (GPa)	G (GPa)	v_p (km s ⁻¹)	v_s (km s ⁻¹)		
Individual inversions																			
0.00(2)	542.12(4)	3.598(11)	345(2)	354(2)	252.3(8)	104.9(8)	107.0(9)	86(1)	73(1)	107(2)	94(2)	0.48	165.5(9)	103.1(4)	9.177(21)	5.353(13)			
1.51(2)	537.29(5)	3.630(11)	366(3)	369(3)	270.3(14)	106.9(14)	116.5(23)	92(2)	78(2)	101(4)	110(3)	0.45	175.0(19)	109.1(8)	9.396(35)	5.482(21)			
4.06(3)	529.60(5)	3.683(11)	389(3)	373(3)	290.1(17)	110.3(7)	114.8(10)	99(2)	92(2)	117(2)	110(2)	0.44	186.9(11)	112.6(5)	9.567(23)	5.530(16)			
8.76(7)	516.79(10)	3.774(11)	408(5)	418(5)	330.9(26)	113.4(12)	123.0(11)	113(2)	105(3)	129(3)	130(3)	0.44	208.9(16)	121.8(8)	9.919(29)	5.681(19)			
11.00(9)	511.19(7)	3.815(11)	423(4)	412(3)	334.8(13)	115.5(7)	120.5(9)	116(2)	113(2)	137(2)	131(2)	0.44	213.8(10)	122.2(5)	9.936(22)	5.659(14)			
13.12(11)	506.18(9)	3.853(11)	432(3)	431(3)	357.0(18)	113.5(10)	122.0(10)	117(1)	125(2)	147(2)	140(2)	0.42	226.3(11)	123.5(5)	10.074(23)	5.662(15)			
16.14(16)	499.41(21)	3.905(12)	431(3)	451(4)	368.7(17)	119.1(7)	124.3(11)	127(2)	131(2)	142(3)	150(2)	0.40	232.5(13)	128.6(5)	10.171(24)	5.739(14)			
19.68(17)	492.04(10)	3.964(12)	452(5)	445(4)	390.9(16)	115.6(10)	132.5(17)	130(3)	139(3)	167(2)	159(3)	0.45	246.2(14)	129.7(8)	10.283(27)	5.721(20)			
Third-order finite-strain parameters based on individual inversions																			
V_0 (Å ³)	542.12(4)	M_0 (GPa)	354(4)	355(3)	255(2)	106(1)	109(2)	88(2)	74(2)	105(3)	97(3)		167.6(15)	104.7(7)					
ρ_0 (g cm ⁻³)	3.598(11)	M'_0	5.8(4)	5.7(3)	7.3(2)	0.9(1)	1.2(1)	2.4(2)	3.5(2)	2.9(3)	3.2(3)		4.27(21)	1.59(9)					
Third-order finite-strain parameters from global inversion																			
V_0 (Å ³)	542.12(4)	M_0 (GPa)	356(2)	357(2)	256(1)	107(1)	108(1)	85(1)	77(2)	107(2)	94(2)	0.46	168.0(10)	104.3(5)					
ρ_0 (g cm ⁻³)	3.598(11)	M'_0	5.5(2)	5.2(2)	7.3(1)	0.9(1)	1.3(1)	2.7(1)	3.1(1)	2.7(2)	3.5(1)		4.13(8)	1.64(4)					

^aMolar mass $M = 146.81(43)$ g mol⁻¹.

^bCalculated from Reuss isothermal EOS.

^cRoot of the mean squared correlation coefficient between elastic constants.

Supplementary References

- Bolfan-Casanova, N., M. Muñoz, C. McCammon, E. Deloule, A. Férot, S. Demouchy, L. France, D. Andrault, and S. Pascarelli (2012). Ferric iron and water incorporation in wadsleyite under hydrous and oxidizing conditions: A XANES, Mössbauer, and SIMS study. *Am. Mineral.* **97**, 1483–1493.
- Chambers, K., A. Deuss, and J. H. Woodhouse (2005). Reflectivity of the 410-km discontinuity from PP and SS precursors. *J. Geophys. Res.: Solid Earth* **110**, B02301.
- Chang, Y.-Y., S. D. Jacobsen, C. R. Bina, S.-M. Thomas, J. R. Smyth, D. J. Frost, T. Boffa Ballaran, C. A. McCammon, E. H. Hauri, T. Inoue, et al. (2015). Comparative compressibility of hydrous wadsleyite and ringwoodite: Effect of H₂O and implications for detecting water in the transition zone. *J. Geophys. Res.: Solid Earth* **120**, 8259–8280.
- Davies, G. F. (1974). Effective elastic moduli under hydrostatic stress—I. Quasi-harmonic theory. *J. Phys. Chem. Solids* **35**, 1513–1520.
- Deon, F., M. Koch-Müller, D. Rhede, M. Gottschalk, R. Wirth, and S.-M. Thomas (2010). Location and quantification of hydroxyl in wadsleyite: New insights. *Am. Mineral.* **95**, 312–322.
- Fei, Y., H.-k. Mao, J. Shu, G. Parthasarathy, W. A. Bassett, and J. Ko (1992). Simultaneous high-*P*, high-*T* X ray diffraction study of β -(Mg,Fe)₂SiO₄ to 26 GPa and 900 K. *J. Geophys. Res.: Solid Earth* **97**, 4489–4495.
- Finger, L. W., R. M. Hazen, J. Zhang, J. Ko, and A. Navrotsky (1993). The effect of Fe on the crystal structure of wadsleyite β -(Mg_{1-x}Fe_x)₂SiO₄, 0.00 ≤ *x* ≤ 0.40. *Phys. Chem. Miner.* **19**, 361–368.
- Fujisawa, H. (1998). Elastic wave velocities of forsterite and its β -spinel form and chemical boundary hypothesis for the 410-km discontinuity. *J. Geophys. Res.: Solid Earth* **103**, 9591–9608.
- Griffin, J. M., A. J. Berry, D. J. Frost, S. Wimperis, and S. E. Ashbrook (2013). Water in the Earth's mantle: a solid-state NMR study of hydrous wadsleyite. *Chem. Sci.* **4**, 1523–1538.
- Gwanmesia, G. D., R. C. Liebermann, and F. Guyot (1990). Hot-pressing and characterization of polycrystals of β -Mg₂SiO₄ for acoustic velocity measurements. *Geophys. Res. Lett.* **17**, 1331–1334.
- Hazen, R. M., J. Zhang, and J. Ko (1990). Effects of Fe/Mg on the compressibility of synthetic wadsleyite: β -(Mg_{1-x}Fe_x)₂SiO₄ (*x* ≤ 0.25). *Phys. Chem. Miner.* **17**, 416–419.
- Hazen, R. M., M. B. Weinberger, H. Yang, and C. T. Prewitt (2000a). Comparative high-pressure crystal chemistry of wadsleyite, β -(Mg_{1-x}Fe_x)₂SiO₄, with *x* = 0 and 0.25. *Am. Mineral.* **85**, 770–777.
- Hazen, R. M., H. Yang, and C. T. Prewitt (2000b). High-pressure crystal chemistry of Fe³⁺-wadsleyite, β -Fe_{2.33}Si_{0.67}O₄. *Am. Mineral.* **85**, 778–783.
- Holl, C. M., J. R. Smyth, S. D. Jacobsen, and D. J. Frost (2008). Effects of hydration on the structure and compressibility of wadsleyite, β -(Mg₂SiO₄). *Am. Mineral.* **93**, 598–607.
- Horiuchi, H. and H. Sawamoto (1981). β -Mg₂SiO₄: Single-crystal X-ray diffraction study. *Am. Mineral.* **66**, 568–575.
- Inoue, T., H. Yurimoto, and Y. Kudoh (1995). Hydrous modified spinel, Mg_{1.75}SiH_{0.5}O₄: A new water reservoir in the mantle transition region. *Geophys. Res. Lett.* **22**, 117–120.
- Inoue, T., Y. Tanimoto, T. Irifune, T. Suzuki, H. Fukui, and O. Ohtaka (2004). Thermal expansion of wadsleyite, ringwoodite, hydrous wadsleyite and hydrous ringwoodite. *Phys. Earth Planet. Inter.* **143–144**, 279–290.

- Isaak, D. G., G. D. Gwanmesia, D. Falde, M. G. Davis, R. S. Triplett, and L. Wang (2007). The elastic properties of β - Mg_2SiO_4 from 295 to 660 K and implications on the composition of Earth's upper mantle. *Phys. Earth Planet. Inter.* **162**, 22–31.
- Isaak, D. G., G. D. Gwanmesia, M. G. Davis, S. C. Stafford, A. M. Stafford, and R. S. Triplett (2010). The temperature dependence of the elasticity of Fe-bearing wadsleyite. *Phys. Earth Planet. Inter.* **182**, 107–112.
- Ita, J. and L. Stixrude (1992). Petrology, elasticity, and composition of the mantle transition zone. *J. Geophys. Res.: Solid Earth* **97**, 6849–6866.
- Jacobsen, S. D., S. Demouchy, D. J. Frost, T. Boffa Ballaran, and J. Kung (2005). A systematic study of OH in hydrous wadsleyite from polarized FTIR spectroscopy and single-crystal X-ray diffraction: Oxygen sites for hydrogen storage in Earth's interior. *Am. Mineral.* **90**, 61–70.
- Katsura, T., N. Mayama, K. Shouno, M. Sakai, A. Yoneda, and I. Suzuki (2001). Temperature derivatives of elastic moduli of $(\text{Mg}_{0.91}\text{Fe}_{0.09})_2\text{SiO}_4$ modified spinel. *Phys. Earth Planet. Inter.* **124**, 163–166.
- Kawazoe, T., A. Chaudhari, J. R. Smyth, and C. McCammon (2016). Coupled substitution of Fe^{3+} and H^+ for Si in wadsleyite: A study by polarized infrared and Mössbauer spectroscopies and single-crystal X-ray diffraction. *Am. Mineral.* **101**, 1236–1239.
- Kleppe, A. K., A. P. Jephcoat, H. Olijnyk, A. E. Slesinger, S. C. Kohn, and B. J. Wood (2001). Raman spectroscopic study of hydrous wadsleyite (β - Mg_2SiO_4) to 50 GPa. *Phys. Chem. Miner.* **28**, 232–241.
- Kohlstedt, D. L., H. Keppler, and D. C. Rubie (1996). Solubility of water in the α , β and γ phases of $(\text{Mg,Fe})_2\text{SiO}_4$. *Contrib. Mineral. Petrol.* **123**, 345–357.
- Kudoh, Y. and T. Inoue (1998). Effect of pressure on the crystal structure of hydrous wadsleyite, $\text{Mg}_{1.75}\text{SiH}_{0.5}\text{O}_4$. In: *Properties of Earth and Planetary Materials at High Pressure and Temperature*. Ed. by M. H. Manghnani and T. Yagi. American Geophysical Union, Washington, DC, 517–521.
- (1999). Mg-vacant structural modules and dilution of the symmetry of hydrous wadsleyite, β - $\text{Mg}_{2-x}\text{SiH}_{2x}\text{O}_4$ with $0.00 \leq x \leq 0.25$. *Phys. Chem. Miner.* **26**, 382–388.
- Kudoh, Y., T. Inoue, and H. Arashi (1996). Structure and crystal chemistry of hydrous wadsleyite, $\text{Mg}_{1.75}\text{SiH}_{0.5}\text{O}_4$: possible hydrous magnesium silicate in the mantle transition zone. *Phys. Chem. Miner.* **23**, 461–469.
- Li, B. and R. C. Liebermann (2000). Sound velocities of wadsleyite β - $(\text{Mg}_{0.88}\text{Fe}_{0.12})_2\text{SiO}_4$ to 10 GPa. *Am. Mineral.* **85**, 292–295.
- Li, B., G. D. Gwanmesia, and R. C. Liebermann (1996). Sound velocities of olivine and beta polymorphs of Mg_2SiO_4 at Earth's transition zone pressures. *Geophys. Res. Lett.* **23**, 2259–2262.
- Li, B., R. C. Liebermann, and D. J. Weidner (1998). Elastic moduli of wadsleyite (β - Mg_2SiO_4) to 7 Gigapascals and 873 Kelvin. *Science* **281**, 675–677.
- (2001). P - V - V_p - V_s - T measurements on wadsleyite to 7 GPa and 873 K: Implications for the 410-km seismic discontinuity. *J. Geophys. Res.: Solid Earth* **106**, 30579–30591.
- Libowitzky, E. and G. R. Rossman (1996). Principles of quantitative absorbance measurements in anisotropic crystals. *Phys. Chem. Miner.* **23**, 319–327.
- (1997). An IR absorption calibration for water in minerals. *Am. Mineral.* **82**, 1111–1115.
- Liu, W., J. Kung, B. Li, N. Nishiyama, and Y. Wang (2009). Elasticity of $(\text{Mg}_{0.87}\text{Fe}_{0.13})_2\text{SiO}_4$ wadsleyite to 12 GPa and 1073 K. *Phys. Earth Planet. Inter.* **174**, 98–104.

- Mao, Z., S. D. Jacobsen, F. Jiang, J. R. Smyth, C. M. Holl, and T. S. Duffy (2008a). Elasticity of hydrous wadsleyite to 12 GPa: Implications for Earth's transition zone. *Geophys. Res. Lett.* **35**, L21305.
- Mao, Z., S. D. Jacobsen, F. M. Jiang, J. R. Smyth, C. M. Holl, D. J. Frost, and T. S. Duffy (2008b). Single-crystal elasticity of wadsleyites, β - Mg_2SiO_4 , containing 0.37–1.66 wt.% H_2O . *Earth Planet. Sci. Lett.* **268**, 540–549.
- Mao, Z., S. D. Jacobsen, D. J. Frost, C. A. McCammon, E. H. Hauri, and T. S. Duffy (2011). Effect of hydration on the single-crystal elasticity of Fe-bearing wadsleyite to 12 GPa. *Am. Mineral.* **96**, 1606–1612.
- Mayama, N., I. Suzuki, T. Saito, I. Ohno, T. Katsura, and A. Yoneda (2004). Temperature dependence of elastic moduli of β -(Mg, Fe) $_2\text{SiO}_4$. *Geophys. Res. Lett.* **31**, L04612.
- McCammon, C. A., D. J. Frost, J. R. Smyth, H. M. S. Laustsen, T. Kawamoto, N. L. Ross, and P. A. van Aken (2004). Oxidation state of iron in hydrous mantle phases: implications for subduction and mantle oxygen fugacity. *Phys. Earth Planet. Inter.* **143–144**, 157–169.
- Mizukami, S., A. Ohtani, N. Kawai, and E. Ito (1975). High-pressure X-Ray diffraction studies on β - and γ - Mg_2SiO_4 . *Phys. Earth Planet. Inter.* **10**, 177–182.
- Mrosko, M., M. Koch-Müller, C. McCammon, D. Rhede, J. R. Smyth, and R. Wirth (2015). Water, iron, redox environment: effects on the wadsleyite–ringwoodite phase transition. *Contrib. Mineral. Petrol.* **170**, 9.
- Paterson, M. S. (1982). The determination of hydroxyl by infrared absorption in quartz, silicate glasses and similar materials. *Bull. Mineral.* **105**, 20–29.
- Prescher, C., C. McCammon, and L. Dubrovinsky (2012). MossA: a program for analyzing energy-domain Mössbauer spectra from conventional and synchrotron sources. *J. Appl. Crystallogr.* **45**, 329–331.
- Purevjav, N., T. Okuchi, N. Tomioka, X. Wang, and C. Hoffmann (2016). Quantitative analysis of hydrogen sites and occupancy in deep mantle hydrous wadsleyite using single crystal neutron diffraction. *Sci. Rep.* **6**, 34988.
- Sano-Furukawa, A., T. Kuribayashi, K. Komatsu, T. Yagi, and E. Ohtani (2011). Investigation of hydrogen sites of wadsleyite: A neutron diffraction study. *Phys. Earth Planet. Inter.* **189**, 56–62.
- Sawamoto, H. (1986). Single crystal growth of the modified spinel (β) and Spinel (γ) phases of (Mg,Fe) $_2\text{SiO}_4$ and some geophysical implications. *Phys. Chem. Miner.* **13**, 1–10.
- Sawamoto, H., D. J. Weidner, S. Sasaki, and M. Kumazawa (1984). Single-crystal elastic properties of the modified spinel (beta) phase of magnesium orthosilicate. *Science* **224**, 749–751.
- Sinogeikin, S. V., T. Katsura, and J. D. Bass (1998). Sound velocities and elastic properties of Fe-bearing wadsleyite and ringwoodite. *J. Geophys. Res.: Solid Earth* **103**, 20819–20825.
- Smyth, J. R., T. Kawamoto, S. D. Jacobsen, R. J. Swope, R. L. Hervig, and J. R. Holloway (1997). Crystal structure of monoclinic hydrous wadsleyite [β -(Mg,Fe) $_2\text{SiO}_4$]. *Am. Mineral.* **82**, 270–275.
- Smyth, J. R., N. Bolfan-Casanova, D. Avignant, M. El-Ghazzi, and S. M. Hirner (2014). Tetrahedral ferric iron in oxidized hydrous wadsleyite. *Am. Mineral.* **99**, 458–466.
- Stixrude, L. and C. Lithgow-Bertelloni (2005). Thermodynamics of mantle minerals – I. Physical properties. *Geophys. J. Int.* **162**, 610–632.
- (2011). Thermodynamics of mantle minerals – II. Phase equilibria. *Geophys. J. Int.* **184**, 1180–1213.
- Suzuki, I., E. Ohtani, and M. Kumazawa (1980). Thermal expansion of modified spinel, β - Mg_2SiO_4 . *J. Phys. Earth* **28**, 273–280.

- Trots, D. M., A. Kurnosov, Tiziana Boffa Ballaran, and D. J. Frost (2012). High-temperature structural behaviors of anhydrous wadsleyite and forsterite. *Am. Mineral.* **97**, 1582–1590.
- Wang, J., J. D. Bass, and T. Kastura (2014). Elastic properties of iron-bearing wadsleyite to 17.7 GPa: Implications for mantle mineral models. *Phys. Earth Planet. Inter.* **228**, 92–96.
- Wehner, R. K. and R. Klein (1971). Adiabatic and isothermal elastic constants from space- and time-dependent response theory. *Physica* **52**, 92–108.
- Woodland, A. B. and R. J. Angel (1998). Crystal structure of a new spinelloid with the wadsleyite structure in the system $\text{Fe}_2\text{SiO}_4\text{-Fe}_3\text{O}_4$ and implications for the Earth's Mantle. *Am. Mineral.* **83**, 404–408.
- (2000). Phase relations in the system fayalite–magnetite at high pressures and temperatures. *Contrib. Mineral. Petrol.* **139**, 734–747.
- Woodland, A. B., R. J. Angel, and M. Koch (2012). Structural systematics of spinel and spinelloid phases in the system $\text{MFe}_2\text{O}_4\text{-M}_2\text{SiO}_4$ with $\text{M} = \text{Fe}^{2+}$ and Mg. *Eur. J. Mineral.* **24**, 657–668.
- Ye, Y., R. A. Schwering, and J. R. Smyth (2009). Effects of hydration on thermal expansion of forsterite, wadsleyite, and ringwoodite at ambient pressure. *Am. Mineral.* **94**, 899–904.
- Ye, Y., J. R. Smyth, A. Hushur, M. H. Manghnani, D. Lonappan, P. Dera, and D. J. Frost (2010). Crystal structure of hydrous wadsleyite with 2.8% H_2O and compressibility to 60 GPa. *Am. Mineral.* **95**, 1765–1772.
- Yusa, H. and T. Inoue (1997). Compressibility of hydrous wadsleyite (β -phase) in Mg_2SiO_4 by high pressure X-ray diffraction. *Geophys. Res. Lett.* **24**, 1831–1834.
- Zha, C.-S., T. S. Duffy, H.-K. Mao, R. T. Downs, R. J. Hemley, and D. J. Weidner (1997). Single-crystal elasticity of $\beta\text{-Mg}_2\text{SiO}_4$ to the pressure of the 410 km seismic discontinuity in the Earth's mantle. *Earth Planet. Sci. Lett.* **147**, E9–E15.

(Eidesstattliche) Versicherungen und Erklärungen

(§9 Satz 2 Nr. 3 PromO BayNAT)

Hiermit versichere ich eidesstattlich, dass ich die Arbeit selbstständig verfasst und keine anderen als die von mir angegebenen Quellen und Hilfsmittel benutzt habe.

(vgl. §64 Abs. 1 Satz 6 BayHSchG)

(§9 Satz 2 Nr. 3 PromO BayNAT)

Hiermit erkläre ich, dass ich die Dissertation nicht bereits zur Erlangung eines akademischen Grades eingereicht habe und dass ich nicht bereits diese oder eine gleichartige Doktorprüfung endgültig nicht bestanden habe.

(§9 Satz 2 Nr. 4 PromO BayNAT)

Hiermit erkläre ich, dass ich Hilfe von gewerblichen Promotionsberatern bzw. -vermittlern oder ähnlichen Dienstleistern weder bisher in Anspruch genommen habe noch künftig in Anspruch nehmen werde.

(§9 Satz 2 Nr. 7 PromO BayNAT)

Hiermit erkläre ich mein Einverständnis, dass die elektronische Fassung meiner Dissertation unter Wahrung meiner Urheberrechte und des Datenschutzes einer gesonderten Überprüfung unterzogen werden kann.

(§9 Satz 2 Nr. 8 PromO BayNAT)

Hiermit erkläre ich mein Einverständnis, dass bei Verdacht wissenschaftlichen Fehlverhaltens Ermittlungen durch universitätsinterne Organe der wissenschaftlichen Selbstkontrolle stattfinden können.

Pasadena, CA, 17. Juni 2019

.....